الجمهورية الجزائرية الديمقراطية الشعبية

République Algérienne Démocratique et Populaire

وزارة التعليم العالي والبحث العلمي

Ministère de l'Enseignement Supérieur et de la Recherche Scientifique

Université Mohamed Khider – Biskra
Faculté des Sciences Exactes et
Sciences de la Nature et de la Vie

جامعة محمد خيضر - بسكرة
كلية العلوم الدقيقة و علوم الطبيعة
و الحياة

Thèse présentée en vue de l'obtention

du diplôme de

Doctorat LMD

Spécialité ou option**: Physique des matériaux**

Study and numerical simulation of (a-Si:H/µc-Si:H) heterojunction solar cells.

Etude et simulation numérique des cellules solaires à hétérojonction (a-Si:H/µc-Si:H)

Présenté par

Abdel Fodhil Bouhdjar

Devant le jury composé de:

Soltani Mohamed Toufik	Professeur	Université de Biskra	Président
Meftah Amjad	Professeur	Université de Biskra	Rapporteur
Sengouga Nouredine	Professeur	Université de Biskra	Examinateur
Meftah Afak	Professeur	Université de Biskra	Examinatrice
Dehimi Lakhdar	Professeur	Université de Batna	Examinateur
Bouras Fethi	MCA	Université d'El-Oued	Examinateur

Acknowledgement

Firstly, I would like to express my sincere gratitude to my advisor Pr. Amjad Meftah for advising me in licence, master and especially in Ph.D. for the continuous support of all my university's journey, study and related research. A great thanks for her patience, motivation, and immense knowledge. Her guidance helped me in all the time of research and writing of this thesis. I could not have imagined having a better advisor and mentor for my Ph.D. study. My sincere thanks also go to all LMSM members for all the facilities they offered and the fraternal atmosphere.

I would like to thank the University of Biskra for its financial support for the scientific visits to the University of Dundee. Thanks also goes to Professor Steve Reynolds "lecturer and director of research studies at School of Engineering, physics and mathematics University of Dundee" for his generous reception and valuable suggestions.

I would also like to thank my committee members, Professor Soltani Mohamed Toufik, Professor Sengouga Nouredine, Professor Meftah Afak, Professor Dehimi Lakhdar, and Professor Bouras Fethi for serving as my committee members.

A special thanks to my family: my parents my brothers and sister for trusting and supporting me spiritually throughout writing this thesis, words cannot express how grateful I am to my mother, and father for all of the sacrifices that they've made on my behalf. Your prayer for me was what sustained me thus far. Last but not the least, I would also like to thank all of my friends who supported me in writing, and pushed me to strive towards my goal, specially "the big four" Samo, Datto and Bobby.

Dedication

I dedicate this work to my father and my mother.

I know I will always burn to be

The one who seeks so I may find

The more I search, the more my need

Time was never on my side

So you remind me what left this outlaw torn

Abstract

It is known that hydrogenated amorphous silicon (a-Si:H) thin films technology has some advantages compared to that of crystalline silicon (c-Si) such as; the fabrication low cost and the facility of deposition on a wide range of substrates. Moreover, the a-Si:H structure makes the electronic devices designed by it, such as the solar cells, more resistive and have a more considerable life time. The essential limitation compared to c-Si is the photo-degradation effect which reduces the a-Si:H solar cell conversion efficiency. Several technologies are used to improve the conversion efficiency such as the growth of the microcrystalline silicon (µc-Si:H) which exhibits a good conductivity and stability against the degradation, and the use of multi-junction design (double or triple junction devices) in order to cover a wide range of the solar spectrum, which enhances the optical absorption and so the conversion efficiency. The combination between a-Si:H and µc-Si:H, known as micromorph(a-Si:H/µc-Si:H) tandem cells, include both advantages of a-Si:H and µc-Si:H, they are less subject to light-induced degradation and show better stabilized efficiencies as compared to those attainable from a-Si:H devices.

The aim of this work is about the study of a-Si:H and µc-Si:H silicon- based solar cells in different configurations; the single one , and the micromorph tandem cell with two terminal (2T) and four terminal (4T) electrical connections respectively. Using the simulation by Silvaco TCAD , we have extracted the external parameters of the studied solar cells such as; the characteristic current density –voltage (*J*-*V*) , the short circuit current density J_{SC}, the open circuit voltage V_{OC} and the conversion efficiency η, and we tried to physically understand and explain the photo-electric behavior of the solar cells, by analyzing the internal parameter profiles such as: the electric field, the charge carrier densities, and the recombination rates. This has been used to optimize the solar cell performance in single and tandem configurations, under various parameter effect such as the photo-degradation, i-layer thickness and mobilities, taking into account the experimental results of other researches. The optimal obtained efficiencies η are 9.07% at initial state (reduced to 7.66% at

degraded state) for the a-Si:H single cell, 9.06% for the µc-Si:H single cell, 12.01% at initial state (reduced to 10.40% at degraded state) for the 2T-micromorph tandem cell, and 12.27% at initial state (reduced to 11.39% at degraded state) for the 4T-micromorph device.

Key words: a-Si:H, µc-Si:H, solar cells, heterojunction, micromorph, simulation.

Résumé

Il est connu que la technologie des couches minces en silicium amorphe hydrogéné (a-Si:H) présente quelques avantages par rapport à celle en silicium cristallin (c-Si:H) tels que ; le faible cout de fabrication et la facilité de déposition sur une large gamme de substrats. De plus, la structure interne du (a-Si:H) rend les dispositifs électroniques conçus à sa base, telles que les cellules solaires, plus résistifs et ayant une durée de vie assez large. La limitation primordiale du a-Si:H par rapport au (c-Si) est l'effet de photodégradation qui réduit le rendement de la conversion photovoltaïque de la cellule solaire. Plusieurs technologies sont employées pour améliorer le rendement de la conversion telle que l'élaboration du silicium microcristallin (µc-Si:H) qui montre une bonnes conductivité et une stabilité contre la dégradation, l'utilisation de la configuration de multi-jonction (dispositifs doubles ou triples jonction) pour couvrir une large gamme du spectre solaire, ce qui augmente l'absorption optique et ainsi le rendement de conversion. La combinaison entre le a-Si:H et le µc-Si:H, connus sous le nom de cellules solaires tandem micromorph(a-Si:H/µc-Si:H), comportent les deux avantages du a-Si:H et du µc-Si:H, ils sont moins sensibles à la dégradation provoquée par la lumière et montrent de meilleurs rendements et une bonne stabilité par rapport aux autres dispositifs à base du a-Si:H.

Le but de ce travail est l'étude des cellules solaires à base du a-Si:H et du µc-Si:H dans des configurations différentes; singulière, et la configuration de cellule tandem micromorph à deux terminales (2T) et quatre terminales (4T) respectivement. En utilisant la simulation par Silvaco TCAD, nous avons extrait les paramètres externes des cellules solaires étudiées comme; la caractéristique densité de courant-tension *(J-V)* , la densité de courant au court-circuit $J_{sc,}$ la tension au circuit ouvert V_{oc} et le rendement de la conversion η, et nous avons essayé de comprendre et expliquer le comportement photo-électrique de ces cellules solaires, en analysant les profils des

paramètres internes comme: le champ électrique, la densité des porteurs de charge, et les taux de recombinaison. Ceci a été utilisé pour optimiser la cellule solaire dans les configurations singulière et tandem, sous l'effet de plusieurs paramètres tel que la photodégradation, l'épaisseur de la couche intrinsèque (i) et les mobilités des porteurs de charge, en tenant compte des résultats expérimentaux d'autres recherches. Les meilleurs rendements η obtenus sont 9.07% à l'état initial (réduit à 7.66% à l'état dégradé) pour la cellule a-Si:H singulière, 9.06% pour la cellule de µc-Si:H singulière, 12.01% à l'état initial (réduit à 10.40% à l'état dégradé) pour la cellule micromorphe tandem à 2T, et 12.27% à l'état initial (réduit à 11.39% à l'état dégradé) pour la cellule micromorphe tandem à 4T.

Mots clés: a-Si:H, µc-Si:H, Cellules solaires, hétérojonction, micromorphe, simulation

ملخص

من المعروف أن تكنولوجيا الطبقات الرقيقّة الخاصة بالسيلّيكّون المهدرج غيرٌ المتبلور تملك العديدٌ من المزاياً مقارنة بتلك الخاصة بالسيلّكّون المتبلور مثل؛ انخفاض تكلفة الإعداد وسهولة توضعه على مجموعة واسعة من المساند. علاوة على ذلك، فإن البنية الداخليةٌ لل a-Si:H تجعل من المركبات الإلكترونيةٌ مثل الخلاياً الشمسيةٌ أكثر مقاومة، وتعطيهًا مدة حياًة أطول . أكثر مساوئ a-Si:H مقارنة مع c-Si هي تدهور بنيتّه بسبب الضوء مما يؤّدي الى تناقص كفاءة التحويل الكهروضوئي؛ عدة تقنيات استعملت لتحسينٌ مردود التحويلٌ الكهروضوئي؛ مثل تنمية السيلّكون المهدرج المتبلور جزئياً (µc-Si:H) والذي يمّتلك ناقلية جيدّة و استقرار ضد التدهور، و استعمال الخلاياً الشمسية متعددة الوصلات (المتضاعفة او الثلاثية) و ذلك لتغطية اكبر قدر ممكن من الطيفٌ الشمسي، ما يرّفع قدر الخليةٌ من امتصاص الضوء وبالتالي رفع المردود. تركيب وصلتين من a-Si:H و µc-Si:H أو ما تعرف بالخلية المتضاعفة (a-Si:H/µc-Si:H) تتضمن على محاسن كل من a-Si:H و µc-Si:H و هي أقل حساسية للتدهور المتولد بالضوء و تظهر مردود حسن و مستقر مقارنة مع الأجهزة المصنوعة فقط من a-Si:H.

يسّتند موضوع هذا البحث على دراسة الخلاياً الشمسيةٌ المتكونة من a-Si:H و µc-Si:H في تركيبًات مختلفة ؛احاديةٌ الوصلة ، ثنائية الوصلة ذات نهايتينٌ و ذات اربع نهاياًت كهربائية على التوالي. اعتمادا على المحاكاة الرقم ةٌ بواسطة Silvaco TCAD تمكنا من استخلاص الخصائص الخارجيةٌ للخليةٌ مثل خاصيةٌ كثافة التيار – جهد، كثافة تيار الدارة القصيرة Jsc ، جهد الدارة المفتوحة Voc، و مردود التحول η. و عبر فحص توزيعات الوسائط الداخلية للخلية مثل الحقل الكهربائي، تركيزٌ حاملات الشحنة، معدلات الالتحام...حاولنا فهم و شرح التصرف الضوئي- الكهربائي للخلايا الشمسية.

في سبيلٌ تحسينٌ أداء الخلية الشمسية في التركيبة أحادية الوصلة و الثنائية، تمت دراسة تأثيرٌ مختلف الخصائص المتعلقة بالخلية ، مثل فعل التدهور بالضوء سمك الطبقة الجوهرية (i) و حركيات حاملات الشحنة آخذين بعين الاعتبار النتائج التجريبيةٌ المتحصّل عليهًا في هذا المجال.

احسن نتائج المردود η كانت 9.07% في الوضع الابتدائي انخفضت إلى 7.66% بعد التدهور بالنسبة للخليةٌ أحادية الوصلة من a-Si:H. 9.06% .بالنسبة للخليةٌ أحادية الوصلة من µc-Si:H، 12.01% في الوضع الابتدائي انخفضت الى 10.40% بعد التدهور بالنسبة للخليةٌ ثنائية الوصلة ذات نهايتٌينٌ و 12.27% في الوضع الابتدائي انخفضت الى 11.39% بعد التدهور بالنسبة للخليةٌ ثنائية الوصلة ذات اربع نهايأٌت.

الكلمات المفتاحية: السيليكون المهدرج غير المتبلور ، السيليكون المتبلور جزئيا ، خلايا شمسية ، وصلات غير متجانسة، محاكاة رقمية

Table of contents

List of figures

List of tables

Chapter I

General Introduction

General Introduction

I.1) Solar photovoltaic energy

Because of the development of industry, transport, means of communication and many other energetic fields, the world growth of the consumption of electricity observed these last decades still will be accentuated. The electric power is generally produced by combustion starting from nonrenewable resources (coal, oil, gas...) whose times of exhaustion are of a few decades. The energy obtained thanks to the photovoltaic cells is regarded more and more as an energy which can contribute to the world production of the electric power taking part effectively in the durable development [1].

Indeed, the sector of photovoltaic has a very significant potential and could become one of the principal sources of long-term energy. Let us specify that energy that the sun sends to us represents an inexhaustible source, equivalent to more than 5000 times the power consumption on ground [2]. As an example, the surface of the roofs directed towards the south would make it possible to cover the totality of the requirements in electricity for the continent. It is of course an image, because the continuous provisioning of energy must be multi-source (hydraulics, wind, biomass, geothermics...). Nevertheless, the field of photovoltaic has many advantages: solar energy is available on all the surface of the sphere and the maximum of photovoltaic production of electricity coincide with the peaks of consumption (day). Moreover devices require little maintenance, are reliable, flexible, not pollutants and silencer.
The photovoltaic (PV) sector has been growing with a compounded annual growth rate of nearly 60% over the last ten years and it is still increasing until now as can be seen in
Figure I.1 [3].

Historically, the United States had been the leader of installed photovoltaics for many years, and its total capacity amounted to 77 megawatts in 1996—more than any other country in the world at the time. Then, Japan stayed ahead as the world's leader of produced solar electricity until 2005, when Germany took the lead [4]. The country is currently approaching the 40,000 megawatt mark [3]. China is expected to continue its rapid growth and to triple its PV capacity to 70,000 megawatts by 2017, becoming the world's largest producer of photovoltaic power any time soon [5, 6].

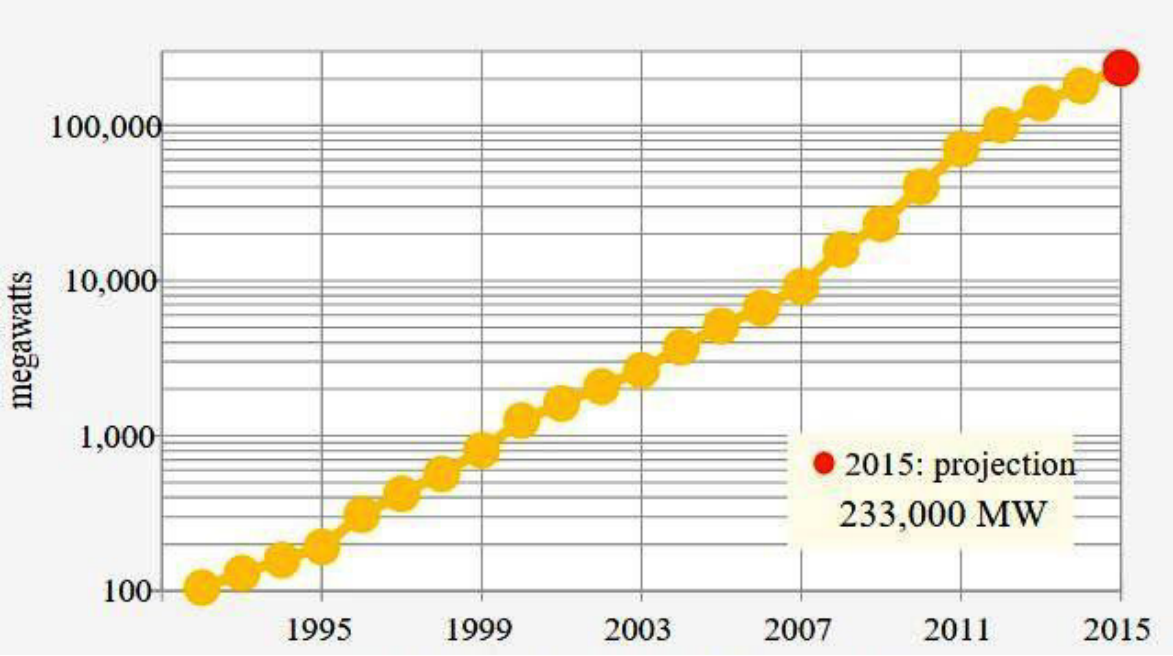

Figure I.1: Global cumulative PV capacity in MW since 1992 [7]**.**

By the end of 2014, cumulative photovoltaic capacity reached at least 178 giga watts (GW), sufficient to supply 1 percent of global electricity demands. Solar now contributes 7.9 % and 7.0 % to the respective annual domestic consumption in Italy and Germany [8]. For 2015, worldwide deployment of about 55 GW is being forecasted, and installed capacity is projected to more than double or even triple beyond 500 GW between now and 2020 [4]. By 2050, solar power is anticipated to become the world's largest source of electricity, with solar photovoltaic and concentrated solar power contributing 16 and 11 %, respectively [4]. This will require PV capacity to grow to 4,600 GW, of which more than half is forecasted to be deployed in China and India [9].

The growth of photovoltaic would probably not have been so fast without the introduction of subsidies by certain countries. Nevertheless, the massive industrialization of the sector of these ten last year's made it possible to appreciably decrease the price of the photovoltaic panels, which did not achieve the discounted goal yet [7].

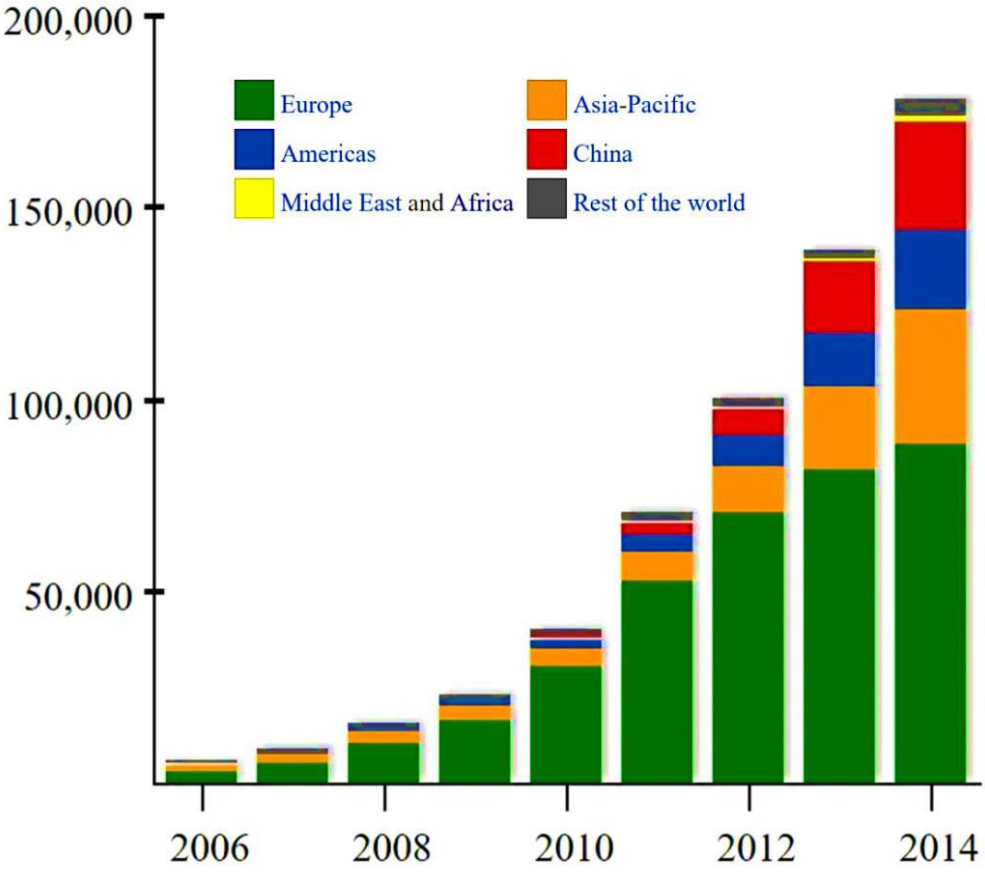

Figure I.2: Cumulative capacity in megawatts peak [MW_p] grouped by region [7].

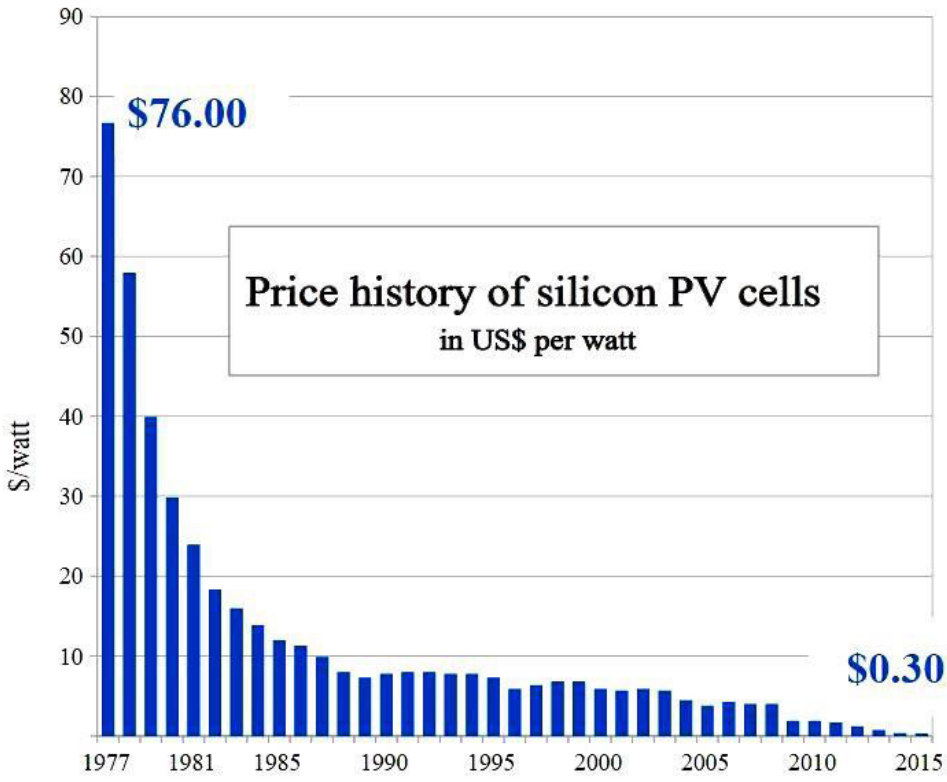

Figure I.3: Price decline of c-Si solar cells [7].

Despite tremendous progress in all aspects of production of Si-based solar cells and the rapid decrease of production cost for PV modules [10] from 10 $/Wp at the beginning of the nineties to 0.3 $/Wp in 2014, the cost/kWh is still too high to compete with other sources of electricity generation [11].

Photovoltaic industry rests primarily on the use of silicon like basic material (~93%) [12]. This semiconductor has indeed various advantages: it is abundant on the surface of the sphere, it is not toxic and its technology is well controlled thanks to the development of micro-electronics. This material is used in various forms: single-crystal, polycrystalline, amorphous or in the form of ribbons. Polycrystalline silicon is of worse quality than its alternative single-crystal, but makes it possible to reach relatively high outputs of conversion at largely less manufacturing costs. Thus, this type of silicon currently occupies the most significant share of the production [13].
More specifically, 36% of the 2013 production is based on single-crystal Si but the main part is based on µc-Si cells substrates and ribbons (55 %). The remainder is based on thin-film solar cell technologies and consists of 2% based on thin-film amorphous Si solar cells and 7% on polycrystalline compound solar cells based on CdTe and CIGS (Figure I.4,Figure I.5) [13].

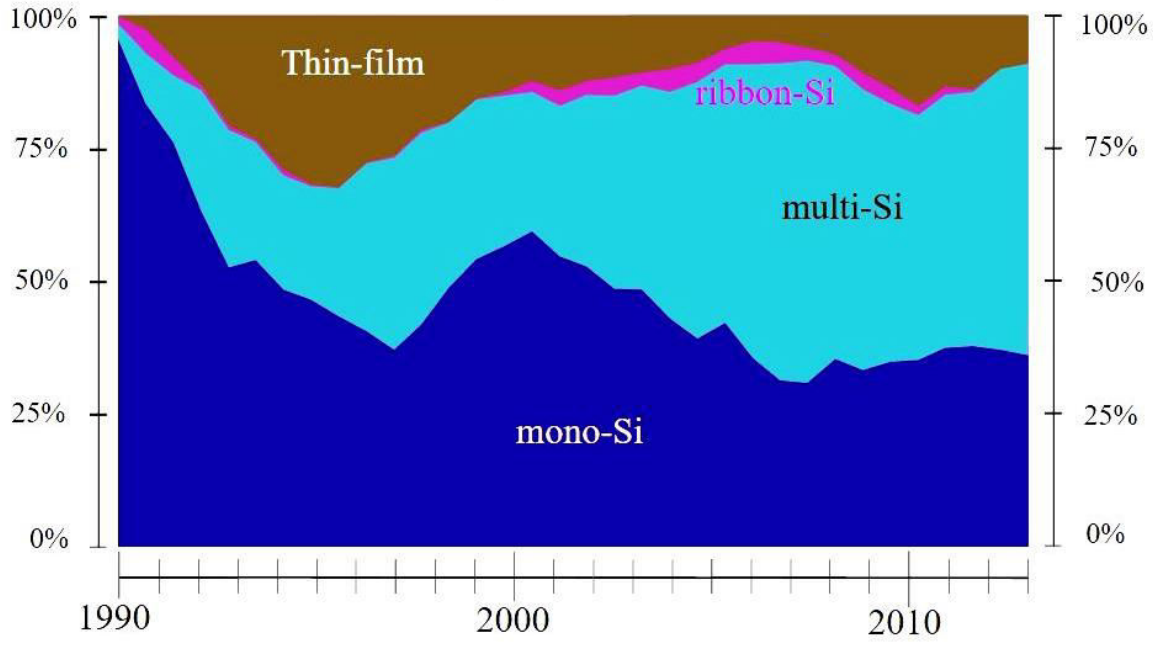

Figure I.4: Global market share by PV technology from 1990 to 2013 [7].

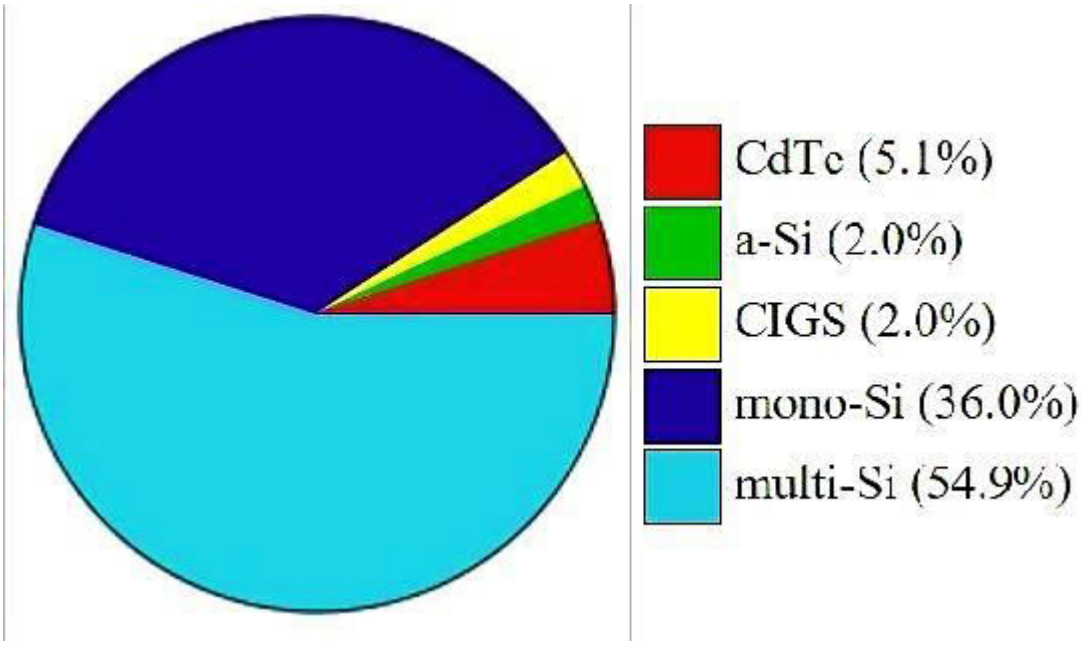

Figure I.5: Global PV market by technology in 2013 [7].

Algeria in particular and the Maghreb countries have a raised solar potential. The solar burn-up rates carried out by satellites by the German Space Agency (Deutsches Zentrum für Luft-und Raumfahrt: DLR), show exceptional levels of sunning of about 1200 kWh/m^2/year in the North of the Large Sahara. On the other hand, the best solar burn-up rates in Europe is about 800 kWh/m2/year and are limited to the southern part of Europe. Following an evaluation by satellites, the German Space Agency (DLR) concluded, that Algeria represents the solar potential most significant of all the Mediterranean basin, that is to say: 169.000 TWh/year for solar thermic, 13,9 TWh/year for the solar photovoltaic one and 35 TWh/year for the wind one [14].

This renewable energy presents at the present time a response to the environmental problems and the gas emissions at effect of greenhouse which threatens whole planet and a durable solution with the current crisis of energy, which places renewable energies, RNE, (hydraulics, wind, photovoltaic, solar thermal, geothermic, biomass, biogas and fuel cell), in the center of the debates carrying on the environment, and more generally the durable development [14].

The Algerian group, specialized in electronics, Condor, communicated the price of the photovoltaic panels manufactured in its unit solar energy. The average cost of the announced Watt, in net of tax, is of 95 DA [15], which is very expensive compared the price of the conventional sources of electricity.

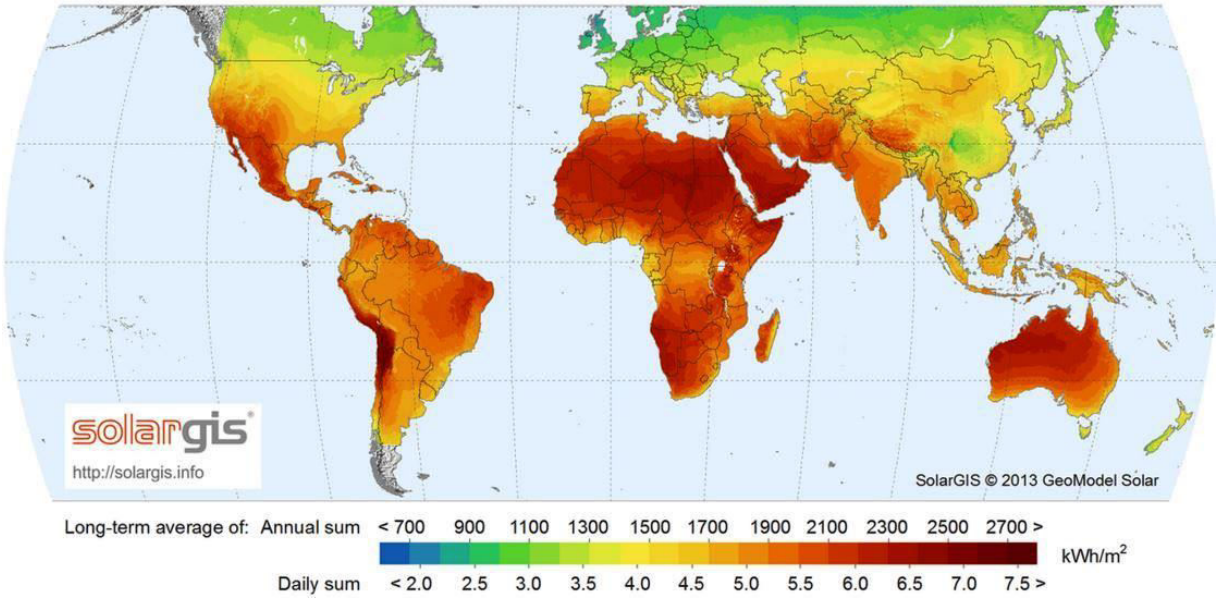

Figure I.6: The annual solar potential of the world [16].

Side of research, one observes a race with the high outputs through several tracks such as the introduction of new photosensitive materials, the improvement of the optical containment of the light penetrating in the component, the combination of several layers of semiconductor materials (multi-junctions) to cover the luminous spectrum broadest. Currently, the technology of crystalline silicon is in a majority on the market of photovoltaic energy in spite of its technological complexity and whose output is hardly acceptable [13].

Due to the initially very high production costs and efforts, crystalline silicon solar cells were first only used in extraterrestrial application but the call for cheaper fabrication led to the use of advanced technologies and investigations on new materials. In 1975, Spear et al. [17] had successfully shown that it is possible to dope thin-film hydrogenated amorphous silicon (a-Si:H), deposited from a gas-mixture of silane and hydrogen [17]. This finding paved the way for the development of amorphous thin-film solar cells using layer thicknesses ~ 100 times thinner than wafer-based solar cells. The first p-i-n solar cell with a-Si:H as absorber material, presented in 1976, had an efficiency of 2.4% [18]. Unfortunately, amorphous silicon exhibits light-induced degradation, which means that sun light creates dangling bonds that act as recombination centers and lead to a reduced solar cell performance [19]. One possibility to increase the stability against degradation is the combination of amorphous silicon-based materials with identical or different band gaps to multijunction solar cells. The individual layers can be deposited much thinner which

reduces the consequences of degradation, and, in case of different band gaps, the solar spectrum is used more efficiently. A stabilized efficiency up to 13.7% was achieved by a triple junction cell made of a-Si:H and a-SiGe:H [20].

Microcrystalline silicon (µc-Si:H) was first deposited by Veprek and Marecek and describes material having small crystallites with a size of a few ten nanometers embedded in amorphous phase [21]. Because of its higher doping efficiency and conductivity, µc-Si:H was initially used as doped layer material in amorphous silicon devices [22]. It was not until 1994 that microcrystalline silicon was used also as absorber material in single junction solar cells [23]. The better absorption behavior is in the infrared wavelength region compared to amorphous silicon, and a negligible degradation made µc-Si:H a suitable candidate for bottom cell intrinsic material in tandem cells as an alternative to a-SiGe:H [24]. Triple junction solar cells with an a-Si:H/µc-Si:H/µc-Si:H structure are also possible and achieved 15% on lab scale [25]. A big advantage of the silicon-based thin-film technology is its possibility to deposit on large areas. At present (2015), a-Si:H/µc-Si:H modules achieve up to 10% (total area) efficiency on $2.6 \times 2.2\ m^2$ size, and just recently Oerlikon Solar reported on efficiencies of 10.0% in mass production on substrates sizes of $1.3 \times 1.1\ m^2$ [26].

I.2) Modelling

Modeling is a very important aspect of research on solar cells and materials used in making solar cells. Using numerical computer modeling or simulations enables researchers to investigate properties of materials that cannot be investigated by means of practical measurements. Most if not all simulators used for solar cells are built on the bases of the Poisson equation and the continuity equations. In solar cells, there are two main properties we look at in order to determine the solar cell functionality and efficiency, these are the optical and the electrical properties. These properties can be investigated using simulations. In this work; this will be done using the SILVACO TCAD simulator which will be described later on.

I.3) Motivation and objectives of thesis

Hydrogenated Microcrystalline silicon (µc-Si:H) is a new material whose research carries out thorough studies. It is a mixed-phase material, consisting of a crystalline phase, an amorphous phase and some voids [27]. This complex structure makes the experimental study of µc-Si:H a challenge. To overcome some of these challenges in the study of µc-Si:H, optical and electrical modeling and simulations are being

employed to study the film properties and their impact on the performance of the solar cell [28-30]**.** Modeling and simulations has the advantage of investigating properties with experimental limitations, this is done in very little time.

This work is aimed at understanding the operation of amorphous and microcrystalline silicon- based solar cells (a-Si:H and µc-Si:H respectively) in view of optimizing its performance by modeling in order to create a better micromorph (a-Si:H/µc-Si:H) tandem solar cell. The electrical characteristics of the a-Si:H and µc-Si:H solar cells in single configuration, and in a micromorph tandem configuration with two-terminal (2T) and four-terminal (4T) electrical connections, will be investigated by modeling with the aim to extract their output photovoltaic parameters for a better performance. For the simulations carried out in this work, we will make use of Atlas simulator which is a module in Silvaco Tcad. ATLAS is a physically-based two and three dimensional device simulator. It predicts the electrical and optical behavior of specified semiconductor structures and devices, and provides insight into the internal physical mechanisms associated with device operation.

I.4) Outline of the thesis

Chapter 1 is a general literature review, a brief introduction of solar photovoltaic energy around the world and Algeria in special case, to thin-film silicon-based solar cells, and works done on typical cells based on a-Si:H and µc-Si:H materials, and on (a-Si:H/µc-Si:H) hetero-junction in multi-junction (tandem, triple) configurations. Chapter 2 describes the structural, electrical and optical properties of a-Si:H and µc-Si:H as materials, including also the defect model and the a-Si:H films degradation (light soaking effect) as they are exposed to solar irradiation. Additionally is presented, the deposition process, usually used to produce a-Si:H and µc-Si:H as thin-layers in solar cells. Chapter 3 presents the solar cell basics and methods of improving the conversion efficiency of typical solar cells based on a-Si:H and µc-Si:H materials, and process of achieving better micromorph tandem solar cell with 2T and 4T terminals, respectively. Chapter 4 is dedicated to the explanation of SILVACO TCAD simulator and the physical models that cover the electrical behavior of a semiconductor device such as the solar cell, and allow to study its electrical properties under illumination, which can include the external parameters such as the current-voltage $(I-V)$ characteristics, the spectral response and the quantum efficiency vs. wavelength, and internal quantities like the recombination rates, the charge carrier densities, the potential and field distributions. Finally Chapter 5

presents and discusses the main results investigated on a-Si:H and µc-Si:H-based solar cells in single configuration, and in a micromorph tandem configuration with 2T and 4T electrical connections. In view of optimizing the solar cell output parameters in single and tandem configurations, the study is carried out by analyzing the effect of the main solar cell parameters such as: the light-induced defect density according to the Staebler-Wronski effect, the absorber intrinsic (i)-layer thickness and the free carrier mobilities.

Chapter II

Material properties of a-Si:H and µc-Si:H

II.1) Introduction

Silicon thin-film solar cells are a particularly attractive option for the photovoltaic technology. Among the various options, the technology of hydrogenated amorphous silicon, a-Si:H, is certainly the most advanced. Various companies manufacture modules with efficiencies of 6-8% [31]. Crystalline silicon, in principle, has the potential for higher cell efficiency. The various approaches may be ordered in the sequence of the process temperatures used. Below a growth temperature of $T_s \sim 300°C$, microcrystalline silicon (µc-Si:H) can be made using the same deposition techniques as for a-Si:H, namely plasma enhanced chemical vapor deposition (PECVD) or hot-wire deposition (HW). Characteristic of these materials is the incorporation of hydrogen which enables very effective *in-situ* passivation [32]. In 1976 D. E. Carlson and C. R. Wronski were the first to produce a hydrogenated amorphous silicon (a-Si:H) solar cell [18]. A year later it was shown that the material itself degrades during light exposure [19] leading to a declining solar cell efficiency (so called Staebler-Wronski effect). As a consequence a lot of research related to a-Si:H has been focusing on understanding and minimizing the degradation loss [33]. In the mid-1990s research groups started to intensify their efforts on hydrogenated microcrystalline silicon (µc-Si:H) [23, 34]. Contrary to hydrogenated amorphous silicon µc-Si:H is not prone to degradation, which makes it very interesting for an application in solar cells. But there are more advantages for using hydrogenated microcrystalline silicon. First, the material can be grown with the same equipment as a-Si:H by adjusting the process parameters. Second, the combination of a-Si:H and µc-Si:H in a tandem solar cell enables higher efficiencies compared to single-junction a-Si:H or µc-Si:H solar cells. Third, because of the particular band gaps of a-Si:H and µc-Si:H the tandem solar cell is ideally suited for the solar spectrum [35].

This chapter describes the basic material properties of a-Si:H and µc-Si:H, such as the structural, electrical and optical properties. Also is presented the defect model, the transport, recombination processes, metastability phenomenon and degradation in a-Si:H. Then, a description of the deposition process, used to produce thin-film silicon, is finally presented.

II.2) Hydrogenated amorphous silicon

II.2.1) Structure:

Hydrogenated amorphous silicon is a semiconductor material which has a tetrahedral structure. It was discovered in 1960 when it was deposited by chittick[36],

after that the researches was started by Carlson and Wronski with the development of the photovoltaic devices. A disordered or amorphous structure obviously means there is no long-range order. However, it exist a short-range order. Recently, measurements using novel microscopy methods have shown that the structure of amorphous semiconductors presents also a medium range order (MRO), linked with the correlation between atom positions in the range of few nanometers. Different models are nowadays developed to explain the MRO in the amorphous structure.

The covalent bonds between the silicon atoms are much the same as in the crystalline silicon, with the same number of neighbors and the same average bond lengths and bond angles. The amorphous material has the same short range order as crystal but lacks the long range order. The first few nearest neighbor distances are separately distinguished, but the correlation between atom pairs loses structure after a few interatomic spacings (see Figure II.1).

To determine the structure of amorphous silicon through experiments only is so difficult, because of the long range disorder. The modeling of amorphous networks is important to try more understanding its structure. Zachariasen first proposed in 1932 a Continuous Random Network (CRN) to explain the atomic arrangement in an amorphous network [37]. The model introduces a homogeneous disorder which is on average the same for each atom. The random network has the property of easily incorporating atoms of different coordination, and elementary defects are defined as coordination defects, when an atom has too many or too few bonds. The Si-Si bonding distortion present in amorphous silicon induces bond strains which can result in broken Si-Si bonds, forming dangling bonds. The dangling bonds are in high concentration in pure amorphous silicon, but they can also occupied by hydrogen.

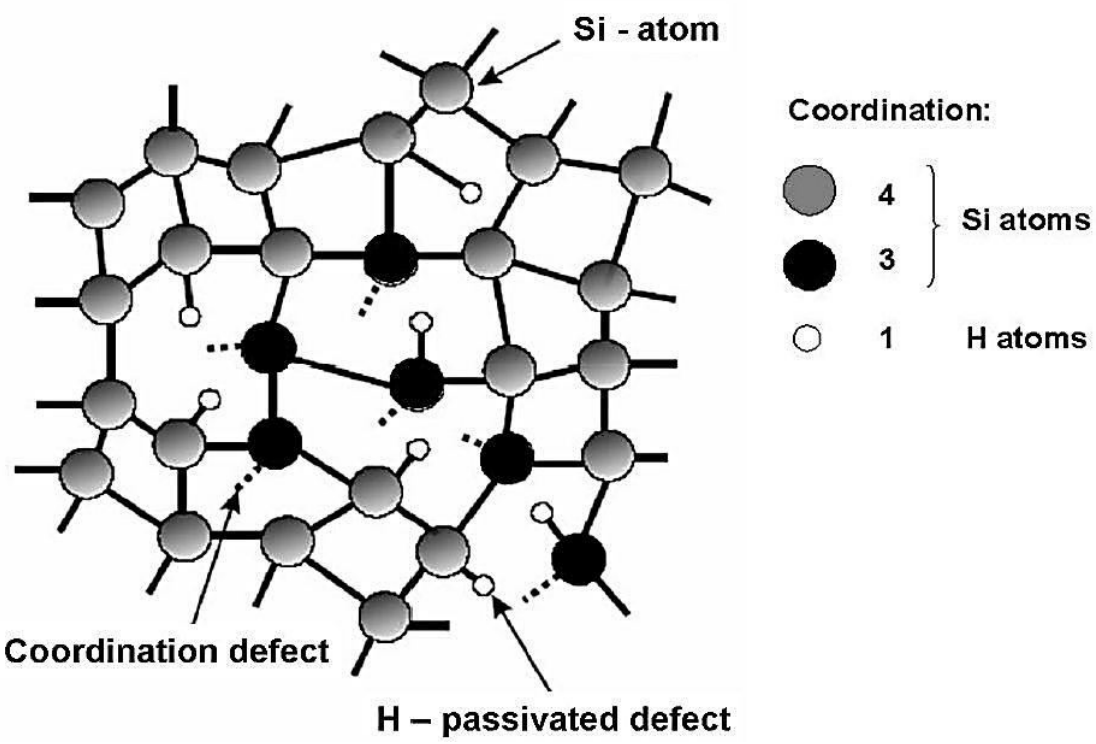

Figure II.1: The atomic arrangement in a-Si:H network**.**

These dangling bonds are the main recombination centers. Carrier collection in p-n type solar cells are obtained by minority carrier diffusion within the p and n layers. Given that diffusion lengths in crystalline solar cells are sufficiently high to ensure pretty good carrier collection. However, in a-Si:H, minority carrier diffusion lengths are extremely small, making it not possible to base minority carrier collection of photo generated carriers on diffusion alone. Therefore, p-i-n diodes are always used for a-Si:H solar cells. In this p-i-n structure, the main part of the absorption takes place in the intrinsic (i) layer, also called absorber layer. Amorphous silicon solar cell has proven to be an attractive device for both the present and the future; however it suffers from the light induced degradation effect known as the Staebler-Wronski effect and stabilizes only at lower efficiency values from the original efficiency value after being exposed for a certain length of time [36].

II.2.2)Electric states

The periodicity of the lattice greatly simplifies the theory for the electronic properties in the crystalline silicon. The periodic potential energy arising from the atomic structure of ordered crystals leads to the Bloch's solutions of the Schrödinger equation. Electrons and holes are described by the wave functions extended through

the entire crystal, with defined momentum k. The energy bands are then described by the function $E(k)$. In the amorphous silicon, the potential energy is not periodic. Bloch's solutions for the wave functions cannot be applied. There is a need for the different theoretical approach to represent the electronic properties of amorphous silicon.

The feature of amorphous silicon bonding structure is the fluctuation in the length and the angle in the Si-Si bonds. These spatial fluctuations create weak bonds, which lead to create a new energy states. The induced energy states are well separated in the lattice site so they became localized, for which no conduction is expected to occur when excited electrons occupy them. The extended states corresponding to the coordinated covalent bonds are delocalized, and the transitions from one state to another are easy [37].

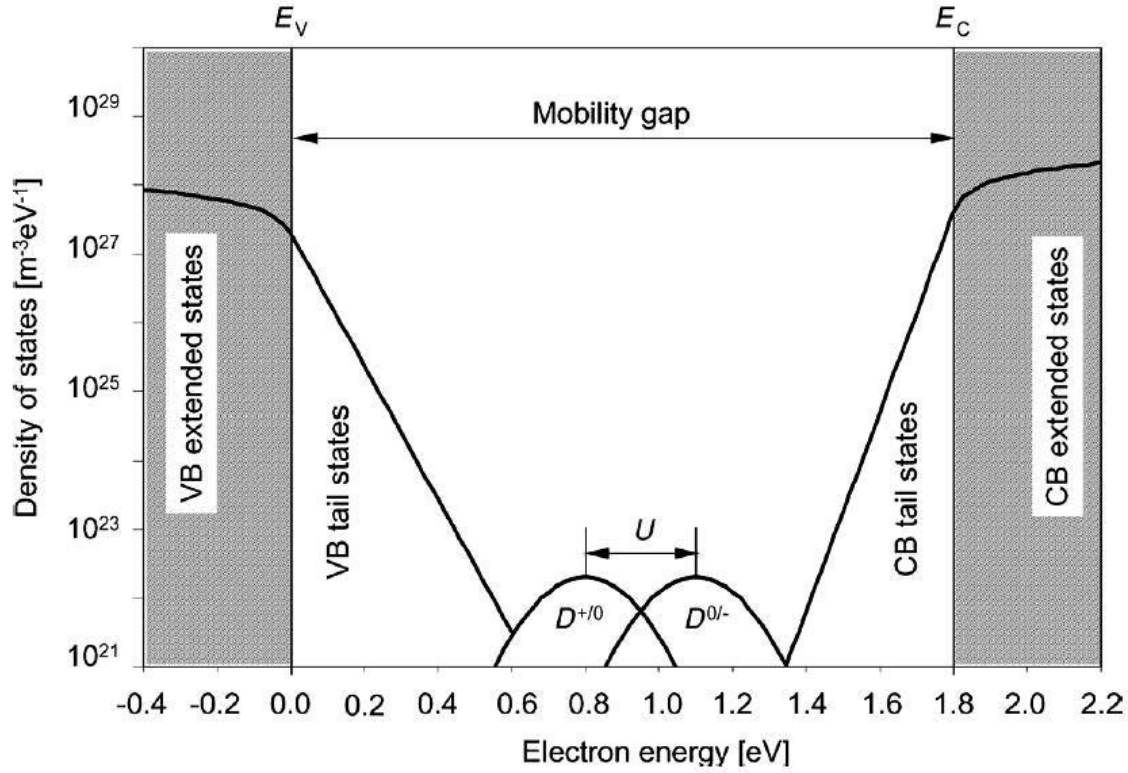

Figure II.2: The standard density of states distribution in a-Si:H**.**

The boundaries between the defined localized states and the extended states of the valence and the conduction bands are called the mobility edges (E_C and E_V), and the region between these two energies defines the gap called the mobility gap. The localized states in the mobility gap originating from spatial bonding fluctuations are called band tails (see Figure II.2).

The exact behavior of the properties of the density of states near the mobility edges and the localized to the extended transition are still nowadays not well understood and characterized. The distribution of the density of states in the band tails can be approximated by the function $E(N)$:

$$E(N) = E_0 exp\left(-E/k_B T\right) \qquad \text{(II.1)}$$

There is no symmetry between the valence band tail (VBT) and the conduction band tail (CBT). The (VBT) has more states than the (CBT) because the (CBT) are less sensitive to the bond angles and lengths disorder. The slope of the tail is described by the characteristic temperature T, for the amorphous silicon, ($k_B T$=45 to 55 meV) for the VBT and ($k_B T$=20 to 30 meV) for the CBT [38].

II.2.3) Defect pool model

Around the middle of the 'gap', there is a significant density of energy states related to defects that exist, and which depend on the conditions under which the material was produced. Extensive works on the defects in the a-Si:H show that the centers can be observed by measurements of electron spin resonance, and are usually identified as dangling bonds which are the predominant defect centers. The total defect density can be as large as 10^{19}cm^{-3} in amorphous silicon. A high reduction of the defect density is obtained by adding hydrogen, for hydrogenated amorphous silicon the defect density can be about 10^{15} to 10^{16} cm^{-3}.

The remaining dangling bond defects D have an amphoteric character: They can be neutral (D^0) with single electron occupancy, empty with positively charged (D^+) and negatively charged (D^-) with double electron occupancy. D^- defects have two electrons localized in the dangling bond. The two electrons repel each other with coulomb interaction, and hence the energy level of (D^-) states is raised by the energy U called the correlation energy. Basing on experimental measurements in hydrogenated amorphous silicon, Spear and Lecomber [38] found that the energy position of (D^0) may vary between 0.9 to 1.3 eV below E_C.For the correlation energy U is assumed to be constant and between 0.2 and 0.4 eV [36].

There is now considerable experimental evidence that the density of states in amorphous silicon is dominated by amphoteric silicon dangling-bond states and that the density of these states is determined by a chemical equilibrium process. The

model for the defect-forming reaction involves the breaking of Si-Si bonds, which are generally thought to be stabilized by diffusive hydrogen motion through breaking and reforming Si-H bonds, although microscopic models that do not require hydrogen have been proposed. The equilibrium density of dangling-bond states depends on the Fermi energy, which leads to a higher density of dangling bonds in doped amorphous silicon than undoped amorphous silicon. When the energy of the dangling-bond state can takes a range of values, due to the disorder of the network, then, proper consideration of the chemical equilibrium model leads to an energy shift of the peak of the formed defects, due to the minimization of free energy.

Furthermore, this energy shift is different for defects formed in the different charge states $(+,0,-)$. This is the so-called defect pool model [39, 40]. For a sufficiently wide pool, the model leads to negatively charged defects in n-type amorphous silicon having a lower energy than positively charged defects in p-type amorphous silicon, even when the correlation energy is positive, a previously puzzling result found in many experiments.

The defect pool model is a theoretical model that has been highlighted by numerous experimental results [15]. It was developed to describe the chemical equilibrium process established by the diffusion of hydrogen (H) through the various sites of the structure, between the ordinary weak bonds (SiSi), the doubly hydrogenated bonds denoted SiHHSi, and the created dangling bonds (SiHD). The distribution of the density of states was determined by applying the mass effect law to the two reactions

$$SiHHSi \leftrightarrow SiSi + 2H \quad \text{And} \quad SiHD \leftrightarrow SiSi + H \qquad \text{(II.2)}$$

These reactions translate the conversion process of the weak bonds of the valence band tails (VBT), assumed exponential, in dangling bonds SiHD taking place around the center of the gap, where these SiHD defects are formed with a Gaussian probability $P(E)$ The density of the states calculated within the framework of this model is:

$$D(E) = \gamma \left(\frac{2}{f^0(E)}\right)^{KT^*/2E_{v0}} P\left(E + \frac{\sigma^2}{2E_{v0}}\right) \qquad \text{(II.3)}$$

$$\gamma = G_v \left(\frac{H}{N_{SiSi}}\right)^{KT/4E_{v0}} \left(\frac{{2E_{v0}}^2}{2E_{v0} - KT^*}\right) exp\left[-\frac{1}{2E_{v0}}\left(E_P - E_v - \frac{\sigma^2}{4E_{v0}}\right)\right] \text{(II.4)}$$

σ is the pool width and E_P is the most probable energy in the distribution of available sites for defect formation. $G_v$is the density of tail states extrapolated to the valence band mobility edge. E_{v0} is the characteristic energy of the exponential. T^* is the equilibrium temperature (freeze-in temperature) for which the density of states is maintained. H and N_{SiSi}, are respectively, the hydrogen and electrons concentration in the material. $f^0(E)$ is the probability of the defect SiHD being neutral D^0 (charged with one electron).

As we mentioned, before the defects can be in three different states:

- Positively charged D^+, when the defect SiHD is occupied by no electrons.
- Neutral D^0, when the defect SiHD is occupied by one electron.
- Negatively charged D^-, when the defect SiHD is occupied by two electrons.

The density of the three states is given by:

$$D^+(E) = f^+(E).D(E)\ D^0(E) = f^0(E).D(E)$$

(II.5)

$$D^-(E) = f^-(E).D(E)$$ Where

$f^+(E)$, $f^0(E), f^-(E)$ are the probabilities of the SiHD defect being in the states D^+, D^0, D^- respectively.

$$f^+(E) = \frac{1}{1 + 2\exp\left(\left[E_f - E\right]/k_BT\right) + \exp\left(\left[2E_f - 2E - U\right]/k_BT\right)}$$

$$f^0(E) = \frac{2\exp\left(\left[E_f - E\right]/k_BT\right)}{1+2\exp\left(\left[E_f - E\right]/k_BT\right)+\exp\left(\left[2E_f - 2E - U\right]/k_BT\right)} \quad \text{(II.6)}$$

$$f^-(E) = \frac{\exp\left(\left[2E_f - 2E - U\right]/k_BT\right)}{1 + 2\exp\left(\left[E_f - E\right]/k_BT\right) + \exp\left(\left[2E_f - 2E - U\right]/k_BT\right)}$$

where *U* is the defect electron correlation energy and E_f.is the Fermi level at thermal equilibrium.

FigureII.3 shows the total distribution of the density of states, including the dangling bond density, $D(E)$, calculated by the defect pool model [41], and the valence and

conduction band tail densities $g_V(E), g_C(E)$ respectively. The parameters used to plot this distribution are extracted from literature [42] and are listed in table II.1.

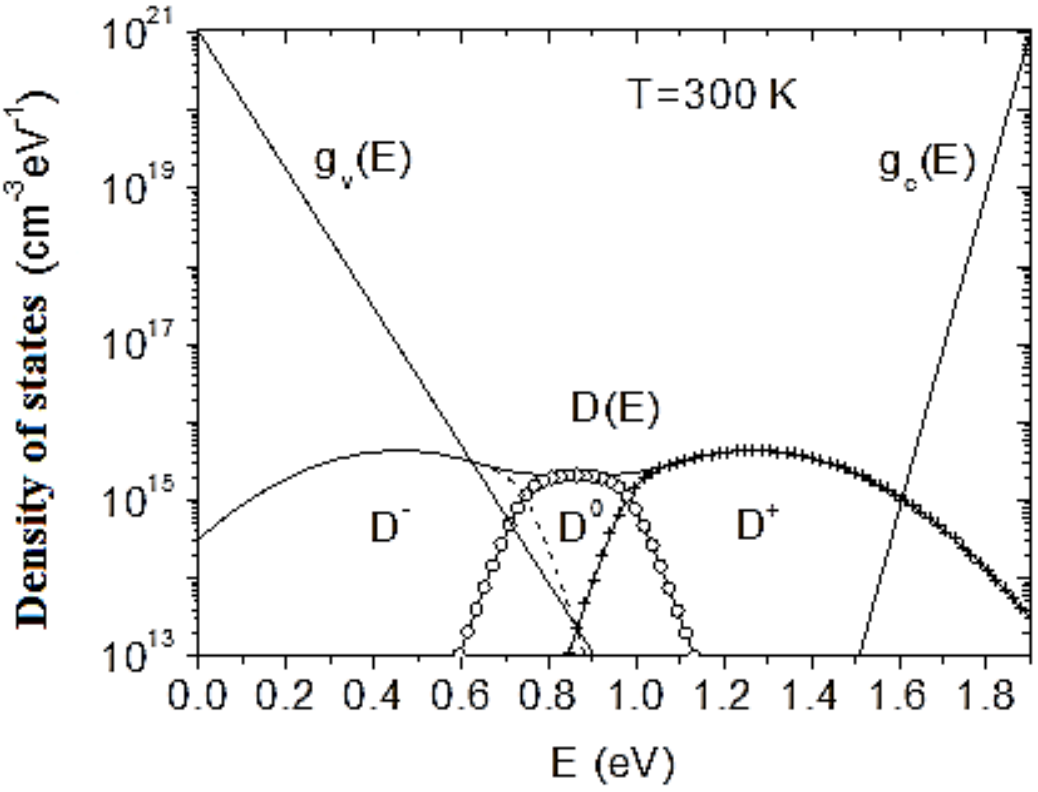

FigureII.3: The total Density of state including band tail and dangling bond states [41].

It is possible to replace this density of the states by an equivalent density $g_d\ (E)$ of monovalent states of which the probability of occupation is related to Fermi-Dirac function. The interest of this equivalence comes owing to the fact that the states detected by the majority of the spectroscopic techniques are considered monovalents. $g_d\ (E)$ is given by the expression:

$$g_d(E) \approx D(E + kTln2) + D(E - U - kTln2) \qquad \text{(II.7)}$$

where the $kTln2$ term comes from the spin degeneracy of the singly occupied state. This is not exact, but it is a very good approximation, leading only to a small error of about $exp(-U/kT)$ in the density. The total density of state including band tail states and dangling bond states is then:

$$g(E) = g_V(E) + g_C(E) + g_d(E) \qquad \text{(II.8)}$$

Parameters	Values
$\sigma(eV)$	0.19
$E_p(eV)$	1.27
$E_c - E_v(eV)$	1.90
$E_{Fi}(eV)$	0.98
$G_c(cm^{-3}eV^{-1})$	10^{21}
$G_v(cm^{-3}eV^{-1})$	10^{21}
$H(cm^{-3})$	5×10^{21}
$N_{sisi}(cm^{-3})$	2×10^{23}
$U(eV)$	0.2

Table II-1: Density of states parameters [41].

II.2.4) Recombination

Radiation can generate excess carriers in a-Si:H, which then populates the conduction and the valence bands. The induced conductivity depends on the trapping in the band tail states, and on recombination rate. The carriers excited to the extended states or to the band tails lose energy by non radiative thermalisation process, the excitation energy being converted into phonons. Carriers in extended states lose energy by the emission of single phonon as they scatter from one state to another. Between the localized states of the band tails, thermalisation occurs at low temperatures by direct tunneling, and becomes slow as the carriers move deeper into the band tail. At higher temperatures (above 200K) [36], the multiple trapping mechanism of sequential excitation and trapping dominates tunneling. The two dominants recombination mechanisms in a-Si:H are radiative transitions between band tails states and non radiative transitions from band edges to defect states (see Figure II.4).

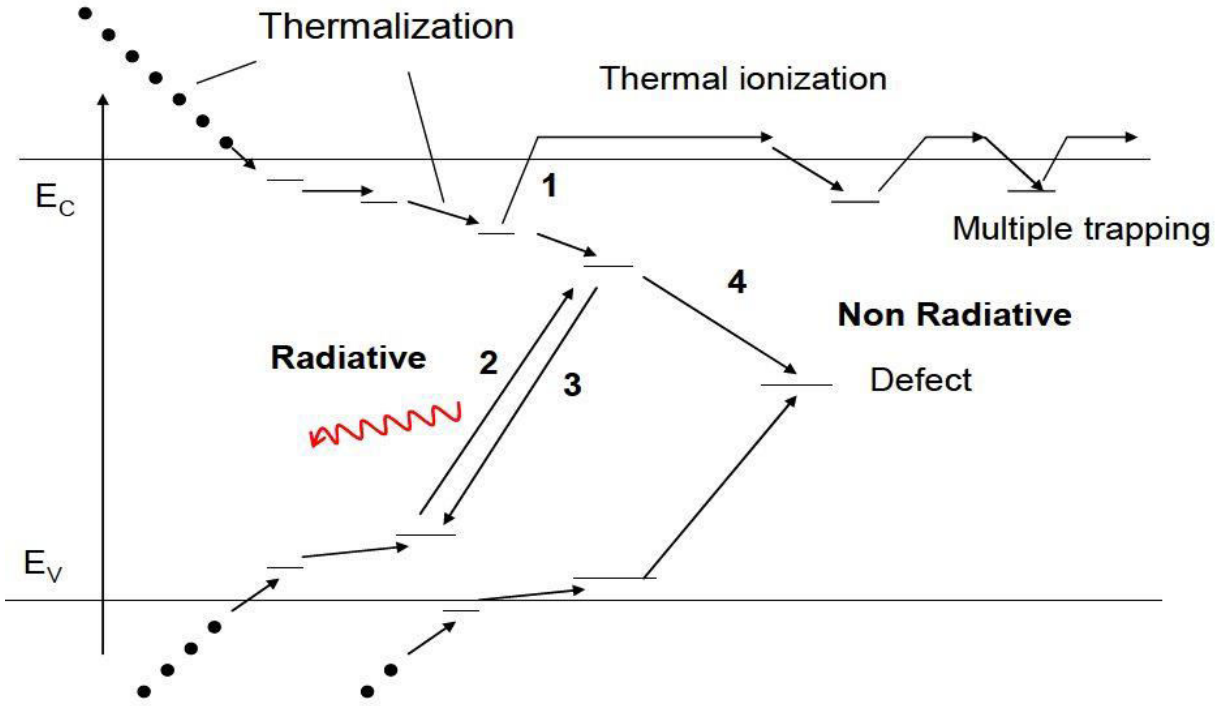

Figure II.4: Illustration of the electron-hole recombination, 1: multiple trapping, 2(3): radiative recombination in conduction (valence) band state, 4: non radiative recombination at a defect state.

The radiative recombination in the tail states tends to dominate at low temperatures (<100 K). Its transition rate is slow but there is a large density of band tail states at which recombination can occur. E_{tn} is the quasi Fermi level for the trapped electrons: the states above this energy preferably act as traps (thermal emission of the electrons is higher), and states below this energy act as recombination centers (capture of a holes is higher). The same concept can be applied for holes with the definition of E_{tp}.

At temperatures higher than about 100 K, carriers diffuse rapidly from site to site, and the faster transition rate at the defect dominates the recombination. The defect recombination is predominantly non radiative. There are four possible trapping transitions of electrons and holes into dangling bond defects. In undoped a-Si:H, the defects are neutral (D^0) and can capture either an electron (resulting a D^- in dangling bond state) or a hole (resulting a D^+ in dangling bond state). In doped a-Si:H, the defects are charged; the negative defect (dominant in n-doped material) can only capture holes, and the positive defect (dominant in p-doped material) can only capture electrons (see Figure II.**5**).

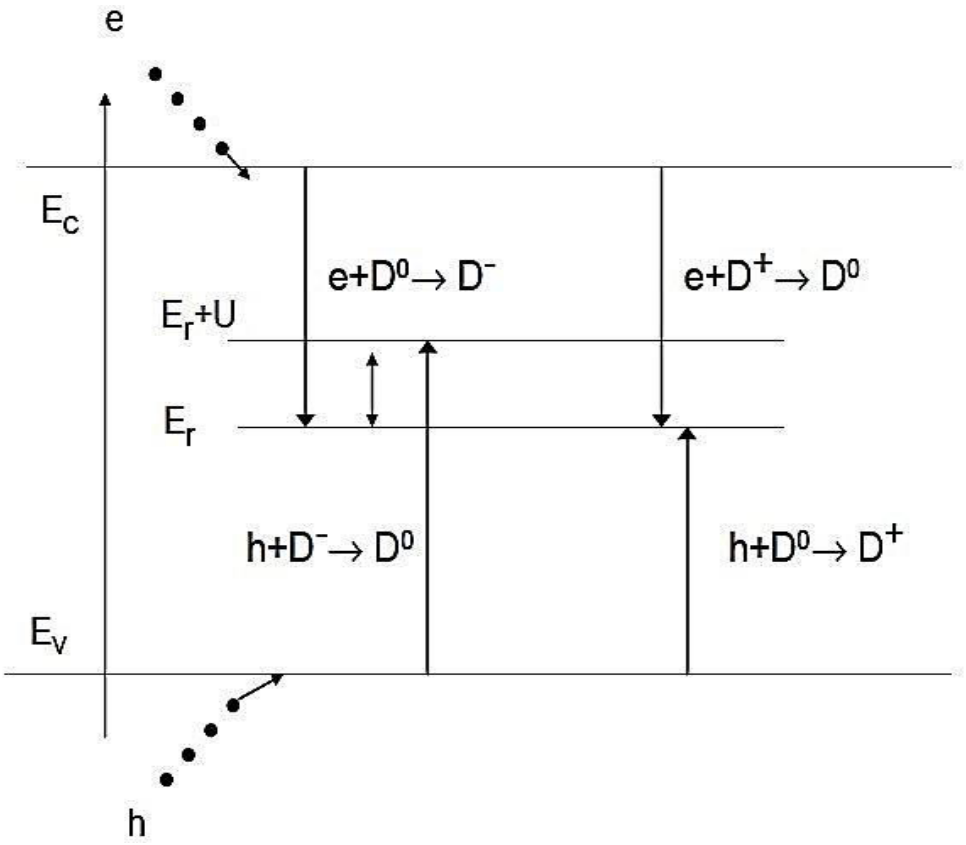

Figure II.5: The four possible transitions for electrons and holes to a defect recombination center.

II.2.5) Optical absorption

Optical absorption in tetrahedral crystalline semiconductors such as Si shows variations with energy corresponding to variations in the bonds and the details of the density of states obtained from the energy-momentum relationships. The lowest energy absorption derives primarily from transitions from p to s orbitals on adjacent atoms in common semiconductors. The distortions in bond angles modify the energies of absorption edges and maxima somewhat. Loss of organization at longer ranges blurs peaks in the absorption spectrum. As bond distortions cause states to move from the band edges into the gap, the effective gap for optical absorption generally increases.

Absorption coefficient data and various contributing mechanisms of a typical amorphous semiconductor are shown in Figure II.6 [42].

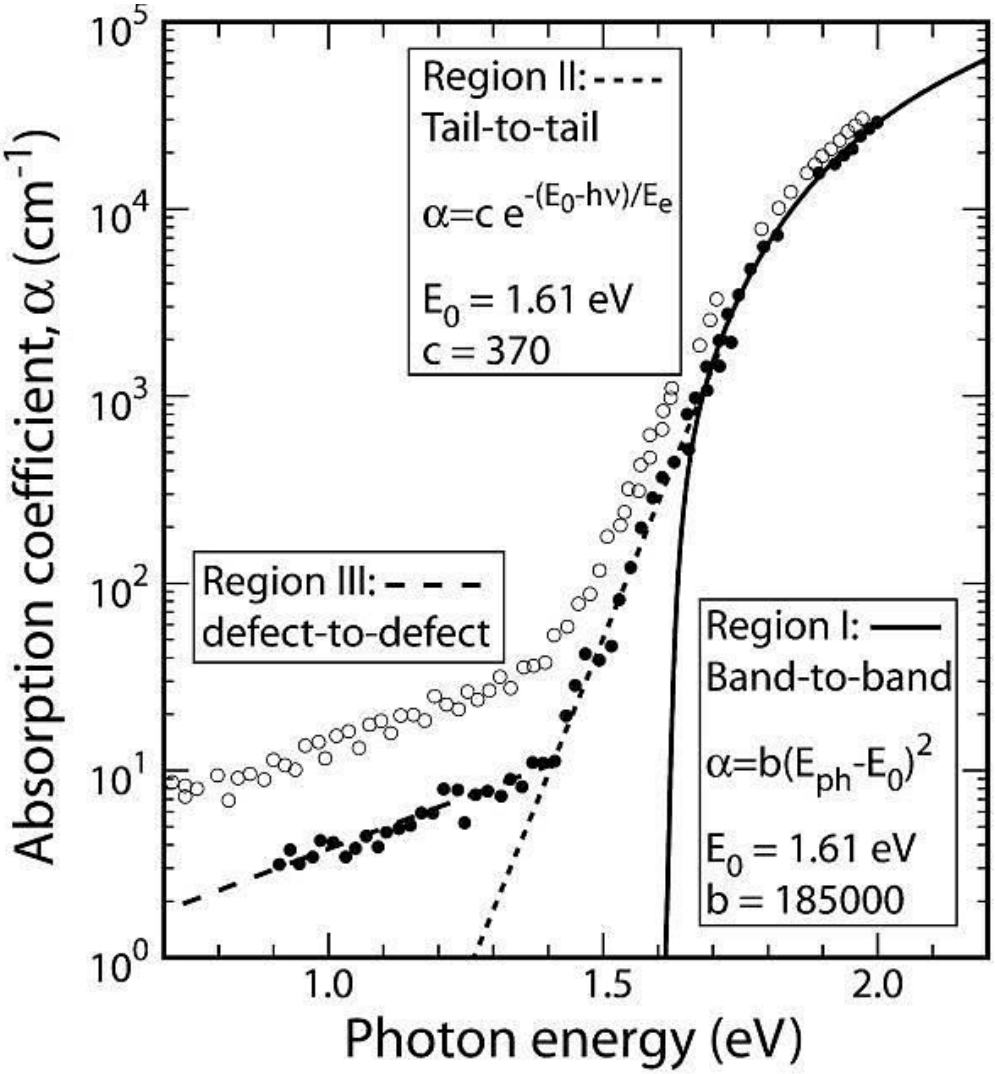

Figure II.6: Optical absorption data for two a-Si:H films deposited by Rf-PECVD using SiH_4source gas. Solid circles indicates as-deposited film results while open circles show the effect of annealing at 500°C for 30 min [44].

There are three primary regions. The high absorption region I corresponds to absorption due to electron transitions across the mobility gap from extended states to other extended states. Region II is absorption from extended states to band tail states or band tail to band tail transitions where the density of states is still rather high. In this region the absorption coefficient is typically falling exponentially. Region III is due to transitions to, from, or among localized states in the mobility gap and absorption is roughly constant [43].

For a free-electron system the band density of states decreases parabolically. The same parabolic decrease is also generally found in amorphous semiconductors. An absorption edge can be defined based on fitting this portion of the absorption spectrum based on the function

$$\alpha(v) = b(hv - E_0)^2 \qquad \text{(II.9)}$$

Where E_0 is the absorption edge energy, hv is the photon energy, and b is a constant. Equation (II.9) assumes free-electron band edges. The true bands in amorphous semiconductors are not exactly parabolic and may distort this behavior.

In all semiconductors and particularly in amorphous materials there are states in the energy gap that decrease in density roughly exponentially as one move into the gap.

These are the band tails described earlier. The resulting absorption coefficient decreasing exponentially below the energy E_0 of Equation (II.9) can be written approximately as [42]:

$$\alpha(hv) = const.\, e^{-(E_0' - hv)/E_e} \qquad \text{(II.10)}$$

Where hv is the photon energy, E_0' is the same as the parabolic energy edge and E_e is the characteristic width of the dominant band edge, typically < 0.1 eV. The wider band edge will set the apparent band-tail width and determine the absorption coefficient behavior. Which edge this is depends upon the details of the semiconductor involved. In amorphous silicon, the band tails will be relatively symmetrical with differences primarily resulting from the effective masses of the bands. Various models have been proposed to explain the source of equation (II.10) and can be found in Connell [43].It is sufficient here to assume that the behavior is due to distorted localized bonds in the structure.

The optical gap (related to the mobility gap) in amorphous Si and other amorphous semiconductors exhibits temperature-dependent behaviors that are qualitatively similar to the temperature-dependences of crystalline materials. For example, a-Si:H shows a decrease in optical gap as temperature increases, as one would expect. Unlike the case for crystalline materials, the temperature dependence of a-Si:H is primarily related to changes in phonon-electron interactions. Thus, rather than a linear-quadratic relationship to the temperature, one finds a change in optical gap of [42]:

$$E_g(T) = E_g(0) - \frac{2a_B}{e^{\emptyset/T} - 1} \qquad \text{(II.11)}$$

Where a_B is the electron-phonon interaction strength, $\emptyset$ is the effective temperature of phonons in the solid, $E_g(0)$ is the gap at initial state and T is the temperature.

The effect of pressure on the optical gap in amorphous semiconductors also differs from the behavior of crystalline materials. In indirect-gap semiconductors we found a negative change in gap with increasing pressure in Si and some other materials due to increasing angular dependence of bonds at short distances. Direct gaps were all found to increase with increasing pressure due to greater orbital overlaps at shorter bond lengths. In amorphous semiconductors one finds an increasing gap with increasing pressure as expected for direct-gap materials. However, there can also be structural changes induced by increasing pressure that can lower the gap.

II.2.6) Transport and mobility

Free carrier movement in a-Si:H, and to an even greater extent in other amorphous semiconductors, is difficult because there are a large number of defect states in the material into which a free carrier might fall. Once trapped in a defect state, the carrier has several possibilities for further motion as illustrated in Figure II.**7**.

First, it can gain energy from the heat in the system sufficient to carry it into the extended states, in which it is free to move as a carrier in a crystalline material would, although with much higher scattering rate. While it lasts, the mobility of such a carrier is not dramatically different from that of a normal crystalline semiconductor. However, after a short time this carrier is trapped again and becomes effectively immobile. Carriers are excited to the mobility edge mostly from states at or near the Fermi level energy.

The number of carriers, n for electrons, excited above the mobility edge is therefore given approximately as [43]:

$$n = kT\, N(E_c)\left(e^{-(E_c - E_f)/kT}\right) \qquad \text{(II.12)}$$

Where E_C is the conduction band mobility edge energy, $N(E_c)$ is the effective density of states at the mobility edge, and E_f is the Fermi energy. Derived a relationship for mobility corresponding to this carrier behavior and having the functional form [45]:

$$\mu = \frac{C}{T} \qquad \text{(II.13)}$$

Where C is a constant and T is the temperature.

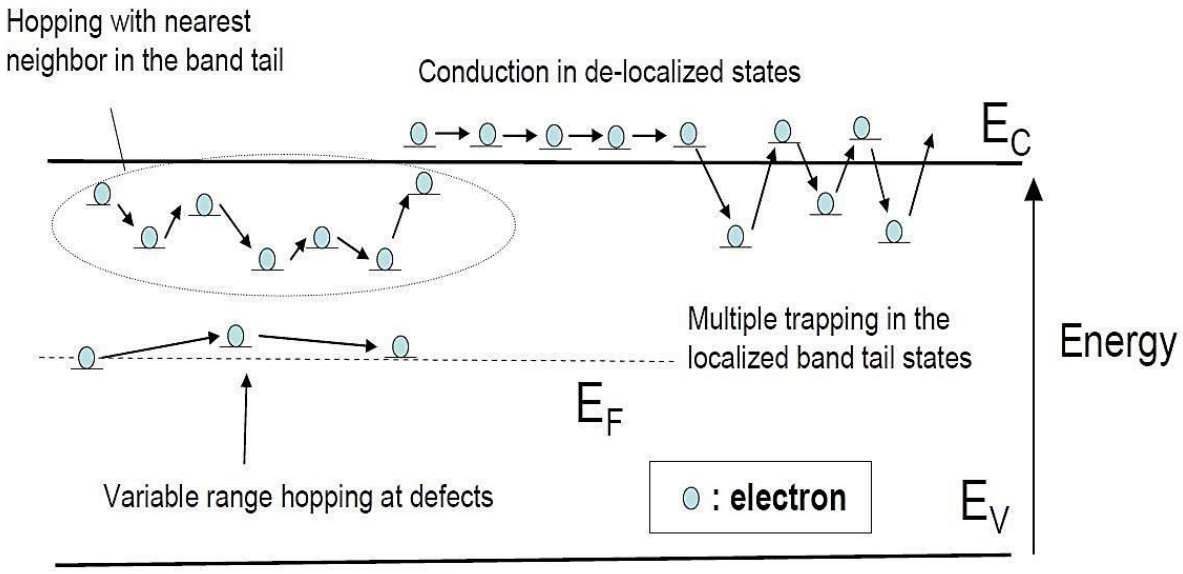

Figure II.7: Electron conduction mechanism in a-Si:H, conduction in the extended states, hopping conduction in localized states, multiple trapping in localized states.

Different treatments have derived different forms for the constant but all agree upon the inverse temperature dependence. The models yield typical room temperature mobilities for a-Si:H of the order of 1-10 $cm^2\ V^{-1}s^{-1}$. Taken together with (II.12) this model suggests an essentially simple exponential temperature dependence of the conductivity by this mechanism. It also shows that this type of conduction freezes out rapidly as the temperature decreases, especially when, as is typical, the Fermi energy is far from a mobility edge. Band-like conduction is generally only significant at high temperatures or when the material contains a relatively low density of states in the mobility gap.

Conduction can also operate in the band tails below the mobility edge when such tails are wide and have a sufficiently high density of states to allow rapid hopping of a carrier from one site to another via thermally-activated processes. In this case, the mobility of a carrier depends exponentially upon the amount of energy it must gain to leave a given state and hop to the next. Thus, it was proposed that the mobility will have the form [46] :

$$\mu_{hop} = \frac{q v_{ph} R^2}{6kT} e^{-W/kT} \qquad \text{(II.14)}$$

Where v_{ph} is the average phonon vibrational frequency of the structure, q is the electron charge, R is the hopping distance in an average hop, and W is the energy gain necessary for the average hop. The net mobility is a weighted average over all states and the weighting factor is determined by the effective density of states at a given energy. The density of states typically falls rapidly (exponentially) below the mobility edge, while the probability for the energy gain decreases exponentially as the barrier for the hop becomes larger.

The final conduction pathway is phonon assisted tunneling. This requires states sufficiently close in energy and momentum and physically close enough in the solid for tunneling from one to the next to occur. The farther the carrier energy is from the mobility edge the slower this process, in general, due to the lower density of states and the higher tunneling barrier. However, in some cases tunneling may be faster than for the mechanisms discussed above. In particular, if there is a relatively high density of states at the Fermi energy, then this mechanism can operate relatively easily. Such a situation is typical when the Fermi energy lies at the energy of dangling bond states and when there are many dangling bonds present in the material. As with hopping in band tails, the phonon-assisted tunneling mechanism conduction has a highly path-dependent effective mobility. Carriers that tunnel between states that are very close to one another in the solid move rapidly and have a higher effective mobility. More widely spaced states result in extremely small effective mobilities. The jumping rate, r, is given by [47]:

$$r = v_{ph} e^{-W/kT} e^{-2\alpha R} \qquad \text{(II.15)}$$

Where tunneling yields the exponential dependence of rate on jump length R, α is the characteristic decay length of the integrated overlap of the wave functions of the two states, and W represents an effective energy barrier. In this case, W is assumed to be modest. From Equation **Erreur ! Source du renvoi introuvable.** an effective mobility can be estimated as [47]:

$$\mu = \frac{qR^2}{6kT} r = \frac{q v_{ph} R^2}{6kT} e^{-2\alpha R} e^{-W/kT} \qquad \text{(II.16)}$$

Which is obtained by noting that the diffusivity is $D = rR^2/6$, and using the Einstein relation, $\mu = qD/kT$. Equation (II.16) is nearly identical to equation (II.14), with the exception of the addition of the exponential tunneling term and includes the same

inverse temperature dependence as in previous formulae (II.14). This would be convenient if it were not for a much more complex behavior in the average jump distance R. Furthermore, the necessity to weight the probability of each jump for the likelihood of occurrence of a given configuration of states of a given type causes very different net temperature dependence. More derivations may be found in Mott [47]. A properly averaged jumping rate gives a term of the form [42]:

$$r = v_{ph} e^{-A/T^{1/4}} \qquad \text{(II.17)}$$

A temperature dependence of the conductivity scaling as an exponential of $T^{-1/4}$ is a standard signature of variable-range phonon-assisted tunneling conduction.

II.2.7) Metastability

Inherent to a-Si:H are changes in its electronic properties under light exposure. This is known today as the Staebler–Wronski effect (SWE) [48], discovered in 1977 by David L. Staebler and Christopher R. Wronski. Since the observation of the SW effect, a large effort has been put into obtaining an understanding of the processes that cause the light induced structural and optoelectronic changes in a-Si:H.

The Staebler-Wronski effect was described as a significant decrease in dark conductivity and photoconductivity as a result of prolonged light soaking (LS) of a-Si:H material. The schematic figure of this experimental result is reproduced in Figure II.8.

Moreover, it was observed that these effects were metastables, i.e. reversible, as the process of thermal annealing caused recovery of conductivity in the amorphous material [48]. Thermal annealing (TA) is a process where a material is heated at a given temperature for a given amount of time. There exists a thermal threshold above which the thermal annealing is effective in a-Si:H, and temperatures above 100 °C are a standard practice [49].

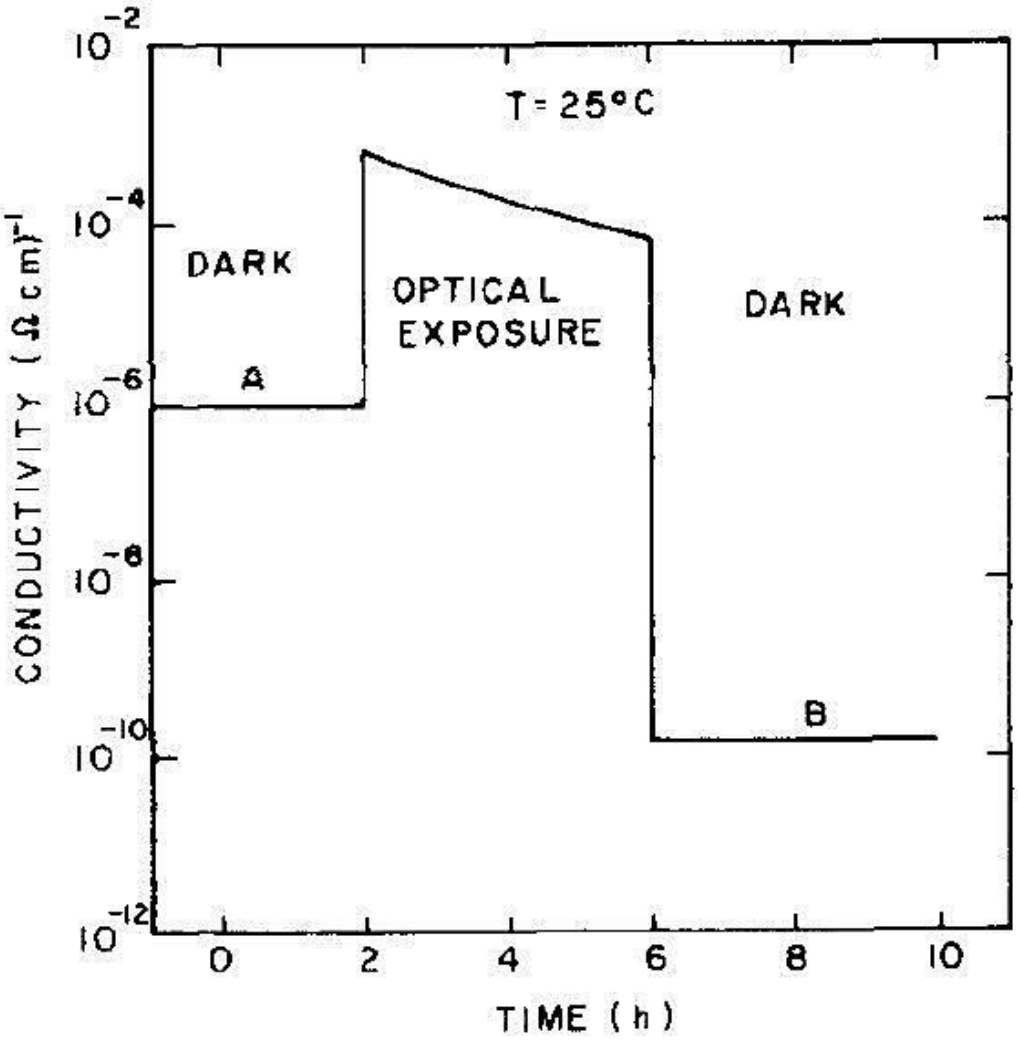

Figure II.8: Conductivity as a function of time before, during, and after exposure to ~ 200 m W / cm^2 of light in the wavelength range 6000-9000 °A [48]**.**

At standard test conditions (STC), the degradation process stabilizes after about 1000 hours of light soaking, after which the performance level of the solar cell stabilizes [1]. In a-Si:H solar cells, the Staebler-Wronski effect causes reductions in efficiency of 10%-30% [49]. As such, the SWE is one of the major obstacles of using a-Si:H in production of high efficiency photovoltaic devices.

While the true cause of the effect continues to elude the scientific community, it has been shown that the concentration of defects in the amorphous material increases by up to two orders of magnitude before stabilization, reaching levels of 10^{17} cm^{-3}, as depicted in Figure II.9 [19].

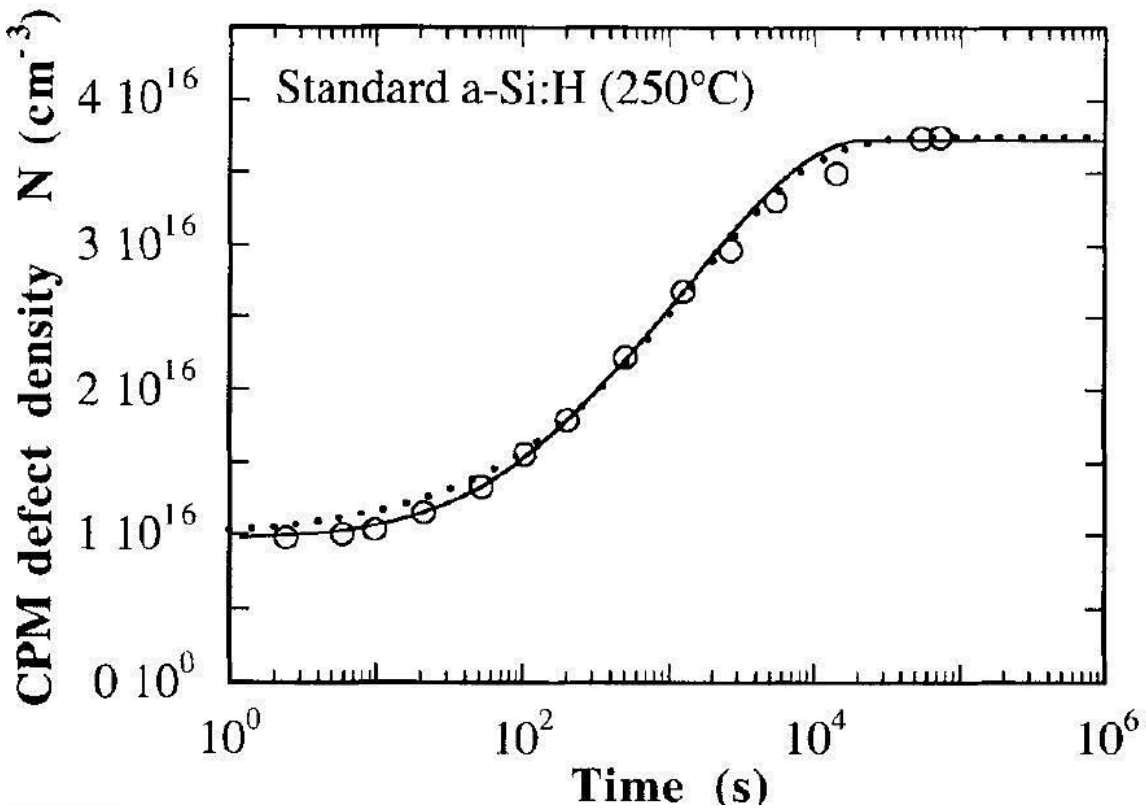

Figure II.9: Dependence of the defect density measured by constant photocurrent method (CPM) on the illumination time using high intensity light [50].

Crystalline silicon is not prone to the SWE, and even microcrystalline material is almost completely resistant to the effect. As the outcome of SWE is a higher defect density, much attention is given to uncovering the nature of the defects within the amorphous material. Nearly 40 years' worth of research exists on the characterization of defect creation dynamics and defect characteristics within a-Si:H. Although a complete and coherent model for the degradation process is lacking, it is common consensus that the presence of hydrogen within the a-Si:H structure plays a large role in the creation mechanisms of metastable defects. It has been shown that hydrogen bonding configurations change as a result of Light Soaking [51]. Because hydrogen atoms within the amorphous silicon material pacify the dangling bonds (DBs) in the structural framework, it is believed that such changes in bonding configurations lead to alterations in defect density and defect density distribution [52, 53].

The creation of the metastable defects induced by the light or the SWE was the principal problem limiting the application of the a-Si:H like solar material. Several studies were made to include/understand the metastability and to reduce its effect in

the a-Si:H. Among the great number of developed models, there are two typical models to describe the mechanism of creation of the dangling bonds by the light : the model of *weak bond rupture* like result of the non-radiative recombination of the photogenerated carriers (Stutzmann, Jackson and Tsai : SJT model) [54], and the model of creation of the metastable dangling bonds by *collision of hydrogen* [53, 55, 56]. The two models lead to the same relation of the rate of creation of the defects. The model of *bond rupture* regards SWE as a local effect, while the *collision of hydrogen* model regards it as being related to the movement, with long range, of hydrogen. The mechanism of the two models considers only one type of the recombination centers, the neutral dangling bonds (D_0).

II.2.7.A) SJT model [54]:

Stutzmann, Jackson and Tsai have undertaken a systematic study of the SWE in undoped hydrogenated amorphous silicon, using electron-spin-resonance and photoconductivity measurements. The influence of impurity concentration, sample thickness, illumination time and intensity, photon energy, and temperature on the creation of metastable defects as well as the variation of the annealing behavior with annealing temperature has been studied in detail. They affirmed that SWE in the intrinsic a-Si:H is caused by the creation of the dangling bonds resulting from the rupture of the weak bonds following the non-radiative recombination of the photogenerated carriers [54].

$$Si - Si \rightarrow 2D \qquad \text{(II.18)}$$

The kinetic of defect creations is expressed by the equation (II.19):

$$\frac{dN_d}{dt} = C_{SW}\left(\frac{G}{N_d}\right)^2 \qquad \text{(II.19)}$$

N_d is the density of formed defects, C_{SW} is constant named SW coefficient and G is the light intensity.

Figure II.10 shows the defect formation process according to the SJT model.

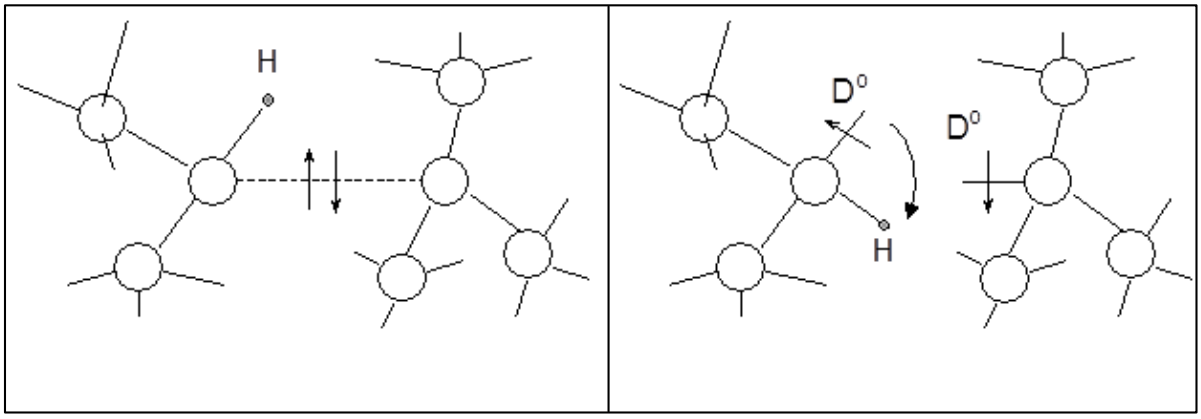

Figure II.10: Defect formation by SJT model [54].

The results of SJT study can be summarized as follows [54]:

(1) The SWE is intrinsic to hydrogenated amorphous silicon and does not depend on the concentration of the major impurities, nitrogen and oxygen, below a critical value of about 10^{19} cm^{-3}. For higher impurity contents an enhancement of the metastable changes with increasing N or O concentration is observed.

(2) The SWE is a bulk effect. However, the probability of creating metastable defects is, by about 1 order of magnitude, larger in a surface/interface layer with a total thickness of about 0,5 µm than in the rest of a sample. Possible reasons for this inhomogeneity are the existence of band bending and/or mechanical stress near the surface or interface.

(3) The kinetic behavior of the metastable dangling bond density and of the photoconductivity, i.e., the dependence of these quantities on illumination time t_{ill} and light intensity I, can be described quantitatively by a model based on the nonradiative direct tail-to-tail recombination of optically excited electrons and holes. The kinetic behavior is sublinear in total exposure, t_{ill}. For example, at long times the dangling bond density increases as $I^{2/3}$ $t_{ill}^{1/3}$. The physical reason for this functional dependence of the spin density on the kinetic parameters is the major role of the dangling bonds as recombination centers in a-Si:H. This results in a self-limiting character of the SWE, confining the densities of metastable dangling bonds to typically 10^{17} cm^{-3}. Moreover, the comparison of the metastable changes observed in the Electron Spin Resonance (ESR) spin density and the photoconductivity shows that the predominant metastable defect caused by prolonged illumination is the

silicon dangling bond, at least as far as the optoelectronic properties of a-Si:H are concerned.

(4) The annealing behavior of the metastable defects can be described consistently by an exponential decay with a thermally activated decay constant. The activation energy of this decay constant is not well defined. A distribution of activation energies between 0.9 and 1.3 eV is obtained from the annealing experiments [54]. This shows that the metastable dangling bond is subject to local variations.

(5) The efficiency for the creation of metastable defects is found to be independent of the photon energy hv in the range $hv = 1{,}2 - 2{,}1\ eV$. This suggests that the defect inducing step, like the radiative, luminescent recombination, occurs after thermalization of the optically excited carriers into deep tail states. Consistent with the experimental results, the defect-creation rate is found to be thermally activated with a small energy of 0.04 eV [54]. Together with the results summarized in point (4), this allows the determination of the steady-state defect density reached asymptotically under illumination at elevated temperatures.

II.2.7.B) The hydrogen collision model

The hydrogen collision Model is described in detail in several works of Branz [53, 55, 56], who creates a framework for understanding light-induced metastability in a-Si:H. Figure II.11 shows a schematic diagram of the Staebler-Wronski dangling bond (DB) creation by H collision model. Photo-carrier recombination excites mobile H from Si-H bonds, leaving behind DB's. Mobile H ''collisions'' (associations) create metastable two-H complexes (M $(Si\text{-}H)_2$) and metastable DB's. In contrast to most previous microscopic models of the SW effect, the H collision mechanism is consistent with ESR experiments and does not involve impurities.

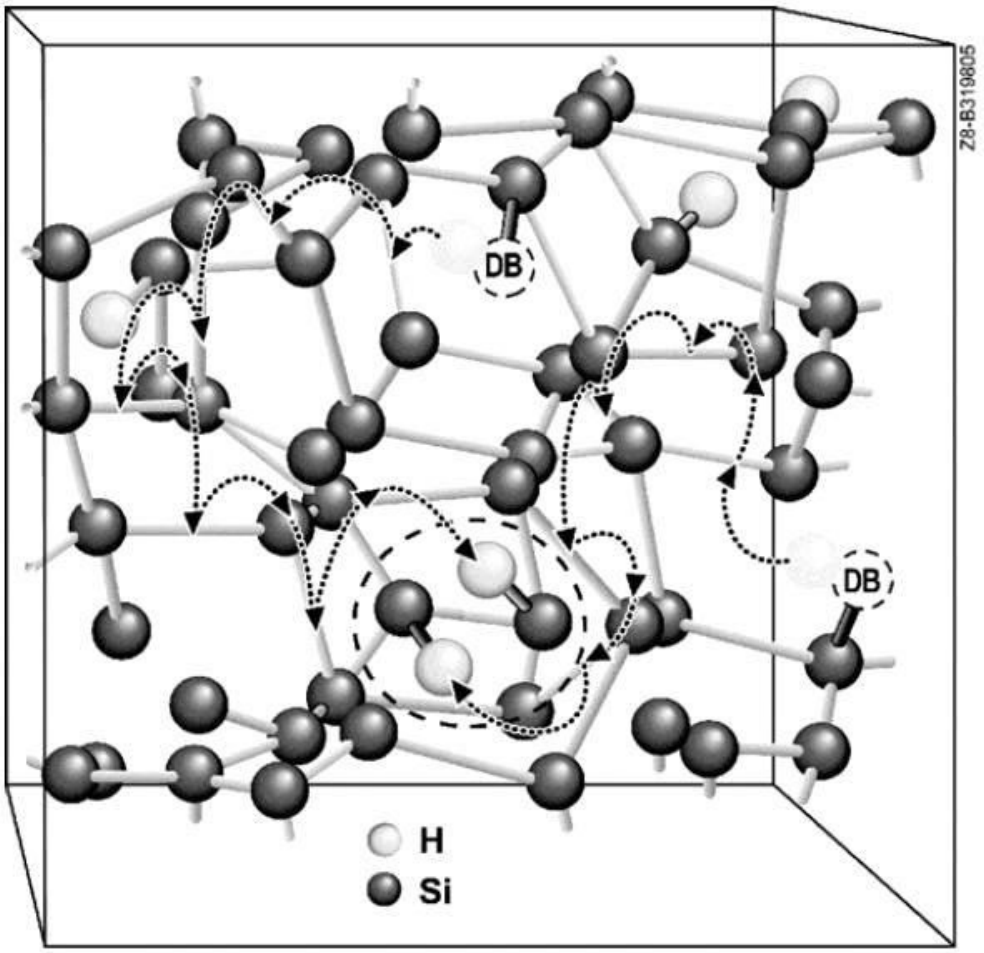

Figure II.11: Schematic diagram of the Staebler-Wronski DB creation by H collision model [56].

Rate equations for the production of mobile H, DB's and M $(Si\text{-}H)_2$ complexes are solved for quantitative predictions [53]. The branching ratio between mobile H collisions and mobile H trapping to DB's yields to $G^{2/3}.t^{1/3}$ DB creation kinetics during continuous illumination. This branching ratio and the $t^{1/3}$ kinetics are unchanged down to 4.2 K, but at low temperatures the photo-carriers must drive mobile H diffusion. The defect density increases as $G.t^{1/2}$ during intense laser-pulse illumination of undoped a-Si:H, because slowly decaying mobile H creates most SW DB's during the dark time between pulses. Earlier electron-hole pair recombination models of continuous and pulsed illumination kinetics lead to similar mathematical forms, but are inconsistent with other experimental results.

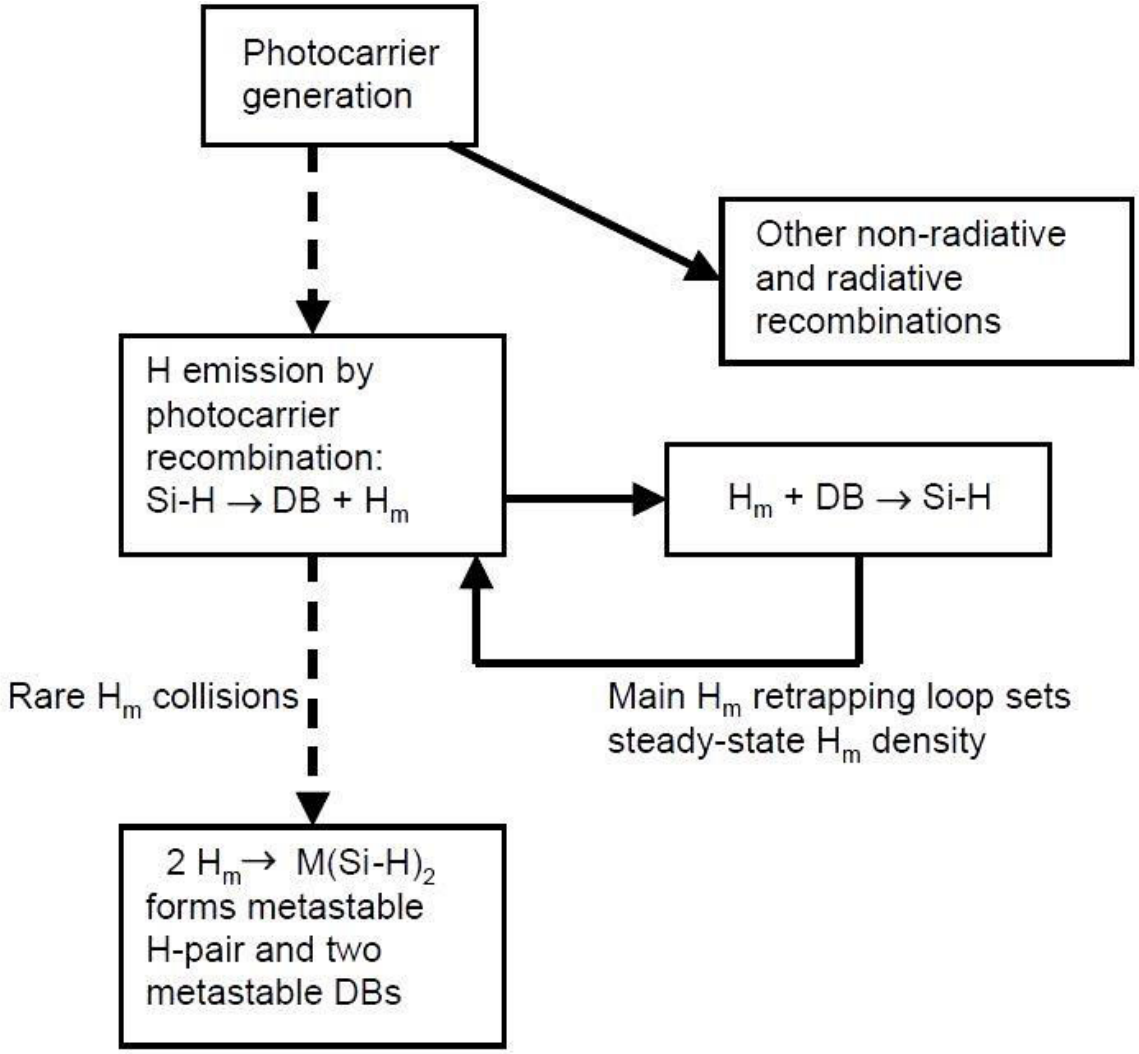

Figure II.12: Flowchart of the H collision model [56].

As critic to the model of breaking Si-Si bonds of Stutzmann et al [54], Branz affirms that it is difficult to include/understand why a broken connection quite simply will not be reconstituted since it is about a barrier of low energy. He adds in more than the need for a jump of the atom of hydrogen to stabilize a pair of dangling bonds is excluded by the hyperfine analysis from the signal ESR which shows that the dangling bonds are in depopulated areas of hydrogen. According to Branz, data ESR will exclude all the class from the models which imply the local movement of hydrogen like stage in the creation of the dangling bonds [56].

II.3) Hydrogenated microcrystalline silicon

The hydrogenated microcrystalline silicon (µc-Si:H) is a new material with a great importance for development of thin film solar cells, it is still far from being understood even the intense researches in recent years. As we observe the complex

relationships between preparation conditions, structure, electrical and optical properties, in this part we will present these properties one by one.

Historically, hydrogenated microcrystalline silicon was first described by S. Veprek and his group in 1968 [21]. In 1979, the first report about the preparation of µc-Si:H with plasma-enhanced chemical vapor deposition (PECVD) was published by Usui [57]. The material was prepared at lower substrate temperature, and it was grown from the gas phase using silane diluted with hydrogen. After a while time the transition between the amorphous and microcrystalline material was controlled easily by the preparation parameters such as discharge power, substrate temperature, pressure, and most importantly, by modifying the hydrogen dilution of the process gas silane.

Over the last 20 years, it was an intense research on all the aspects of µc-Si:H materials and devices, it is not possible to cover all the important literature and developments on µc-Si:H in this part, but only some milestones are cited. µc-Si:H solar cells formed by PECVD at low temperatures are assumed to have a shorter lifetime than single-crystal cells, and it is common to employ a p-i-n structure in the same way as in amorphous solar cells, while the p-type is the window layer. A group from the MIT (Massachusetts Institute of technology) Neuchâtel has published an important work [58-60] on single junction solar cells with µc-Si:H absorber layers, and on a-Si:H/µc-Si:H tandem junction solar cells which they call it later “micromorph” tandem solar cells. They showed that their single junction µc-Si:H cell has a negligible light-induces degradation compared to a-Si:H solar cells. They also demonstrated that the µc-Si:H cell can replace the unstable amorphous hydrogenated silicon-germanium alloys (a-SiGe:H) as an effective red-light absorber as a bottom cell in a tandem device.

A considerable progress in investigations on the structure and growth properties and their influence on the material quality or on device performance has done over many years. All this works were accompanied by modeling of the growth process of µc-Si:H which pushed forward the efficiencies of this these solar cells [61]. Today; µc-Si:H is established as a bottom cell red light absorber with improved stable efficiencies. Applications as a single cell device with about 10% stable efficiency; and as bottom cell in micromorph tandem cells, have found their way into production equipment [62] and they are already on market [63].

II.3.1) Structure:

Microcrystalline silicon (µc-Si:H) can easily be prepared with the same deposition process as a-Si:H. The structural composition is the important parameter that determines the distribution and density of defects, as well as the optical and electronic properties.

µc-Si:H is a mixture of crystalline grains, disordered regions and voids in various amounts and dimensions. There is no standard µc-Si:H and a definition just by the grain size is not appropriate. The name “microcrystalline” silicon suggests a predominance of micrometer-size features. This is not the case. Feature sizes vary from a few nanometers to more than a micrometer in one and the same sample. One can consider three basic configurations (Figure II.13): (a) isolated grains in an amorphous matrix; (b) extended crystalline fibers or crystalline grains forming percolation paths, which would be important for electronic transport; or (c) volume crystalline material with disorder only at the grain boundaries and in the inter-grain regions [64].

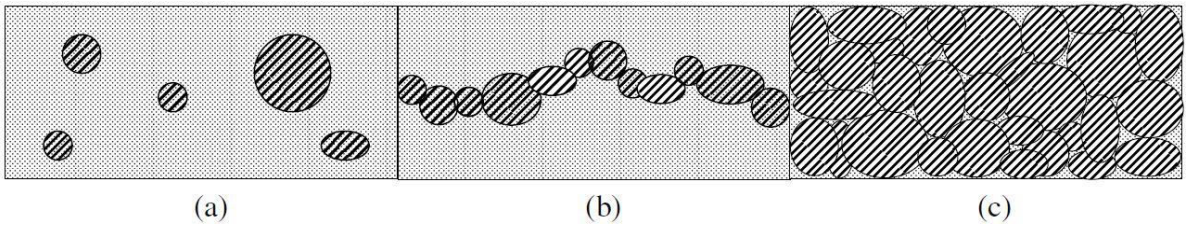

Figure II.13: Schematic of the three principle different configurations of amorphous and crystalline structure in the phase-mixture material µc-Si:H. (a) isolated crystalline grains; (b) crystalline regions forming percolation paths; (c) fully crystalline with disorder located at the grain boundaries only [64].

The structural composition depends on the deposition process. By varying the silane/hydrogen mixture in the process gas, one can comfortably grow material all the way from highly crystalline layers to fully amorphous layers. Other deposition parameters such as the process pressure, gas flow, excitation power, excitation frequency, temperature and so on, also influence the resulting material structure. Therefore the gas mixture is, in general, not sufficient to determine the structural composition; this is particularly true when comparing materials from different deposition methods. The silane/hydrogen gas mixture is quantified as the silane

concentration (SC), i.e. the ratio between the silane gas flow to the process chamber and the total gas flow (silane plus hydrogen) [64].

$$SC = \frac{[SiH_4]}{[SiH_4]+[H_2]} \qquad \text{(II.20)}$$

Where [SiH_4] indicates the flow of silane and [H_2] the flow of hydrogen into the process chamber. Alternatively, the hydrogen dilution R is defined as [64]

$$\mathrm{R} = \frac{[H_2]}{[SiH_4]} \qquad \text{(II.21)}$$

II.3.2) Optical properties

As shown in Figure II.14), absorption coefficient of microcrystalline silicon layers, as a function of photon energy is compared to monocrystalline layers and intrinsic amorphous silicon layers. It can be noted that:

- The absorption coefficient of the microcrystalline layer closely follows the monocrystalline with a shift towards higher values of the absorption coefficient. This shift occurs as a result of light scattering due to rough surfaces in the microcrystalline layer. It could also be due to additional absorption from the amorphous fraction contained within the µc-Si:H layers, especially in spectral region where photon energy is greater than 1,8 eV [29].

- Although the band gap of µc-Si:H seems to be greater than that of c-Si, the effect is solely due to light scattering. If a correction for the scattered light is carried out, the same band gap of 1,12 eV can be seen for both c-Si and µc-Si:H [29].

- The absorption (photon energies between 0,6 to 0,8 eV) of the µc-Si:H layers is very low, the low absorption region has been measured with the help of Photo-thermal Deflection Spectroscopy (PDS) and Constant Photocurrent Method (CPM**)**. Such low values of absorption are an indication that defect densities in these layers are relatively low, and certainly an indication that grain boundaries are passivated by hydrogen in these layers [29].

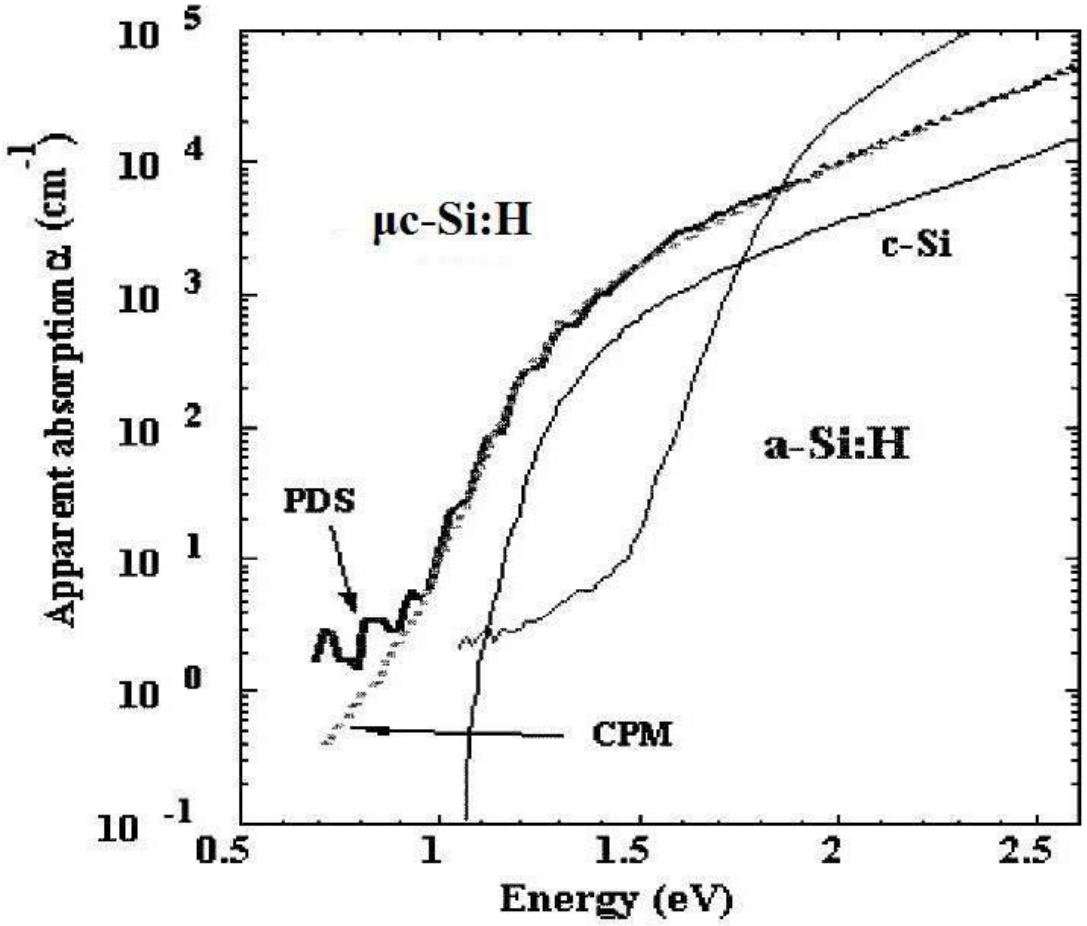

Figure II.14: A comparison of optical absorption between a-Si:H and µc-Si:H [29].

Because of the facts that hydrogenated microcrystalline silicon is a material with an indirect band gap; hence, its absorption coefficient in the visible part of the solar spectrum is relatively low. This implies that thick layers are necessary to obtain sufficient absorption and photgeneration [65]. The fact that the many grain boundaries present can cause obstruction of electronic transport in microcrystalline silicon layers if the grain boundaries are not well passivated by hydrogen, make the use of hydrogenated microcrystalline silicon as the PV active layer within a thin-film solar cell not straight forward. Hence it took many years before microcrystalline intrinsic layers were attempted in thin-film silicon solar cells. Fully microcrystalline silicon solar cells can be advantageous when combined in a hybrid form with amorphous silicon solar cells in tandem known as micromorph structure. This configuration greatly increases the efficiency when compared to the single microcrystalline structure, yielding stable efficiency results [64].

In µc-Si:H applications for solar cells, the increase in effective optical absorption due to light scattering by the rough surfaces is beneficial, it allows reduction in solar cell thickness, hence reduction of bulk and manufacturing costs.

II.3.3) Carrier transport

To improve the efficiency of these solar cells in the future, it is absolutely essential to gain some understanding of the relationship between the crystalline microstructure including grain boundaries and the carrier transport process; in particular, the carrier lifetime (diffusion length) that determines the solar cell characteristics and the recombination velocity at grain boundaries. However, in a microcrystalline silicon cell, the general non-uniformity that is typical of its grain structure has a direct and complex effect on carrier transport, and thus there have been no conclusive reports relating to these physical properties by direct measurement and analysis. Rather, the efficiency of these solar cells has only recently come to light, so only the first steps have been made in the research of their fundamental properties [66].

Werner and al [67] discussed why the very small crystals produced at low temperature exhibit relatively favorable cell characteristics. Although the cell characteristics are the product of current, voltage and fill factor, the open circuit voltage is directly related to the cell's lifetime and is used as a guide to the overall cell characteristics. This is because the current is related to light trapping effects and the cell film thickness.

According to Werner et al.[67], the reason why a microcrystalline silicon cell exhibits a characteristic of 10% or more regardless of its small grain size is because of the very low recombination speed at its grain boundaries. This low recombination speed originates from the small barrier height at the grain boundaries, is guaranteed by (a) the passivation of hydrogen at grain boundary defects, (b) uncharged intrinsic grains (low oxygen density), and (c) the (110) orientation of the crystal grains [68].

The actual crystalline structure of a microcrystalline silicon solar cell has been investigated by transmission electron microscopy (TEM) and atomic force microscopy (AFM). For example, Meier et al [58], at Neuchâtel University, have classified the crystalline structures. Of course the microstructures differ depending on the production process and conditions. It has also been reported that diffusion transport mechanisms are dominant within the grains whereas drift transport is more prominent at the grain boundaries [69]. These grain boundaries exhibit amorphous characteristics which give rise to a passivation effect, and it has been pointed out that this may reduce the boundary recombination velocity [68].

One has to assume that the transport behavior in the different structural phases differs considerably and is, furthermore, affected by transport across the boundaries between the phases. A transport model such as that used for disordered but homogeneous amorphous silicon, or that used for polysilicon, where the grains sizes are much larger, will not be applicable to µc-Si:H. So one can expect to be able to measure only “average” or “effective” microscopic quantities for electronic transport in µc-Si:H [68].

Ignoring for the moment the microscopic details, the conductivity is, in general terms, given by

$$\sigma = q\,\mu\,n \qquad \text{(II.22)}$$

where n is the carrier density, μ the carrier mobility and q the carrier charge. Adopting this description for µc-Si:H and looking (as an approximation) only at the electrons, one can write

$$\sigma = e\,\mu_{n0} n_f \qquad \text{(II.23)}$$

where n_f is the density of free electrons, μ_{n0} the band mobility and e the electron charge. An analogous equation can be written for holes in *p*-type material. Both quantities n_f and μ_{n0} certainly vary between the ordered crystalline and the disordered amorphous phase. When describing instability in µc-Si:H, one finds two main effects [68]:

(1) Adsorption and oxidation at (inner) surfaces, related to the porosity of the material. The effects of adsorption and oxidation on electronic conductivity should be considered very carefully when carrying out studies on electronic transport. In devices where µc-Si:H is used as a bottom cell absorber sandwiched between other layers, these effects could be less pronounced [70].

(2) light-induced degradation (Staebler-Wronski Effect) of the amorphous phase in mixed-phase µc-Si:H. Light-induced degradation depends, not surprisingly, on the amorphous content of the material [28, 66, 71]. In Figure II.15 ; one sees the results of degradation studies of µc-Si:H solar cells with different Raman intensity ratios of the absorber material (i.e. of the intrinsic layer). Highly crystalline material is stable under illumination [64].

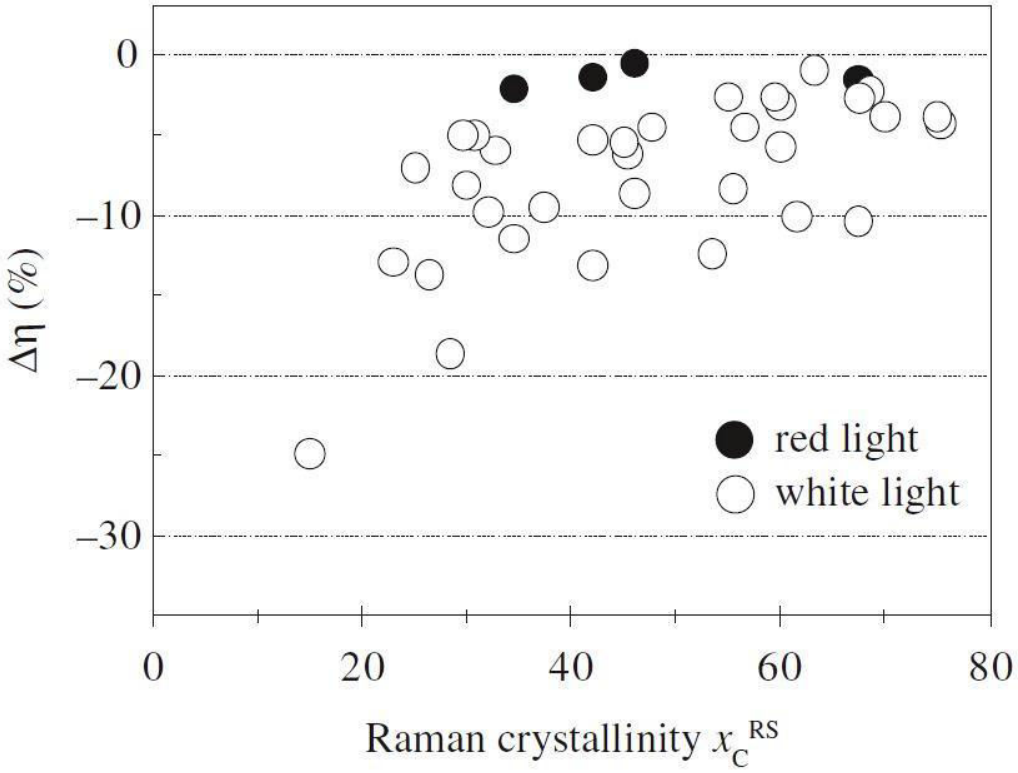

Figure II.15: Relative change in efficiency of solar cells in pin configuration with µc-Si:H absorber layer of different crystallinity, upon 1000 h illumination: (open circles) with white light equivalent to AM1.5 and (full circles) red light equivalent to the situation of the µc-Si:H in the bottom cell of a tandem device (By courtesy of Y. Wang et al., Forschungszentrum Julich) [64].

Solar cells incorporating *i*-layers with a substantial amorphous phase (i.e. cells which generally have the highest efficiencies because of their high FF and their high V_{OC}) degrade slightly and, in fact, the degradation depends on the amorphous volume fraction. Overall the degradation is lower as compared with a-Si:H. For high-efficiency single-junction cell, the relative degradation is only about 5 % [28, 66]. In addition, when the µc-Si:H cell is used as a bottom cell in a "micromorph" tandem cell, the light intensity and the excitation energy for the µc-Si:H *i*-layer would be much lower than in a single-junction µc-Si:H cell, because the high-energy photons are absorbed by the top cell. One can simulate this situation by using a red filter for the white light excitation. Indeed the cells are stable after red light illumination, even after 1000 h [64].

II.4) Alloys

As for amorphous silicon, microcrystalline silicon material has the potential of being alloyed with several elements, and alloys of µc-Si:H with Ge, O and C have already been developed and explored [64]. Similar to a-Si:H, the alloying is obtained through basic appropriate admixture of corresponding gases in the deposition process. The main effect of alloying is that the optical gap will be shifted to lower energies (alloying with Ge) or to higher energies (alloying with O, C). The resulting alloy materials have been explored for applications such as infrared absorbers (Ge) [72], as window layers (C and O) [73], or as intermediate reflectors in stacked cells [73]. On the wide band gap side we have µc-SiC:H, which is the true stoichiometric alloy and not the µc-Si:H crystallites in a-SiC:H matrix. Such an alloy would have high potential as a window layer for solar cells. The material is more difficult to prepare. One approach is to use HWCVD with monomethylsilane, a gas which already contains the Si-C bond in a 50-50 mixture. This gives material with excellent crystallinity and a high optical band gap. In the as-deposited state, this material is very highly conductive *n*-type, which could be due to impurity doping or highly conductive structure phases. Applying such material in *n*-side illuminated solar cells with µc-Si:H absorber layers yields high current values and quantum efficiency due to the good transparency [74]. Meanwhile, also successful *p*-type doping of µc-SiC:H has been performed [75, 76].

II.5) Elaboration methods

In general, thin films may be fabricated either by physical vapor deposition (e.g., evaporation or sputtering) of the bulk material, or by chemical vapor deposition from the decomposition of suitable gases that contain the desired film material [64].

In the previous section, the properties of Si-based thin films have been described. In the context of depositing such films, the role of hydrogen is essential. Historically both evaporation and sputtering of elemental silicon were used to obtain thin films of amorphous silicon. However, these films contained high defect concentrations, mostly caused by poorly coordinated Si atoms. Due to these high defect concentrations, the gap state density between the valence and conduction bands far exceeds the doping densities that can be typically achieved. Therefore, this material is not suitable for use in an electronic semiconductor device, which essentially requires the presence of *n*- and/or *p*-type regions [64].

The high density of defect states can be somewhat reduced by heating the films in a hydrogen atmosphere, or, in the case of sputtering, by adding hydrogen to the sputtering gas. However, these methods of film preparation have not proved successful in the further development of suitable PV-grade materials. Since it was recognized that silicon films deposited at low temperatures require the presence of hydrogen to ”saturate” or “passivate” the dangling bonds, Chemical Vapor Deposition (CVD) methods have been chosen with a source gas containing both silicon and hydrogen, which is then decomposed by supplying thermal or electrical energy to generally form hydrogenated amorphous silicon (a-Si:H) films. Thus, in 1969, the decomposition of silane (SiH_4) in a glow discharge yielded hydrogenated amorphous silicon films with good photoconductivity [77], indicating a defect concentration well below the generated photo carrier concentration.

Adding a doping gas to the silane, glow discharge deposition has opened the way for the effective doping of a-Si:H thin films, and hence for the possibility of creating electronic thin-film devices.

Since then, the development of Si-based thin films for PV applications has remained based on the decomposition of silane as the central source material. Both forms of energy supply have been developed further, namely:

-Electrical energy, supplied in a glow discharge (plasma) for plasma-enhanced chemical vapor deposition (PECVD).

-Thermal energy by heating a filament, for thermo-catalytic chemical vapor deposition (Cat-CVD), more commonly called Hot-Wire CVD (HWCVD).

To date, only PECVD has reached industrial relevance, whereas HWCVD has so far not gone beyond industrial feasibility studies [64]. Here, we will mainly describe the basic features of PECVD.

PECVD is conducted in a plasma reactor that usually consists of:

- A vacuum chamber, equipped with an inlet for the reaction gases, and pumps to remove unreacted and reacted gases.
- A pair of parallel electrodes, one grounded and acting as the support for the substrate to be coated, and the other connected to an electrical power supply, and possibly also acting as a shower head to uniformly distribute the reaction gases.
- A gas handling system.
- Substrate heating.

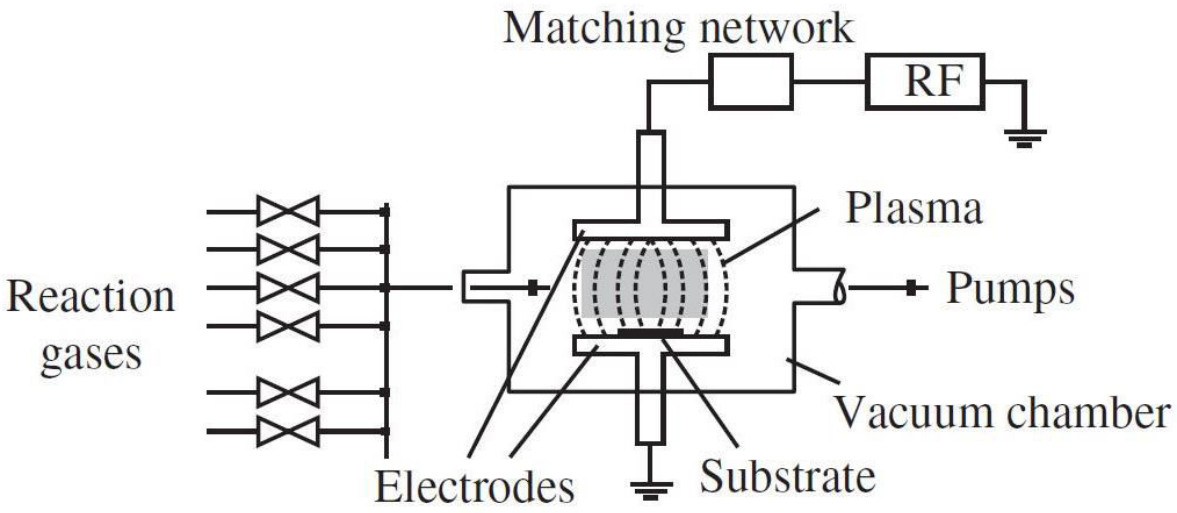

FigureII.16: Schematic diagram of a PECVD reactor [64].

This arrangement, schematically shown in FigureII.16, facilitates the sequential deposition of the entire semiconductor structure, either in a single-junction or a multijunction (tandem or triple cell) configuration, as *pin* or *pin*/*pin* etc. To this end, not only silane is used (as is basically sufficient for the intrinsic *i*-layer), but also doping gases containing boron and phosphorus, such as diborane (B_2H_6) or trimethylboron [$B(CH_3)_3$], and phosphine (PH_3), for depositing *p*- and *n*-layers, respectively.

Additionally, the energy gaps of the semiconductor film may be varied by adding gases containing other group-IV elements:

- Methane (CH_4) in order to alloy with carbon and, thus, to increase the energy gap of the *p*-layer to create a window layer.
- Germane (GeH_4) in order to alloy with germanium and, thus, to decrease the energy gap of the *i*-layer for enhanced red-response, particularly for multijunction cell structures.

The application of a sufficiently high RF voltage (typically at the industrial frequency of 13.56 MHz) to a capacitive configuration of parallel electrodes in a container filled with a gas at low pressure leads to the generation of a low-pressure plasma.

The plasma reactions occur while the gas and the parts exposed to the plasma remain at relatively low temperatures. The plasma is ignited by the generation of electrons and ions, due to the ionization of gas molecules, followed by subsequent secondary electron emission from the electrodes, and further ionizations with charge

carrier multiplication. The ignition of the plasma may sometimes require high voltage pulses supplied from a Tesla coil via a high-voltage feed through [64].

In this section, guidelines for the deposition conditions leading to microcrystalline silicon µc-Si:H will be presented. The PECVD offers the possibility of depositing a wide range of Si-based film material, ranging from amorphous to microcrystalline structures of different quality. The invention of the "micromorph" tandem cell by the Neuchatel group [59] has opened up a novel way of achieving significantly higher stabilized efficiencies, as compared to conventional structures, based solely on amorphous materials. This work [59] was done with a VHF (very high frequency) PECVD system; in fact, it turned out that VHF deposition was specially suitable for the fabrication of device-grade µc-Si:H layers and high-quality cells. However, the VHF technology originally employed is not applicable in a direct straight forward way to economically viable large-area production. Therefore, lower plasma frequencies ranging from 13.56 MHz to 40.68 MHz have been explored for deposition of the microcrystalline material to be used in the bottom cells of micromorph tandem cells [64]. The deposition of microcrystalline material is favored by a high hydrogen dilution $= [H_2]/[SiH_4]$, i.e. by low silane concentrations $SC = [SiH_4]/([H_2] + [SiH_4])$. This can be explained by simultaneous etching of poorly coordinated bonds during the deposition, a process that is favored by high hydrogen dilution ratios. In order to compensate for the low deposition rates due to simultaneous etching, higher plasma powers then need to be used. The plasma deposition conditions for microcrystalline growth have been discussed in more detail in a relatively simple plasma chemistry model [78]. Accordingly, a ratio Q between deposition and etch rates is determined, namely: $Q < 0.5$ for a-Si:H deposition, $0.5 < Q < 1$ for µc-Si:H deposition. This ratio Q depends on three dimensionless parameters [64]:

- The hydrogen dilution ratio $R = [H_2]/[SiH_4]$.
- The ratio between the silane dissociation rate and the pumping speed, which are equals.

Since for RF frequencies at 13.56 MHz, the silane dissociation rates are much smaller than for VHF, the pumping speed must also be chosen correspondingly smaller.

- The ratio between the dissociation rate of SiH_4 (for Si deposition) and the dissociation rate of H_2 into atomic hydrogen (for Si etching).

Figure II.14 shows the schematic range of film structures obtained with different PECVD parameters; the dashed lines indicate the amorphous to microcrystalline transitions (the a →(a + µc) and (a + µc) →µc transitions respectively).

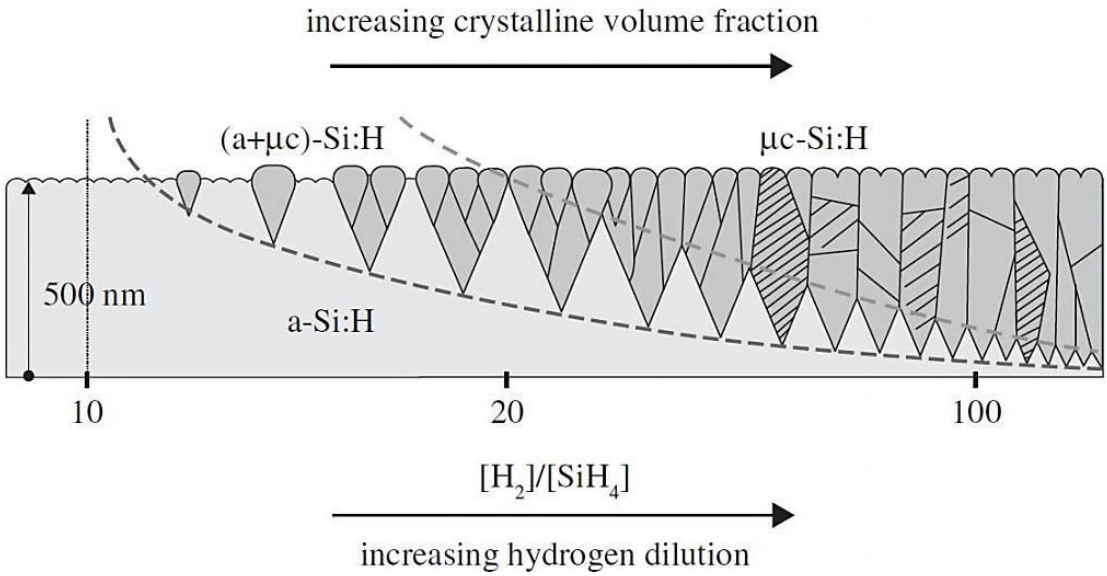

Figure II.17 : Range of film structures (schematic), obtained with different PECVD parameters; the dashed lines indicate the $a \rightarrow (a + \mu c)$ and $(a + \mu c) \rightarrow \mu c$ transitions, respectively [64].

II.6) Conclusion

In this chapter, we presented the basic material properties of a-Si:H and µc-Si:H respectively, such as the structural, electrical and optical properties. Subsequently, a detailed description was introduced for the defect model, the transport, recombination processes, metastability phenomenon and degradation in a-Si:H. Finally, the deposition process, usually used to produce a-Si:H and µc-Si:H thin-films, was presented.

Chapter III

Solar cell fundamentals

III.1) Introduction

A solar cell is a device that converts sunlight directly into electricity through the photovoltaic effect [79]. The efficiency of the cell quantifies the fraction of solar energy that it converts into electrical energy. In principle it depends on two parameters: the generation of current by absorbed incident illumination, and the loss of charge carriers via so-called recombination mechanisms. A built-in field of p-n diode separates charge carriers of opposite polarity, and drives the light-generated current through the cell and to the terminals. Several solar cells will be electrically connected and encapsulated as a module [80].

In this chapter, we present fundamental concepts related to solar cell operation mode such as the solar spectrum, the photovoltaic conversion processes and parameters, and the transport model. The last sections present a description of typical solar cells based on hydrogenated amorphous and microcrystalline silicon (a-Si:H and µc-Si:H respectively) with different configurations: single-junction solar cell, two-terminal and four-terminal tandem solar cell.

III.2) Light spectrum

Our planet receives photons continuously coming from the sources of light present in the universe. The majority of these photons are generated during nuclear reactions which take place in the heart of stars. Their energy varies according to the source considered, but also from the possible interactions during their course to the Earth. Although distant of almost 150 million kilometers, the Sun is the principal transmitter of light in the surroundings of the Earth. At such a distance and with a ray of 6380 km, the latter on average receives only $4.52*10^{-8}$ % [81] of the energy emitted by our star. It is thus completely useless to be interested in the other stellar sources for the space photovoltaic applications (to the neighborhoods of the Earth) and terrestrial. In this context, and an aim of adapting the converters of light to the principal source, it is essential to know well the distribution in energy of the photons coming from the Sun.

The quantity of light absorbed by a semiconductor depends on the bandgap energy, but also on the spectrum of the incoming light (i.e. the energy distribution of the incident light as a function of wavelength). Figure III.2 shows the spectrum of light emitted by the sun (which can be considered as a black body at 6000 K), as well as the spectrum of sunlight received at the earth, both outside the atmosphere and at

ground level. The difference between the last two is due to the path through the earth's atmosphere, which attenuates the solar spectrum (Rayleigh scattering, scattering by aerosols, absorption by the constituent gases of the atmosphere: UV absorption by ozone, infrared absorption by water vapor, etc.). This attenuation effect is characterized by the "Air Mass" coefficient AM = 1/cosα, where α is the angle between the solar ray and a vertical line Figure III.1. Thus, AM0 corresponds to the solar spectrum outside the atmosphere and AM1 to the solar spectrum on the earth's surface when the sun is directly (vertically) overhead. During mornings and evenings, when the incidence of sunlight is almost horizontal, we may have "Air Mass" coefficients AM3 or even higher. AM1.5 (i.e. α ≈ 45°)2 is considered to be the "standard" value for testing and specifications in terrestrial applications, as it corresponds to a "reasonable average value" of the air mass through which the incoming sunlight passes. Note that not only the spectrum is defined by this coefficient, but also the intensity of the incoming sunlight. However, the intensity is generally normalized to 1000 W/m^2 in order to calibrate the efficiency of photovoltaic systems [82].

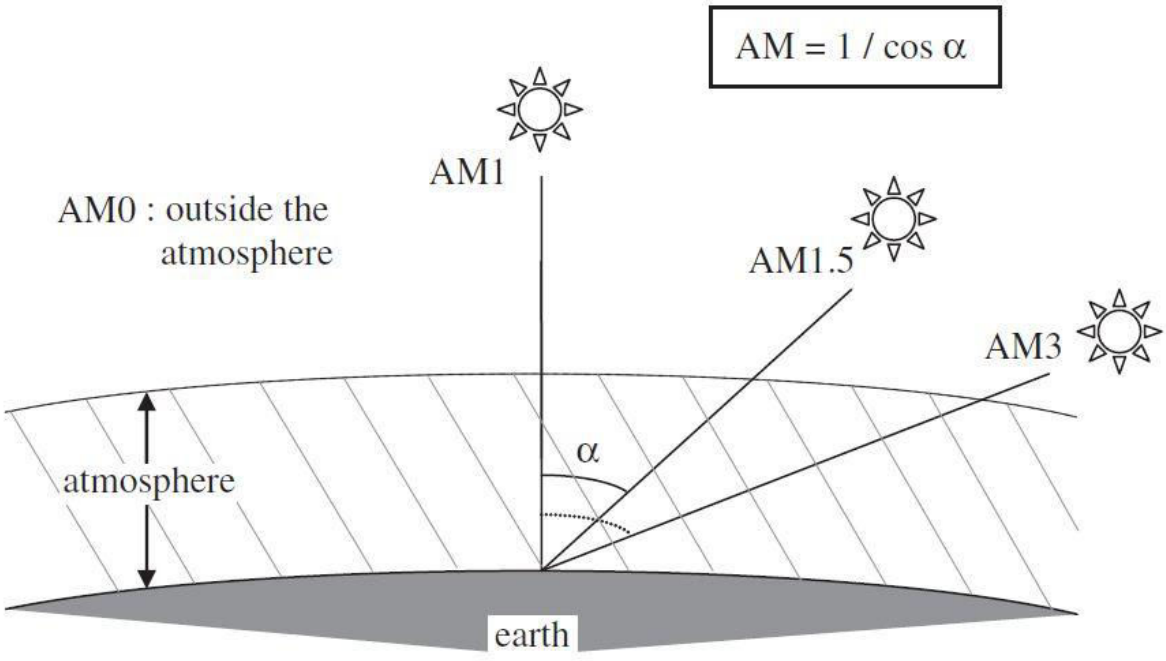

Figure III.1: Diagram illustrating the definition of AM0, AM1, AM1.5 and AM3.

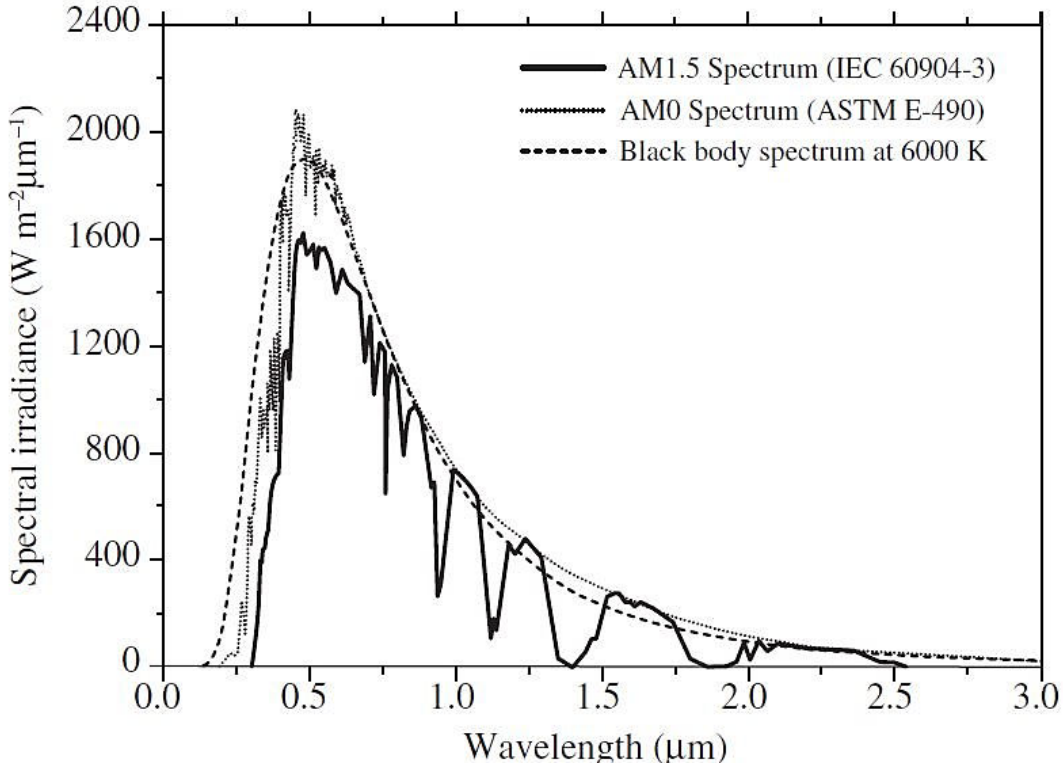

Figure III.2: Spectral distribution of the solar spectrum received on the earth's surface (AM1.5) and outside the atmosphere (AM0) compared with the radiation of a blackbody at 6000 K.

A semiconductor with a lower value of bandgap energy will be able to absorb a wider range of the solar spectrum (i.e. more photons) compared to one with a larger bandgap. However, in the first case, a substantial part of the incident energy will be lost by thermalization (i.e. by the energy difference between the energy of each photon and the bandgap energy). On the other hand, a semiconductor with a higher value of bandgap energy will only be able to absorb a relatively narrow range of the solar spectrum (i.e. a relatively small amount of high-energy photons only), but less energy will be lost through thermalization. One can thus intuitively understand that to maximize the spectral conversion efficiency, one must choose an optimum value for the bandgap that is somewhere in an intermediate range, corresponding approximately to the bandgap of crystalline silicon of $E_g = 1.12\ eV$.

III.3) Photovoltaic conversion

A semiconductor device as the solar cell produces electrical current (and then sends it through an external load) when exposed to light (photovoltaic effect). The operation of a solar cell consists of two main steps:

(1) Creation of electron-hole pairs, i.e. generation of free electrons and holes through the absorption of photons.

(2) Separation of the free electrons and holes in order to actually produce electricity.

The efficiency η of a solar cell is the ratio of the electrical output power to the incident light power.

III.3.1) Creation of electron-hole pairs

When light illuminates a solar cell, photons are absorbed by the semiconductor material and pairs of free electrons and holes are created (Figure III.3). However, in order to be absorbed, the photon must have an energy $E_{ph} = h\nu$ (where h is the Planck's constant and ν the frequency of light) higher or at least equal to the bandgap energy E_g of the semiconductor. The bandgap energy is the difference in energy levels between the lowest energy level of the conduction band (E_C) and the highest energy level of the valence band (E_V) (Figure III.4). For a given semiconductor, E_g is a fixed material constant that only slightly depends on temperature.

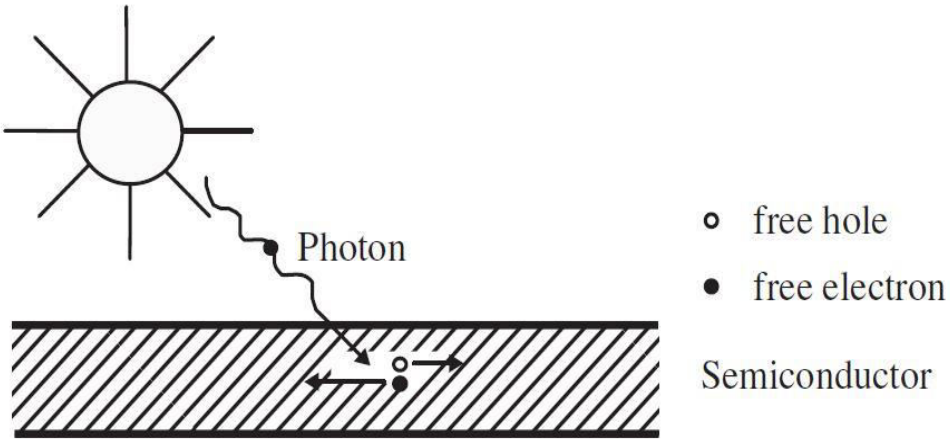

Figure III.3: Creation of an electron-hole pair through absorption of a photon of energy.

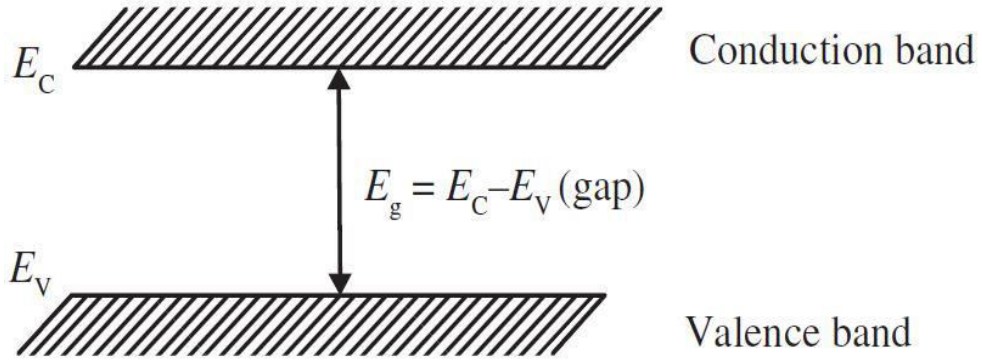

Figure III.4: Bandgap energy E_g of a semiconductor.

Depending on the energy of the photon and on the bandgap energy of the solar cell material, three cases can occur:

(1) $E_{ph} = E_g$: in this case, the photon can be absorbed and will then generate a single electron-hole pair, without any loss of energy (Figure III.5).

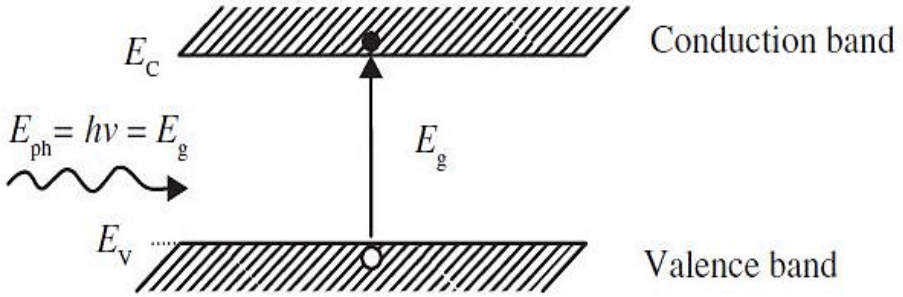

Figure III.5: Absorption of a photon when $E_{ph} = E_g$.

(2) $E_{ph} > E_g$: in this case, the photon can be easily absorbed and will then, in general, create a single electron-hole pair. The excess energy $E_{ph}-E_g$ is rapidly transformed into heat (thermalization; Figure III.6). In some rare cases (which have absolutely no bearing on present-day solar cells), a second electron-hole pair can be successively created by impact ionization, provided that $E_{ph} >> E_g$.

(3) $E_{ph} < E_g$: the energy of the photon is not high enough to be absorbed. The photon will either be reflected or absorbed elsewhere, and its energy is lost. Note that in some rare cases where a sufficiently high density of states exists within the gap (due to impurities or defects in crystallinity), a photon with $E_{ph} < E_g$ can still be

absorbed (Figure III.7). However, in general, and for present-day solar cells, this mechanism will not contribute to the effective electric current produced by the cell.

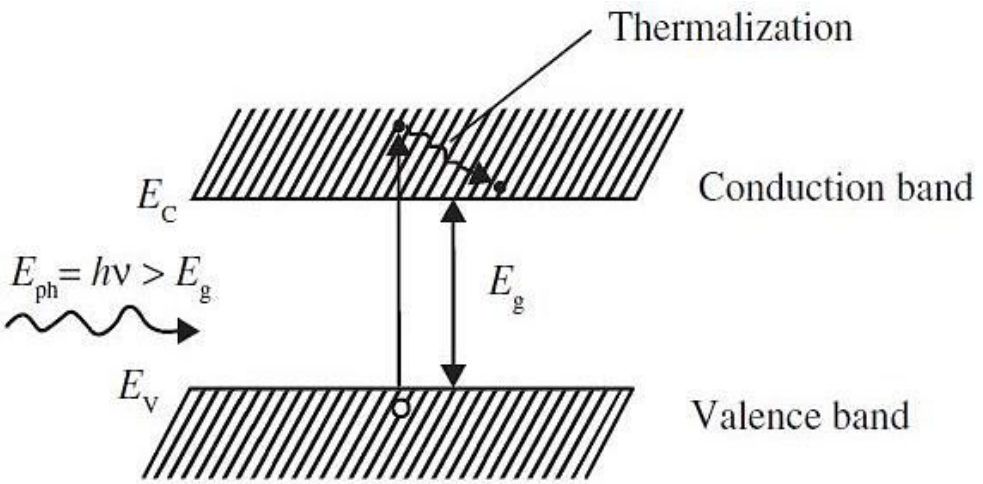

Figure III.6: Absorption of a photon when $E_{ph} > E_g$; thermalization.

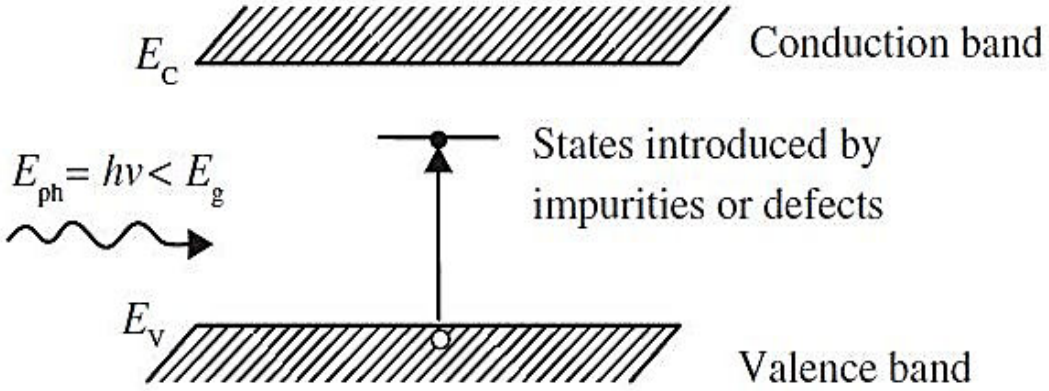

Figure III.7: Possible absorption of a photon when $E_{ph} < E_g$.

III.3.2) Direct and indirect bandgaps

The terms “direct” and “indirect” refer here to the interaction between incoming light and the semiconductor itself. The semiconductor is considered to have a direct gap when the absorption of an incoming photon is directly possible without the interaction of a phonon within the semiconductor. In this case, the maximum of the valence band corresponds to the minimum of the conduction band. GaAs, CdTe and $CuInSe_2$ are typical examples of semiconductors with a direct gap. The semiconductor is considered to have an indirect gap when the absorption of an incoming photon is only possible with the interaction of a phonon within the semiconductor. In this second case, the maximum of the valence band does not correspond to the minimum

of the conduction band. Because a phonon must now be emitted (or absorbed) for a photon to be absorbed (see Figure III.8), the absorption probability is significantly reduced, as compared to the case of a semiconductor with a direct bandgap. Si, Ge and C are typical examples of semiconductors with indirect gaps.

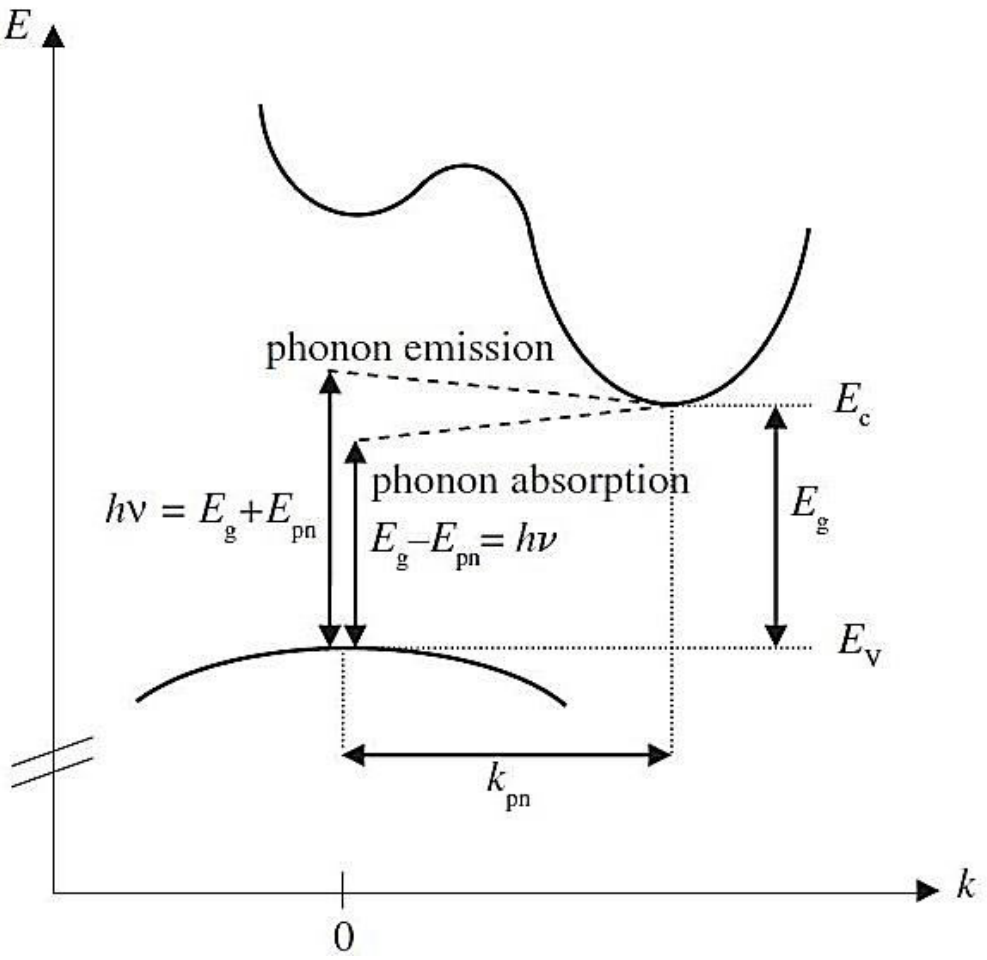

Figure III.8: Diagram of energy E versus momentum, for a semiconductor with indirect band gap E_g.

III.3.3) Separation of electrons and holes

The first step within the photovoltaic conversion process is the generation of pairs of electrons and holes within the semiconductor.

Now, as the second step, these electron-hole pairs have to be separated: the electrons have to be sent to one side and the holes to the other side of the solar cell device. Such a separation is only possible by an electric field. Electrons and holes have opposite electric charge and therefore move in opposite directions within an

electric field. To create an electric field, solar cells are formed as diodes: usually as p-n type diodes but, in the case of thin film silicon solar cells, as pin-type diodes.

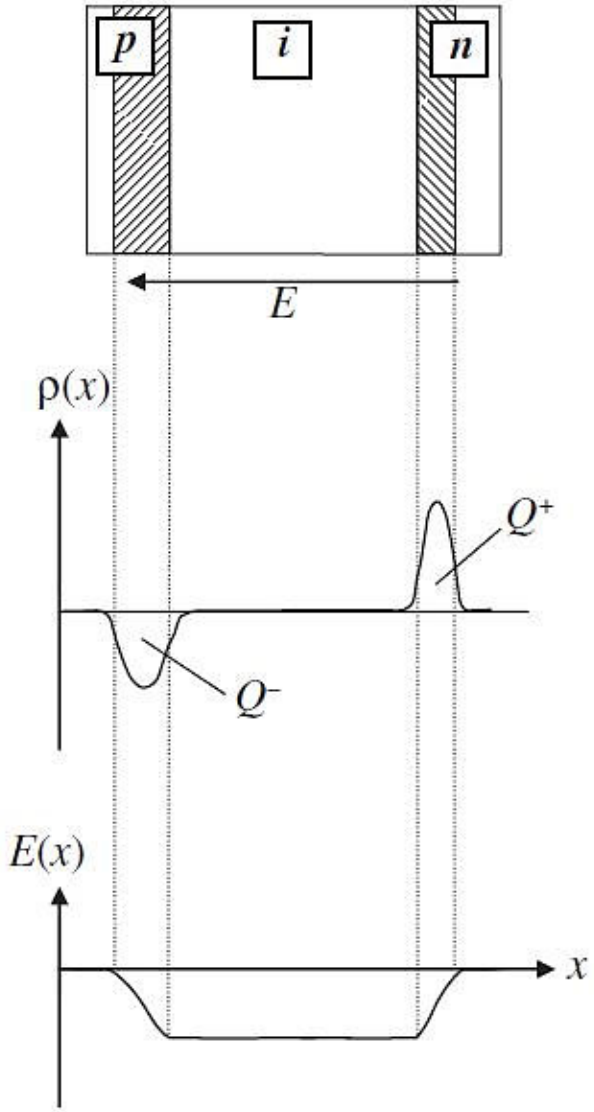

Figure III.9: Formation of internal electric field E and of built-in voltage V_b in a *pin* type diode[64].

Within a diode, an internal electric field is always formed. As schematically shown in Figure III.9, the internal electric field is limited to the depletion layer in the p-n type diode, whereas it extends over the whole of the i-layer (intrinsic layer) in the pin-type diode. The generation of the internal electric field is governed by the so-called "built-in voltage V_b". V_b is always smaller than (E_g/q), see the evaluation of V_b in Figure III.10. The value of V_b for all forms of silicon solar cells is roughly 1 V, provided that the p- and n-type layers within the solar cell have been "properly" doped.

This second step of charge separation comes at the price of additional energy losses: about one-third to one-half of the remaining energy has now to be sacrificed. The charge separation process is evidently more efficient if the internal electric field is stronger, i.e. if V_b is higher. This means that, in the optimal case, the charge process is more efficient if the bandgap energy is higher. Therefore the optimum bandgap energy for maximizing the energy conversion efficiency of the whole solar cell, including the second step of charge separation, is shifted to higher values when compared to the optimum for the first step alone.

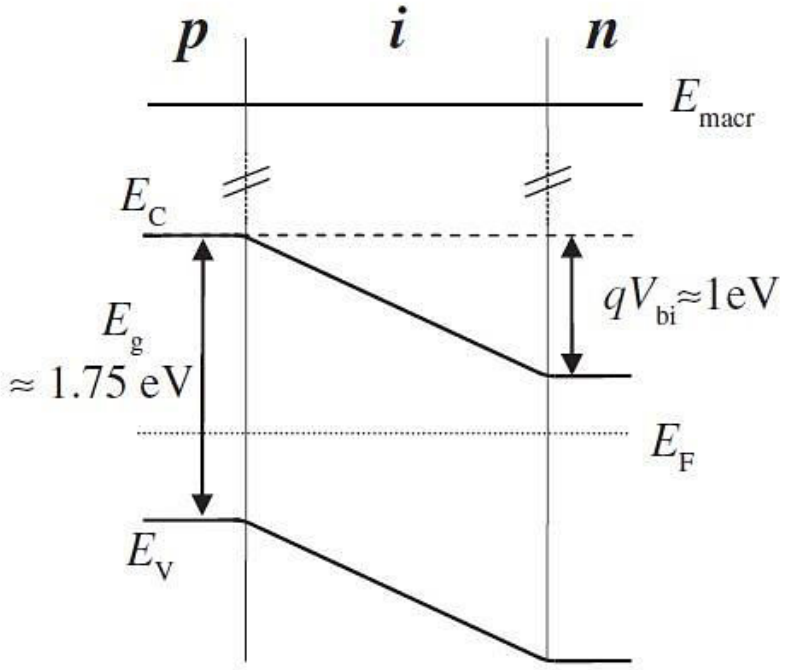

Figure III.10: Band diagram showing schematically the evaluation of V_b in a-Si pin-type diode [64].

III.4) Basic equations and parameters

Years of research into device physics have resulted in a mathematical model that operates on any semiconductor device [83]. This model consists of a set of fundamental equations, which link together the electrostatic potential and the carrier densities, within some simulation domain. These equations, which are solved inside any general purpose device simulator, have been derived from Maxwell's laws and consist of Poisson's Equation, the continuity equations and the transport equations. Poisson's Equation relates variations in electrostatic potential to local charge densities. The continuity and the transport equations describe the way that the electron and hole densities evolve as a result of transport processes, generation processes, and recombination processes.

III.4.1) Poisson's equation

Poisson's Equation relates the electrostatic potential to the space charge density:

$$div(\varepsilon \nabla \Psi) = -\rho \qquad \text{(III.1)}$$

Where ψ is the electrostatic potential, $\mathcal{E}$ is is the local permittivity, and ρ is the local space charge density. The reference potential can be defined in various ways; this is always the intrinsic Fermi potential ψ_i. The local space charge density is the sum of contributions from all mobile and fixed charges, including electrons, holes, and ionized impurities.

$$\rho = q.(p - n + N_d^+ - N_a^- + N_{tail} + N_{DS}) \qquad \text{(III.2)}$$

where q is magnitude of the charge on an electron, p and n are the free hole and electron densities, $Nd+$ and $Na-$ are the concentrations of ionized donors and acceptor, $Ntail$ and NDS are the net charge densities due to the trapping of holes and electrons in tail states and dangling bond states, respectively.

The electric field is obtained from the gradient of the potential:

$$\vec{E} = -\nabla \Psi \qquad \text{(III.3)}$$

III.4.2) Carrier continuity equations

The continuity equations for electrons and holes are defined by equations:

$$\frac{dn}{dt} = \frac{1}{q} div\overrightarrow{J_n} + G_n - R_n \qquad \text{(III.4)}$$

$$\frac{dp}{dt} = \frac{1}{q} div\overrightarrow{J_p} + G_p - R_p \qquad \text{(III.5)}$$

Where n and p are the electron and hole concentration, $\overrightarrow{J_n}$ and $\overrightarrow{J_p}$ are the electron and hole current densities, G_n and G_p are the generation rates for electrons and holes, R_n and R_p are the recombination rates for electrons and holes, and q is magnitude of the charge on an electron.

III.4.3) Transport equations

Equations (III.1), (III.4) and (III.5) provide the general framework for device simulation. But further secondary equations are needed to specify particular physical models for:$\overrightarrow{J_n}$, $\overrightarrow{J_p}$, G_n, R_n, G_p and R_p.

The current density equations, or charge transport models, are usually obtained by applying approximations and simplifications to the Boltzmann Transport Equation. These assumptions can result in a number of different transport models such as the drift-diffusion model, the Energy Balance Transport Model or the hydrodynamic model. The choice of the charge transport model will then have a major influence on the choice of generation and recombination models.

The simplest model of charge transport that is useful is the Drift-Diffusion Model. This model has the attractive feature that it does not introduce any independent variables in addition to ψ, n and p. Until recently, the drift-diffusion model was adequate for nearly all devices that were technologically feasible. The drift-diffusion approximation, however, becomes less accurate for smaller feature sizes. More advanced energy balance and hydrodynamic models are therefore becoming popular for simulating deep submicron devices.

Derivations based upon the Boltzmann transport theory have shown that the current densities in the continuity equations may be approximated by a drift-diffusion model. In this case, the current densities are expressed in terms of the quasi-Fermi levels ϕ_n and ϕ_p as:

$$\vec{J}_n = -q\mu_n n \nabla \phi_n \qquad \text{(III.6)}$$

$$\vec{J}_p = -q\mu_p n \nabla \phi_p \qquad \text{(III.7)}$$

Where μ_n and $\mu_p$are the electron and hole mobilities. The quasi-Fermi levels are then linked to the carrier concentrations and the potential through the two Boltzmann approximations:

$$n = n_i \exp\left[\frac{q(\psi-\phi_n)}{k_B T}\right] \qquad \text{(III.8)}$$

$$p = n_i \exp\left[\frac{-q(\psi-\phi_p)}{k_B T}\right] \qquad \text{(III.9)}$$

Where n_i is the effective intrinsic concentration, k_B Boltzmann constant and T is the lattice temperature. These two equations may then be re-written to define the quasi-Fermi level potentials:

$$\phi_n = \psi - \frac{kT}{q}\ln\left(\frac{n}{n_i}\right) \qquad \text{(III.10)}$$

$$\phi_p = \psi + \frac{kT}{q}\ln\left(\frac{p}{n_i}\right) \qquad \text{(III.11)}$$

The Effective electric fields are normally defined whereby:

$$\overrightarrow{E_n} = -\nabla\left(\psi + \frac{kT}{q}\ln n_i\right) \qquad \text{(III.12)}$$

$$\overrightarrow{E_p} = -\nabla\left(\psi - \frac{kT}{q}\ln n_i\right) \qquad \text{(III.13)}$$

which then allows the more conventional formulation of drift-diffusion equations to be written:

$$\vec{J}_n = q\mu_n n\overrightarrow{E_n} + \mathrm{q}D_n\nabla n \qquad \text{(III.14)}$$

$$\vec{J}_p = q\mu_p p\overrightarrow{E_p} - \mathrm{q}D_p\nabla p \qquad \text{(III.15)}$$

It should be noted that this derivation of the drift diffusion model has tacitly assumed that the Einstein relationship holds. In the case of Boltzmann statistics this corresponds to:

$$D_n = \frac{kT}{q}\mu_n \qquad \text{(III.16)}$$

$$D_p = \frac{kT}{q}\mu_p \qquad \text{(III.17)}$$

III.4.4) Solar cell parameters

When a forward bias is applied across a solar cell, a potential difference develops between the front and rear contacts. This potential difference creates a current, usually called the dark current (J_{dark}), which is in the opposite direction of the photocurrent. Since a solar cell is essentially a large diode, it is rectifying and the dark current can be described by equation (III.18), where J_0 is a constant that is proportional to the total recombination in the device, V is the potential across the device, k_B is the Boltzmann constant and T is the temperature:

$$J_{dark} = J_0\left(e^{\frac{qV}{k_BT}} - 1\right) \qquad \text{(III.18)}$$

When the cell is under illumination, There three important points are identified, that is the short-circuit current density J_{sc}, the open circuit voltage V_{oc} and the current

density J_m and voltage V_m that gives the maximum power density $P_m = J_m \times V_m$. The total current can then be approximated as the sum of the dark current and the photocurrent:

$$J_T = J_{light} - J_{dark} \qquad \text{(III.19)}$$

By definition, under open circuit condition the total current in the device is zero, therefore, we can define the open circuit voltage as the voltage at which J_{dark} and J_{sc} are equal. An expression for V_{oc} can be derived from equations (III.18) and (III.19) by substituting 0 for J_T, V_{oc} for V, and solving for V_{oc} which can be expressed as:

$$V_{OC} = \frac{K_B T}{q} ln\left(\frac{J_{light}}{J_{dark}} + 1\right) \qquad \text{(III.20)}$$

The open circuit voltage varies dependent on the recombination in the solar cell which is again dependent on the band gap of the semiconductor. The open circuit voltage is expected to vary linearly with the band gap of the semiconductor [84].

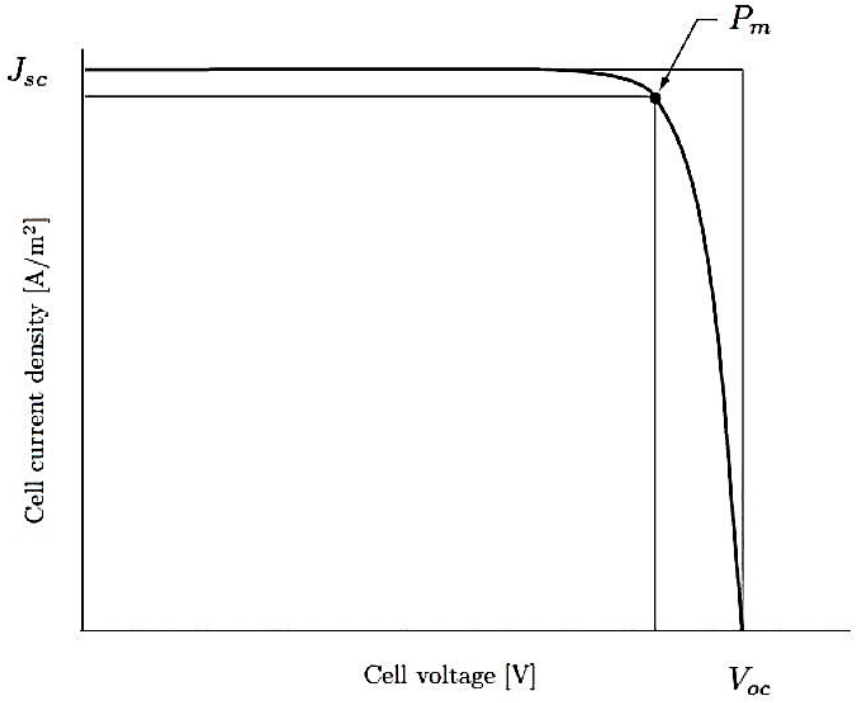

Figure III.11: Current density-voltage $J - V$ behavior for a solar cell showing the short-circuit current density J_{sc}, the open circuit voltage V_{oc} and the current density J_m and voltage V_m that gives the maximum power density P_m.

To obtain efficient solar cells, the main subject is to maximize the power. The ratio of maximum power density to the product of J_{sc} and V_{oc} is given the name fill factor, FF:

$$FF = \frac{P_m}{J_{sc} \cdot V_{oc}} \qquad \text{(III.21)}$$

The fill factor is always less than one and describes the squareness of the $J - V$ curve. The most important term describing solar cells is the conversion efficiency, η, given as:

$$\eta = \frac{P_m}{P_{in}} \qquad \text{(III.22)}$$

To consider the behavior of real solar cells series and shunt resistances have to be included, as shown in Figure III.12. The series resistance R_s is included due to the contact resistance to the front and back contact and the resistance of the cell material. The effect of series resistance is most important for high current densities and increases at high temperatures and high light intensities. Series resistance is always present in practical devices. A shunt resistance R_{sh} represents current leakage through the cell and at its edges. Leakage through the cell can be due to dislocations, grain boundaries or crystal defects. Due to the higher output voltage of GaAs solar cells compared to Si solar cells, shunt resistance is more important in GaAs. However, Shunt resistance is usually not important in practical devices at common intensities [85].

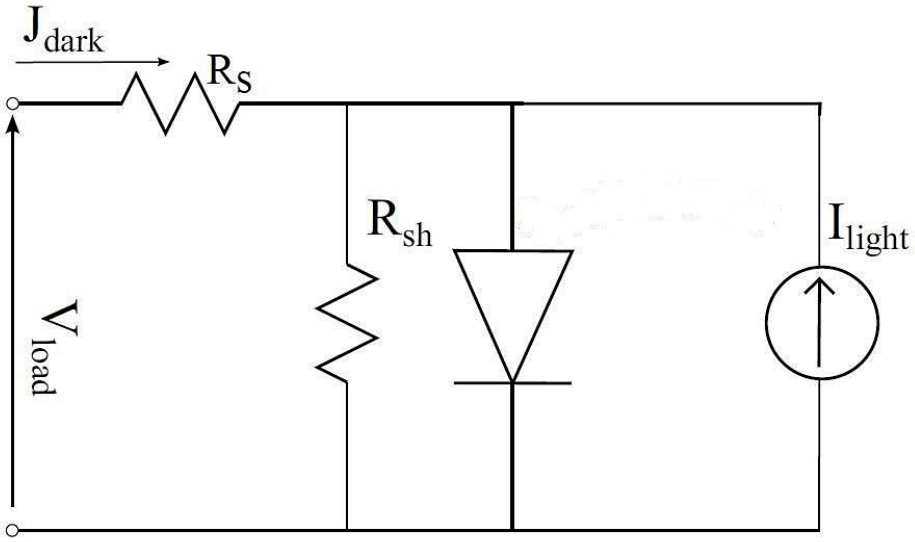

Figure III.12: The equivalent Electric circuit of a real photovoltaic cell.

III.4.5) Quantum efficiency

A solar cell's quantum efficiency value indicates the amount of current that the cell will produce when irradiated by photons of a particular wavelength. If the cell's quantum efficiency is integrated over the whole solar electromagnetic spectrum, one can evaluate the amount of current that the cell will produce when exposed to sunlight. The ratio between this energy-production value and the highest possible energy-production value for the cell (i.e., if the QE were 100% over the whole spectrum) gives the cell's overall energy conversion efficiency value. Note that in the event of multiple excitation generation (MEG), quantum efficiencies of greater than 100% may be achieved since the incident photons have more than twice the band gap energy and can create two or more electron-hole pairs per incident photon. Two types of quantum efficiency of a solar cell are often considered:

- **External Quantum Efficiency (EQE)** is the ratio of the number of charge carriers collected by the solar cell to the number of photons of a given energy shining on the solar cell from outside (incident photons).

$$EQE = \frac{electrons/sec}{photons/sec} = \frac{current/(charge\ of\ one\ electron)}{(total\ power\ of\ photons)/(energy\ of\ one\ photon)} \quad \text{(III.23)}$$

- **Internal Quantum Efficiency (IQE)** is the ratio of the number of charge carriers collected by the solar cell to the number of photons of a given energy that shine on the solar cell from outside *and* are absorbed by the cell.

$$IQE = \frac{electrons/sec}{absorbed\ photons/sec} = \frac{EQE}{1-Reflection-Transmission} \quad \text{(III.24)}$$

The IQE is always larger than the EQE. A low IQE indicates that the active layer of the solar cell is unable to make good use of the photons. To measure the IQE, one first measures the EQE of the solar device, then measures its transmission and reflection, and combines these data to infer the IQE.

The external quantum efficiency therefore depends on both the absorption of light and the collection of charges. Once a photon has been absorbed and has generated an electron-hole pair, these charges must be separated and collected at the junction.

A "good" material avoids charge recombination. Charge recombination causes a drop in the external quantum efficiency.

The ideal quantum efficiency graph has a square shape, where the QE value is fairly constant across the entire spectrum of wavelengths measured. However, the QE for most solar cells is reduced because of the effects of recombination, where charge carriers are not able to move into an external circuit.

The external quantum efficiency accounts for any losses related to the solar cell structure. Hence, these losses depend on the properties of the substrate, the transparent conductive oxide (TCO) layers and the semiconductor layers. A very detailed analysis of the optical and electrical losses can be found in ref [86].
Figure II.13 shows the external quantum efficiency of an a-Si:H and a µc-Si:H solar cell. The µc-Si:H solar cells absorbs photons in a much wider wavelength range due to its lower band gap of 1.1 eV. This results in higher short-circuit current densities compared to a-Si:H solar cells [33].

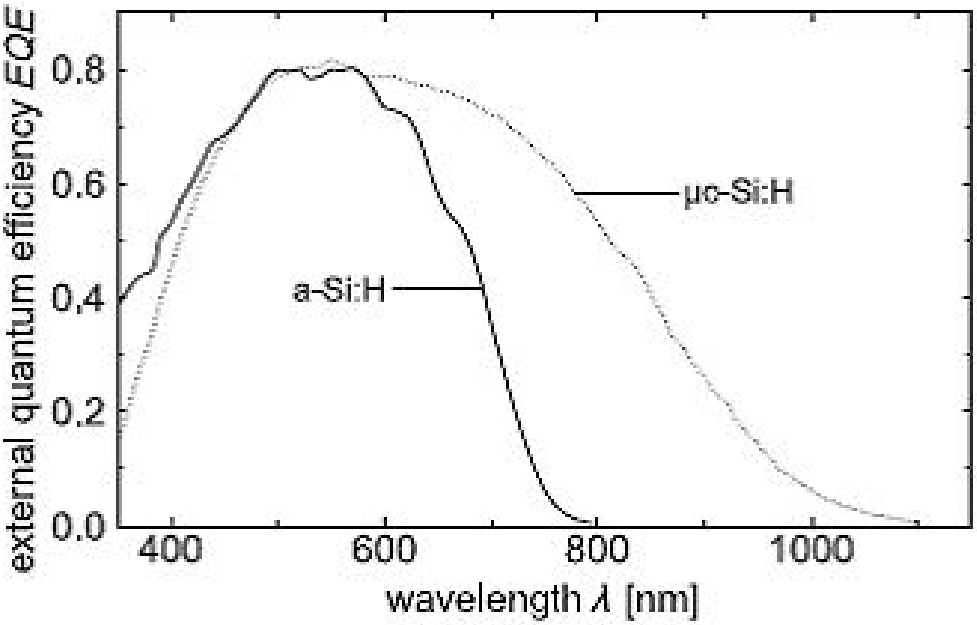

Figure III.13: Exemplary external quantum efficiency as a function of the wavelength for an a-Si:H solar cell (solid line) and a µc-Si:H solar cell (dotted line). [33].

III.5) a-Si:H and µc-Si:H-based solar cells

A typical a-Si:H solar cell is represented by a single junction solar cell. There are two configurations of the single junction a-Si:H solar cell, namely the p-i-n superstrate configuration and the n-i-p substrate configuration. The type of configuration reflects

the deposition sequence of the a-Si:H based layers. In the p-i-n configuration the p-type layer is deposited first, then the intrinsic layer and the n-type layer is deposited as the last one. In the n-i-p configuration the sequence of the deposition is vice versa. When glass or another transparent material is used as a substrate, the p-i-n configuration is used. In case of a stainless steel or another non-transparent material, the n-i-p deposition sequence is applied. The reason for these two approaches is that the light enters the bulk of a solar cell through the p-type layer.

In the study of both hydrogenated amorphous and microcrystalline silicon (a-Si:H and μc-Si:H) thin-film solar cells, we must deal with two different aspects, as compared to the crystalline counterparts:

- The absorption coefficients of amorphous and to some extent of microcrystalline, silicon are high. Therefore, the penetration depth of the incident irradiance is correspondingly small, so a thin cell material suffices to fully absorb the incoming light. The ratio between the light penetration depth and cell thickness may be further enhanced by light-trapping techniques, which are particularly relevant for microcrystalline silicon.
- The transport properties of photo-generated carriers in both amorphous and microcrystalline silicon layers are far inferior compared to those of crystalline silicon. As a result, the excess carriers recombine within very short distances from their origin, within distances much shorter than the cell thickness. The question is: how can we design and fabricate a thin-film silicon solar cell where the collection length for the photo- generated carriers is comparable or even higher than the penetration depth of sunlight?

The principle of any solar cell is the separation of electron-hole pairs by the action of an internal electric field. The location of this electric field is governed by the requirement that all photo-generated carriers can travel sufficiently far to reach that field.

In crystalline silicon solar cells this travel distance is determined by the carrier diffusion length, which is of the same order of magnitude as the cell layer thicknesses. The electric field, concentrated within the depletion layers of the p- and n-layers, i.e. within a very thin zone at the p-n junction, is within reach for all the photo-generated carriers which have to be separated. Thus, crystalline silicon solar cells work as p-n diodes.

Due to the extremely short travel distances of photo-generated carriers in amorphous and microcrystalline silicon materials, the electric field needs to be present at the

origin of photo-generation, in order to assist carrier travel and "immediately" separate electrons and holes and, thus, to avoid their recombination. The field-assisted travel distance is given by the drift length. For optimum utilization of the incident irradiance, the electric field must extend throughout the entire cell thickness. This is accomplished by inserting an i-layer between the p- and n-layers, whereby a pin diode is formed. With the relatively low light-penetration depths and, hence, with the low values of i-layer thicknesses, the electric field strength $E(x)$, determined by the built-in voltage and the i-layer thickness, reaches a sufficient magnitude for efficient carrier separation. This means that it is possible, thanks to the pin structure, to use materials such as amorphous and microcrystalline silicon, which would give only very poor results if the p-n structure were used.

The main difference between p-n diodes and p-i-n diodes is the extension of the internal electric field in the diode; this is illustrated in Figure III.14.

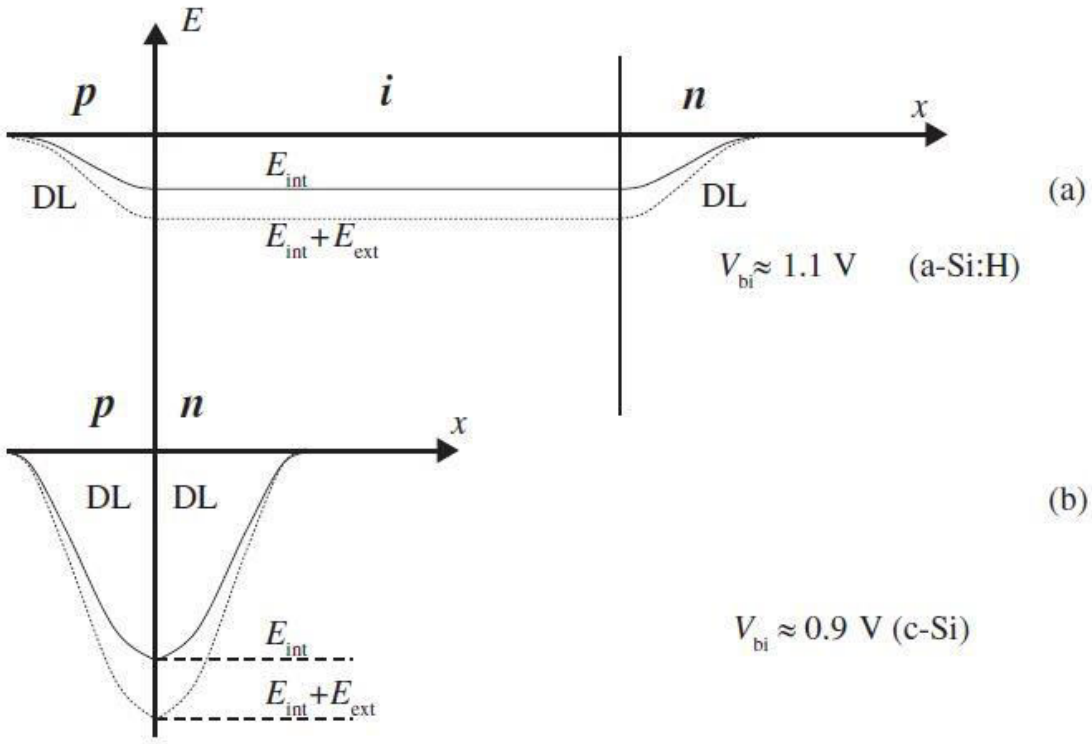

Figure III.14: Internal electric field $E(x)$, for (a) pin and (b) p-n type diodes.

The overwhelming majority of semiconductor devices use doped regions (p- and n-type regions) and not intrinsic regions (i-regions). The pin-diodes employed as solar cells for the case of thin film silicon (amorphous and microcrystalline silicon) constitute one of the very few exceptions to this general rule.

In the case of the p-n diode, collection is governed by the minority carrier diffusion length L_{diff}. In the case of the pin diode, collection is governed by the drift length L_{diff} of both electrons and holes within the intrinsic layer.

It can be shown, that, under "reasonable conditions" (which are in general fulfilled), the drift length L_{diff} has a value that is about 10 times larger than the minority carrier diffusion length L_{diff}; [65] with $\kappa = d_i/L_{drift} \approx 0.5$, where d_i is the thickness of the intrinsic layer.

One therefore has the following situation: if material quality (as expressed by the diffusion length) is excellent, a p-n diode should be used as solar cell structure; if material quality is "mediocre", a pin diode should be used; if material quality is poor, no reasonable solar cell can be fabricated. It so happens that the best intrinsic amorphous and microcrystalline layers fall precisely into the category of layers with "mediocre" quality.

In amorphous silicon there is yet another reason to use pin-type diodes instead of p-n diodes: it turns out to be basically impossible to deposit doped amorphous layers with reasonable quality. In fact, as we increase the doping level of the layer, we invariably increase the defect density, i.e. the density of recombination centers. Therefore, the doped layers within an amorphous silicon solar cell are only used to form a difference in potential and to create an internal electrical field, and do not actively contribute to the photo-generated current. All light that is absorbed within these layers is "lost": as soon as the hole-electron pairs are generated here, they almost immediately disappear through recombination. Because of this, the doped layers in an amorphous silicon solar cell are usually kept very thin. This is especially true of the p-type layer, which is a "window layer" through which the light is usually made to enter into the cell. It has to be just sufficiently thick to enable the internal electric field to be formed. In practice, the p-type layer in amorphous silicon is additionally alloyed with carbon, so as to increase its bandgap and further reduce its absorption coefficient.

How far this reasoning applies also to microcrystalline silicon solar cells is less clear, because too little is known about microcrystalline silicon doped layers. In practice, however, one tends to keep the doped layers very thin, also within microcrystalline silicon solar cells.

Schematic of an a-Si:H pin-single solar cell developed by the Kaneka Company is shown in Figure III.15. The efficiency of this device is close to 7% [87]. The cell is

fabricated in superstrate configuration. The a-Si:H absorbing layer is deposited on a transparent conductive oxide (TCO) film serving as a front electrode. The front TCO should exhibit a low sheet resistance (no more than $\sim 10\ \Omega/\mathrm{sq}$) and high optical transmission (no less than 85%) in the range from near UV to near IR [88]. The surface of the TCO layer is textured in order to improve light trapping. A double-layer stack consisting of ZnO:Al and Ag films acts as a back surface reflector [87, 88].

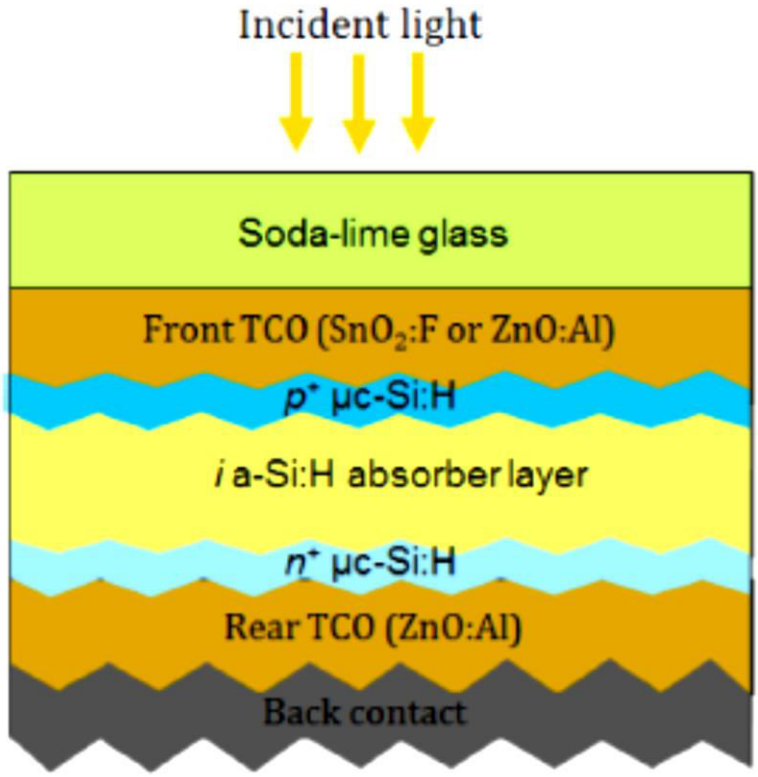

Figure III.15: Schematic of a state-of-the-art a-Si:H pin solar cell fabricated on a TCO-coated glass superstrate [87].

Unfortunately, the efficiency of a-S:H solar cells working under light exposure degrades with time due to the Staebler-Wronski effect [19], which is directly related to formation of defects (dangling bonds, microvoids, stressed regions) acting as recombination centers [89]. As a result, the efficiency of commercial modules exposed to sunlight drops to 5%-6% over a period of months despite the initial efficiencies exceeding 12% for laboratory a-Si:H cells [90]. One of the possible solutions to the light-induced degradation of a-Si:H solar cell is reducing the amorphous layer thickness. Another approach is optimizing growth conditions in order to achieve the microstructure close to the amorphous-to-microcrystalline transition region [91]. The highest stable efficiency of 10.1% for a small-area a-Si:H

single cell has been reported by Benagli et al [92]. The stable efficiency for large commercial single-junction modules does not exceed 7% [93].

III.5.1) µc-Si:H solar cells

Microcrystalline silicon (µc-Si) can be used not only for high conductivity p- and n-type contacts, but also as a material for active layers in thin-film solar cells [92]. The first µc-Si:H solar cells showing reasonable efficiency of 4.6% were fabricated in 1994 [23]. The bandgap of µc-Si:H is close to that of crystalline Si, which allows extension of the absorption range to red and infrared light. Hydrogen passivation suppresses carrier recombination at grain boundaries, thus improving device performance. Most importantly, µc-Si solar cells are less subject to light-induced degradation and show better stabilized efficiencies as compared to those attainable from a-Si:H devices. µc-Si:H with the properties best suited for solar cell applications (combination of highest FF, highest J_{sc} and highest V_{oc}) are obtained under deposition conditions close to the amorphous-to-microcrystalline transition point [94]. With this approach, single-junction cells with stabilized efficiencies exceeding 10% (typical values $V_{oc} = 0.52\,V$, $FF = 0.74$) have been achieved [95].

The major disadvantage of µc-Si is that its absorption coefficient is lower than that of amorphous material; therefore, thicker layer of µc-Si (1-2 µm) are required for efficient light absorption. In addition, the deposition rate for µc-Si films is much lower (few nm/min) as compared to that for a-Si (10-30 nm/min), which increase the cost of µc-Si-based cells. The photovoltaic modules based on single-junction µc-Si:H cells do not seem to be commercially viable at present. Therefore, considerable effort is exerted on developing deposition techniques capable of providing higher rates without degrading the power conversion efficiency.

III.5.2) Efficiency improvements

As mentioned previously, a single p-i-n junction a-Si:H solar cell is deposited on glass substrate coated with a transparent conductive oxide TCO. The TCO forms the top electrode and aluminum or silver is used as the bottom electrode. Since only the a-Si:H intrinsic layer contributes to the current generation, the optimal optical design of the cell structure maximizes absorption in the intrinsic layer and minimizes absorption in all the other layers. A standard a-Si:H p-i-n cell that has been fabricated at Delft University of Technology and at Utrecht University is designed to have a thin (0.01 µm) p-type layer; a thicker (0.45 µm) intrinsic layer; and a thin (0.02 µm) n-type

layer [96]. Figure III.16 shows the typical structure of a pin type amorphous silicon solar cell.

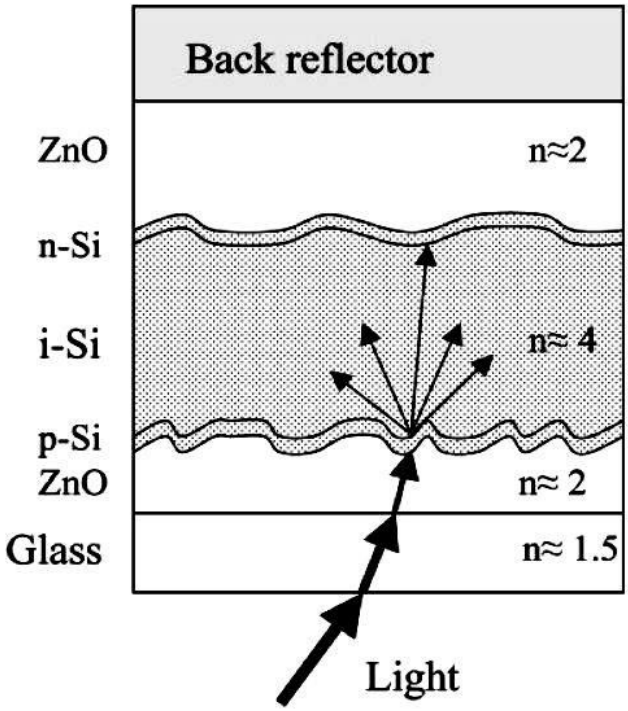

Figure III.16: Typical structure of pin-type a-Si:H solar cell [68].

The approaches applied to achieve optical confinement in the intrinsic layer are commonly described by the term light trapping. In addition to light trapping, there are other design rules that facilitate the collection of photogenerated carriers.

The following are some important practical design approaches for making highly efficient Silicon solar cells, which are schematically depicted in Figure III.16:

- In practice, light enters the a-Si:H solar cell through the p type layer. The lower mobility of holes in comparison to electrons in a-Si:H is the reason for this design. Since most of the photogenerated carriers are generated in the front part of the solar cell, on average, holes have to travel over a shorter distance to the collecting electrode than electrons. In this way, the collection efficiency of the holes is enhanced.
- Because light enters the solar cell through the p type layer, there is substantial absorption in this layer. The photogenerated carriers in the p type layer do not contribute to the photocurrent because in this layer the electrons, here the minority carriers, quickly recombine. It is therefore desirable to minimize the absorption in the p type layer, which is done by minimizing the thickness and alloying the p type a-Si:H layer with carbon. This p type a-SiC:H layer has an optical bandgap of about 2 eV and is referred to as the window layer.

- The solar cell performance is sensitive to the p-i interface region. The p-i interface is a heterojunction with band offsets between the energy bands of a wide bandgap p type and an intrinsic layer. The band offset in the valence band forms a barrier for the photogenerated hole to the doped layer. One has to keep in mind that the generation rate of the carriers in this region is the highest in the intrinsic layer. A lot of attention is paid to the p-i interface region in order to accommodate the band offset, to optimize the electric field profile in this region, and to prevent back diffusion of the photogenerated electrons into the p type layer. Usually, wide bandgap, thin, high quality layers of intrinsic or lightly doped a-Si:H or a-SiC:H are introduced at the p-i interface. These layers can also serve as diffusion barriers, preventing boron from diffusing from the p type into the intrinsic layer. These layers are called the buffer layers.
- The thickness of the Si film that forms the active layer in amorphous and microcrystalline silicon solar cells is small, so it is not able to absorb enough incidents light compared with solar cells using ordinary crystalline substrates. As a result, it is difficult to obtain a high photoelectric current. Light-trapping technology provides a means of extending the optical path of the incident light inside the solar cell by causing multiple reflections, thereby improving the light absorption in the active layer. Light trapping can be achieved in two ways:

(i) The substrate that is used for deposition of a-Si:H layers is practically always surface textured. The surface texture of the top TCO layer in the superstrate configuration and the TCO/metal back contact in the substrate configuration introduces rough interfaces into a solar cell. When light reaches a rough interface, part of it will be scattered in various directions instead of propagating in the specular direction. In this way the average light path in the absorber layer is increased and light absorption enhanced.

(ii) Typically, the back contact consists of a ZnO layer and a metal layer, usually Ag. This combination results in a highly reflective back contact that helps to enhance the absorption of light in the absorber layer in the long wavelength region (wavelengths above 600 nm) due to effective reflection from the back side of the cell.

A solar cell with a textured surface and a back reflective layer for increasing absorption is said to have a STAR (Surface Texture and enhanced Absorption with a back Reflector) structure.

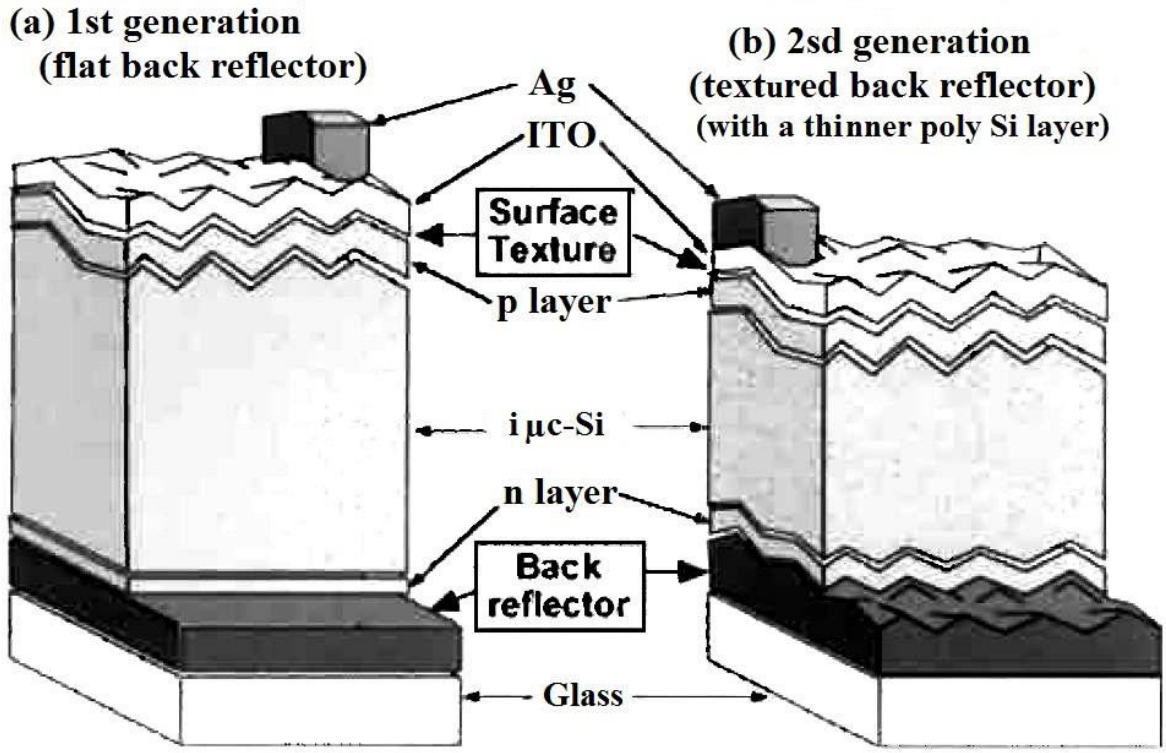

Figure III.17: Cross-sections through light-trapping microcrystalline silicon (µc-Si) solar cell devices. (a) First generation (flat back reflector); (b) second generation (textured back reflector, thinner µc-Si layer) [68].

At present, two types of light trapping structure are in use. Figure III.17 (a) shows a cell that uses a flat highly reflective layer at the back surface, and Figure III.17 (b) shows a cell that uses a textured type of highly reflective layer.

This highly reflective back layer also acts as the solar cell's back electrode. Thin-film polycrystalline silicon forms naturally with a textured structure on its surface, and the size of this texture is strongly dependent on the film thickness. When the film is relatively thick (4 µm or more), the surface texture is suitable for light trapping, but when the film is relatively thin (1.5 µm or less), It is necessary to use a textured reflective layer at the back surface. Of course, to be precise the texture characteristics depend on the fabrication conditions as well as on the film thickness.

This result provides experimental verification of the contribution made by the minute textured structures to light trapping. In the future, it will be necessary to aim at increasing the efficiency by obtaining larger currents in the thin film through the formation of better light trapping structures by controlling the profile of the microcrystalline silicon surface and the underlying reflective layer.

III.6) Micromorph (a-Si:H/uc-Si:H) tandem solar cells

In the previous sections, we assumed that all active layers forming the cell witch contribute to the photogeneration, are formed by the same material and have the same gap. Solar cells with such a structure are called “homojunction” solar cells.

A further degree of liberty arises when combining, within the same junction, two different materials, preferably with two different band gaps: we thus obtain so-called “Heterojunction” solar cells. The theoretical study of this type of solar cell is more difficult; however, one basically does not increase the efficiency limits when compared to “homojunction” solar cells. Still, there may be at times technical reasons for combining materials of different band gaps within the same diode. Solar cells made up entirely of thin film silicon layers, are also extensively called “heterojunctions”, specifically when combining microcrystalline silicon and amorphous silicon within the same junction or when using different types of unalloyed silicon, silicon-carbon and silicon-germanium alloys within the same junction. The functioning of such thin-film heterojunctions is complex and is not fully understood, although in practice many advantages can be obtained.

In this section, we will take a look at more fundamental way of combining two different materials: This is the so-called tandem concept, where two junctions are optically situated one on top of the other, in such a way that the light passes first through a top sub-cell (where it is partially absorbed) and thereafter through a bottom sub-cell (where the remaining part of the light has a possibility to be absorbed). The tandem concept can be extended to three junctions (triple-junction cells) or to even more than three junctions. The principle of the tandem cell is shown in Figure III.18. Such a tandem cell can have two individual electrical contacts and is then called a “two terminal tandem cell”.

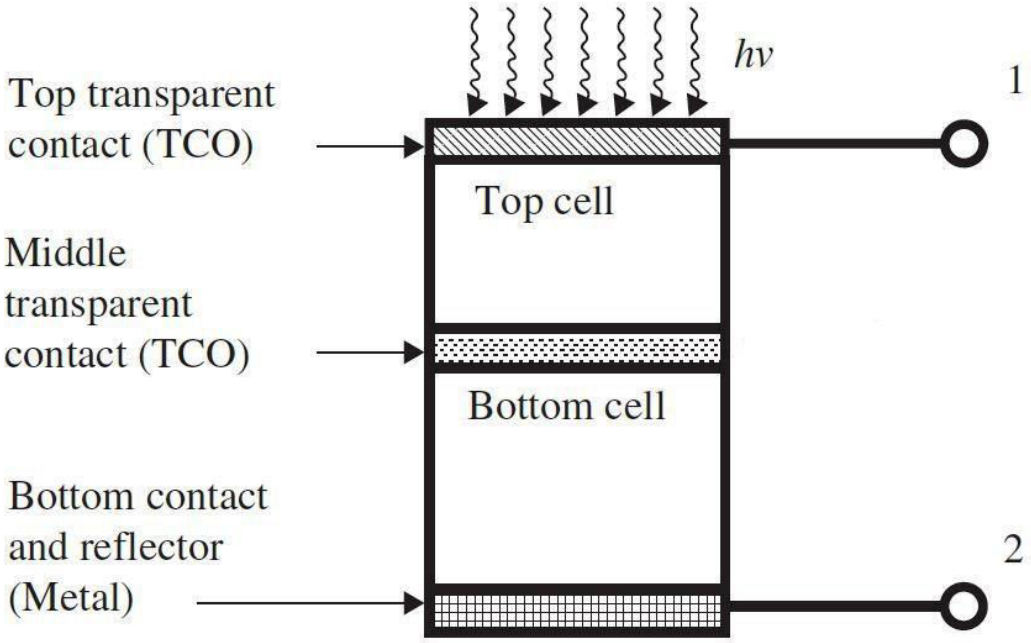

Figure III.18: Schematic diagram of 2T tandem solar cell [64].

In a two-terminal tandem cell, both the top sub-cell and the bottom sub-cell are electrically in series. If we use the following symbols:

J_{top}, V_{top} : top sub-cell current density and voltage.

J_{bottom}, V_{bottom}: bottom sub-cell current density and voltage.

J_{tandem}, V_{tandem}: tandem cell current density and voltage

We will then have:

$$J_{tandem} = J_{top} = J_{bottom} \quad \text{(III.25)}$$

$$V_{tandem} = V_{top} + V_{bottom} \quad \text{(III.26)}$$

The construction of the corresponding diagram for J_{tandem} (V_{tandem}) is shown in **Figure III.19** It is easy to convince one from this figure that:

$$J_{sc.tandem} \approx Min\,(J_{sc.top}, J_{sc.bottom}) \quad \text{(III.27)}$$

$$V_{oc.tandem} \approx V_{oc.top} + V_{oc.bottom} \quad \text{(III.28)}$$

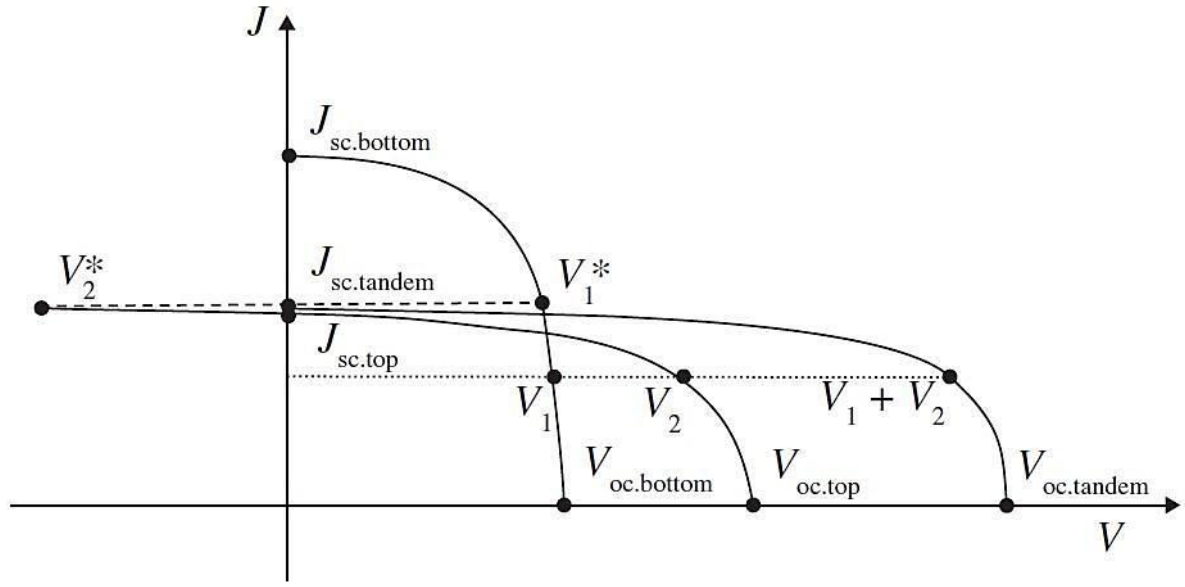

Figure III.19: Construction of the $J-V$ diagram for a two-terminal tandem solar cell.

Equation (III.27) leads to the current-matching condition; for optimal performance one should have:

$$J_{sc.top} \approx J_{sc.bottom} \qquad \text{(III.29)}$$

If, on the other hand, there is a large difference between $J_{sc.top}$ and $J_{sc.bottom}$, the short-circuit current density of the tandem will be given by the smaller of the 2 short circuit current densities of the sub-cells. The sub-cell with the higher short- circuit current density will then not be using its full current potential.

As far as open-circuit voltages are concerned, Equation (III.28) is only approximately fulfilled. In fact the open-circuit voltage of the tandem is always slightly lower than the sum of the open-circuit voltages of the two sub-cells. There are two reasons for this:

(a) Each sub-cell will be absorbing less light than an individual single-junction cell of the same gap and this will lead to a corresponding decrease in its V_{oc}.

(b) The recombination junction will also lead to a further reduction of the total tandem voltage; this reduction depends on the exact nature of the layers present in the recombination junction it may be estimated to be in the range of 20 to 40 mV.

The fill factor FF of the tandem cell merits a special comment. If we do have current-matching, the FF may be considered to lie within the fill factors of the top and of the

bottom sub-cells. However, if the currents are not matched, the FF of the tandem is very often quite a bit higher. On the other hand, we will, by such a current mismatch, certainly be losing more in current than we will be gaining in FF, so that it is not worthwhile to try to obtain mismatch conditions when attempting to increase tandem cell efficiency. It is in general a rather complicated task to predict the FF of tandem and multi-junction cells.

At different wavelengths of the solar spectrum, microcrystalline and amorphous silicon layers have an edge over each other for either long wavelength regions or short wavelength regions. The combination of a high a-Si:H band gap (1.7 eV to 1.85 eV) and a low µc-Si:H band gap (1.1 eV) yields the so-called micromorph (a-Si:H/µc-Si:H) tandem solar cell [97], and will further maximize the efficiencies of solar cells. The "micromorph" tandem cells were introduced first under the name of "mixed stacked a-Si:H/µc-Si:H cells" by IMT Neuchatel in 1994 [98], the term "micromorph" cells was only coined later [99]. The advantage of such a structure is the ability to absorb more efficiently a larger part of the solar spectrum by stacking materials with different band gaps. Figure III.20 shows the external quantum efficiencies of top and bottom subcell of an exemplary micromorph (a-Si:H/µc-Si:H) tandem solar cell [92].

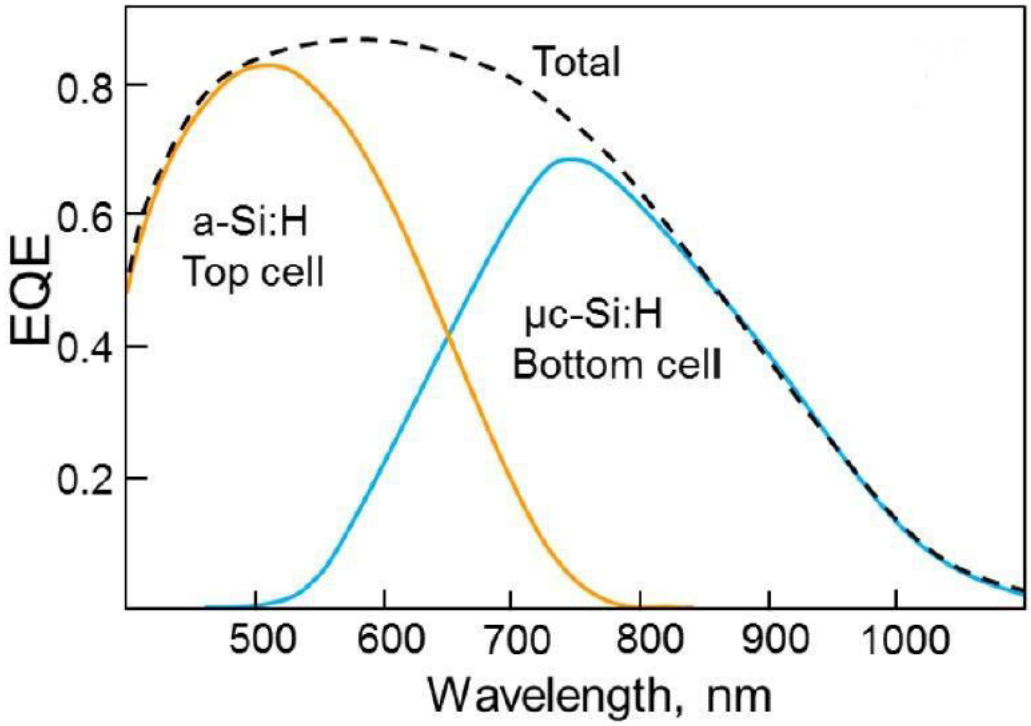

Figure III.20: External quantum efficiency (EQE) of an exemplary micromorph (a-Si:H/µc-Si:H) tandem solar cell [92].

The basic structure with typical layer thicknesses and electron micrograph of such tandem solar cell are respectively shown in Figure III.21 [64].

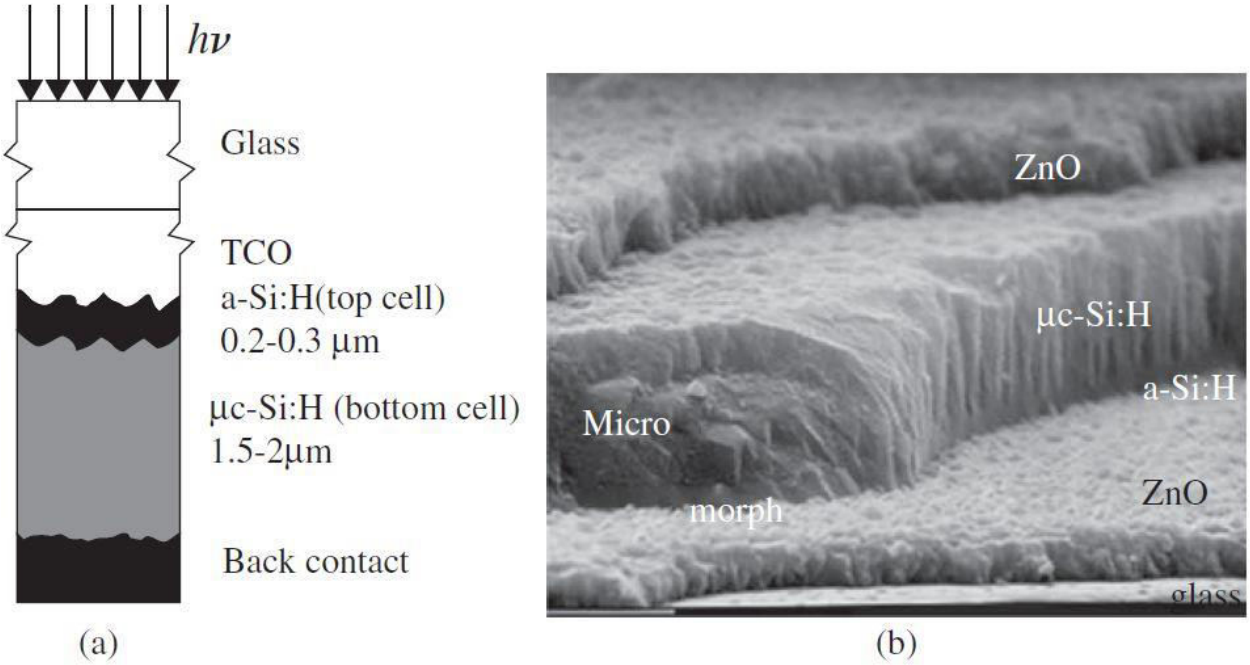

Figure III.21: Micromorph tandem a-Si:H/µc-Si:H solar cell: (a) basic structure; (b) electron micrograph [64].

From a practical point of view, tandem cells are interesting, if the same deposition temperature and process can be used for both the top and the bottom cell. This the case when using VHF-PECVD as deposition process, with deposition temperature set to 200°C [64]. The best cells have achieved so far a confirmed stabilized efficiency of 11.7 % [100].

One would, of course, wish to increase the stabilized efficiencies of "micromorph" tandem cells. Previous studies indicate that an efficiency of over 30 % should be possible [64]. Why then, are "micromorph" tandem cells at present limited, even in the laboratory, to the range of 10 to 12 %?.

The stability of the micromorph silicon solar cells is mostly limited by the a-Si:H top sub-cell, due to Staebler–Wronski degradation process [19] in a-Si:H material. Therefore, it is essential to use a thin a-Si:H top-cell in order to reduce the light-induced degradation. The a-Si:H top sub-cell generates a lower current compared with the µc-Si:H bottom sub-cell and thus the total current of the tandem cell is limited by the top sub-cell. One way to increase the top sub-cell performance is to introduce an intermediate reflector (IR) between the top and the bottom sub-cells in such a way

that the short-wavelength components of the light are reflected back into the a-Si:H top sub-cell but the long-wavelength components are (as far as possible) passed on, with little attenuation, into the µc-Si:H bottom sub-cell. The IR material should has a refractive index n lower than that of the a-Si:H ($n \sim 4$) or µc-Si:H ($n \sim 3.4$) [92, 101], and should be electrically conductive to connect the top and the bottom sub-cells and avoid Ohmic losses. The Zinc oxide (ZnO), with a refractive index $n = 2$, was an excellent candidate used in the first trials [93]. Currently, alternative materials such as silicon oxide (SiO_X), silicon nitride (SiN_X) and Indium-tin oxide (ITO) are employed [102-105].

In 2T tandem solar cell, the two sub-cells are directly stacked by successive layer deposition, which makes them both optically and electrically coupled [106, 107]. Only two contact electrodes are connected to the top cell p-type layer and to the bottom cell n-type layer. By this way, the two sub-cells are physically series connected to give a two- terminal (2T) device. To achieve an optimal power output in such device, the current matching requirement between the two sub-cells must precisely be fulfilled for example by a careful adjustment of the absorber-layer thickness. This induces some constraints on the thicknesses. While the a-Si:H top sub-cell is recommended to be as thinnest as possible to minimize the Staebler-Wronski effect [19], the current matching requirement imposes a current value unachievable with a very thin top sub-cell. So, to avoid too thick i-layers, additional layers such as intermediate reflectors have been introduced [108, 109], although the use of such layers adds more process steps and introduces resistive losses in the final device [110].

Regarding the environmental operating conditions, the 2T micromorph tandem cell is typically optimized for the standard global AM1.5 spectrum (1000 W/m2) at 25°C. Any shift or modification in the solar spectrum from that condition induces a mismatch of the currents and thus a considerable reduction in performance. For example when the sun is low in the sky, there is a larger proportion of red light and the devices can be top cell-limited whereas during sunny days with clear sky the solar spectrum can present a larger portion of blue light and induce a bottom cell-limitation behavior. In the same way, operating under real outdoor conditions can lead to high module temperature which can in turn introduce current mismatch due to the different temperature coefficients of a-Si:H and µc-Si:H sub-cells [110].

III.6.1) Four terminal micromorph solar cells

To overcome the factors limiting the 2T tandem cell performance, a four-terminal (4T) device configuration has been developed [T15-18T, Reynolds 12], in which the two sub-cells are separated by an insulating material (e.g. glass, plastic or SiN_X), and each one of them has its own electrodes connected to its own p-type and n-type layers (Figure III.22). So, the two sub-cells are optically coupled and electrically decoupled. The current matching constraint being released in such configuration, the electrical characteristics of each sub-cell can be obtained individually in order to independently optimize its power output whatever the currents are.

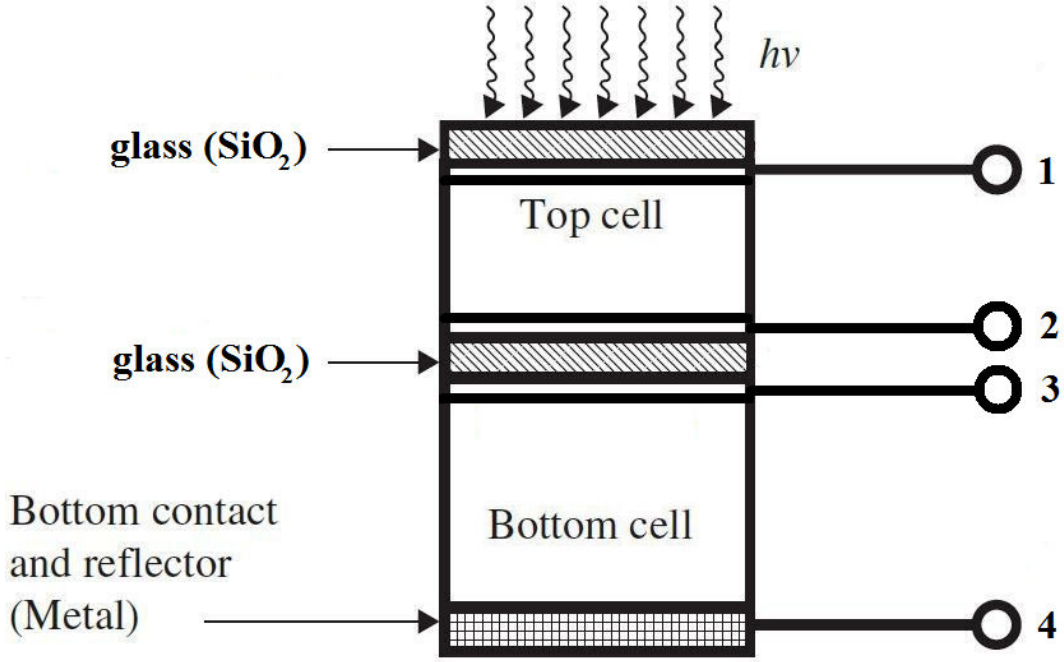

Figure III.22: Schematic diagram of 4T tandem solar cell [64].

As we said; in a four terminal tandem cell, both the top sub-cell and the bottom sub-cell are electrically separated. If we use the following symbols:

$P_{m.top}$ the maximum power obtained from the top sub-cell

$P_{m.bottom}$ the maximum power obtained from bottom cub-cell

η_{top} the efficiency of the top cub-cell

η_{bottom} the efficiency of the bottom sub-cell

We will then have:

$$P_{m.tandem} = P_{m.top} + P_{m.bottom} \qquad \text{(III.30)}$$

$$\eta_{tandem} = \eta_{top} + \eta_{bottom} \quad \text{(III.31)}$$

For the fill factor:

$$FF_{top} = \frac{J_{top}.V_{top}}{J_{sc.top}.V_{oc.top}} \quad \text{(III.32)}$$

$$FF_{bottom} = \frac{J_{bottom}.V_{bottom}}{J_{sc.bottom}.V_{oc.bottom}} \quad \text{(III.33)}$$

By applying surfaces calculation in Figure III.23:

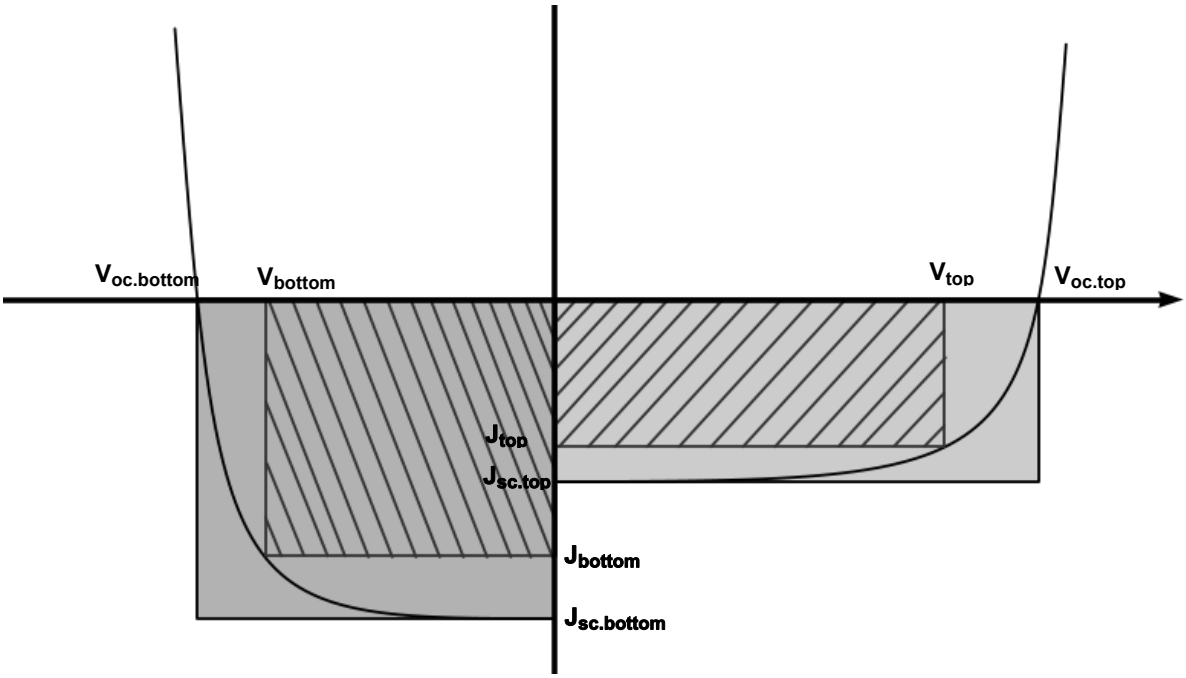

Figure III.23: Construction of J-V curve for four-terminal configuration.

$$FF_{tandem} = \frac{J_{top}.V_{top}+J_{bottom}.V_{bottom}}{J_{sc.top}.V_{oc.top}+J_{sc.bottom}.V_{oc.bottom}} \quad \text{(III.34)}$$

A number of operational advantages may in principle be gained by 4T connection. Since the a-Si:H top-cell need no longer support the generation current of the µc-Si:H bottom-cell, it can be thinner and will be more stable as a result. The “intermediate tunnel junction” between the sub-cells and its attendant resistive losses is obviated. Variations in service conditions such as changes in intensity and spectral quality of the incident light will not unbalance the cell. Assuming the tandem cell has been optimized for AM1.5, this will pass through the top-cell and generate most current in

the bottom-cell. Thus in 2T connection the power deliverable to an external load under these conditions would be strongly limited by the top-cell. Similarly, if the light contains a larger blue fraction then the tandem becomes bottom-cell limited. In 4T connection no such limitation exists, and provided the maximum-power point of each component cell is tracked independently the electrical matching remains optimal [111].

III.7) Solar cells characterization

Although the fabrication of the p-i-n diodes containing a-Si:H is inexpensive compared to the other materials (GaAs, InP...), the metastable character of the defects, that can contain such a material, can influence on the efficiency of these devices and involves of this fact their degradation.

The comprehension of the mechanisms implied in the processes of degradation, passes in particular by the study of the properties of transport in a-Si:H p-i-n diodes. Witch allows, thereafter, improving the electric and optoelectronic characteristics of these devices. For this reason, several experimental techniques of characterization were developed to study the structures of the p-i-n thin films with a-Si:H and its alloys [112-114]. Among these techniques, one can quote the technique of characterization by current-voltage $I-V$ characteristics [38], the technique time of flight (TOF) to measure the density and the distributions of defects [114] , hall effect to measure the mobility.

Figure III.24 shows the equipment used for the extraction of IV characteristic [38]. To measure the current I with the voltage V applied, one uses a computer to control the system. For the $I-V$ curve in the dark, the computer sends a program which controls an electrometer to apply a voltage during an interval of time given. Then the program takes the value of the current and save it like data, and so on for the following values of the voltage.

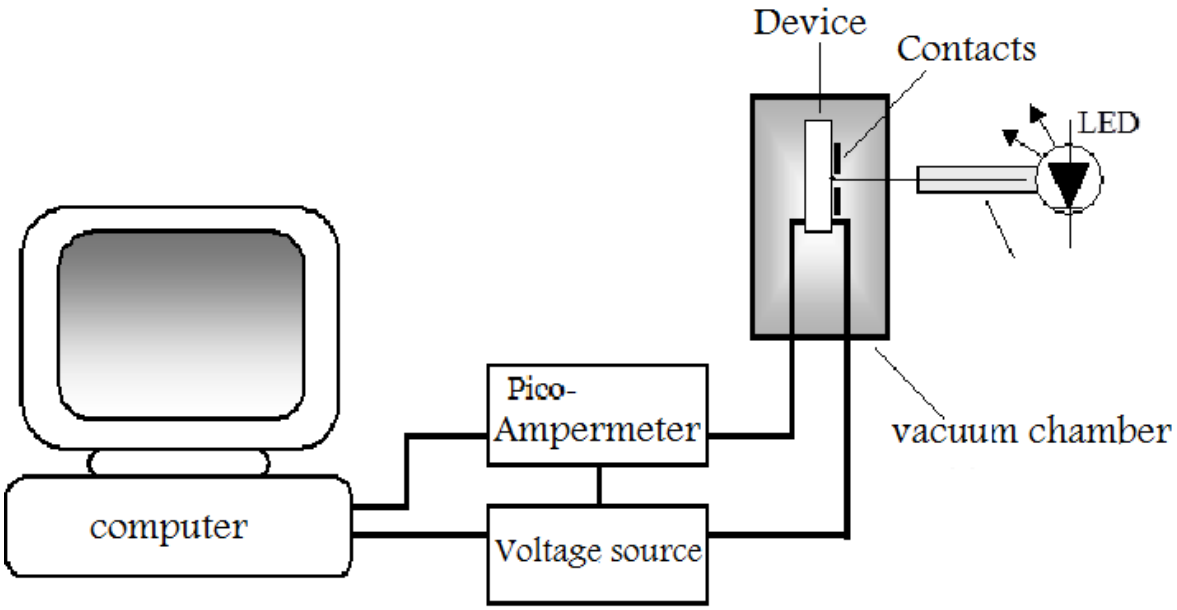

Figure III.24: $I-V$ Characteristics measure equipment [38].

$I-V$ Characteristics in the dark or illuminated can give direct information on the characteristics of the device and constitute a significant means of measurement of the quality of the p-i-n solar cells such as the current produced by the cell, the fill factor and the efficiency. factor and the conversion efficiency. The dark current-voltage (ID-V) measurements can be a powerful probe for characterizing the gap states in the intrinsic (i)-layer of the solar cell [115], and the recombination properties within the bulk or in the interface region [116]. The temperature dependent ID-V can be a useful method to determine the mobility band gap of an a-Si:H solar cell [117], which is an important parameter for the solar cell diagnostic.

The external quantum efficiency (EQE) measures the response of a solar cell as a function of the wavelength of light and gives the fraction of photons that is transferred to collected electron-hole pairs. Figure II.25 shows a setup that can be used to measure the EQE curves [118]. Light from a Xenon lamp is firstly modified by a chopper with a certain frequency. The modified light with a certain wavelength is selected by the monochromator, and then focused onto the test solar cell by a lens. The photo-generated current in the solar cell is then measured by an electrometer. The signals from the monochromator, chopper, and the electrometer are then analyzed by a computer. Finally the spectral response of the testing solar cell on each wavelength light is then measured and presented in the computer. Bias light is also available in this EQE setup and can be focused on the test solar cell,

which is used to bias the solar cell when measuring the multi-junction solar cells. The measurement wavelength range for silicon based solar cell is between 300 nm and 1200 nm with a step of 10 nm [118].

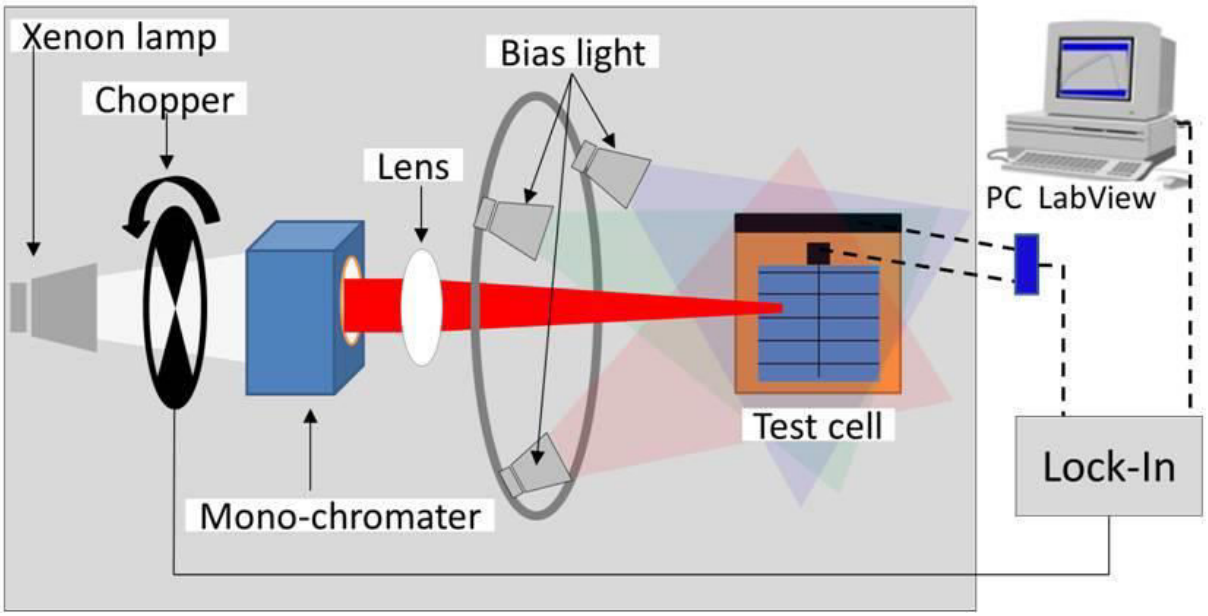

Figure III.25: Setup used to measure the EQE curves [118].

III.8) Conclusion

In this chapter, we presented fundamental concepts related to the solar cell operation conditions, the main processes and parameters of the photovoltaic conversion, and the transport model described by its physical/mathematical equations. In the last sections, we presented a description of typical solar cells based on hydrogenated amorphous and microcrystalline silicon (a-Si:H and µc-Si:H respectively) in different configurations: single-junction solar cell, two-terminal and four-terminal tandem solar cell, four-terminal tandem solar cell, and the experimental techniques usually used to characterize a such devices.

Chapter IV

SILVACO TCAD Simulator

IV.1) Introduction

To simulate the electrical and optical characteristics of the solar cells, we used the commercially available software Silvaco TCAD from Silvaco Inc; which is a privately owned provider of electronic design automation (EDA) software [119] and TCAD process and device simulation software [120]. The Technology CAD (or Technology Computer Aided Design: TCAD) is a branch of electronic design automation that models semiconductor fabrication and semiconductor device operation. The modelling of the fabrication is termed Process TCAD, while the modelling of the device operation is termed Device TCAD. Included are the modelling of process steps (such as diffusion and ion implantation), and modelling of the behaviour of the electrical devices based on fundamental physics, such as the doping profiles of the devices. TCAD may also include the creation of compact models, which try to capture the electrical behaviour of such devices. First, it is necessary to know some basic concepts on simulation in general and on this software in particular, using examples illustrating our work.

Simulation provides an edge between the experimental world and the theoretical world as figure shows. It supplements the theory and the experiment to build the physical reality.

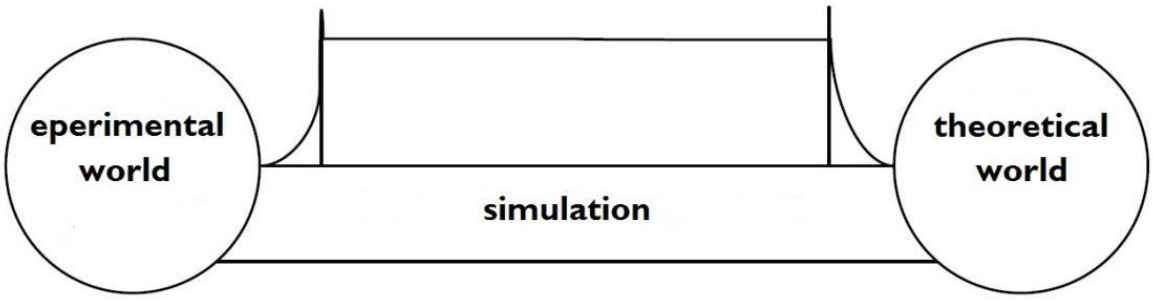

Figure IV.1: The importance of simulation.

The physical model is always distinct compared to an electric device, although its behavior is similar to that of the device, therefore the model is not equivalent but only presents an approximation.

Silvaco TCAD is a Device simulation helps users understand and depict the physical processes in a device and to make reliable predictions of the behavior of the next device generation. Two-dimensional device simulations with properly selected

calibrated models and a very well-defined appropriate mesh structure are very useful for predictive parametric analysis of novel device structures. Two- and three-dimensional modeling and simulation processes help users obtain a better understanding of the properties and behavior of new and current devices. This helps provide improved reliability and scalability, while also helping to increase development speed and reduce risks and uncertainties.

IV.2) Silvaco TCAD simulator

SILVACO (Silicon Valley Corporation) is an American company, having its seat with Santa Clara in California. It is one of the principal suppliers of professional chains of software of simulation by finite elements and computer-aided design for technologies of electronics TCAD (Technology Computer Aided Design). These tools are used by the companies of micro-electronics in the field of the research, the development and the design of devices.

Historically the company was founded in 1984 by Dr. Ivan Pesic to meet the needs for the designers of integrated circuits (IC) analogical for models SPICE (Simulation Program with Integrated Circuit Emphasis) increasingly precise and linear [121].

The entree of SILVACO in technology took place in 1989 [121], and it was based on a research of the Department of the Physical Devices of University of Stanford, starting with Athena like a simulator of the processes and ATLAS like a simulator of the devices. The framework of ATLAS combines several one-, two-, and three-dimensional simulation tools into one comprehensive device simulation package. This allows for the simulation of a wide variety of modern semiconductor devices [122].

IV.3) Silvaco modules

Silvaco provides several software tools to perform process and device simulation which make it the most powerful simulation software.

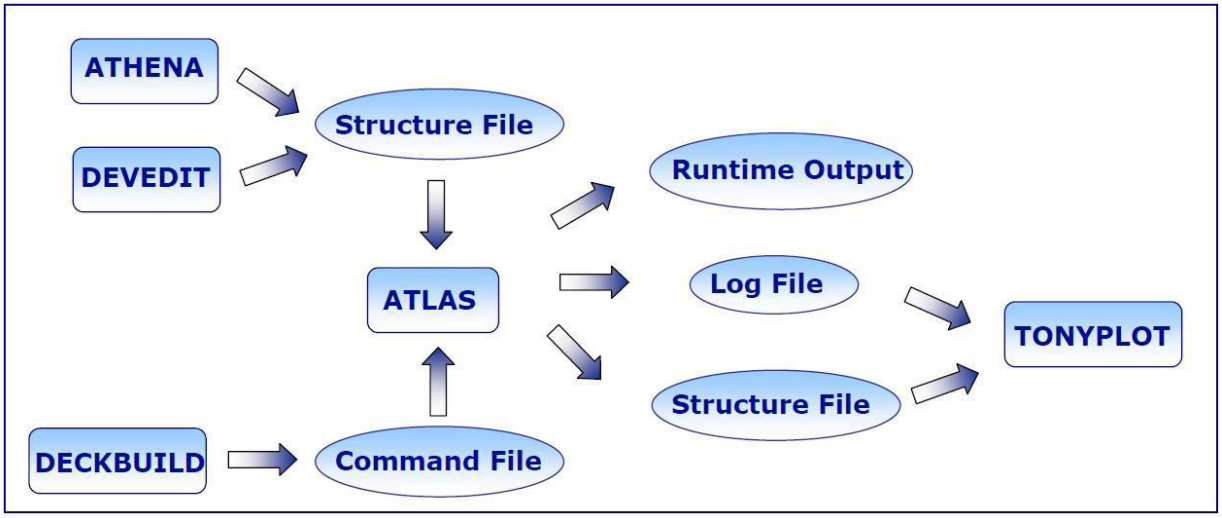

Figure IV.2: Silvaco modules.

- **ATLAS** is a 2D and 3D device simulator that performs DC, AC, and transient analysis for silicon, binary, ternary, and quaternary material-based devices. Atlas enables the characterization and optimization of semiconductor devices for a wide range of technologies. To simulate a device in ATLAS, a description of the device is required. Descriptions of the device meshed with a two- or three-dimensional grid are provided via ASCII command line instructions supplied to ATLAS. The two- or three-dimensional grid approximating the device structure consists of a number of grid points known as nodes. The maximum number of grid points is limited to 20,000, a constraint set by ATLAS[123].

- **ATHENA** is a framework program that integrates several smaller programs into a more complete process simulation tool. This program focuses upon the simulation of fabrication processes. In ATHENA, devices are created through simulation of the fabrication process. To optimize the device characteristics, changes in process parameters supplied to the ATHENA process simulator environment are required, as certain process parameters change the device characteristics. ATHENA consists of four primary and several secondary tools. The primary tools are SSuprem4 for simulating ion implantation, diffusion, oxidation, and silicidation process for silicon; Flash for simulating implantation and diffusion for advanced materials; Elite for topography simulation; and Optolith for lithography simulation. ATHENA also

provides options for modeling silicides, Monte Carlo modeling of ion implantation, etc.

- **TonyPlot** is the graphical plotting program used to plot the data extracted from the simulation using ATLAS. Simulation results do not automatically load into TonyPlot when a simulation is complete. Users have to save results into a file that can be opened directly from TonyPlot. The data can be plotted as desired by the user either in 1D x-y data, 2D contour data, Smith charts, or polar charts. Measured data can also be imported and plotted in the above-mentioned types. The overlay feature helps in comparing the multiple simulation runs. It annotates plots to create meaningful figures for reports and presentations. It enables 2D structure plots to be cut by multiple, independently controlled 1D slices. It supports plotting of user-defined equations with the variables being either electrical data (e.g., drain current) or physical parameters (e.g., electric field).

- **DEVEDIT** is a program that allows for structure editing, structure specification and grid generation graphically by drawing on the screen. All of Silvaco's programs use a mesh or grid. Mesh or grid is used to determine the level of detailing the simulation will generate in a specific area of the device. Therefore, it allows users to cut down the simulation time by removing detailing from areas with less interest containing uniform or no reaction to change/alter simulation results. The creation of these meshes is the main function of DEVEDIT; however, it is also used for the editing and specification of two- and three-dimensional devices created with the VWF tools.

- **Virtual Wafer Fab or "VWF"** is a group of TCAD products that automate and emulate physical wafer manufacturing. These tools facilitate the input, execution, run-time optimization, and results processing of TCAD simulations into a flow managed through a common database. It can be used for such tasks as designing more efficient solar cells for use in space [124].

- **DECKBUILD** is the key to rapid familiarization with SILVACO's TCAD software and the feature laden runtime environment (see Figure IV.3). DeckBuild features include: automatic creation of process input files, editing of existing input files, creation of Design Of Experiments (DOE), powerful parameter extraction routines and the ability to make anything in the input file a variable.

Most importantly for the first time user however, DeckBuild includes literally hundreds of examples for many different types of electrical, optical and magnetic technologies. The top half of the DECKBUILD window is the command input listed in the form of a program created by a text editor

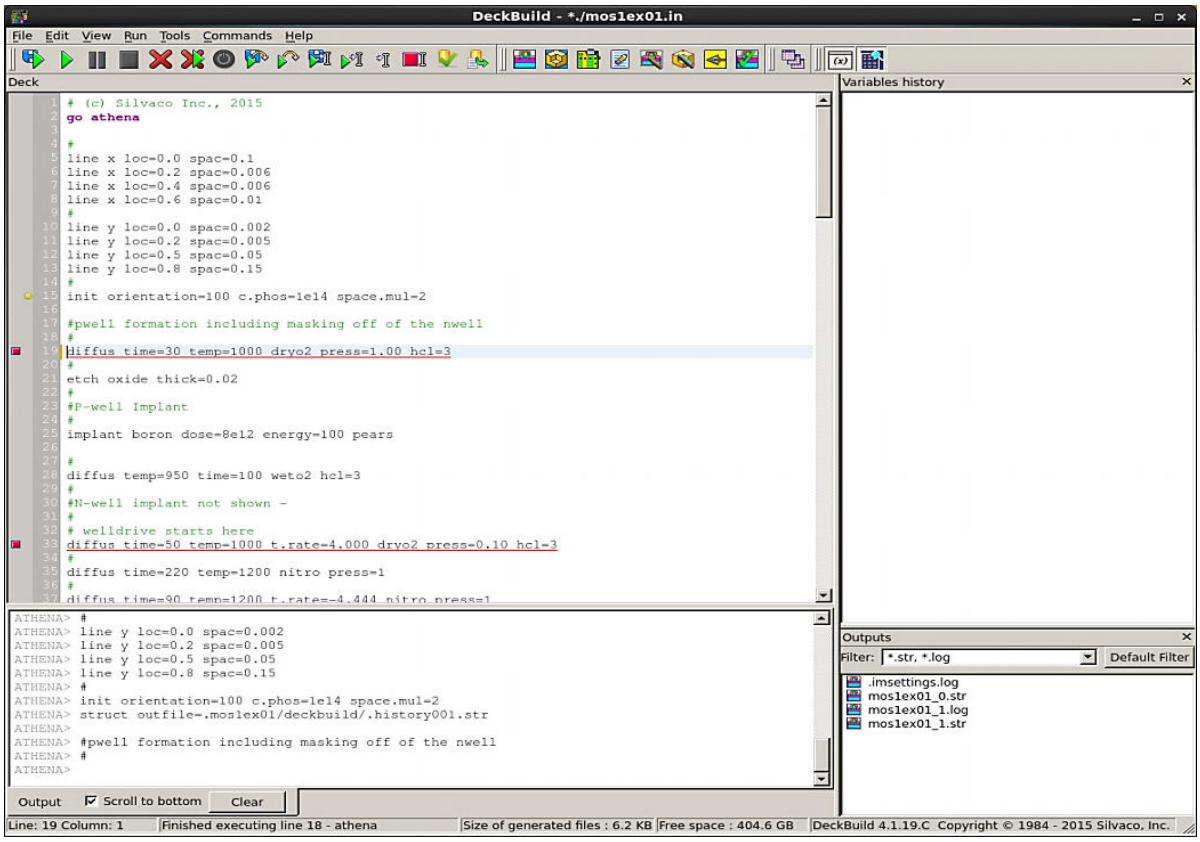

Figure IV.3: DeckBuild windows.

The bottom half of the DECKBUILD window is where program execution and extracted information and results are listed as the program runs. The execution/results are displayed as shown in Figure IV.4.

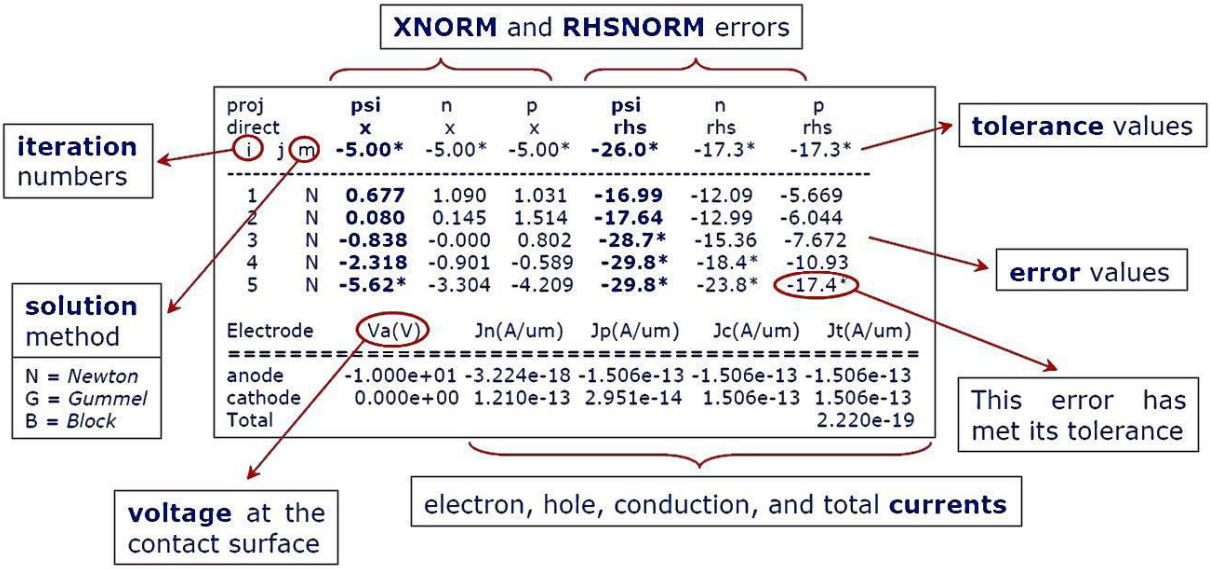

Figure IV.4: Output window.

Errors occurring during the simulation run will be displayed in this output. Not all errors are fatal because DeckBuild tries to interpret the file and continue. This may cause a statement to be ignored, leading to unexpected results. During the running simulation it is recommended to check the run-time output to intercept any errors or warnings [125].

IV.4) Statements and parameters

Silvaco Atlas receives input files through DeckBuild. The code entered in the input file calls Atlas to run with the following command: *go atlas* following that command, the input file needs to follow a pattern.

Atlas follows the following format for statements and parameters:

<STATEMENT> <PARAMETER>=<VALUE>

There are four types of values; real, entire, logic and character. The order of parameters is not necessary, abbreviation is possible but without confusing with another statement. It's possible also to write a comment using the symbol # and it will not executed by the simulator.

ATLAS can read 256 characters in one line [123], but it is better separate the lines with backslash \ on the end of the line in case of long statement.

For the ease of changing various parameters, the input file lists constants as the first lines of code. To set new constants or change parameter values we use the

command set in the first lines of the code. When the constant is employed by program a “$” must proceed it to notify the program that it was previously defined. An example is shown below:

Set cellWidth=2000

Set cellthick=$cellWidth/2

In this example two constants are defined cellwidth and cellthick. Cellthick take the value of cellwidth which is 2000 divided by 2.

To finish the execution of the code one should use the command “quit”.

IV.5) The Order of Atlas Commands

The order in which statements occur in an Atlas input file is important. There are five groups of statements that must occur in the correct order (see Figure IV.5).

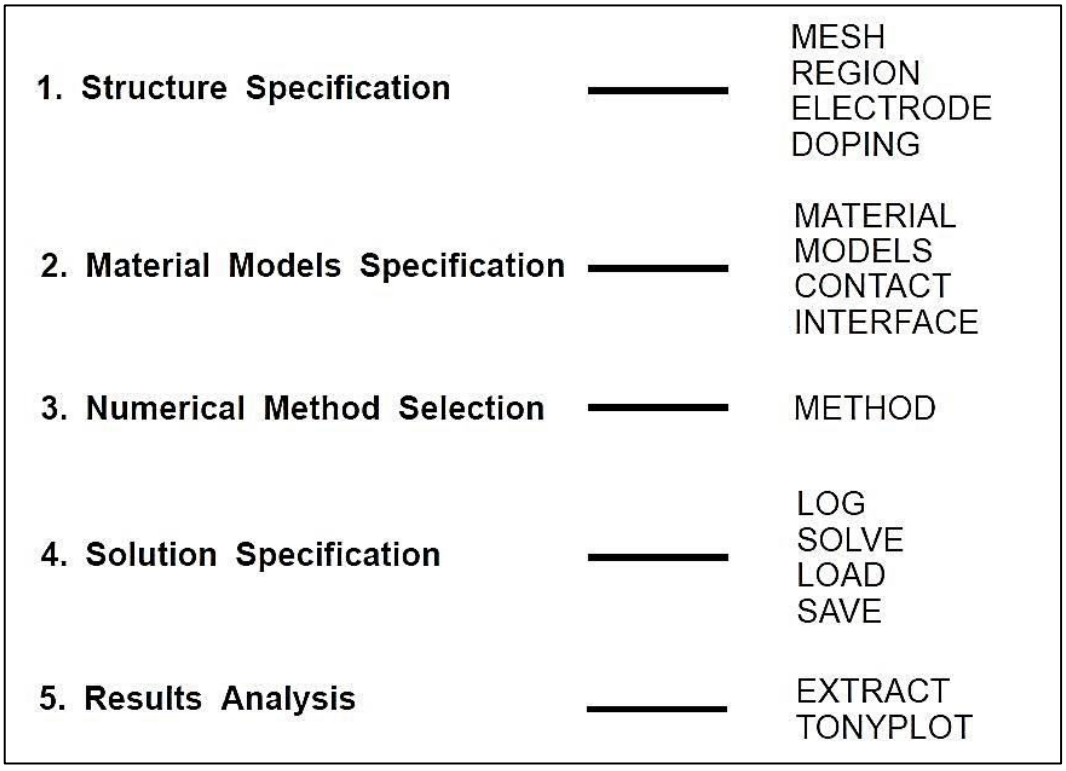

Figure IV.5: Order of atlas statements.

Otherwise, an error message will appear which may cause incorrect operation or termination of the program. For example, if the material parameters or models are set in the wrong order, then they may not be used in the calculations. The order of statements within the mesh definition, structural definition, and solution groups is also

important. Otherwise, it may also cause incorrect operation or termination of the program.

IV.6) Structure specification

There are three ways to define a device structure in Atlas. The first way is to read an existing structure from a file. The structure is created either by an earlier Atlas run or another program such as Athena or DevEdit. A MESH statement loads in the mesh, geometry, electrode positions, and doping of the structure. For example:

MESH INFILE=<filename>

The second way is to use the Automatic Interface feature from DeckBuild to transfer the input structure from Athena or DevEdit. The third way is create a structure by using the Atlas command language, which is our case.

IV.6.1) Mesh

To define the structure device through the Atlas command language, you must first define a mesh. This mesh or grid covers the simulated device. The mesh is defined by a series of horizontal and vertical lines and the spacing between them. Atlas sets some limits on the maximum number of grid nodes that can be used. In the standard version, this limit is 20,000 nodes [123].

The general format to define the mesh is:

X.MESH LOCATION=<VALUE> SPACING=<VALUE>

Y.MESH LOCATION=<VALUE> SPACING=<VALUE>

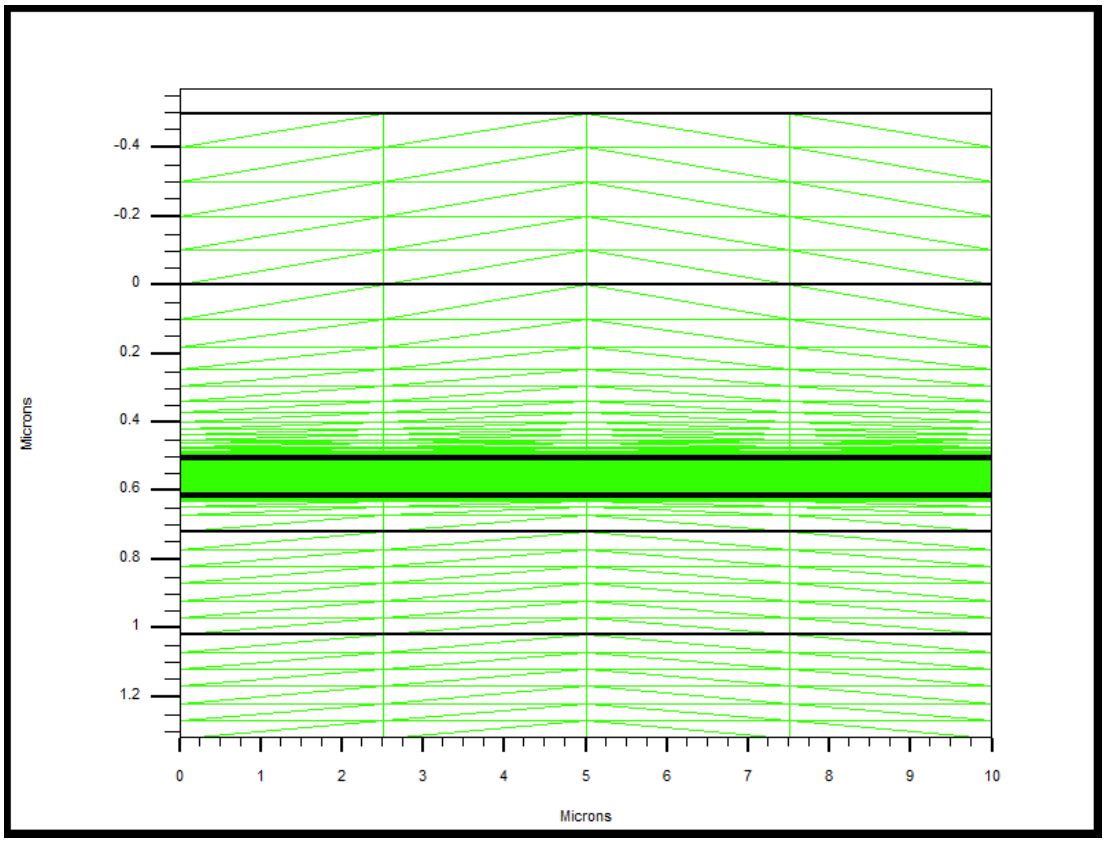

Figure IV.6: Mesh form of an a-Si:H single solar cell.

A coarse or fine mesh determines the accuracy of the simulation. A coarse mesh produces a faster simulation, but less accurate results. A fine mesh produces a slower simulation, but more accurate results. The areas that have a finer mesh, therefore, are of greatest interest in the simulation. The most efficient way to work is to allocate a fine grid only in critical areas (around junctions and depletion regions, areas of high electric field, areas of current flow, base region of BJTs, areas of considerable recombination effects, areas of high impact ionization…etc.) and a coarser grid elsewhere (see Figure IV.6).

IV.6.2) Regions

Once the mesh is specified, every part of it must be assigned a material type (see Figure IV.7). This is done with REGION statements. For example:

REGION number=<integer> <material type> <position parameters>

Region numbers must start at 1 and are increased for each subsequent region statement. You can have up to 15000 different regions in Atlas [126]. A large number of materials are available. If a composition-dependent material type is defined, the x and y composition fractions can also be specified in the REGION statement. The

position parameters are specified in microns using the X.MIN, X.MAX, Y.MIN, and Y.MAX parameters.

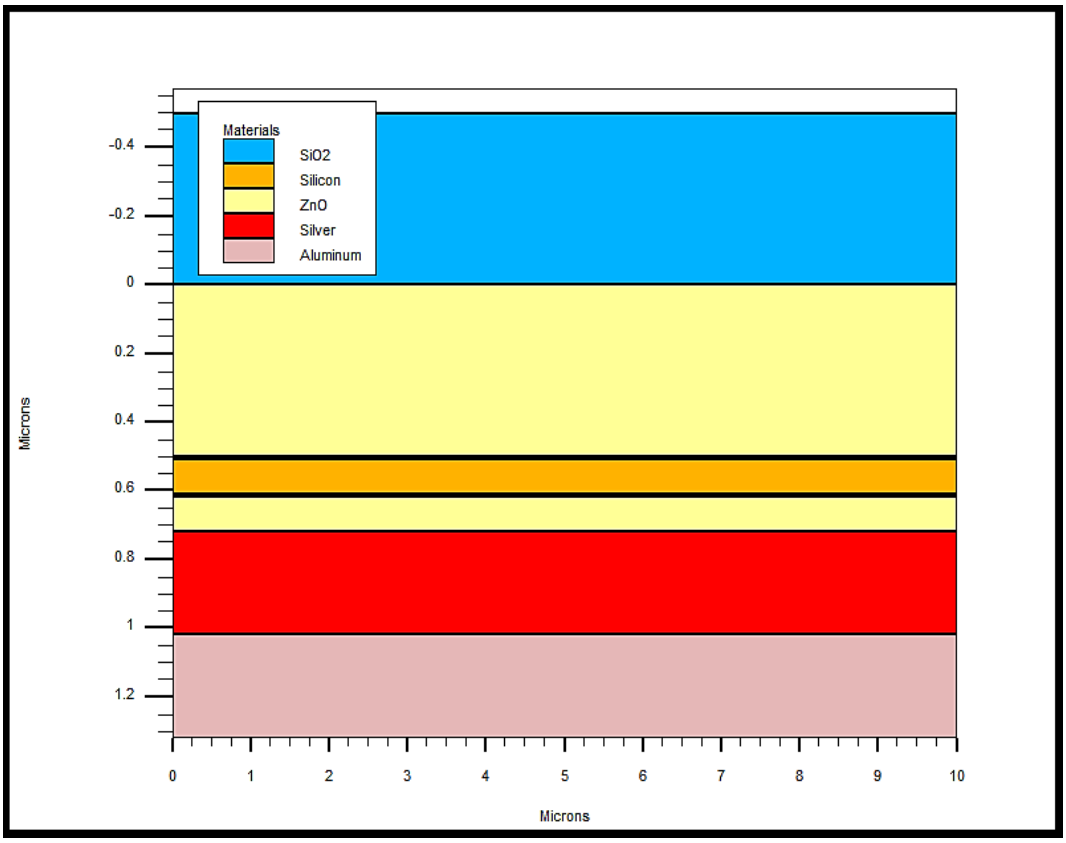

Figure IV.7: Regions and materials specification for a-Si:H.

If the position parameters of a new statement overlap those of a previous REGION statement, the overlapped area is assigned as the material type of the new region. Make sure that materials are assigned to all mesh points in the structure. If this isn't done, error messages will appear and Atlas won't run successfully.

IV.6.3) Electrodes

The next structure specification corresponds to electrodes. Typically, in this simulation the only electrodes defined are the anode and the cathode. However, Silvaco Atlas has a limit of 50 electrodes that can be defined [126]. The format to define electrodes is as follows:

ELECTRODE NAME=<electrode name> <position parameters>

The position parameters are specified in microns using the X.MIN, X.MAX, Y.MIN, and Y.MAX parameters. Multiple electrode statements may have the same electrode name. Nodes that are associated with the same electrode name are treated as being electrically connected.

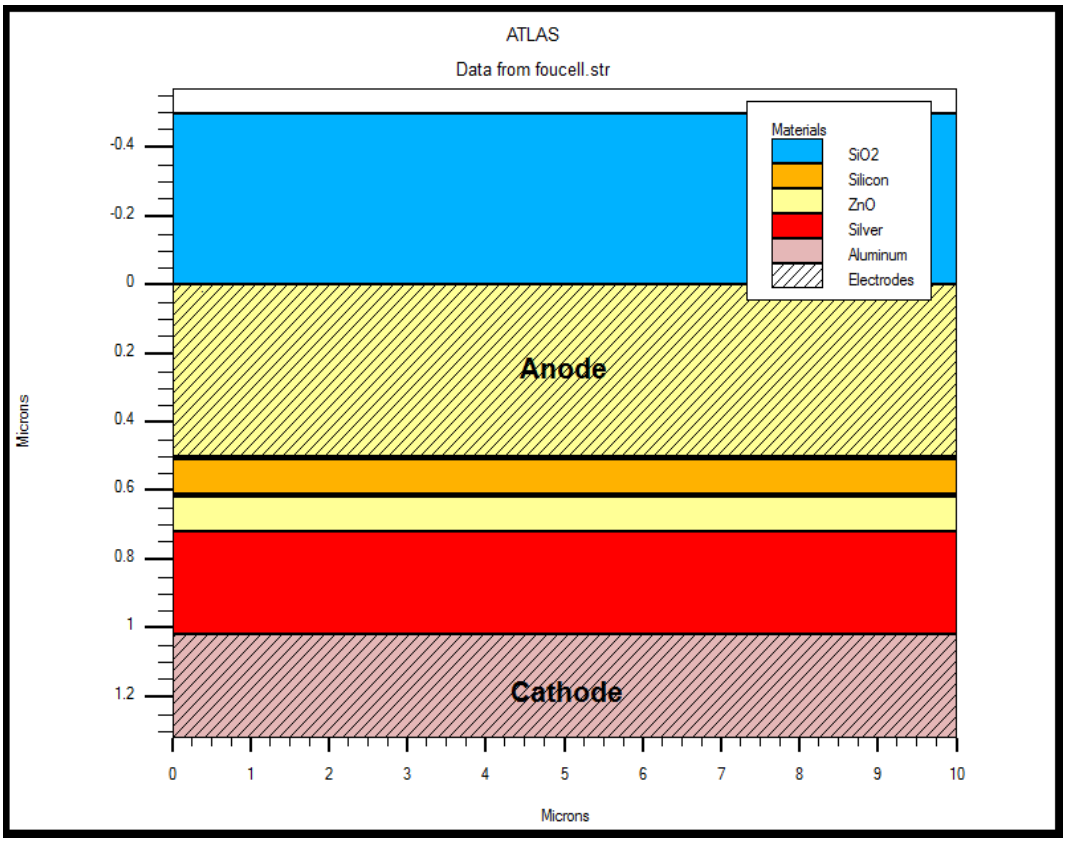

Figure IV.8: a-Si:H Single solar cell electrodes.

Some shortcuts can be used when defining the location of an electrode. If no Y coordinate parameters are specified, the electrode is assumed to be located on the top of the structure. You also can use the RIGHT, LEFT, TOP, and BOTTOM parameters to define the location. For example:

ELECTRODE NAME=SOURCE LEFT LENGTH=0.5

Specifies the source electrode starts at the top left corner of the structure and extends to the right for the distance LENGTH.

IV.6.4) Doping

You can specify analytical doping distributions or have Atlas read in profiles that come from either process simulation or experiment. You specify the doping using the DOPING statement. For example:

DOPING <distribution_type> <dopant_type> <position_parameters>

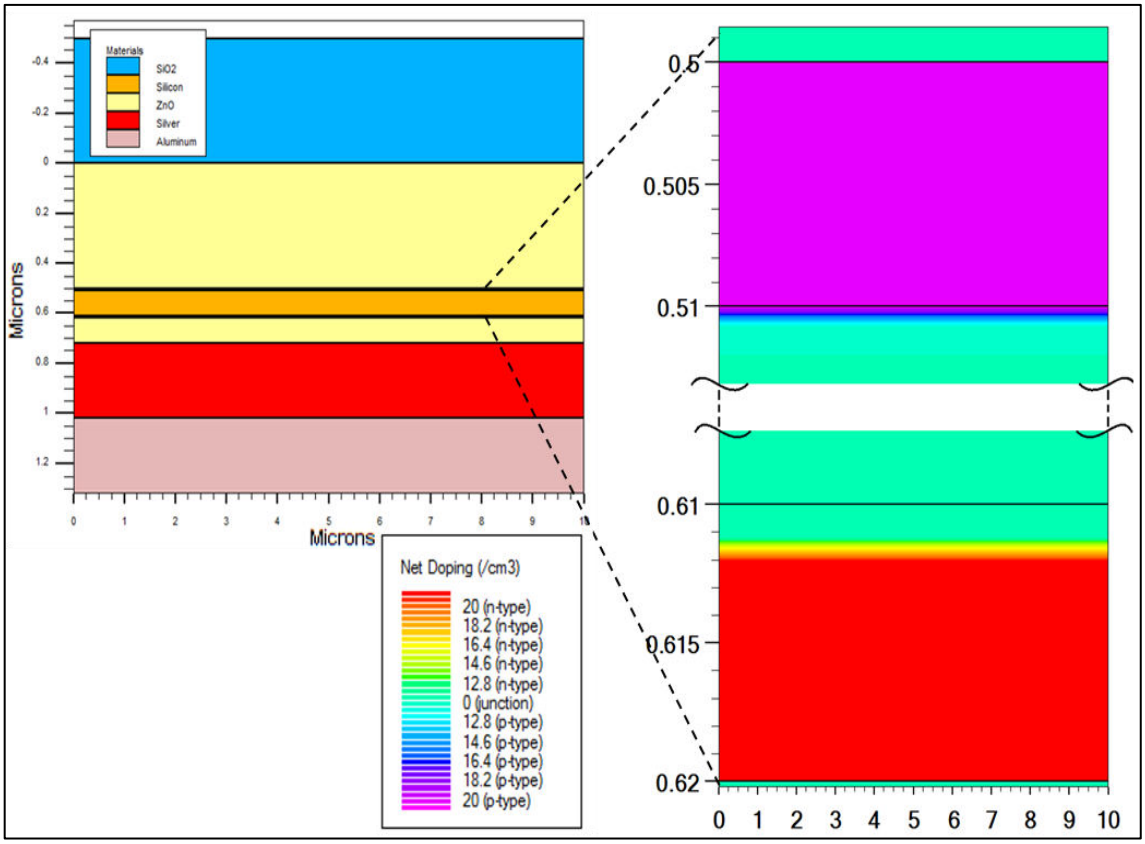

Figure IV.9: Doping profile for a-Si:H single cell.

Analytical doping profiles can have uniform, Gaussian..., the parameters defining the analytical distribution are specified in the DOPING statement. Two examples are shown below Figure IV.9 with their combined effect.

```
doping region=2 uniform p.type conc=1e20
doping region=4 uniform n.type conc=1e20
```

The DOPING statement specifies a uniform p-type doping density of 10^{20} cm^{-3} in the region that was previously labeled as region #2, while the second statement specifies a uniform n-type doping density of 10^{20} cm^{-3} in the region that was previously labeled as region #4. The position parameters X.MIN, X.MAX, Y.MIN, and Y.MAX can be used instead of a region number.

IV.7) Material and model specification

After one define the mesh, geometry, and doping profiles, he can modify the characteristics of electrodes, change the default material parameters, and choose which physical models Atlas will use during the device simulation. To accomplish these actions, use the CONTACT, MATERIAL, and MODELS statements respectively. Interface properties are set by using the INTERFACE statement.

IV.7.1) Material

All materials are split into three classes: semiconductors, insulators and conductors. Each class requires a different set of parameters to be specified. For semiconductors, these properties include electron affinity, band gap, density of states and saturation velocities. There are default parameters for material properties used in device simulation for many materials.

The MATERIAL statement allows you to specify your own values for these basic parameters. Your values can apply to a specified material or a specified region. For example in our case:

material material=Aluminum sopra=Al.nk

That means sets the index of refraction in all Aluminum regions in the device from the Sopra database. If the material properties are defined by region, the region is specified using the REGION or NAME parameters in the MATERIAL statement. For example, the statement:

MATERIAL region=2 taun0=1e-6 taup0=1e-6 eg300=1.7 nc300=3e20 nv300=3e20

That means sets the electron and hole Shockley-Read-Hall recombination lifetimes, band gap and the effective density of states of the conduction and valence band respectively at 300 K for region number two.

The description of the MATERIAL statement provides a complete list of all the material parameters that are available. Such as the band gap at room temperature (EG300), electron mobility (MUN), electron (TAUN0) and hole (TAUP0) recombination lifetimes, conduction band density at room temperature (NC300), among others.

IV.7.2) Contact

An electrode in contact with semiconductor material is assumed by default to be ohmic. If a work function is defined, the electrode is treated as a Schottky contact. The CONTACT statement is used to specify the metal workfunction of one or more electrodes.

Lumped resistance, capacitance, and inductance connected to an electrode can be specified using the RESISTANCE, CAPACITANCE, and INDUCTANCE parameters in the CONTACT statement. For example, the statement:

Contact name=anode workf=4.28 RESISTANCE=30.0 CAPACITANCE=1e-12

Specifies the workfunction of the anode is 4.28 eV and parallel resistance of 30 ohms and a capacitance of 1pF.

IV.7.3) INTERFACE

The INTERFACE statement is used to define the interface charge density and surface recombination velocity at interfaces between semiconductors and insulators. The following example shows the usage of the interface statement:

interface s.s y.min=0.5 y.max=0.52 s.n=1e5 s.p=1e5

The max and min values determine the boundaries. The S.S parameter expands the interface statement to take into consideration the semiconductor-semiconductor interface. The *S.N* value specifies the electron surface recombination velocity. *S.P* is similar to *S.N*, but for holes.

IV.7.4) Light source

The illumination by solar spectrum is defined by the beam statement. The origin and angle of incidence need to be defined. An angle of 90 degrees means normal incidence from the top. The parameter *power.file* points to an external file that contains a list of wavelengths vs. intensity. The file *'solarex12.spec'* contains data for the Air Mass 1.5 Solar Spectrum. The intensity in the file can be considered just as relative intensity between the wavelengths [127].

Beam num=1 x.orig=5 y.orig=-10 angle=90 power.file=solarex12.spec verbose back.reflect reflect=2

The *verbose* command enables a higher level of diagnostic run-time printing. The *back.reflect* command Specifies that back side reflections are to be taken into account while the *reflect* value specifies the number of reflections that will be traced.

It is possible to store the optical intensity of the illumination by specifying output file (opt.int) at any time before saving a structure file. The photogeneration rate will appear in the solution structure file by default.

IV.7.5) Models

The accuracy of the results obtained by device simulation process using ATLAS depends on the models used in the simulation process. Normally physics-based models are used to account for the complex dependencies of the device properties

on dimensions and other process variables. Generally, the model parameters are derived from measurements and characteristics of the devices [128].

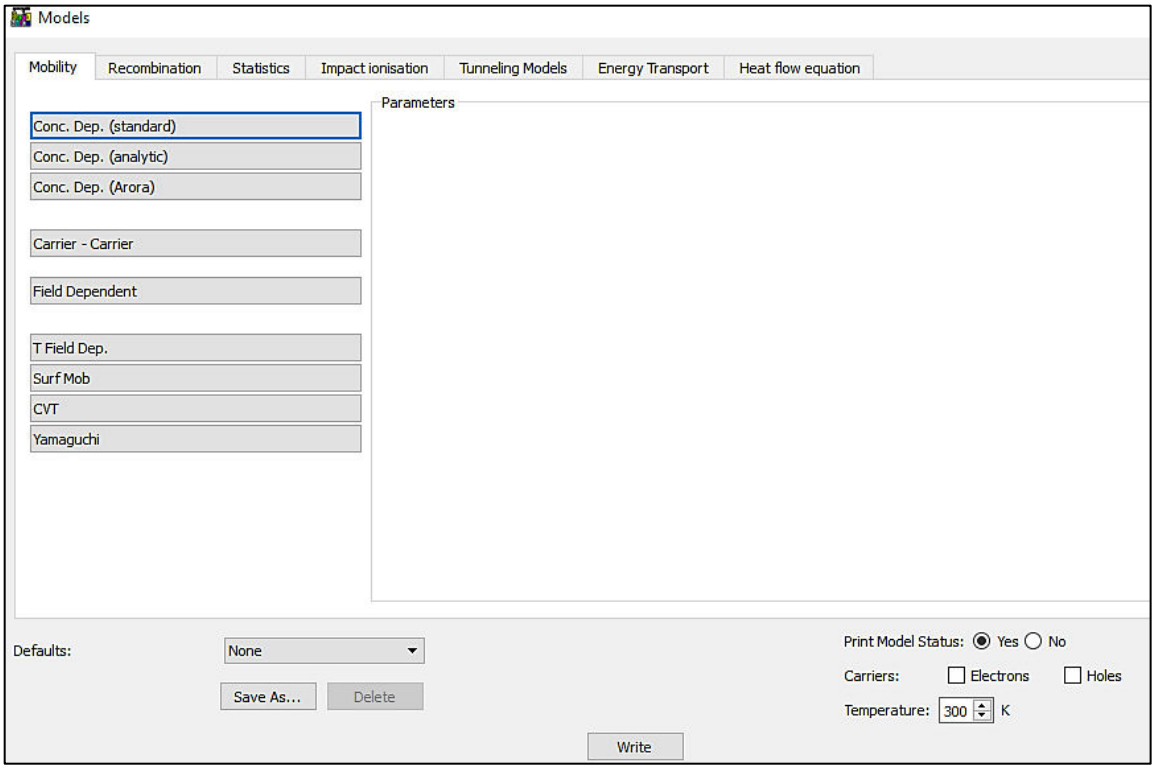

Figure IV.10: Models window in DeckBuild Atlas.

Physical models are specified using the MODELS and IMPACT statements. Parameters for these models appear on many statements including: MODELS, IMPACT, MOBILITY and MATERIAL. The physical models can be grouped into five classes: mobility, recombination, carrier statistics, impact ionization, and tunneling.

All models with the exception of impact ionization are specified on the MODELS statement. Impact ionization is specified on the IMPACT statement. For example the statement:

MODELS CONMOB FLDMOB SRH FERMIDIRAC PRINT

Specifies that the standard concentration dependent mobility, parallel field mobility, Shockley-Read-Hall recombination with fixed carrier lifetimes and Fermi Dirac statistics are included. The PRINT parameter lists to the run time output the models and parameters, which will be used during the simulation. This allows you to verify models and material parameters [129].

IV.7.5.A) Mobility models

Electrons and holes are accelerated by electric fields, but lose momentum as a result of scattering processes, which includes; lattice vibrations (phonons), impurity ions, other carriers, material imperfections (surface roughness …).

Since the effects of all of these microscopic phenomena are lumped into the macroscopic mobilities introduced by the transport equations these mobilities are therefore functions of the local electric field, lattice temperature, doping concentration, and so on. The most important mobility models are resumed in Table IV-1.

model	Syntax	notes
Concentration dependent	Conmob	The doping versus mobility table valid for 300K only
Concentration and temperature dependent	Analytic	Caughey-thomas formula. Tuned for 77-450K.
Carrier-carrier scattering	Ccsmob	Important when carrier concentration is high
Parallel Electric Field	Fldmob	Required to model any type of velocity saturation effect.
Lombardi(CVT) model	CVT	Complete model including N, T, E// and E effects. Good for non-planar devices.
Yamaguchi model	Yamaguchi	Includes N, E// and E effects. Only for 300K.
Klaassen model	KLA	Includes N, T, and n dependence. Recommended for bipolar devices.

Table IV-1: Most important mobility models.

Where N, T, E// and E are respectively the doping concentration, temperature and parallel electric field.

IV.7.5.B) Carrier Generation-recombination models

Carrier generation-recombination is the process through which the semiconductor material attempts to return to equilibrium after being disturbed from it. The processes responsible for generation-recombination are known to fall into six main categories: Phonon transitions, photon transitions, Auger transitions, surface recombination, impact ionization, tunneling.

The Table IV-2 describes the most common models implemented into Atlas that attempts the simulation of these six types of generation-recombination mechanisms.

model	Syntax	notes
Shockley-read-hall	SRH	Uses fixed minority carrier lifetimes. It should be used in most simulations.
Concentration dependent	CONSRH	Specifies SRH recombination using concentration dependent.
Auger	AUGER	Specifies Auger recombination. Important at high current densities.
Optical recombination	OPTR	Recommended for direct-gap materials
Band to Band Tunneling (standard)	BBT.STD	For direct transitions. Required with very high fields.
Thermionic Emission	EMISS.xx	Used to model transport across potential barriers at heterojunctions
Fermi-Dirac statistics	FERMI	High concentration effects

Table IV-2: The most common generation recombination models implemented into Atlas.

IV.8) Numerical method selection

After the materials model specification, the numerical method selection must be specified. The only statement that applies to numerical method selection is *method*.

The equations can be solved either by a fully coupled (Newton), de-coupled (Gummel), or combined (Block) manner. The coupled solutions with all equations solved at once are best when the interactions between the equations are strong (e.g.,

high current producing sufficient local heating). Newton's method is a fully coupled procedure that solves the equations simultaneously, through a generalization of the Newton-Raphson's method for solving the roots of an equation. However, they need a good initial guess as to the solution variables for reliable convergence. Unless special techniques such as projection are used for calculating the initial guess, the voltage step size during a bias ramp in a fully coupled solution might be small in order to obtain reliable convergence. Also, the Newton method may spend extra time solving the quantities that are weakly coupled or almost constant. Newton's method is the default method of drift-diffusion calculation in ATLAS.

On the other hand, de-coupled solutions where a subset of the equation is solved while others are held constant has shown an advantage when the interaction between the equations is small (typically low voltage and current levels). They tolerate a relatively poor initial guess for convergence. They tend to either diverge or take excessive central processing unit (CPU) time once the interaction among the equations becomes stronger. Gummel's method cannot be used with lumped elements or current boundary conditions.

In general, Gummel's method is useful where the system of equations is weakly coupled, but it has only linear convergence. The Newton method is useful when the system of equations is strongly coupled and has quadratic convergence.

BLOCK method can provide for faster simulations times compared to *NEWTON* and *GUMMEL*. It can be useful to start a solution with a few *GUMMEL* iterations to generate a better guess. Then, switch to *NEWTON* to complete the solution.

It is possible to supply parameters to the *METHOD* statement to specify which carrier (electron, hole, or both) continuity equation is to be solved. The choice can be made using the parameters *CARRIERS*. For example, to include both electron and hole, the user must specify "CARRIERS = 2" and for only holes "CARRIERS = 1 HOLE" in the *METHOD* statement.

IV.9) Solution Specification

Atlas can calculate DC, AC small signal, and transient solutions. Obtaining solutions is similar to setting up parametric test equipment for device tests. You usually define the voltages on each of the electrodes in the device. Atlas then calculates the current through each electrode. Atlas also calculates internal quantities, such as carrier concentrations and electric fields throughout the device. In all simulations, the device

starts with zero bias on all electrodes. Solutions are obtained by stepping the biases on electrodes from this initial equilibrium condition. This section concentrates on defining solution procedures.

IV.9.1) Log

Log files store the terminal characteristics calculated by Atlas. These are current and voltages for each electrode in DC simulations. In transient simulations, the time is stored. In AC simulations, the small signal frequency and the conductances and capacitances are saved. For example, the statement:

LOG OUTFILE=foucell.log

It is used to create a log file called foucell. Terminal characteristics from all SOLVE statements after the LOG statement are then saved to this file along with any results from the PROBE statement.

To not save the terminal characteristics to this file, use another LOG statement with either a different log filename or the OFF parameter.

IV.9.2) Solve

To obtain convergence for the equations used, supply a good initial guess for the variables to be evaluated at each bias point. The Atlas solver uses this initial guess and iterates to a converged solution. For isothermal drift diffusion simulations, the variables are the potential and the two carrier concentrations. If a reasonable grid is used, almost all convergence problems in Atlas are caused by a poor initial guess to the solution.

When no previous solutions exist, the initial guess for potential and carrier concentrations must be made from the doping profile. This is why the initial solution performed must be the zero bias (or thermal equilibrium) case. This is specified by the statement:

SOLVE INIT

Typically, the first step in solar cells analysis is to illuminate the device. You can turn on the illumination by assigning the beam intensity on a *SOLVE* statement as follows:

SOLVE B1=1.0

Here, we assign a value of one "sun" to the intensity of the optical source indexed as number "1" (B1).

As we had assigned **AM1.5** on the BEAM statement, this corresponds to standard test conditions. In some cases, we may encounter convergence difficulties and may need to ramp the light intensity as shown in the following:

SOLVE B1=0.01

SOLVE B1=0.1

SOLVE B1=1.0

You may also choose to assign the beam intensity to a value greater than one to simulate solar concentrator effects. Since we have not yet assigned any bias voltages, the current in the run time output corresponds to the short circuit current (I_{sc}).

Then, we can simply capture the spectral response using a wavelength ramp defined on the *SOLVE* statement as follows:

SOLVE B1=0.001 BEAM=1 LAMBDA=0.3 WSTEP=0.02 WFINAL=1.2

Here, the B1 parameter sets the intensity to 1 mW. The *BEAM* parameter identifies the index of the optical source that is going to be involved in the wavelength ramp. *LAMBDA* specifies the initial wavelength in microns, *WFINAL* specifies the final wavelength in microns, and *WSTEP* specifies the wavelength step in microns.

To capture the $I-V$ characteristic, you need to ramp the voltage past the open circuit voltage (V_{oc}) as in the following:

Solve vanode=0.0 name=anode vstep=0.02 vfinal=1.4

Here we assume that the anode is P type and the characteristic is extracted on positive anode voltages. We ramp from 0 to 1.4 volts in 0.02 volt steps.

IV.9.3) Load and save

Solution files or structure files provide an image of the device at a particular bias point. This gives you the ability to view any evaluated quantity within the device structure in question, from doping profiles and band parameters to electron concentrations and electric fields. The *SAVE* statement enters all node point

information into an output file. The *LOAD* statement enters previous solutions from files as initial guess to other bias points. The following are examples of *LOAD* and *SAVE* statements.

```
SAVE OUTF=mycell.STR
```

In this case, *mycell.STR* has information saved after a SOLVE statement. Then, in a different simulation, mycell.STR can be loaded as follows:

```
LOAD INFILE=mycell.STR
```

IV.10) Results Analysis

Once a solution has been found and saved in files, the information can be displayed graphically with *TonyPlot* (see Figure IV.11), for example:

```
TONYPLOT foucell.log
```

We can also use the DeckBuild *Extract* capability to capture the various solar cell figures of merit. We first initialize the Extract capability with the captured input file as in the following example:

```
EXTRACT INIT INFILE="foucell.LOG"

EXTRACT NAME="IV" curve(v."anode", I."cathode") OUTFILE="IVcurve.dat"
```

Extract also can be used to determine some important values such as the short circuit current (I_{sc}), open circuit voltage (V_{oc}), maximum power (Pm), voltage at maximum power (Vm), current at maximum power (I_m), and fill factor (FF). The following lines demonstrate the extraction of these values:

```
EXTRACT NAME="Isc" Y.VAL FROM CURVE(V."anode", I."cathode") WHERE
X.VAL=0.0
EXTRACT NAME="Voc" X.VAL FROM CURVE(V."anode", I."cathode") WHERE
Y.VAL=0.0
EXTRACT NAME="Pm" MAX(CURVE(V."anode", (V."anode" * I."cathode")))
EXTRACT NAME="Vm" X.VAL FROM CURVE(V."anode", (V."anode"*I."cathode") ) \
WHERE Y.VAL=$"Pm"
EXTRACT NAME="Im" $"Pm"/$"Vm"
EXTRACT NAME="FF" $"Pm"/($"Jsc"*$"Voc")
```

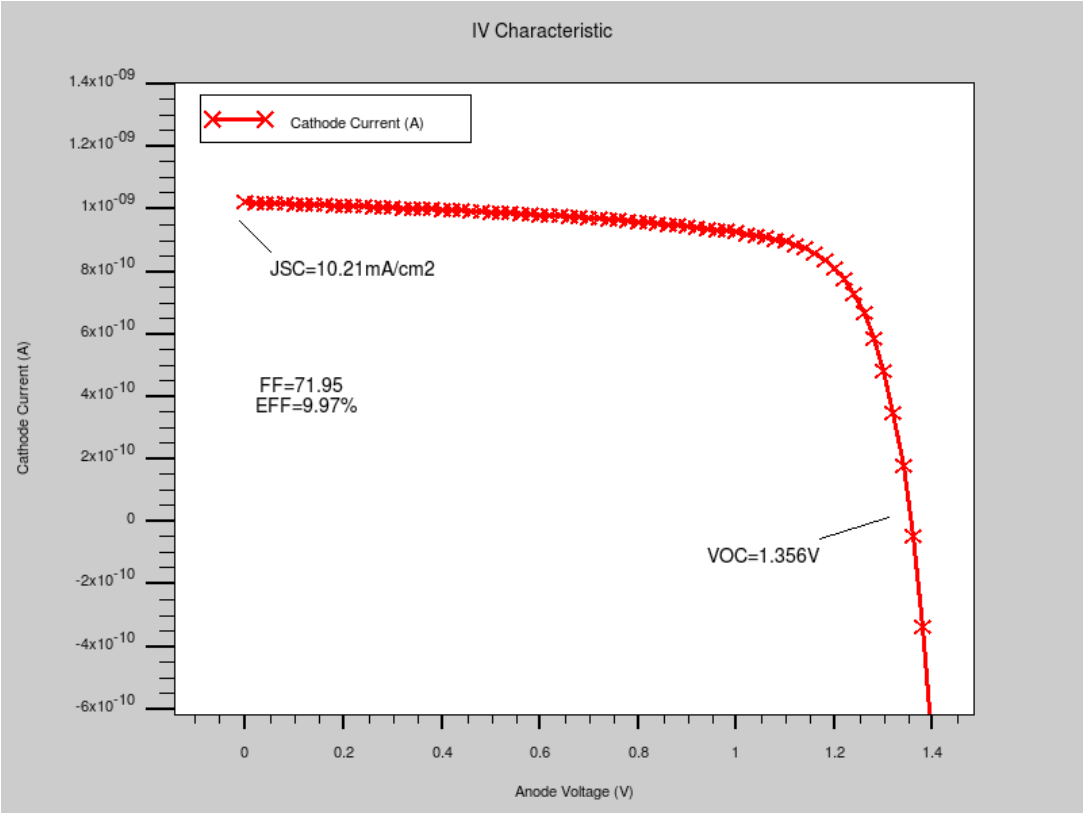

Figure IV.11: $I-V$ curve of a micromorph (a-Si:H/µc-Si:H) tandem solar cell plotted using TonyPlot.

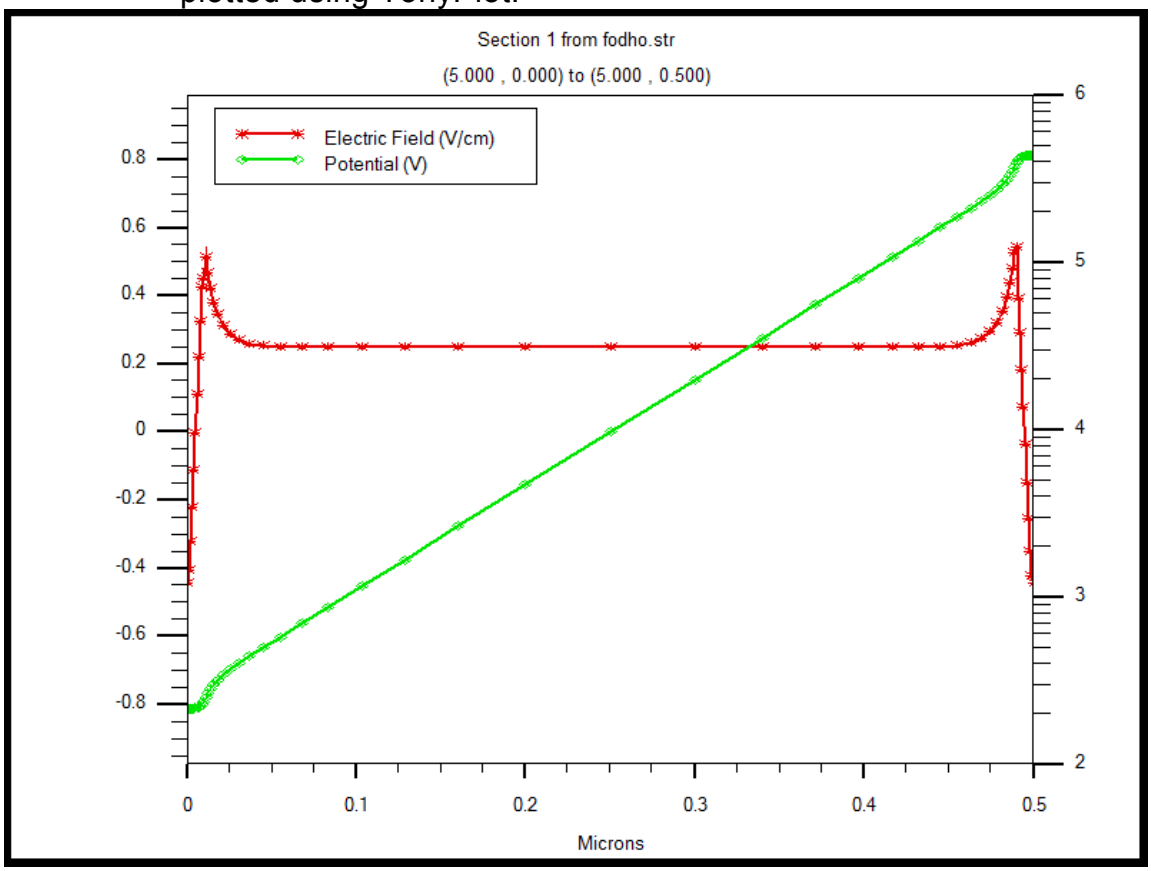

Figure IV.12: internal electric field and potential of p-i-n a-Si:H cell using TonyPlot

IV.11) Conclusion

In this chapter, we presented a detailed description of the numerical simulator used in this study. Indeed, Silvaco TCAD simulator provides a complete solution for researchers interested in solar cell technology. It enables researchers to study the electrical properties of solar cells under illumination in both Two-and Three dimensional domains. The simulated properties include external parameters such as *I-V* characteristics, spectral response and quantum efficiency vs. wavelength, and internal quantities like recombination rates, charge carrier densities, potential and field distributions… etc. In addition, the software is also capable to simulate many configurations of amorphous silicon-based solar cells consisting of single, tandem and triple junctions. Silvaco is the promoted vendor for all companies interested in advanced solar cell technology simulation solutions.

Chapter V

Results and discussion

V.1) Introduction

Most of solar cells based on hydrogenated amorphous and microcrystalline silicon (a-Si:H, µc-Si:H respectively) are usually designed in a p-i-n diode (see chapter)[18, 94, 98]. The p-doped and n-doped layers serve as contacts and establish a potential gradient for the separation and collection of photogenerated carriers. These layers must be kept as thin as possible (typically tens of nanometers) to reduce optical absorption losses. The thicker undoped intrinsic i-layer (typically hundreds of nanometers for the a-Si:H and thousands of nanometers for the µ-Si:H) is the absorber in which the photo-generated electron-hole pairs immediately experience the internal electric field that separates electrons and holes from each other. The separated carriers drift under the influence of the internal electric field towards the doped layers (electrons towards the n-type layer and holes towards the p-type layer) and are collected by the electrodes. The device performance is limited by the absorber layer defect (particularly owing to the light induced creation of metastable defects in a-Si:H or the so called Staebler–Wronski effect [18] as we mentioned before(chapter)) which make it one of the most important parameters that should be taken into consideration when improving the solar cell performance,. Moreover, the degradation is strongly dependant on the thickness of the used device, which prevents the use of a thick absorption region. So an optimization of the i-layer thickness must be taken into consideration.

Relatively to the single-junction structure, the multi-junction one is a proven way to increase device efficiency in many solar cell technologies. In the thin-film silicon technology, one of the most common approaches is to combine an amorphous (a-Si:H) silicon cell and a microcrystalline (µc-Si:H) silicon cell into the so-called micromorph (a-Si:H/µc-Si:H) tandem solar cell [130]. The advantage of such structure is the ability to absorb more efficiently a larger part of the solar spectrum by stacking materials with different band gaps. In a conventional tandem device, the two sub-cells are directly stacked by successive layer deposition, which makes them both optically and electrically coupled [106, 107, 131]. Only two contact electrodes are connected to the top cell p-type layer and to the bottom cell n-type layer. By this way, the two sub-cells are physically series connected to give a two- terminal (2T) device. The stability of such a device is mostly limited by the a-Si:H top sub-cell, due to Staebler–Wronski degradation process [19] in a-Si:H material. Therefore, it is essential to use a thin a-Si:H cell, with high built-in electric field in order to reduce the

recombination of free carriers due to light-induced metastable defects. The absorbance in the µc-Si:H cell can be increased by choosing a larger thickness of the absorption layer. The a-Si:H top sub-cell generates a lower current compared with the µc-Si:H bottom sub-cell and thus the total current of the tandem cell is limited by the top sub-cell. To circumvent the instability problems in 2T-device, a four-terminal (4T) device configuration has been developed [111, 132-135], in which the two sub-cells are separated by an insulating material (e.g. glass, plastic or SiN_x), and each one of them has its own electrodes connected to its own p-type and n-type layers. So, the two sub-cells are optically coupled and electrically decoupled.

This work is devoted to the study of a-Si:H and µc-Si:H- based solar cells in view of optimizing their performance by **modeling using the commercially available software Silvaco TCAD from Silvaco Inc**. First, we investigate the photo-degradation (SW) effect on a single (a-Si:H) p-i-n cell illuminated by a monochromatic light beam (530-540 nm), then by the standard solar spectrum (AM1.5), on the basis of the model of the light-induced defect creation in a-Si:H developed by AF. Meftah et al [136, 137]. Thereafter, we present the (i)-layer thickness and free carrier mobility effects on the output parameters of the solar cell in single structure configuration, and 2T- 4T- micromorph tandem configuration, in both un-degraded and the light-soaked states. The main results are expressed and analyzed in term of the device performance parameters such as the current density- voltage ($J-V$) characteristics, the short-circuit current density (J_{sc}), the open-circuit voltage (V_{oc}), the fill factor (FF), the conversion efficiency (η) and the external quantum efficiency (EQE).

V.2) Photodegradation effect in a-Si:H p-i-n solar cell

The main problem which limits the applicability of the hydrogenated amorphous silicon (a-Si:H) materials in photovoltaic domains is the degradation of transport proprieties during illumination. The majority of models proposed to understanding the microscopic mechanisms that cause this effect suggest that it is due mainly to a light-induced defect creation, stimulated by the non radiative recombination of the photogenerated free carriers. The energy released from such recombination can break weak bonds [52, 54, 138-140], or liberates bounded hydrogen atoms [50, 55, 141, 142] that can diffuse and break weak bonds and then, further dangling bonds (further defects are created).

During illumination, the increase of the dangling bond density of states in the a-Si:H gap is obtained on the basis of the model of the light-induced defect creation

in a-Si:H developed by AF.Meftah et al [136, 137]. The proposed model is based on experimental observation concerning the presence of the doubly hydrogenated weak SiSi bond (SiHHSi) configuration [140, 143], the hydrogen diffusion [144] and the main role of the hydrogen in the light-induced defect annealing.

The varying density of states is then used in the numerical modelling of the a-Si:H p-i-n solar cell, illuminated first with monochromatic light beam (λ=530-540 nm). The considered wavelength corresponds to the case of non-uniform absorption (absorption coefficient $\alpha = 10^5 \mathrm{cm}^{-1}$), which means an exponential decay of generation rate away from the illuminated p-side of the device. Taking the photon flux ϕequal to 10^{17} cm^{-2} s^{-1}, this give an optical generation rate *G* in the photo-generation region equal to 10^{22} cm^{-3} s^{-1} , which is slightly lower than the value assured later by the total AM1.5 spectrum illumination. We analyse the degradation in term of internal variables' profiles; free carrier densities, recombination rates, space charges, band structure, potential, electrical field, and current densities. We present also the light-induced degradation effect on the cell photo-parameters, i,e,. the open circuit voltage V_{oc}, the short circuit current density J_{sc}, the fill factor *FF* and the maximum power density P_{max} .

V.2.1) SWE model

In AF.Meftah et al model [136, 137], the basic processes for light-induced creation of dangling bonds are given as follows: the defect creation occurs by a non radiative recombination between photoexcited electrons and holes at a weak SiSi bond adjacent to a SiHHSi bond. This can be justified by the fact that the majority of hydrogen is located in SiHHSi configurations rather than in isolated SiH bonds [140]. This weak SiSi bond is energetically favourable for recombination due to the additional stress imposed by the two hydrogen atoms. As a result of the released energy after recombination, one of the two hydrogen atoms moves to the site of the broken SiSi bond, forming two adjoining SiHD defects. The hydrogen atom is located at the tetrahedral site, rather than the bond centred site, of the broken SiSi bond, and the separation of the Si dangling bond and hydrogen atom is in the range 4-5 A^o, which is consistent with ESR experiments [140]. The recombination at the SiHD defect site allows the production and diffusion of a mobile hydrogen atom through the material. If the dissociated hydrogen atom is inserted in the nearby SiHD defect, this will be annihilated and, in this case there will be no defect creation and no SWE as a consequence. Thus, the hydrogen atom remains mobile until it meets a distant SiHD

defect where they annihilate to form a SiHHSi bond. The hydrogen atom can also be re-trapped by colliding with a second metastable H. In this case, both metastable H are trapped to form a SiHHSi bond again.

Taking into account the processes described above, the rate equations governing the kinetics of SiHD and metastable H under illumination are given as follows [41, 136, 137, 145].

$$\frac{\mathrm{d}N_d}{\mathrm{d}t} = R_{SiSi} - R_{SiHD} - C_d^c N_H N_d \qquad (\text{V.1})$$

$$\frac{\mathrm{d}N_H}{\mathrm{d}t} = R_{SiHD} - C_d^c N_H N_d - 2C_H^c N_H^2 \qquad (\text{V.2})$$

where t is the illumination time, N_d and N_H are densities of SiHD and metastable H, respectively. $R_{SiSi} = k_d\, n\, p$, where k_d expresses the light-induced creation of SiHD. n and p are the free electron and free hole densities. $R_{SiHD} = k_H\, n\, p$, where k_H represents dissociation of a hydrogen atom from a SiHD defect. C_d^c and C_H^c are rate constants for the two trapping processes of the hydrogen atom. We assume that n and p are determined by the steady state numbers and are, in the case of moderate illumination where the recombination is monomolecular, proportional to illumination intensity G and inversely proportional to the defect density N_d:

$$n = p = \frac{G}{C_c N_d} \qquad (\text{V.3})$$

where C_c (10^{-8} cm^3 s^{-1}) is the capture coefficient of free carriers by dangling bonds. Then, the rate equation 1.(a)-(b) are rewritten as follows:

$$\frac{\mathrm{d}N_d}{\mathrm{d}t} = \frac{k_d G^2}{C_c^2 N_d^2} - \frac{k_H G^2}{C_c^2 N_d^2} - C_d^c N_H N_d \qquad (\text{V.4.a})$$

$$\frac{\mathrm{d}N_H}{\mathrm{d}t} = \frac{k_H G^2}{C_c^2 N_d^2} - C_d^c N_H N_d - 2C_H^c N_H^2 \qquad (\text{V.5.b})$$

The initial conditions are $N_d = 10^{16}\mathrm{cm}^{-3}$ and $N_H = 0$ and the values of the different involved constants are those used previously in Ref [136, 137] which reproduced well Godet's measurement: $k_d = 5 \times 10^{-15}\mathrm{cm}^3\mathrm{s}^{-1}$, $k_H = 3 \times 10^{-15}\mathrm{cm}^3\mathrm{s}^{-1}$, $C_d^c = 4 \times$

$10^{-19}\mathrm{cm}^3\mathrm{s}^{-1}$ and $C_H^c = 10^{-17}\mathrm{cm}^3\mathrm{s}^{-1}$. From the simulated curve shown in figure V.1, the dangling bond (SiHD) density increase from 10^{16} cm^{-3} initially to a steady state value of 3.75×10^{16} cm^{-3} for illumination time $> 10^4$s.

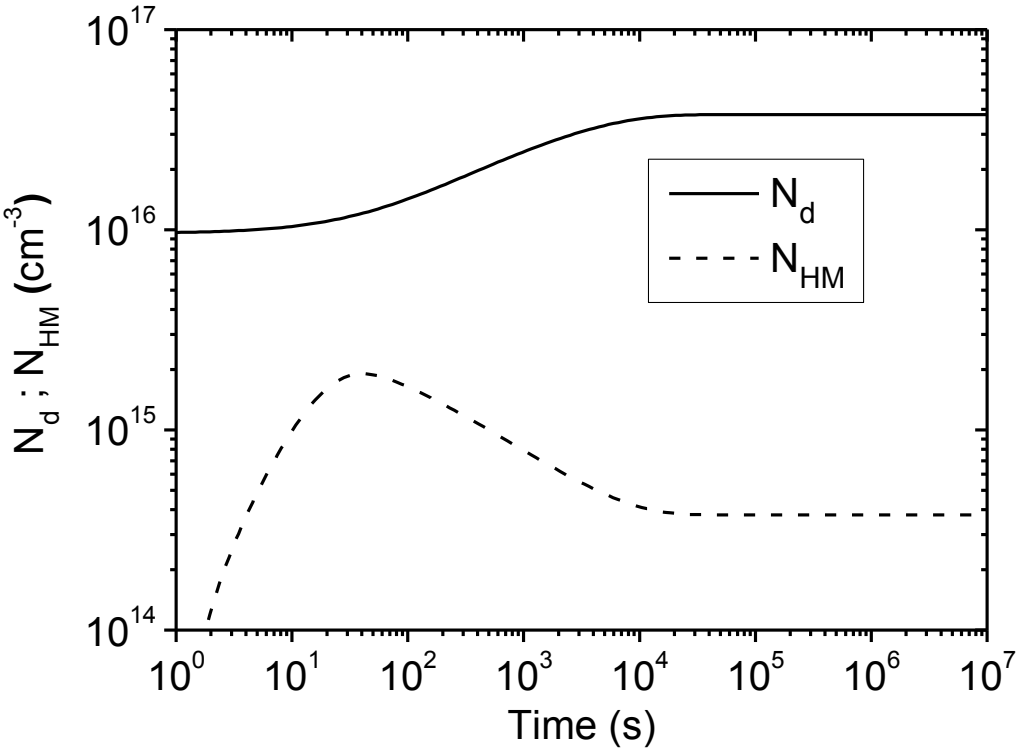

Figure V.1: The simulated light-induced defect and mobile hydrogen densities versus illumination time by Af Meftah et al model [136, 137].

The metastable hydrogen increases nearly exponentially until 40 s what delays the increase of the SiHD density. After 40 s, the decrease of the metastable hydrogen occurs parallel to the inverse of the SiHD density until 2×10^4 s, after which a steady state is established for the two densities.

V.2.2) Physical model of the a-Si:H density of states

The typical density of localised states, $g(E)$, in the a-Si:H gap is comprised of valence and conduction band tail state densities, $g_V(E)$ and $g_C(E)$ respectively, which decay exponentially from the band edge, and of dangling bond state density, $g_d(E)$, which is calculated according to the defect pool model improved by Powell and Deane [40].

$$g(E) = g_V(E) + g_C(E) + g_d(E) \qquad (V.6)$$

where E is the energy level in the band gap E_g.

The two exponential tails are defined as:

$$g_V(E) = G_V exp\left(\frac{E_V - E}{K_B T_V}\right) \qquad (V.7)$$

$$g_C(E) = G_C exp\left(\frac{E - E_C}{K_B T_C}\right) \qquad (V.8)$$

where G_V and G_C are the density of valence (donor-like) and conduction (acceptor-like) band tail states at the band edge E_C and E_V respectively. T_V and T_C are the characteristic temperatures that describe the exponential slope of both band tails.

The defect pool model has been proposed to evaluate the dangling bond state density as equilibrium properties of a-Si:H, which can account for a wide range of experimental results [39, 40]. The equilibration mechanism was identified as a conversion of weak bonds to dangling bonds according to the following reaction: SiHHSi+SiSi↔2SiHD. The density of state distribution was determined by applying the law of mass action to both reactions: SiHD↔SiSi+H and SiHHSi↔SiSi+2H, between weak bond energy in the valence band tail and energy level in the gap where the defect is formed. The density of state calculated within the framework of the defect pool model is expressed as follows [39]:

$$D(E) = \gamma \left[\frac{2}{f^o(E)}\right]^{K_B T^*/2E_{vo}} P\left[E + \frac{\sigma^2}{2E_{vo}}\right] \qquad (V.9)$$

with

$$\gamma = \left[\frac{G_v 2E_{vo}^2}{[2E_{vo} - K_B T^*]}\right] . \left[\frac{H}{N_{SiSi}}\right]^{K_B T^*/4E_{vo}} exp\left[\frac{-1}{2E_{vo}}\left[E_P - E_v - \frac{\sigma^2}{4E_{vo}}\right]\right] \qquad (V.10)$$

$P(E)$ is the defect pool function assumed to have a Gaussian distribution. σ and E_p are, respectively, the pool width and peak position.G_v and E_{vo} are, respectively, the density of states at E_v and the valence band tail width. $T^*$is the equilibrium temperature (freeze-in temperature) for which the density of states is maintained. *H* is the total hydrogen concentration and N_{SiSi} is the total electron concentration in the material. $f^0(E)$ is the neutral dangling bond state occupancy. See (equation II.5, II.6).

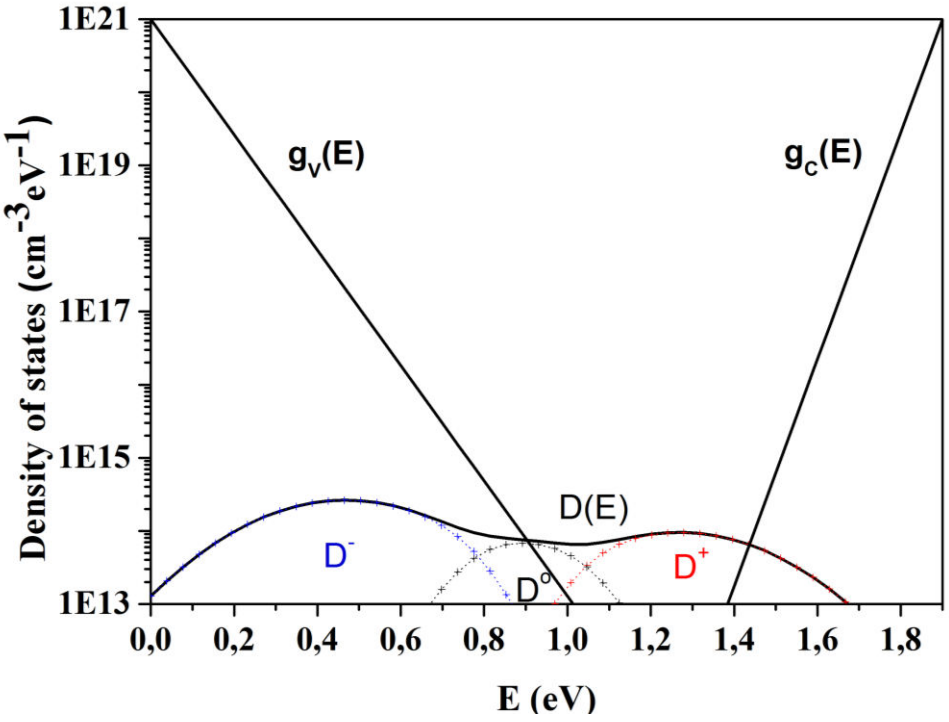

Figure V.2: The total density of state including band tail states and dangling bond states in the middle of the i-layer of the a-Si:H p-i-n cell at T=300 K.

Figure V.2 shows the distribution of the total density of states in the middle of the i-layer of the a-Si:H p-i-n cell at thermal equilibrium. Included are the valence and conduction band tail densities $g_V(E)$ and $g_C(E)$ respectively, and the dangling bond density, $D(E)$ with its three components $D^+(E)$, $D^0(E)$, et $D^-(E)$.

It is possible to replace the defect density of the states $D(E)$ by an equivalent density $g_d(E)$ of monovalent states of which the probability of occupation is related to Fermi-Dirac function. The interest of this equivalence comes owing to the fact that the states detected by the majority of the spectroscopic techniques are considered monovalents. $g_d(E)$ is given by the expression:

$$g_d(E) \approx D(E + kTln2) + D(E - U - kTln2) \quad (V.11)$$

where the $kTln2$ term comes from the spin degeneracy of the singly occupied state. This is not exact, but it is a very good approximation, leading only to a small error of about $exp(-U/kT)$ in the density. The total density of state including band tail states and dangling bond states is then:

$$g(E) = g_V(E) + g_C(E) + g_d(E) \quad (V.12)$$

Taking into account the doping effect through the p-type and n-type layers of the a-Si:H p-i-n cell, the Fermi level position E_f, will change relatively to E_V (or E_C) from p-

type region to n-type region, this leads to a component (D^+ in p-type layer and D^- in n-type layer) much bigger than the others. The defect state density, $D(E)$ so $g_d(E)$ and then the total state density, $g(E)$, will change from p-type layer to i-type layer to n-type layer as shown in figure V.3.

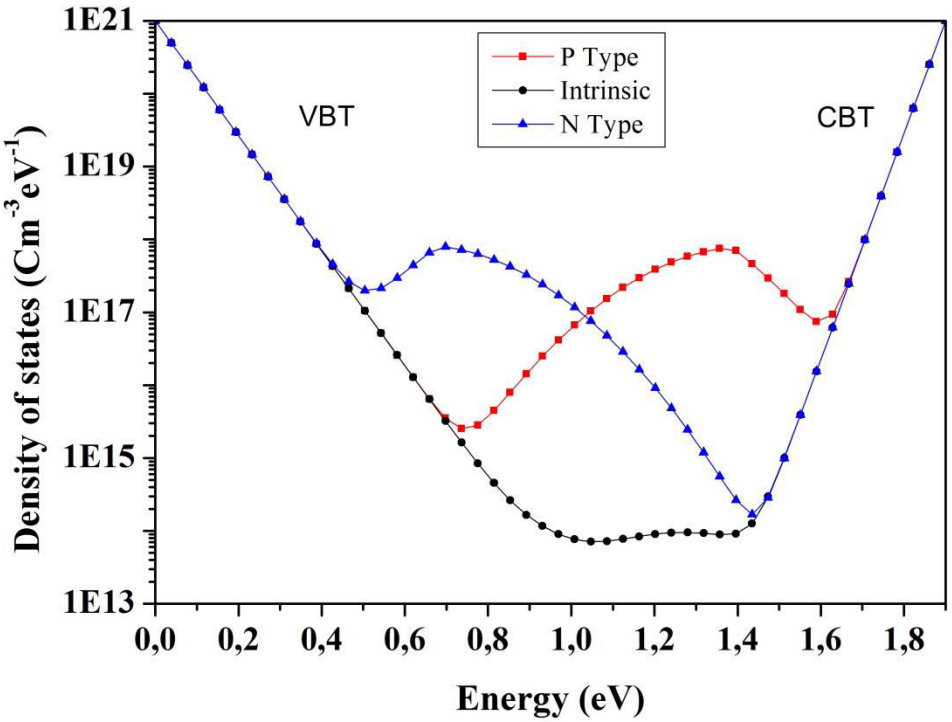

Figure V.3 The total density of state at different regions of the solar cell (p-type, i-type and n-type) at thermal equilibrium.

The parameters used to plot the gap density of states of both figures V.2 and V.3 are listed in Table V.1.

Under illumination, the areas of defect Gaussian distributions increase similarly to the defect concentration N_d ($N_d = \int_{E_c}^{E_v} D(E)dE$) while their positions and widths remain unchanged. The valence and conduction band tails are supposed to be constants. These suppositions are made on the basis of experimental study performed by Refs [146, 147].

Pool width σ (eV)	0.19
Defect electron correlation energy, U (eV)	0.2
	1.27

Pool peak position E_p (eV)	5×10^{21}
Total hydrogen concentration H (cm^{-3})	2×10^{23}
Total electron concentration N_{sisi} (cm^{-3})	500
Defect state density freeze-in temperature T^* (°K)	570
Characteristic temperature of the valence band tail T_v (°K)	246
Characteristic temperature of the conduction band tail T_c (°K)	0.98
Intrinsic Fermi level E_{fi} (eV)	1.9
Mobility gap, E_g (eV)	0.28
Activation energy in the *p*-layer, E_{fp}(eV)	0.24
Activation energy in the *n*-layer,E_{fn}(eV)	1×10^{21}
Density of states at E_c and E_v, G_c, G_v ($cm^{-3}eV^{-1}$)	5×10^{18}
p- and n-layer doping densities, N_a, N_d (cm^{-3})	2×10^{20}
Effective density of states in conduction band at 300°K, $N_{C,300}$($cm^{-3)}$	2×10^{20}
Effective density of states in valence band at 300°K, NV,300($cm^{-3)}$	1×10^{16}
Annealed *i*-layer DOS (cm^{-3})	1×10^{-7}
Capture coefficient of charged tail's states, C_{ct} ($cm^3\ s^{-1}$)	1×10^{-8}
Capture coefficient of neutral tail's states, C_{nt} ($cm^3\ s^{-1}$)	1×10^{-7}
Capture coefficient of charged dangling bond's states, C_{cd} ($cm^3\ s^{-1}$)	1×10^{-8}
Capture coefficient of neutral dangling bond's states, C_{nd} ($cm^3\ s^{-1}$)	534
Incident light beam wavelengthλ (nm)	10^{17}
Incident light beam intensityϕ ($cm^{-2}\ s^{-1}$)	10^5
Absorption coefficient α (cm^{-1})	

Table V-1: Parameters used for the a-Si:H density of state model.

Figure V.4 shows the evolution of the defect state density versus illumination time taking into account the assumptions above. The parameters used to calculate the defect density of states are listed in table V.1, and they give an initial (equilibrium, annealed) defect density N_d of 10^{16} cm^{-3}. Under illumination, the latter reaches 4×10^{16} cm^{-3} for standard a-Si:H film soaked by monochromatic light beam with an intensity of 10^{22} $cm^{-3}s^{-1}$ and λ<570 nm [50]. Afterwards, this density of states, varying with illumination time, is implanted in the numerical modelling of the a-Si:H p-i-n solar cell to showing the related degradation effect on the internal variables as well as on the photo-parameters of the cell.

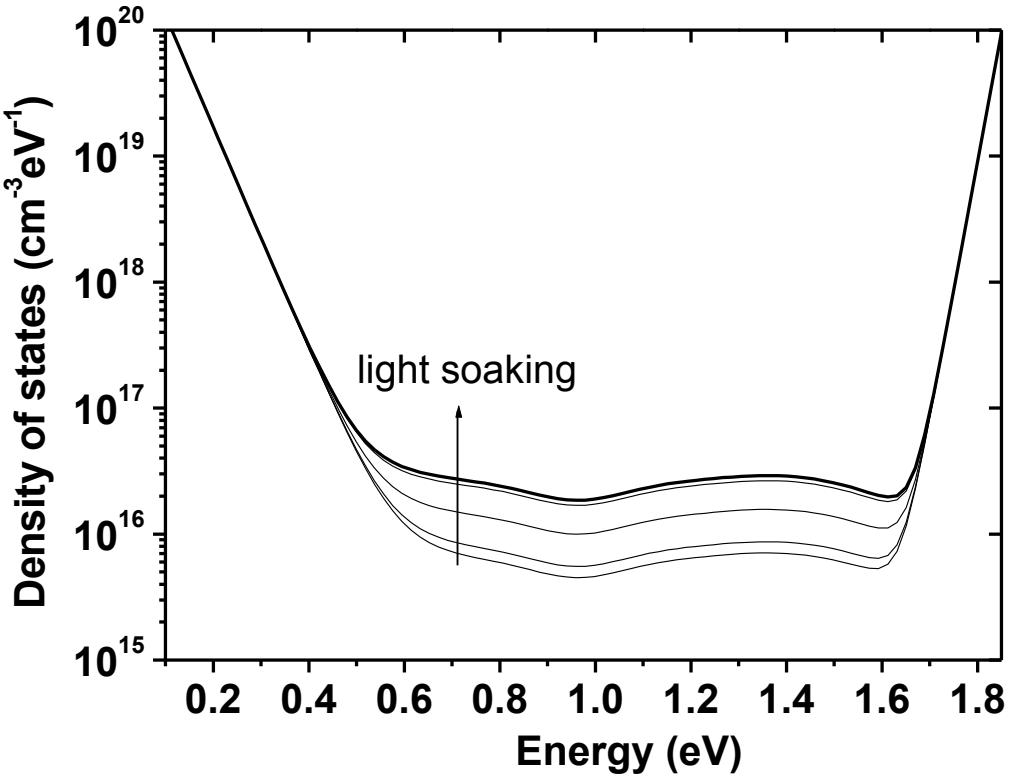

Figure V.4: Light-induced increase of the total density of state in the gap of the a-Si:H.

V.2.3) Numerical modeling of the a-Si:H p-i-n cell:

To simulate the a-Si:H solar cell performance, we employed the commercially available software Silvaco TCAD, from Silvaco Inc., which is a powerful semiconductor device and process simulator. Among a number of examples in Silvaco-ATLAS, we selected the most suitable one; the "solarex12.in" example, which calculates the , the current - voltage ($I-V$) characteristic, and extracts the output parameters J_{sc}, V_{oc}, FF and η of a 2T micromorph tandem solar cell based on Ref [148] with the structure: ZnO:Al (500nm)/p-a-Si:H (10nm)/ i-a-Si:H (200nm)/ n-a-Si:H (15nm)/p-µc-Si:H (10nm)/i-µc-Si:H (2.2µm)/n-µc-Si:H (15nm)/ ZnO (100nm)/Ag, where the ZnO/Ag forms the back reflector.

The simulation program uses the drift-diffusion model for the Poisson equation coupled with the continuity equations of electrons and holes, and solves them for the virtual device by dividing the whole structure into finite elements, and using a standard procedure for amorphous materials, including the continuous density of states (DOS) model, Shockley–Read–Hall (SRH) and Auger recombination mechanisms [atlas_users1]. Numerical solution of equations mentioned above allows to calculate the internal parameters of the device such as: the electrostatic potential

and field, the free electron and hole densities, the space charge density, the electron and hole current densities, the recombination rates for electrons and holes, and then, the external parameters such as the current density - voltage characteristic ($J - V$) and the external quantum efficiency (EQE).

Appropriate modifications were made to "solarex12.in" example to simulate the a-Si:H-based single cell shown on figure V.5 with parameters listed in table V.2.

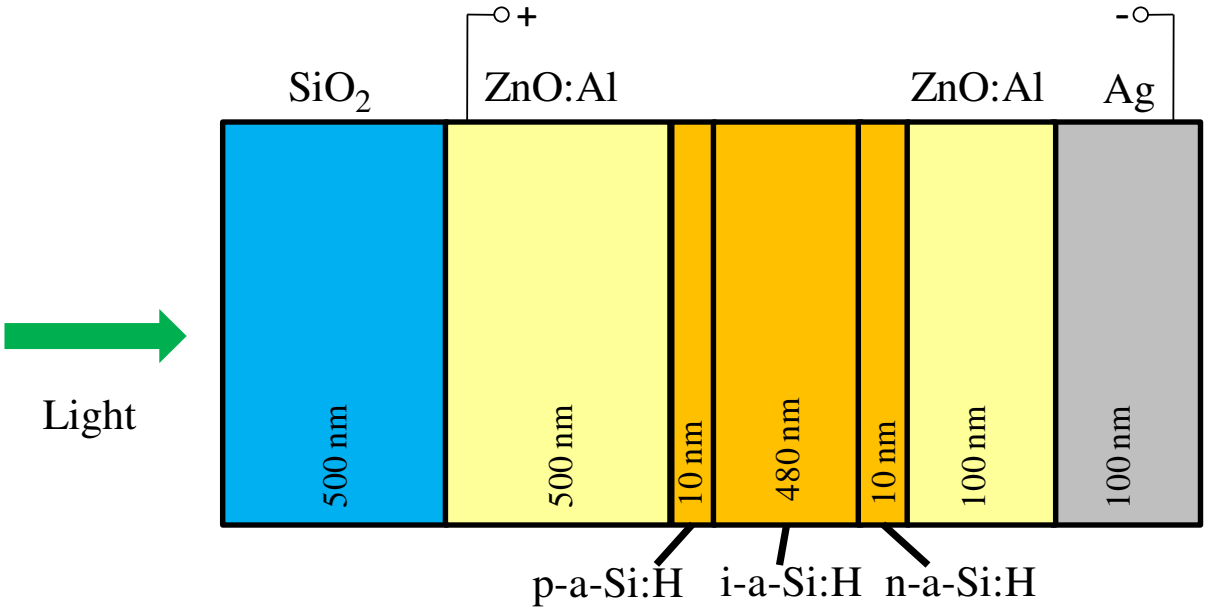

Figure V.5: Structure of the simulated a-Si:H-based single solar cell.

The light enters the device through the silicon dioxide (SiO_2) glass layer used as a transparent superstrate, which ensures the transparency and maintain the mechanical and thermal device stability [149], the layer thickness is about 500 nm. The aluminium-doped zinc oxide (ZnO:Al) TCO layer, acting as a transparent front contact, guarantees the light trapping, the antireflection role, the electrical contact and the charge extraction, its thickness is also about 500 nm. A thin p-type layer (10 nm) follows the TCO layer, then a thicker i-layer (480 nm), and another thin n-type layer (10 nm). The back contact consists of about 100 nm of (ZnO:Al) TCO which improves the light reflection at the back metal layer and so the optical confinement, and about 100 nm of the silver (Ag) conductive layer which acts as reflector for the light non-absorbed through the p-i-n structure, The cell structure as meshed by Silvaco-Atlas is shown in figure V.6.

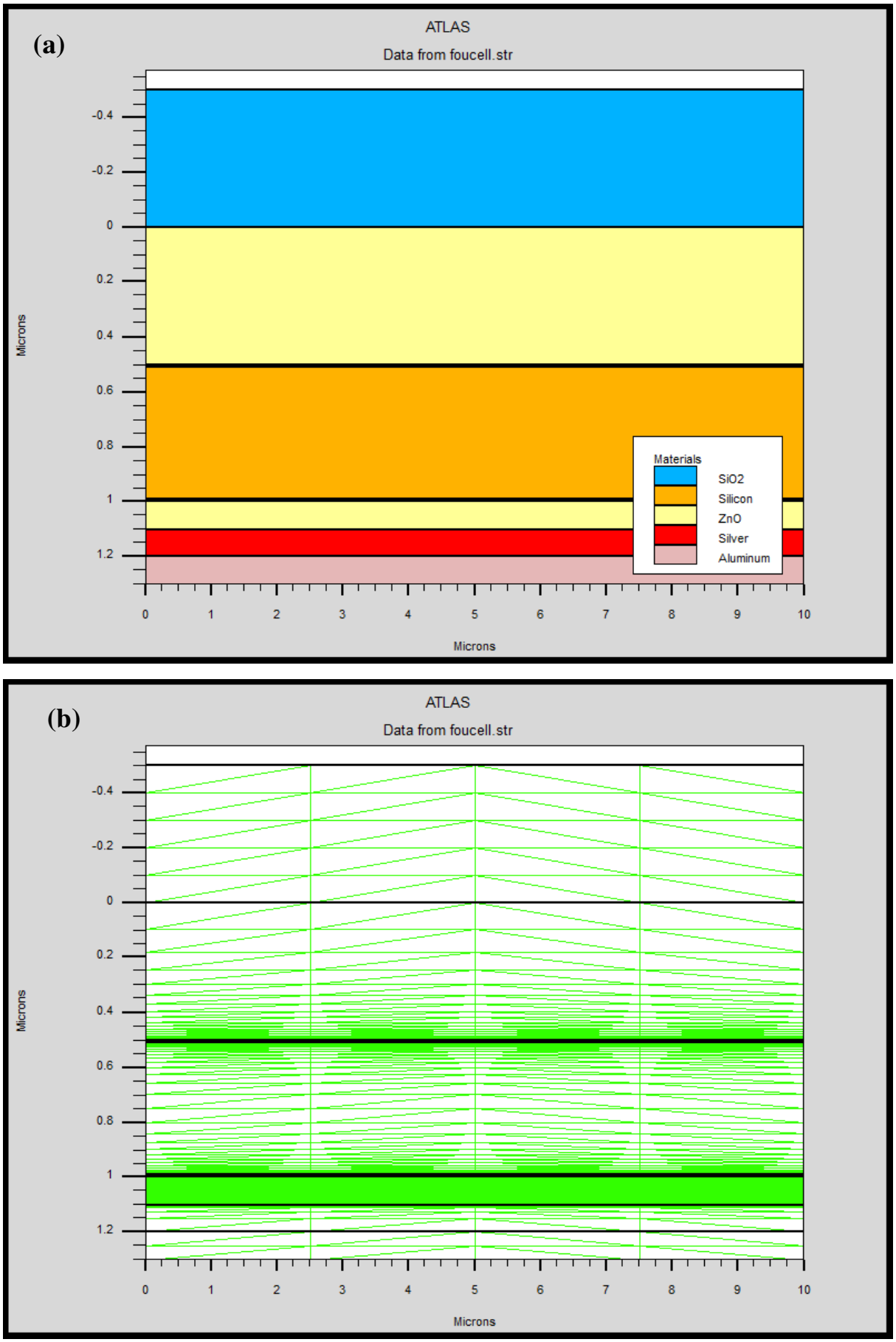

Figure V.6: Structure of the a-Si:H single cell as simulated by Silvaco-Atlas: (a) different regions of the cell, (b) mesh form

The stationary simultaneous solution of Poisson's equation and the hole and electron continuity equations is achieved taking into account the 3-D variation of the defect density of states $D(E)$ resulting from the spatial variation of the Fermi-level position within the energy gap (figure V.7) [136, 137].

Permittivity of SiO_2	3.9
Permittivity of ZnO	8.49
Permittivity of a-Si:H	11.8
Band gap of ZnO (eV)	3.37
Electron affinity of ZnO (eV)	4.5
Electron affinity of a-Si:H (eV)	4.17
p-layer thickness (nm)	10
i-layer thickness (nm)	480
n-layer thickness (nm)	10
Free electron's mobility, μ_n (cm^2/Vs)	20
Free hole's mobility, μ_p (cm^2/Vs)	2
Glass/TCO substrate transmittance	0.9 [25]
TCO/metal contact reflectivity	0.9 [25]

Table V-2: Parameters used for the simulation of the a-Si:H single cell based on references [148], [25] and Silvaco ATLAS database.

The transmittance *T* of the glass/TCO (transparent conductive oxide) substrate and the back reflection *R* of the TCO/metal contact are taken into account. By neglecting the internal multi-reflection of light, the generation rate *G* distribution, in the monochromatic illumination case, is given simply by the following expression:

$$G(x) = T\,\alpha\,\phi\,\left[\exp(-\alpha x) + \mathrm{R}\,\exp\left(-\alpha(2d - x)\right)\right] \quad \text{(V.13)}$$

Where α is the absorption coefficient, ϕ is the photon flux and *d* the thickness of the device.

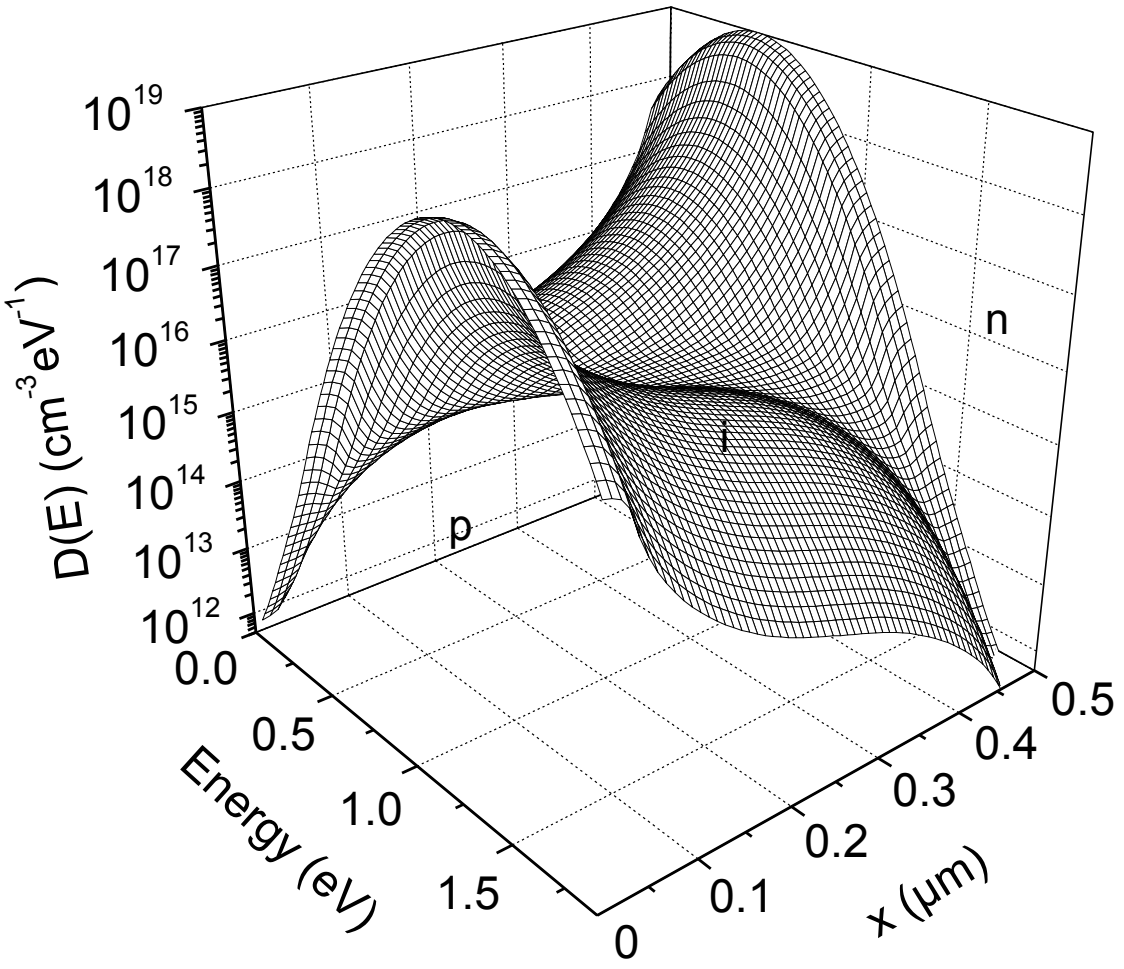

Figure V.7: 3D variation of the defect state density.

V.2.4) Results

The knowledge about the distribution of internal variables is important for the understanding of the changes resulting from the light-induced degradation in the p-i-n device. To simulate the cell behaviour under light-socked condition, the dangling bond density of states in the intrinsic layer (i-layer) has to be raised using AF.Meftah et al model of the light-induced defect increase in the gap states [136, 137] (Figure V.4). As a result of the nonuniform light absorption, therefore non uniform generation, the light-induced increase in the dangling bond density (cm^{-3}) profile occurs inhomogeneously along the device (figure V.8).

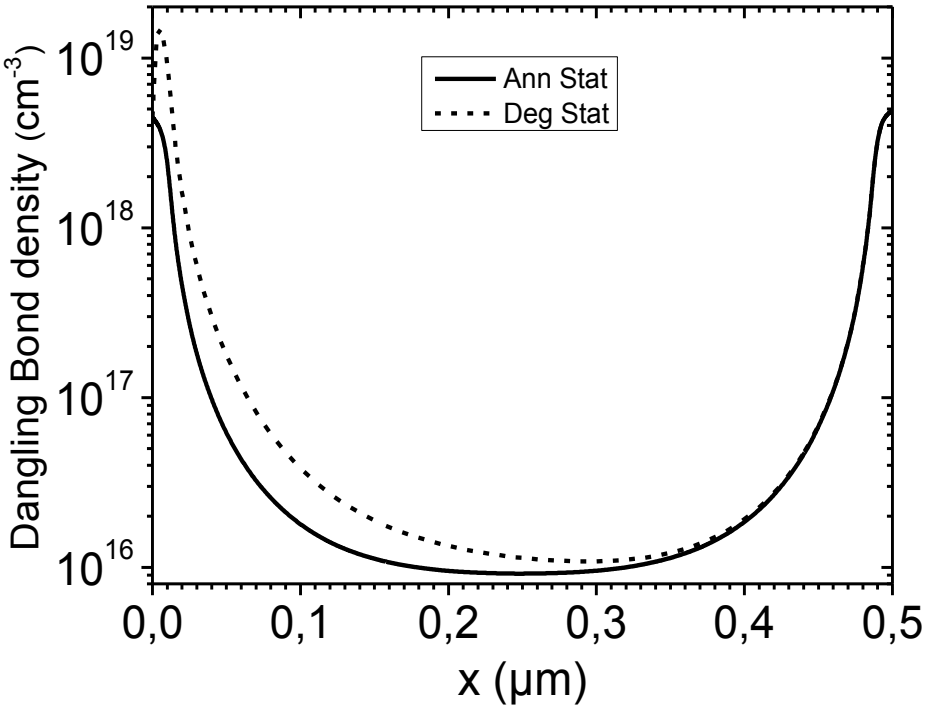

Figure V.8: Dangling bond concentration profiles.

Figure V.9 shows the free electron and hole densities' profiles obtained by simulation under short circuit condition, at the annealed and degraded states.

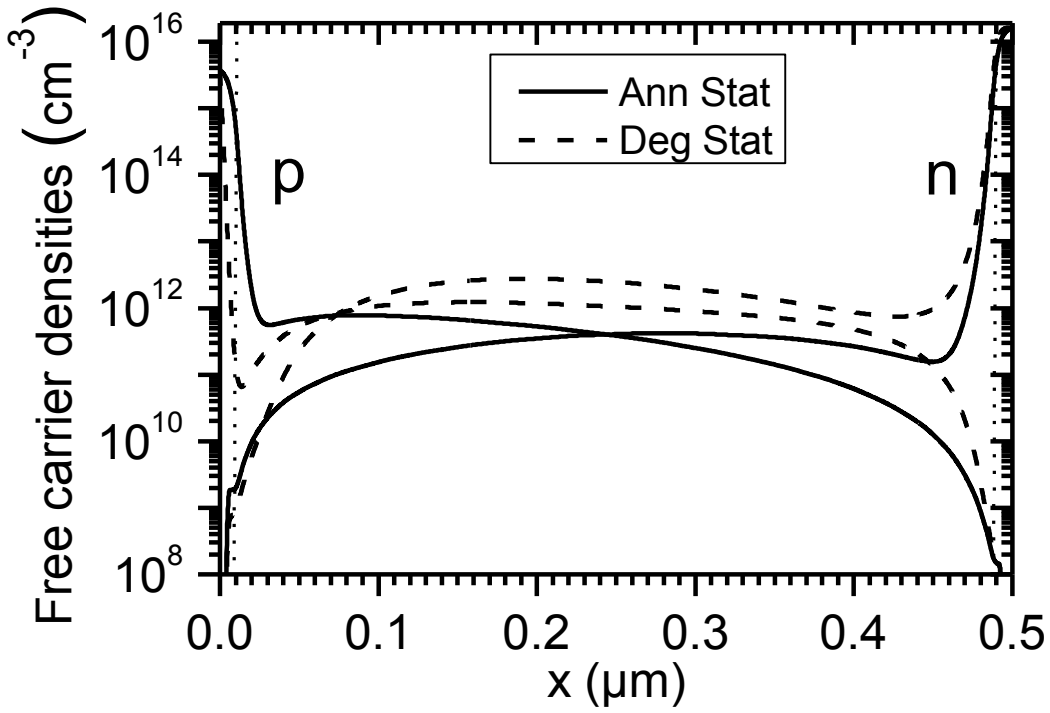

Figure V.9: *n* and *p* density profiles, under short circuit condition.

In the first case, the free hole density (*p*) dominates until 0.23 µm. Afterwards, the free electrons (*n*) become the dominating free charge carriers. In the degraded, state an important decrease in hole density occurs around the p-i interface. This is obvious since the defect density at the p-i interface is nearly 4 times or more great than that of the annealed state. Holes remain the dominating carriers but only until 0.07 µm, then electrons become the dominating free carriers for the remaining part of the device. Moreover, there is a considerable increase of electron and hole densities along the i-layer, which raises the $n.p$ product. However, no further increase of the $n.p$ product is expected at the i-n interface since there are no changes in *n* and *p*, while it decreases certainly at the p-i interface due to the important holes' density decrease in this region.

Figure V.10 shows the recombination rate profile at annealed and degraded states, and the generation rate profile.

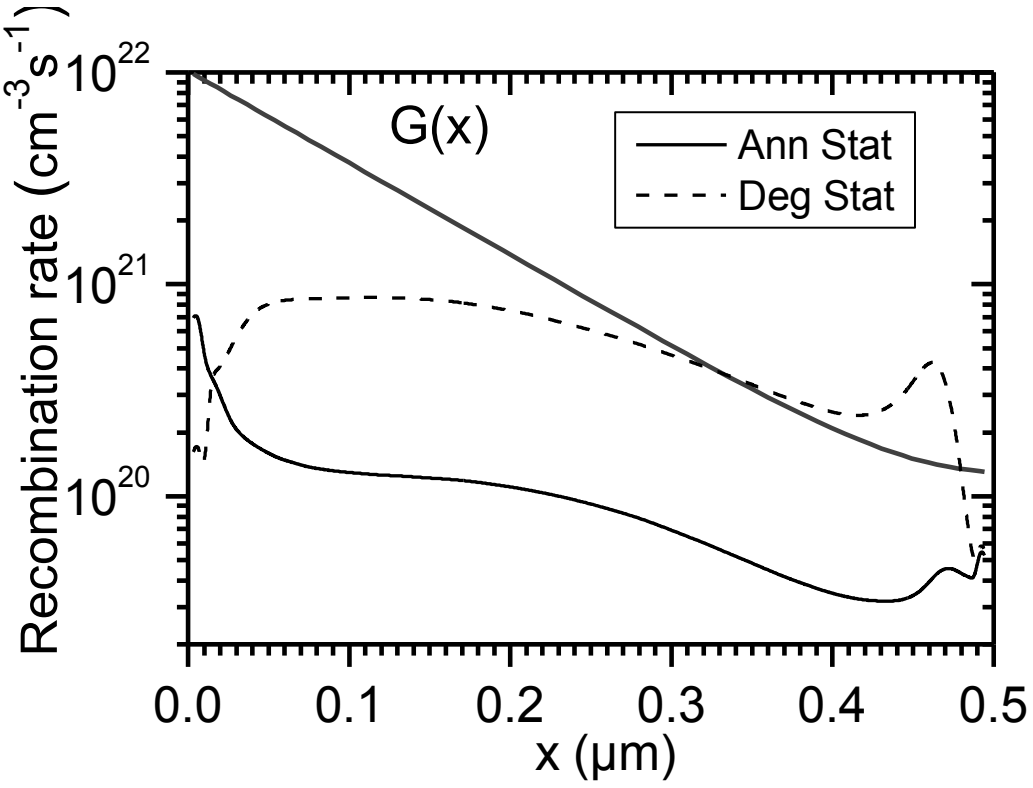

Figure V.10: Generation and recombination rate profiles.

We remark that the recombination rate that was higher at the interface regions in the annealed state decreases in the p-layer and at the p/i interface. This can be attributed to the important decrease of the free hole density in this region. In the rest

of the device there is however an increase in the bulk recombination related mainly to the increase of both *n* and *p* densities, except behind the i/n interface.

In Figure V.11 (a,b) is plotted the trapped charge at the different gap states in the annealed and degraded states.

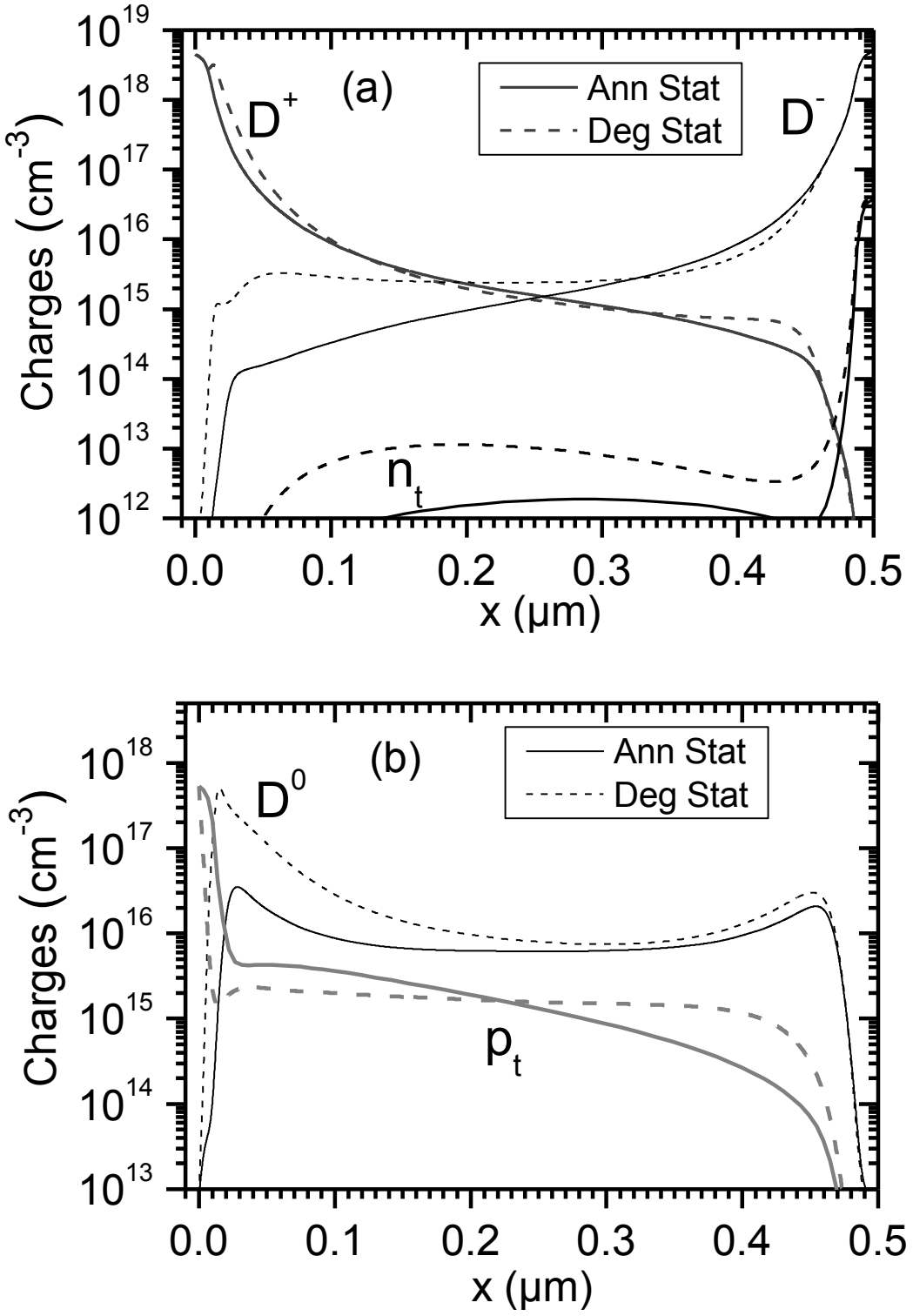

Figure V.11: Trapped charge density profiles in band tails, n_t, p_t, and dangling bonds D^+, D^-, D^0 .

In the first case, the dominating charge in the front of the device is in D^+ (positively charged states of the dangling bond density of states). From 0.1 to 0.23 µm, the charge trapped in the valence band tail (p_t) contributes significantly to the positive charge which dominates in this region. Beyond 0.3 µm, D^- (negatively charged states of the dangling bond density of states) take over as the dominating charged states, which leads to the sign reversal.

In the degraded state, D^- increases from the p-i interface up to 0.3 µm while it decreases slightly between 0.34 and 0.46 µm, p_t decreases from the p-edge to 0.2 µm and increases in the rest of the device, D^+ increases slightly except in the middle of the structure, D^o increases inhomogeneously, similarly to the dangling bond density profile, and finally n_t increases over nearly the totality of the device.

The augmentation of the negative charge in the region where the positive one dominates and vice versa, leads to the diminution of the space charge in the considered regions, and consequently we expect that the electric field also decreases.

Figures V.12 – 15 show, respectively, the band structure, the electric potential, the electric field and the space charge profiles, in both annealed and degraded states.

From figure V.12 (a)-(b), we see clearly that the light-induced defects cause an abrupt band bending near the p-i interface and consequently a very high electric field, while a low electric field in the i-layer is expected. Indeed, these two points are revealed in figures V.13 and V.14. As shown on figure V.13, the potential profile in the degraded state varies strongly around the p-i interface while it becomes nearly constant along the i-layer. Examining figure V.14, showing the electric field profile, we see that the electric field increases from the edges of the device to the interfaces p-i and i-n, then it decreases towards the i-layer. The high interface fields are caused by the large space charge densities in the p and n layers (figure V.11). For the annealed state, if one referred to figure V.15, we find that the depletion regions resulting from the p-i and i-n interfaces meet at the i-layer. In the degraded state, a very high electric field is found indeed at the p-i interface as expected above, while it decays through the i-layer and reaches 300 Vcm^{-1} at 0.3 µm. This means that the depletion regions resulting from the p-i and i-n interfaces are well separated, and the field reverses immediately if a very small voltage bias is applied. The separation of the depletion regions is illustrated by figure V.15 and approves what has been advanced previously when we treated the trapped charge profiles in different gap states.

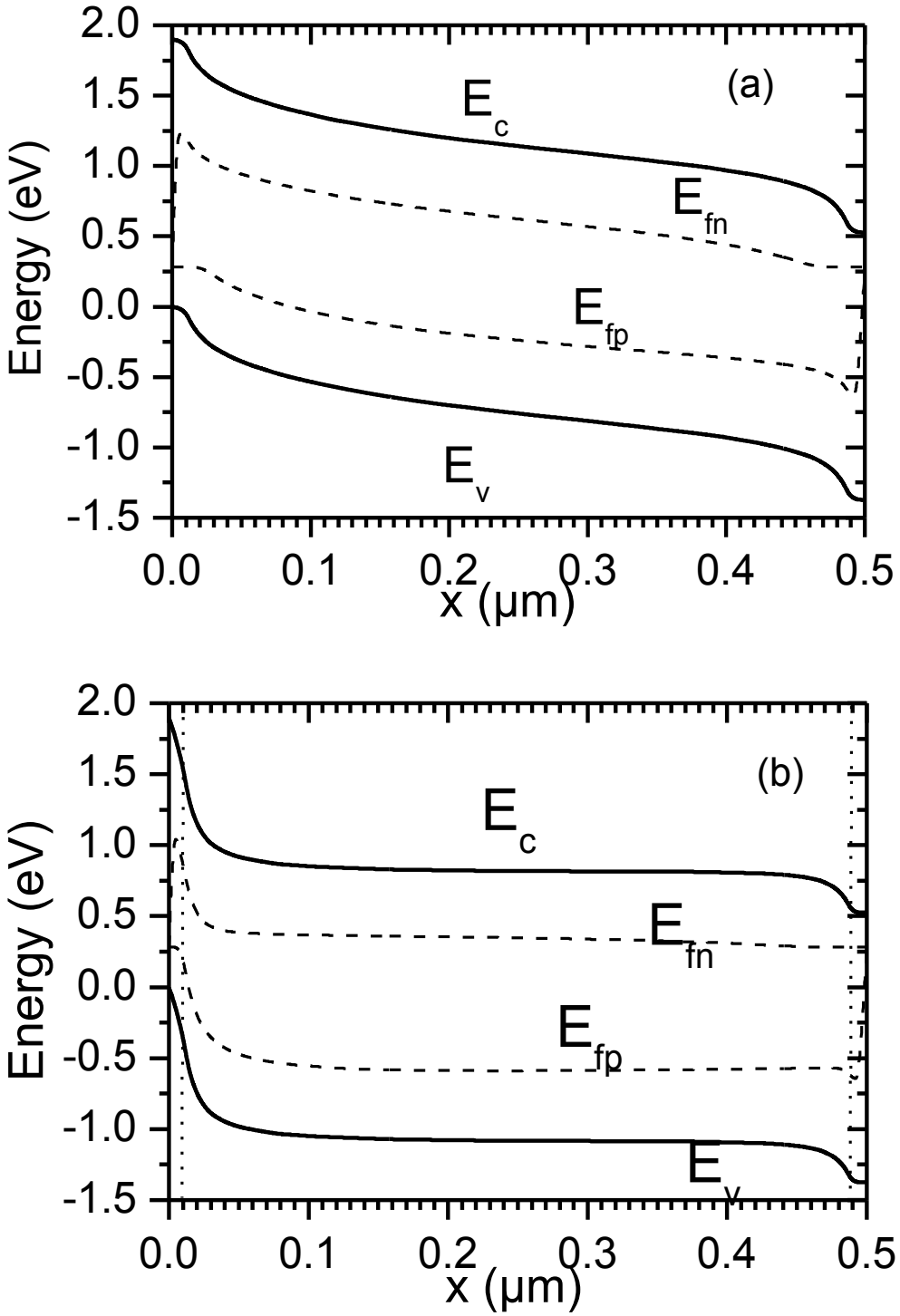

Figure V.12: Gap structure, under short circuit condition, in (a) annealed state, (b) degraded state.

The reduction of the electric field through the i-layer gives reason for the increase of the free carriers in comparison with the annealed state. Then, additional recombination is induced, which was indeed found from the recombination rate profiles (figure V.10).

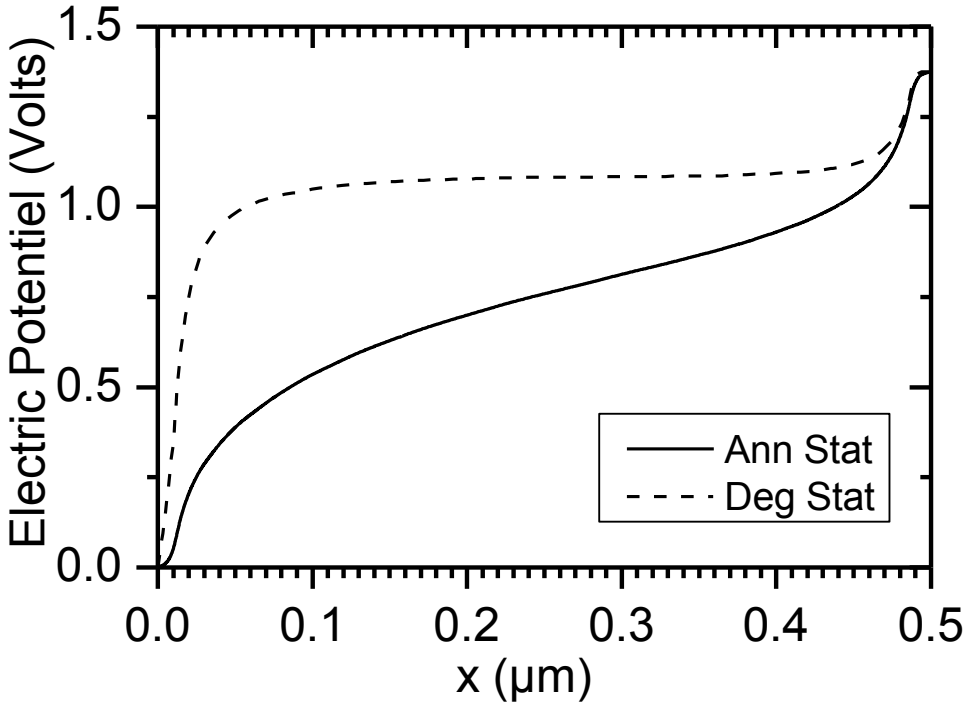

Figure V.13: Electric potential profile, under short circuit condition

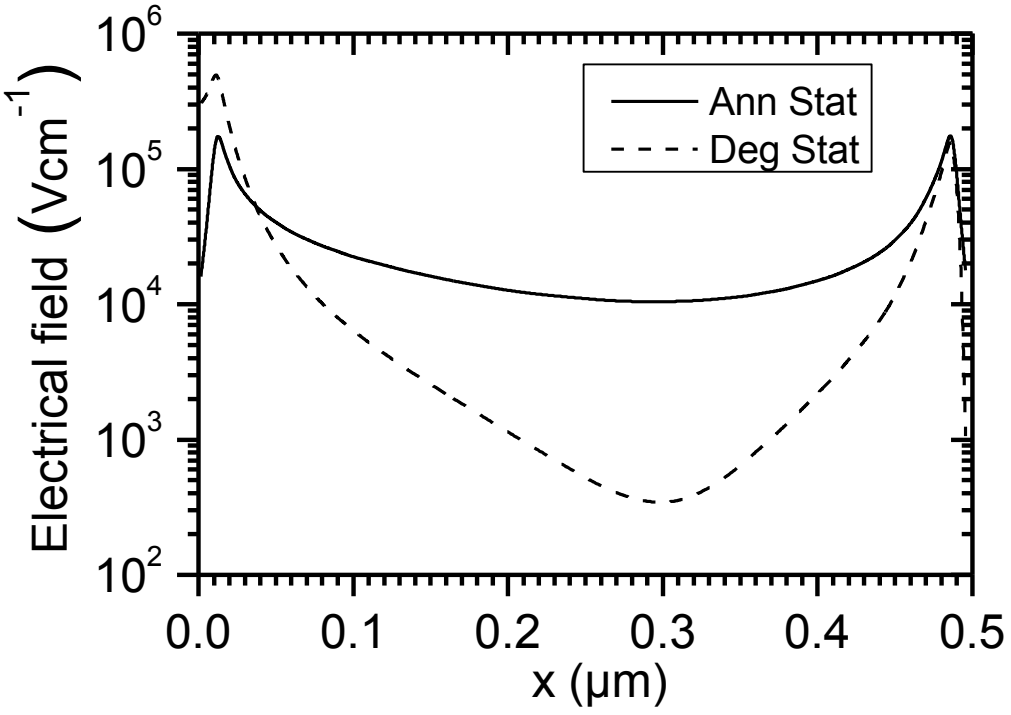

Figure V.14: Electric field profile, under short circuit condition.

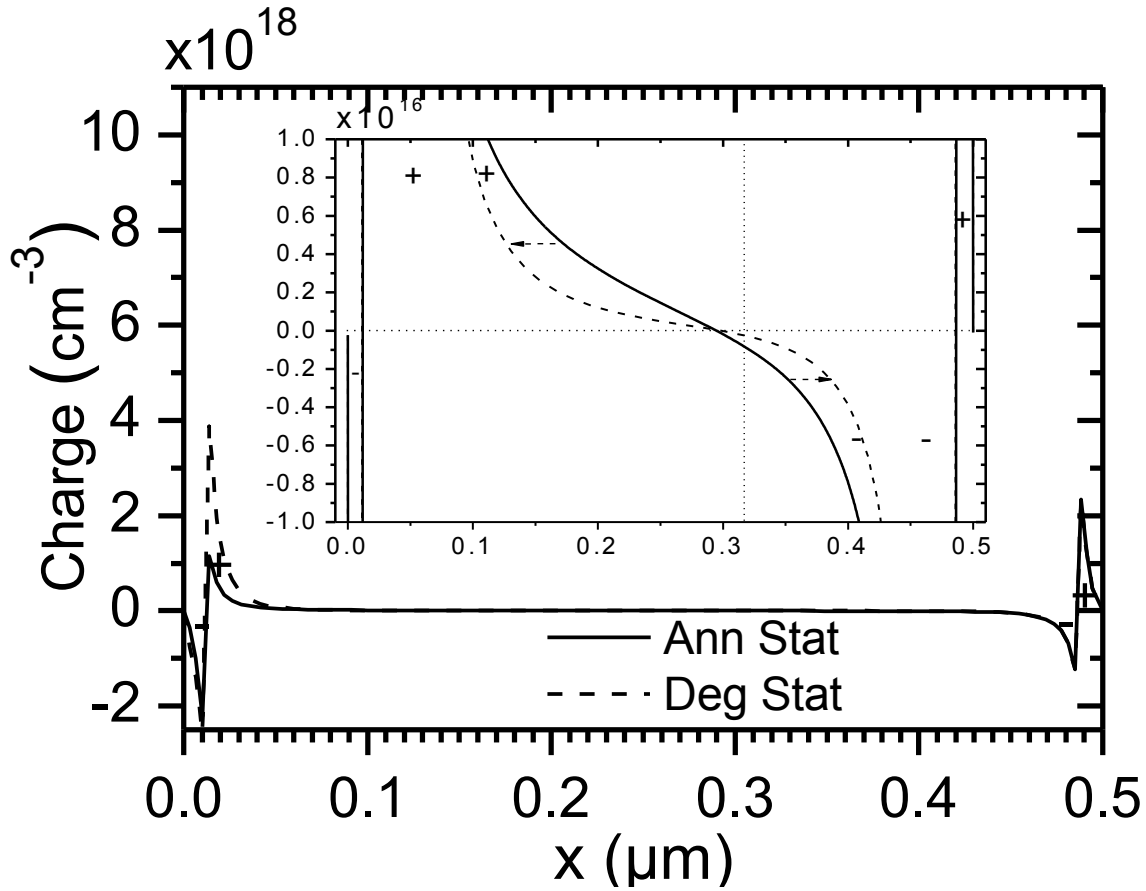

Figure V.15: Space charge profile, under short circuit condition.

Figure V.16 shows electron, hole and total currents densities profiles calculated under short-circuit condition, at annealed and degraded states.

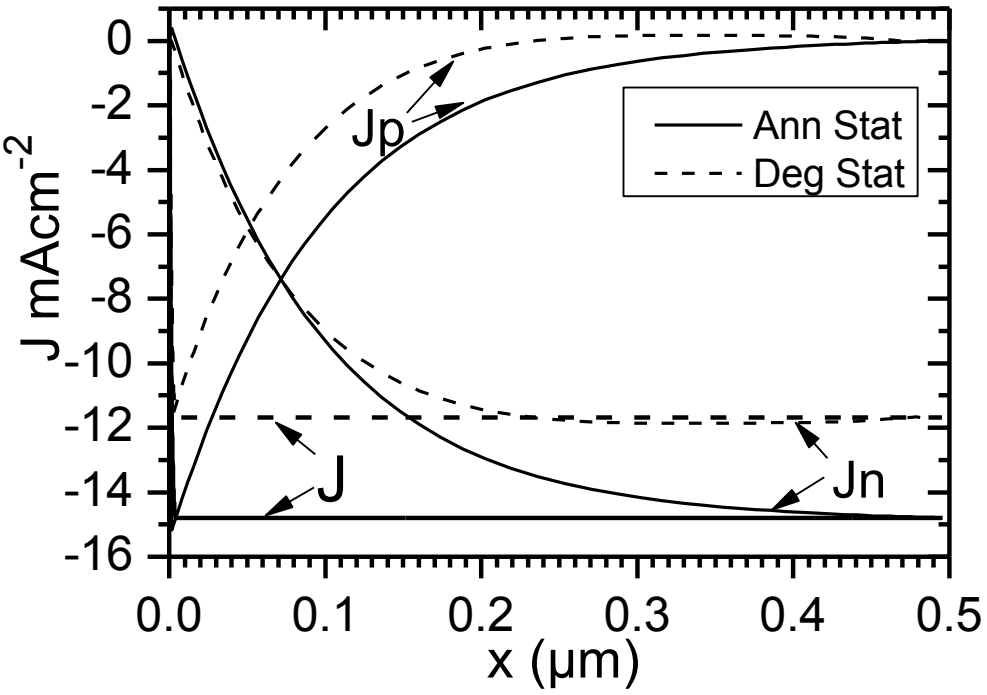

Figure V.16: Electron and hole current densities' profiles.

Comparison of electron and hole currents densities, which are both negative, with the total current density, shows that the current is mainly carried by electrons. Only in the region close to the p-i interface (0.07 µm in the annealed state, 0.05 µm in the degraded one), where the holes concentration is much higher than that of electrons, the hole current density constitutes the total current density. The degradation of the electron and the hole current densities is clearly shown and causes the decrease of the total current density from 14.79 $mAcm^{-2}$ to 11.68 $mAcm^{-2}$. Moreover, we remark a very weak decrease in both electron and hole current density profiles from 0.44 µm at the degraded state. This is explained by the recombination rate which exceeds locally the generation rate as it can be seen if one referred again to figure V.10.

In order to analyse in more details the transport mechanism, in figure V.17 (a)-(d), electrons and holes currents densities are separated into drift and diffusion components. For both annealed and degraded states, the majority carriers current densities compete between drift and diffusion in the very front of the sample (close to the p-i interface) as in the back (close to the i-n interface). In the very front of the sample the hole current, mainly drift current (since the hole current density is negative as the drift one), dominates. Similar results hold for electrons in the back of the device. We note here that an exception in the degraded state is found for holes at the p-i interface, where there is a large decrease of free hole density, which are captured by the high D^+ density, compared to the annealed state (figure V.9). Consequently, the hole-diffusion current density decreases significantly and the transport process remains drift-dominated in this region.

Throughout the i-layer, for electrons as for holes, the drift current density (negative) is the dominant partial current density in the annealed state, for which the electric field strength is high in the active region. However, the competition between the drift and diffusion current densities persists in the degraded state. The region where the diffusion current density dominates the electric field is low, weakening thus the drift current density.

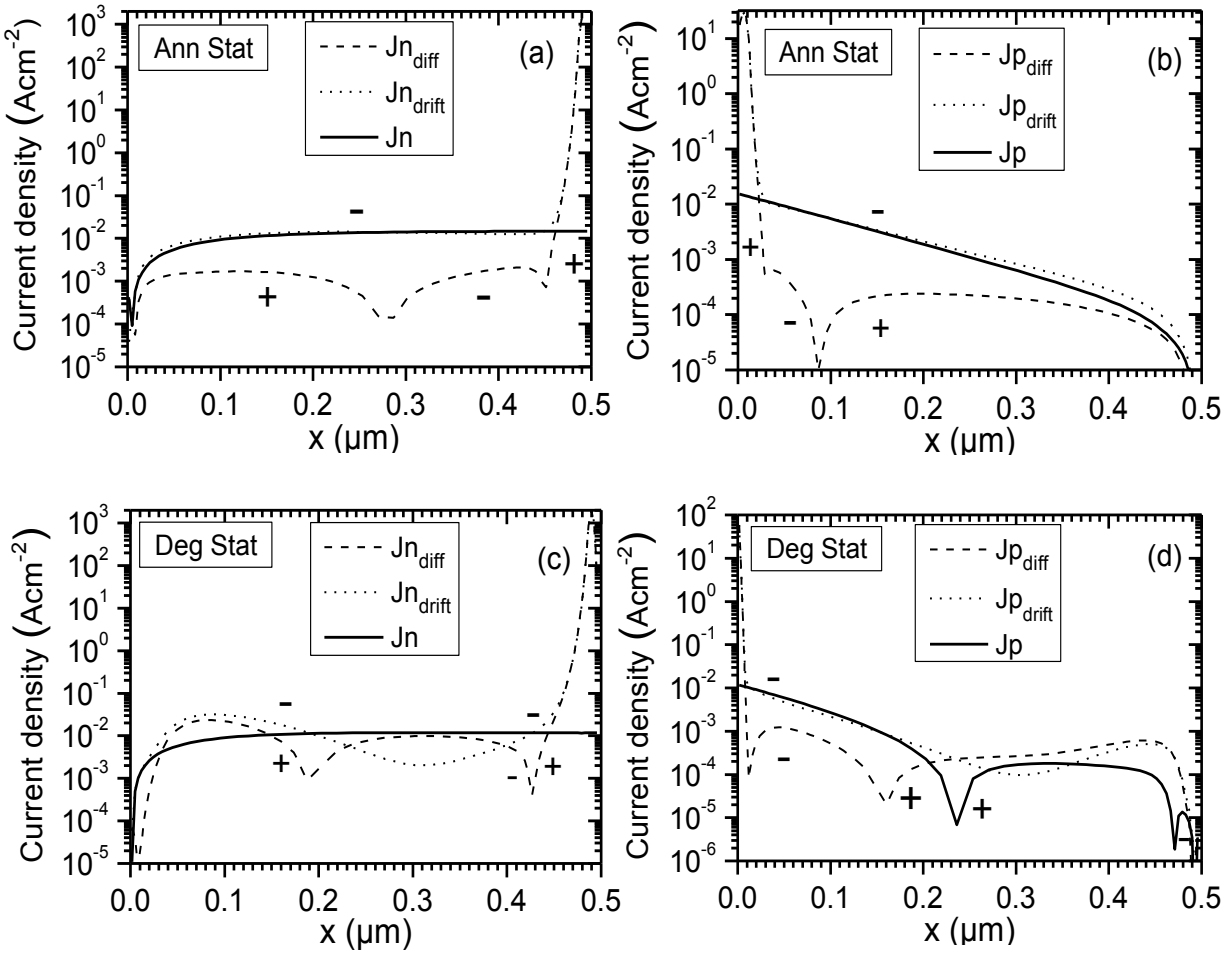

Figure V.17: (a) Drift- and Diffusion-electron current density profiles in annealed state, (b) Drift- and Diffusion-hole current density profiles in annealed state, (c) Drift- and Diffusion-electron current density profiles in degraded state, (d) Drift- and Diffusion-hole current density profiles in degraded state.

In Figures V.18-V.19 is presented, respectively, the calculated current density J and the power density P provided by the cell, as a function of bias voltage under illumination; results are given for the annealed and the different degradation states. The degradation of the current density-voltage ($J-V$) and the power density-voltage ($P-V$) curves is clearly observed with an increasing number of dangling bonds, distributed inhomogeneously in the sample.

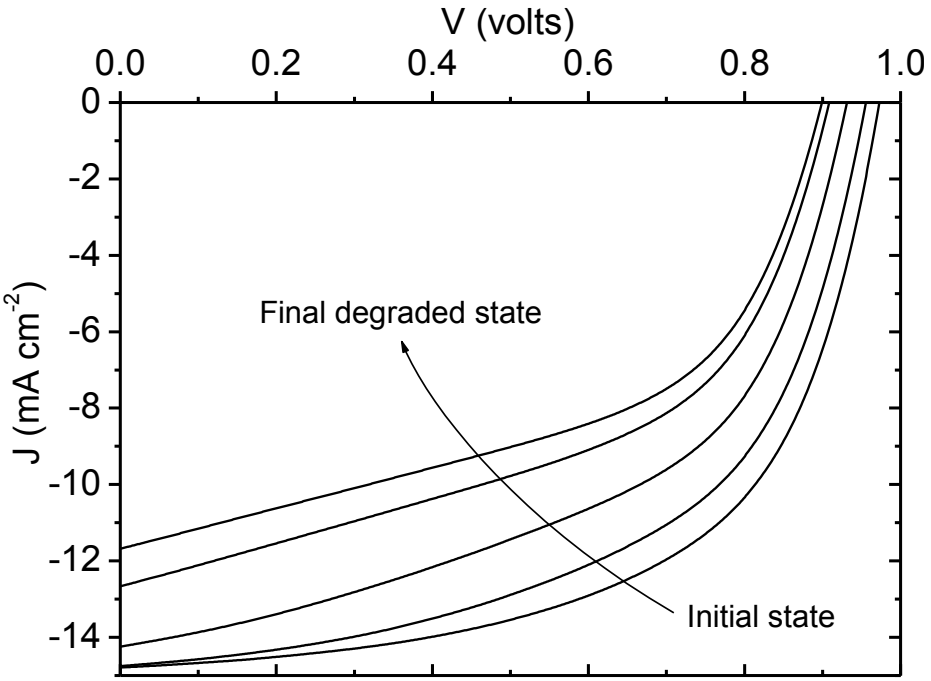

Figure V.18: $J-V$ characteristic degradation.

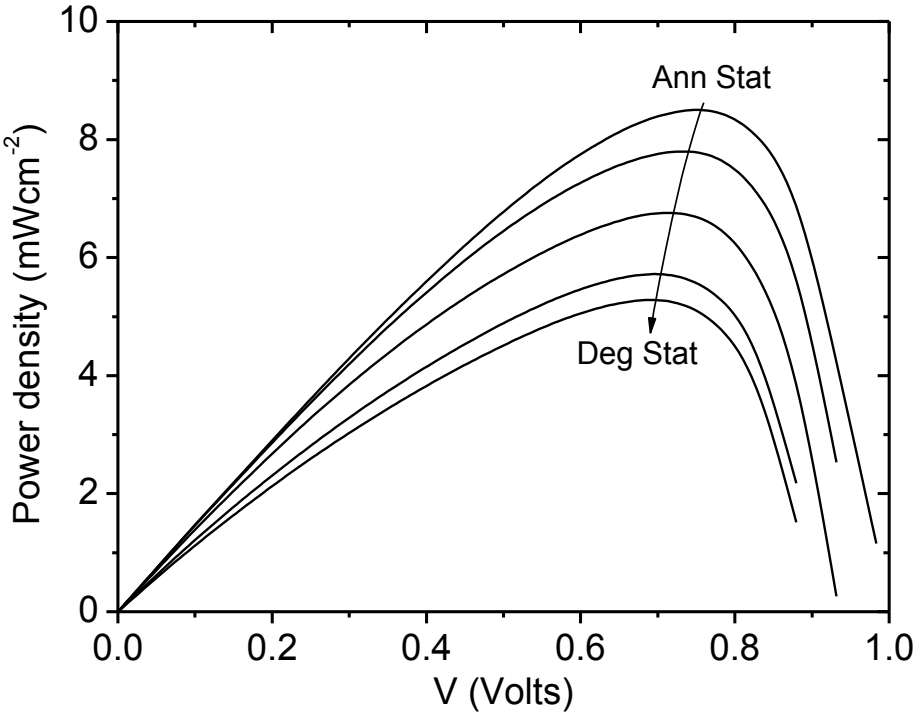

Figure V.19: $P-V$ characteristic degradation

In figure V.20 (a)-(d), the degradation effect is shown on the cell output parameters; where J_{sc}, V_{oc}, FF and P_{max} are plotted against the $N_d(t)/N_d(0)$ ratio. We remind that $N_d(t)$ is the dangling bond defect concentration in the sample at the different illumination times, t, and $N_d(0)$ is the initial (annealed) concentration of the dangling bonds.

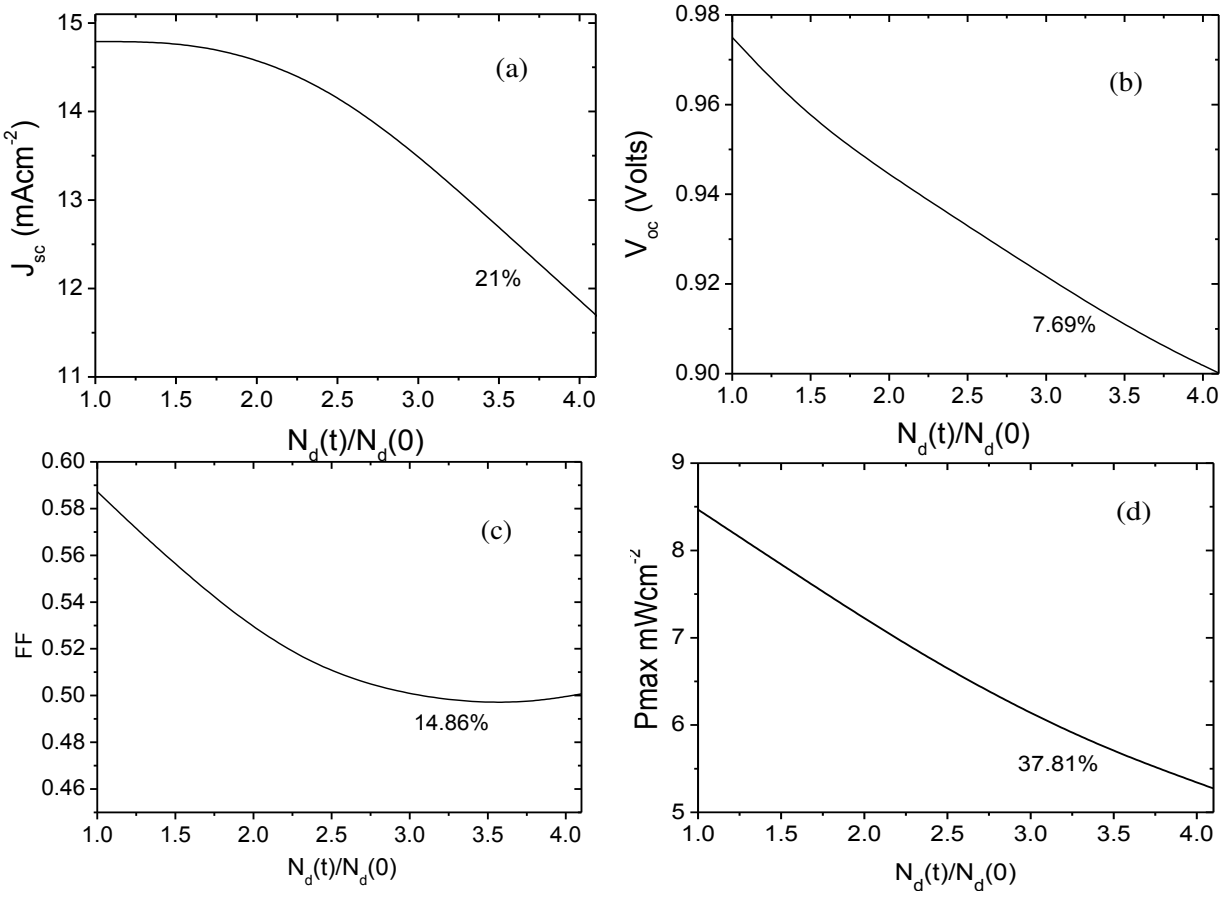

Figure V.20: Solar cell output parameters versus $N_d(t)/N_d(0)$ ratio. (a) J_{sc}, (b) V_{oc} (c) FF, and (d) P_{max}.

From these figures, J_{sc} exhibits a degradation of 21%, while V_{oc} decreases only by 7.69%, FF which is related to the curvature of the $J-V$ characteristic shows a considerable degradation of 14.72% and P_{max} which reflects the cell conversion efficiency, degrades by 37.81%. These results indicate that V_{oc} is the less sensitive parameter to the variation of the dangling bond density. However, P_{max} is the most affected parameter by degradation since it depends on the maximum current density and the maximum voltage, which are both affected by degradation.

Table V.3 summarizes the photodegradation effect on the output parameters of the cell, and also the effect of increasing the free carrier mobilities μ_n and μ_p, given in more details in previous work [23].

μ_n/μ_p 20/2	J_{sc} (mAcm^{-2})	V_{oc} (V)	*FF*	P_{max} (mWcm^{-2})	μ_n/μ_p 25/6	J_{sc} (mAcm^{-2})	V_{oc} (V)	*FF*	P_{max} (mWcm^{-2})
Ann stat	14.79	0.975	0.58	8.46	*Ann stat*	15.08	0.972	0.652	9.65
Deg stat	11.68	0.9	0.50	5.27	*Deg stat*	14.5	0.915	0.56	7.43
	ΔJ_{sc} %	ΔV_{oc} %	ΔFF %	ΔP_{max} %		ΔJ_{sc} %	ΔV_{oc} %	ΔFF %	ΔP_{max} %
	-21	-7.69	-14.86	-37.81		-4.11	-5.86	-14.27	-22.61

Table V-3: The solar cell output parameter degradation when μ_n/μ_p= 20/2 (cm^2/Vs) and μ_n/μ_p= 25/6 (cm^2/Vs).

For a good solar cell, a fill factor of more than 0.65 can be expected. In the case μ_n/μ_p=20/2 of table V.3, the FF is relatively low because the dangling bond density of states is calculated before the degradation according to the defect pool model improved by Powell and Deane [15]. The presence of the doubly hydrogenated weak SiSi bond (SiHHSi) configuration [6,13] , the hydrogen diffusion, and the carrier life time much shorter than the transit time (when there is no applied reverse bias as in a-Si:H solar cell case); all this contributes to make recombination governing the behaviour of the device, and a relatively low fill factor can be expected. However, the value 0.58 for the FF stays better than other simulation works which used the defect pool model; as an example we can refer to values of ~ 0.4 - 0.425 obtained in W. Gao works [24]. We also indicate that the value 0.58 for the FF remains in the experimental range as notified in many works [25, 26, 27] realised with conditions close to those of the current result. Although the fill factor is relatively low, the short - circuit current density has an improved value in the annealed state.

Finally, table V.4 presents the solar cell output parameters at the annealed and degraded state, obtained under the global standard solar spectrum (AM1.5) illumination and using for the absorption coefficient, the measured data corresponding to the full spectrum AM 1.5 given in reference [28]. Relatively to the monochromatic light case, a pretty increase is notified in the short-circuit current density and so in the maximum power density provided by the cell for both cases; annealed and degraded state.

μ_n/μ_p=20/2	J_{sc} (mAcm^{-2})	V_{oc} (V)	*FF*	P_{max} (mWcm^{-2})
Ann stat	16.73	0.975	0.58	9.46
Deg stat	12.63	0.9	0.50	5.68

Table V-4: The solar cell output parameters under the full solar spectrum (AM1.5) illumination in the annealed and degraded state.

V.3) Thickness effect on a-Si:H and µc-Si:H-based solar cell performance.

We study, in this part, the effect of the i-layer thickness on the performance parameters of the p-i-n solar cell based on a-Si:H and µc-Si:H, and of the micromorph (a-Si:H/ µc-Si:H) tandem cell with 2T and 4T electrical connections, respectively. Assuming the standard global solar spectrum (AM1.5G) illumination with 100 mW/cm^2 total incident power density and 25°C ambient temperature, both un-degraded state and the light-soaked one are taken into account.

The i-layer thickness of both (a-Si:H) single cell and the top sub-cell of the micromorph tandem cell is varied in the range 0.05 µm- 0.5 µm. However, the i-layer thickness of both (µc-Si:H) single cell and the bottom sub-cell of the micromorph tandem cell is changed in the range 0.5 µm – 5 µm. Thickness effect is investigated on the device performance parameters such as the current density- voltage ($J-V$) characteristics, the short-circuit current density (J_{sc}), the open-circuit voltage (V_{oc}), the fill factor (FF), the efficiency (η) and the external quantum efficiency (EQE).

V.3.1) Device structure and input parameters

The different simulated solar cells: a-Si:H and µc-Si:H-based single cells, and the micromorph tandem cell with 2T and 4T connections, are shown in figures V.21 and V.22 respectively.

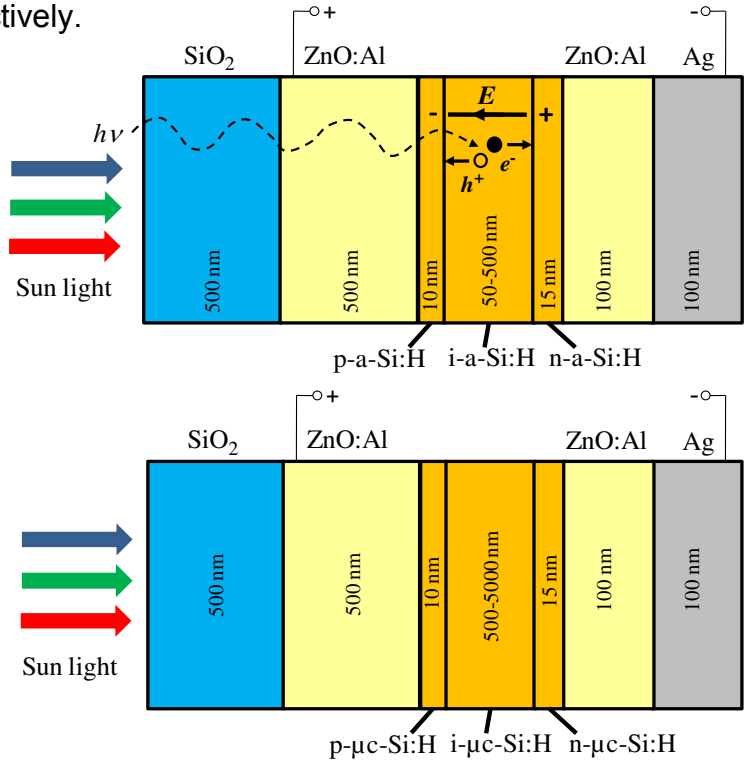

Figure V.21: The simulated a-Si:H and µc-Si:H-based single cells.

A 500nm (SiO_2) glass layer, as a transparent superstrate, guarantees the transparency and maintain the mechanical and thermal device stability [ref8]. A 500nm (ZnO:Al) TCO layer, as a transparent front contact, ensures the light trapping, the antireflection role, the electrical contact and the charge extraction. The semiconductor layers are then deposited in sequence p-i-n; about 10 nm for p-type and n-type layers, the i-layers are much thicker (50-500 nm for a-Si:H and 500-5000nm for µc-Si:H). The back contact consists of about 100 nm of (ZnO:Al) TCO which improves the optical confinement and the light reflection at the back metal layer, and about 100 nm of the silver (Ag) conductive layer which acts as reflector for the light non-absorbed through the p-i-n structure.

Excess electrons are actually provided from the n-type layer to the p-type layer, leaving the layers positively and negatively charged (respectively), and creating a considerable "built-in" electric field (E) (typically more than 10^4 V/cm [150]). Sunlight enters the solar cell as a flux of photons that pass through the p-type layer. Most of the photons, which are absorbed in the much thicker i-layer, will generate electron and hole photocarriers [151, 152]. The photocarriers are swept away by the built-in electric field to the n-type and p-type layers, respectively, generating consequently solar electricity.

The 2T micromorph tandem solar cell (figure V.22) consist of a glass (500nm)/ZnO:Al (500nm) superstrate, a thin (10nm) Indium-tin oxide (ITO) layer as an intermediate reflector (IR) and a ZnO (100nm)/Ag (100nm) back reflector. The respective band-gaps of the a-Si:H top sub-cell and the µc-Si:H bottom sub-cell are approximately 1.7eV and 1.16eV, which is nearly optimal for a dual-junction tandem cell operating under the AM 1.5 solar irradiance. In the 4T micromorph tandem cell configuration, the two sub-cells are separated by SiO_2 glass layer (500 nm) an insulating material.
The input parameters used to simulate the different solar cell structures are listed in tables V.5 et V.6 respectively.

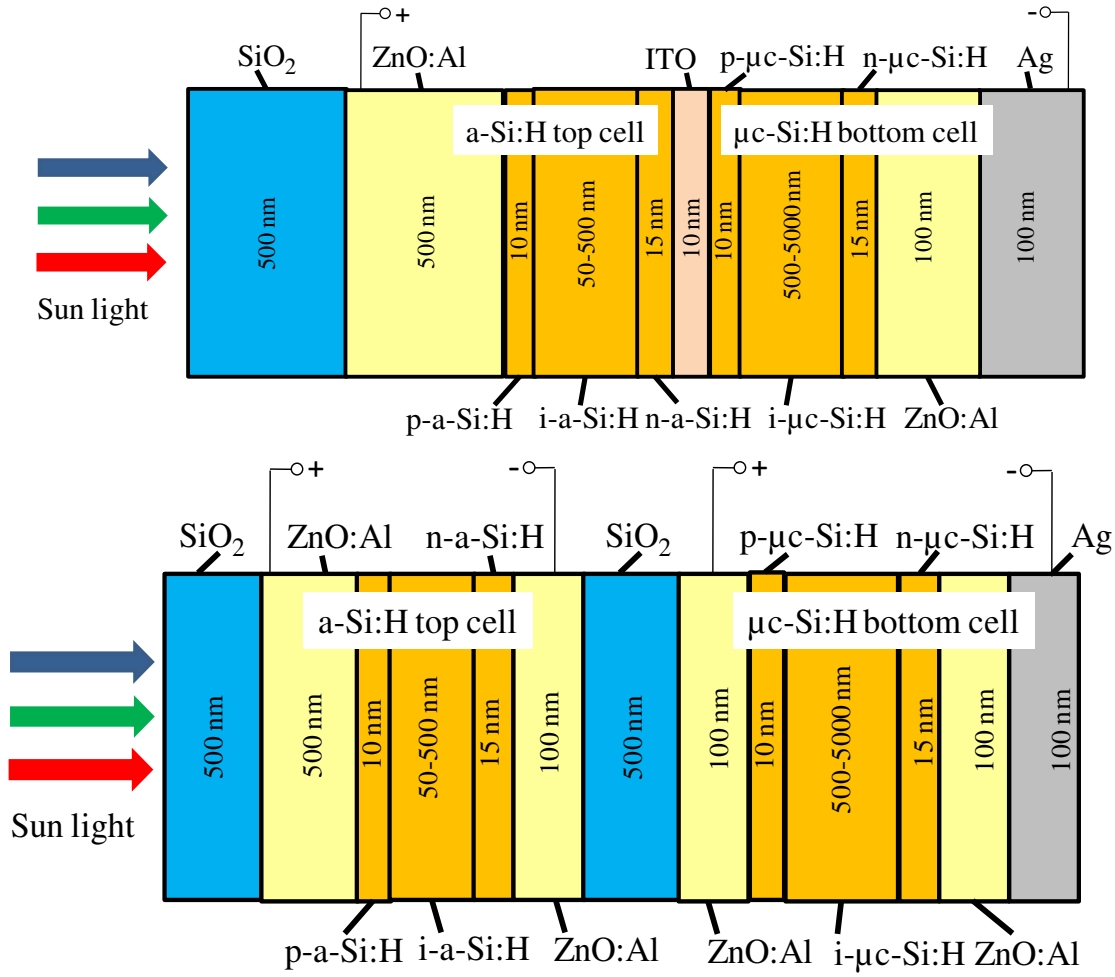

Figure V.22: The simulated micromorph tandem cells with 2T and 4T electrical connections respectively.

Permittivity of SiO_2	3.9
Permittivity of ZnO	8.49
Permittivity of a-Si:H	11.8
Permittivity of µc-Si:H	11.8
Electron affinity (eV) of ZnO	4.5
Electron affinity (eV) of a-Si:H	4.17
Electron affinity (eV) of µc-Si:H	4.17
Band gap (eV) of ZnO	3.37
Band gap (eV) of a-Si:H	1.7
Band gap (eV) of µc-Si:H	1.16
p-type region doping concentration (cm^{-3})	10^{20}
a-Si:H i-type region doping concentration (cm^{-3})	1×10^{12}
µc-Si:H i-type region doping concentration (cm^{-3})	1×10^{12}
n-type region doping concentration (cm^{-3})	10^{20}
Effective density of states in conduction band at 300°K, $N_{C,300}$(cm^{-3})	3×10^{20}
Effective density of states in valence band at 300°K, $N_{V,300}$(cm^{-3})	3×10^{20}
Electron mobility of a-Si:H doping layers (cm^2/V.s)	1
Hole mobility of a-Si:H doping layers (cm^2/V.s)	0.1
Electron mobility of a-Si:H i-type layer (cm^2/V.s)	2

Hole mobility of a-Si:H i-type layer (cm^2/V.s)	0.2
Electron mobility of µc-Si:H doping layers (cm^2/V.s)	5
Hole mobility of µc-Si:H doping layers (cm^2/V.s)	0.5
Electron mobility of µc-Si:H i-type layer (cm^2/V.s)	15
Hole mobility of µc-Si:H i-type layer (cm^2/V.s)	2

Table V-5: Parameter used to simulate the different solar cell structures, based on references [123, 148, 153-155].

VALENCE BAND TAIL STATES		
	a-Si:H	**µc-Si:H**
Density of donor-like valence band tail states, N_{TD} (cm^{-3})	2×10^{20}	5×10^{19}
Valence band tail characteristic energy, W_{TD} (eV)	0.055	0.020
Hole capture cross section of valence band tail, σ^0_{pTD}, (cm^2)	5×10^{-16}	5×10^{-16}
Electron capture cross section of valence band tail , σ^+_{nTD}, (cm^2)	10^{-15}	10^{-15}

CONDUCTION BAND TAIL STATES		
	a-Si:H	**µc-Si:H**
Density of acceptor-like conduction band tail states, N_{TA} (cm^{-3})	2×10^{20}	5×10^{19}
Conduction band tail characteristic energy, W_{TA} (eV)	0.028	0.010
Electron capture cross section of conduction band tail, σ^0_{nTA} (cm^2)	5×10^{-16}	5×10^{-16}
Hole capture cross section of conduction band tail, σ^-_{pTA} (cm^2)	10^{-15}	10^{-15}

DANGLING BOND STATES	
	a-Si:H
Pool peak position E_P (eV)	1.27
Pool width σ (eV)	0.19
Defect electron correlation energy, U (eV)	0.2
Valence band tail width, E_{vo} (eV)	0.055
Effective density of states at E_v, N_{vo} (cm^{-3})	2×10^{20}
Total hydrogen concentration H (cm^{-3})	5×10^{21}
Total electron concentration N_{sisi} (cm^{-3})	2×10^{23}
Defect state density freeze-in temperature T^* (°K).	500
Annealed i-layer density of states (cm^{-3})	1×10^{16}
Degraded i-layer density of states (cm^{-3})	4×10^{16}
Electron capture cross section of neutral defect states, σ^0_n (cm^2)	5×10^{-15}
Hole capture cross section of neutral defect states, σ^0_P (cm^2)	5×10^{-15}
Electron capture cross section of positive defect states, σ^+_n (cm^2)	10^{-14}
Hole capture cross section of negative defect states, σ^-_P (cm^2)	10^{-14}

Table V-6: The parameters used for the a-Si:H and µc-Si:H density of state models based on [40, 136, 137, 145, 148, 153, 154].

Figures V.23 and V.24 show the tandem cell structure, with 2T and 4T connections respectively, as meshed by Silvaco-Atlas. For this example, thicknesses of a-Si:H top i-layer and µc-Si:H bottom i-layer are respectively 0.2 µm and 2.5 µm.

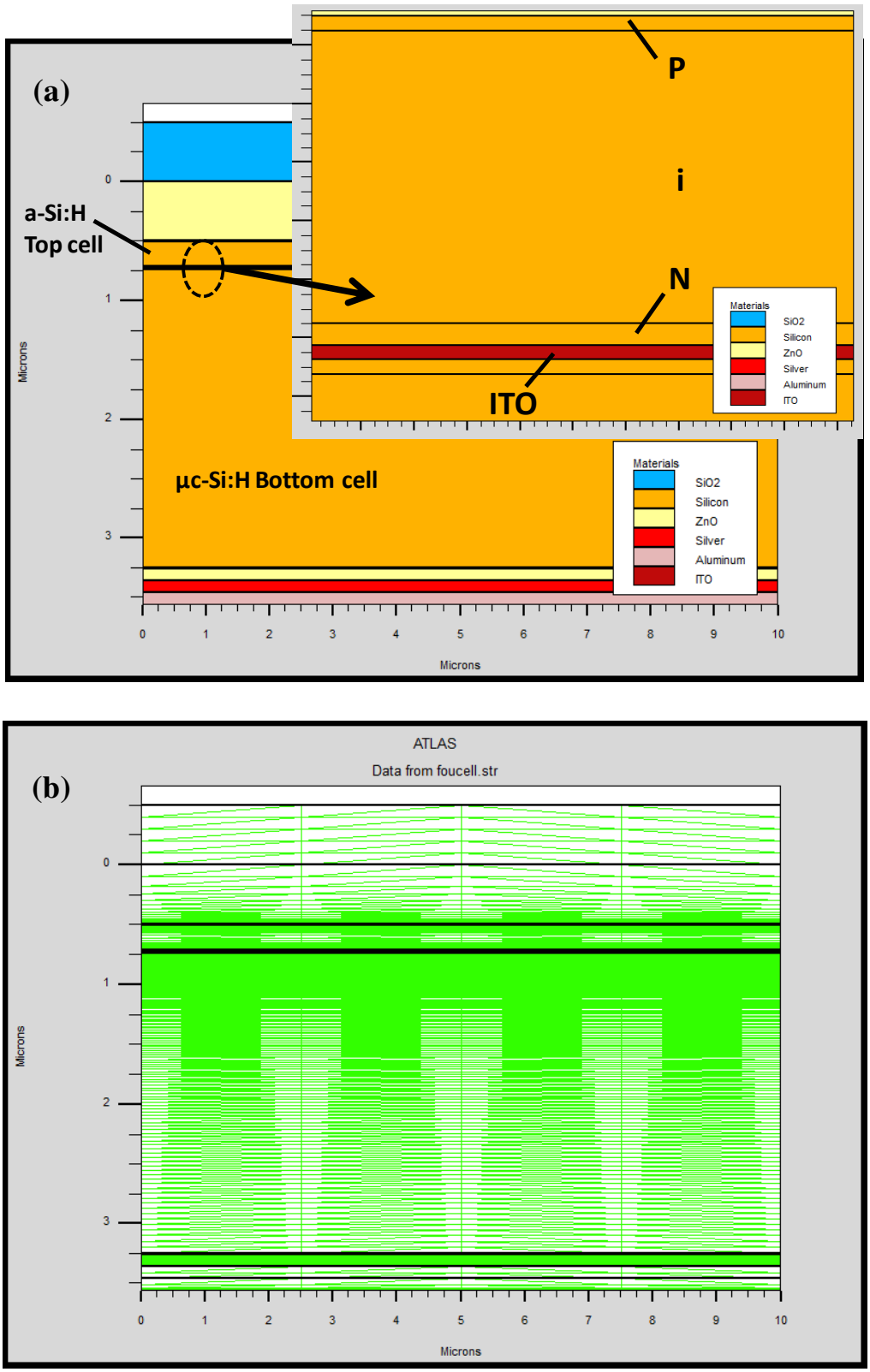

Figure V.23: Structure of the 2T-micromorph tandem cell as simulated by Silvaco-Atlas: (a) different regions of the cell, (b) mesh form.

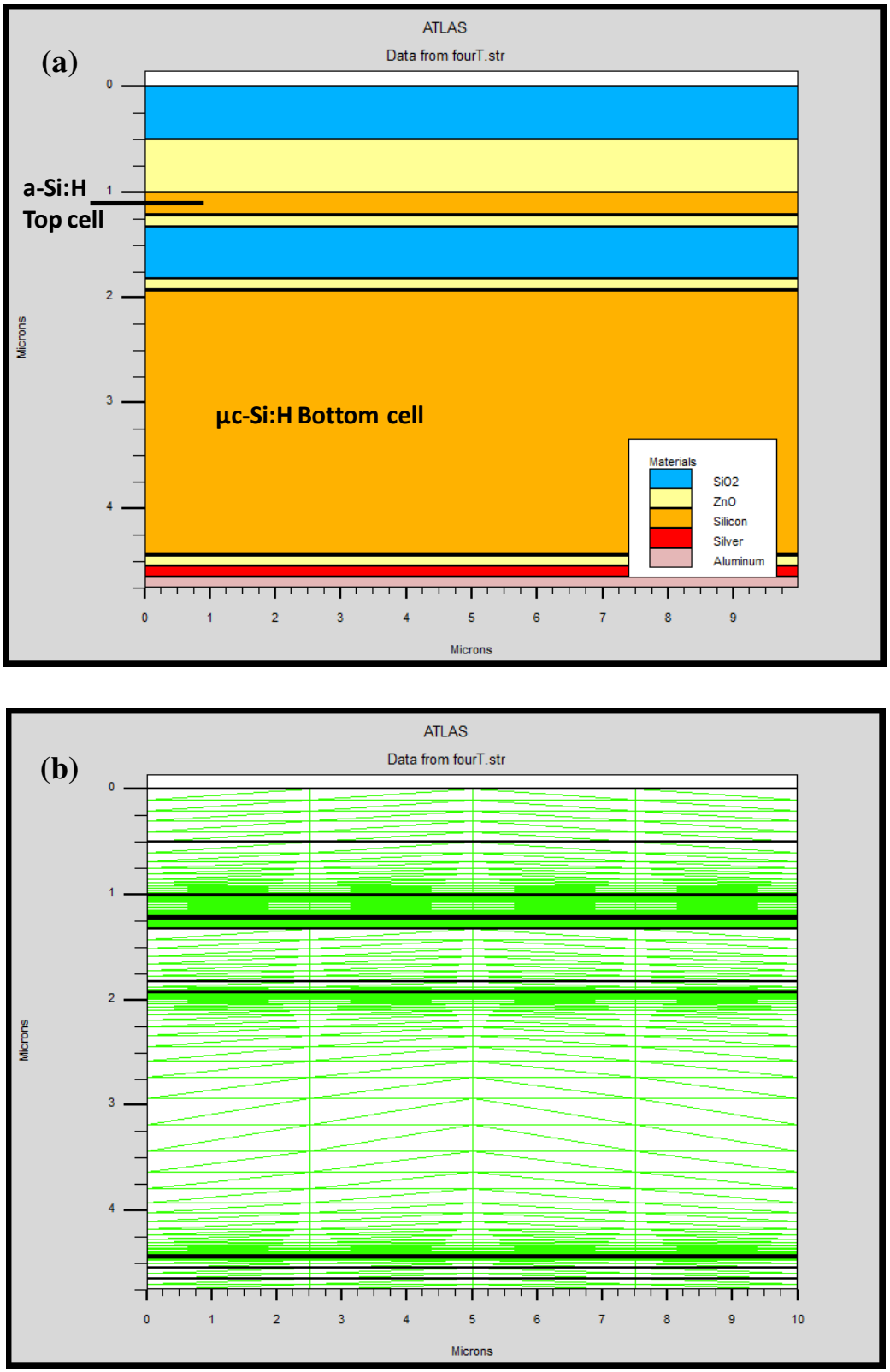

Figure V.24: Structure of the 4T-micromorph tandem cell as simulated by Silvaco-Atlas: (a) different regions of the cell, (b) mesh form.

V.3.2) Optical model

The optical constants (the refractive index n and the extinction coefficient k) of the different layers (p-i-n) of the a-Si:H top cell and µc-Si:H bottom cell are calculated from the complex dielectric function using Eqs.1 and 2 [atlas_users1].

$$n = \sqrt{\frac{\sqrt{\varepsilon_1^2+\varepsilon_2^2}+\varepsilon_1}{2}} \qquad \text{(V.14)}$$

$$k = \sqrt{\frac{\sqrt{\varepsilon_1^2+\varepsilon_2^2}-\varepsilon_1}{2}} \qquad \text{(V.15)}$$

where ε_1 and ε_2 are respectively the real and the imaginary parts of the complex dielectric function $\varepsilon = \varepsilon_1 - i.\varepsilon_2 = (n - i.k)^2$.

The imaginary part ε_2 is calculated by the generalized model of Tauc-Lorentz dielectric function including the exponential Urbach Tail (TLU) proposed by Foldyna et al [123, 156].

$$\varepsilon_2(E) = \begin{cases} \frac{1}{E}.\frac{A.E_0.C.(E-E_g)^2}{(E^2-E_0^2)^2+C^2E^2} & E \geq E_C \\ \frac{A_u}{E}exp\left(\frac{E}{E_u}\right) & 0 < E < E_C \end{cases} \qquad \text{(V.16)}$$

Here, E_g, A, E_0 and C denote the band gap energy, the amplitude, the Lorentz resonant frequency, and the broadening parameter, respectively. For energies $\geq E_C$, the standard Tauc-Lorentz function is used while for energies $0 < E < E_C$, the Urbach tails are parameterized as an exponential function of energy with two matching parameters A_u and E_u that are calculated with respect to continuity of the optical function including first derivative. This leads to the relations Foldyna et al.[123, 156]:

$$E_u = (E_C - E_g).\left[2 - 2.E_C.(E_C - E_g).\frac{C^2+2.(E_C^2-E_0^2)}{C^2.E_C^2+(E_C^2-E_0^2)}\right]^{-1} \qquad \text{(V.17)}$$

$$A_u = exp\left(-\frac{E_C}{E_u}\right).\frac{A.E_0.C.(E_C-E_g)^2}{(E_C^2-E_0^2)^2+C^2E_C^2} \qquad \text{(V.18)}$$

The real part ε_1 of the dielectric function is obtained using analytical integration of the Kramers-Krönig (KK) relation Foldyna et al.[123, 156]:

$$\varepsilon_1(E) = \varepsilon_{1,\infty} + \frac{2}{\pi}.(C.P.)\int_0^{\infty} \frac{\xi\varepsilon_2(\xi)}{\xi^2 - E^2}.d\xi \qquad \text{(V.19)}$$

where $(C.P.)$ denotes the Cauchy principal value of the integral. The integral itself is resolved using some analytic forms the details of which are given in ref [156].

The model parameters were calibrated to fit the experimentally determined EQE of the micromorph tandem solar cell [148] (figure V.25).

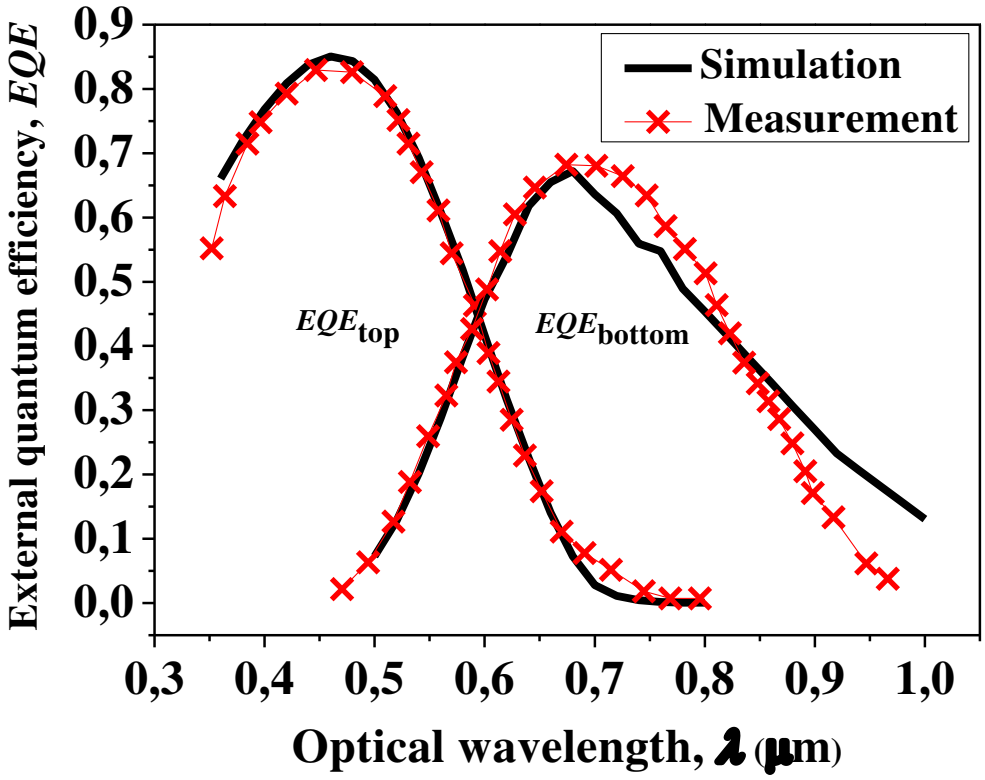

Figure V.25: Calibration of the optical model to fit the experimental measurements of Zeeman et al [157] for the micromorph tandem solar cell.

Figure V.26 shows the optical constants used for the different layers of the simulated cells. As mentioned above, those of the semiconductor layers (p-i-n) are calculated according to the generalized model of Tauc-Lorentz dielectric function including the exponential Urbach Tail (TLU- model), while for the remaining layers (Al, Ag, SiO_2, ZnO and ITO), we use the measured data of Ref [157] saved in Silvaco data base.

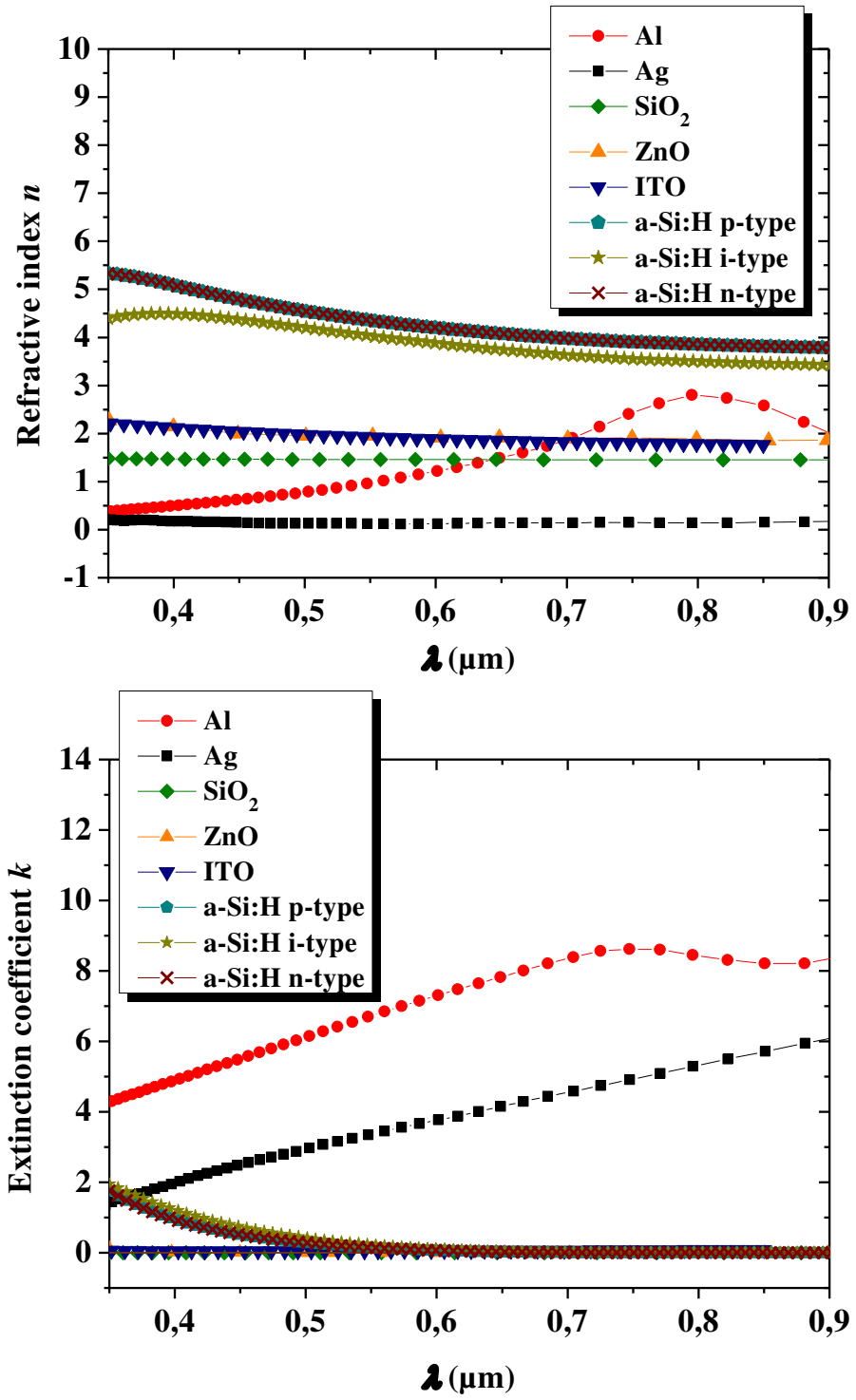

Figure V.26: Optical constants used for the different layers of the simulated cells[157].

V.3.3) Results

Figure V.27 shows the $J-V$ characteristic and EQE of the a-Si:H single cell vs. i-layer thickness, in initial and degraded states.

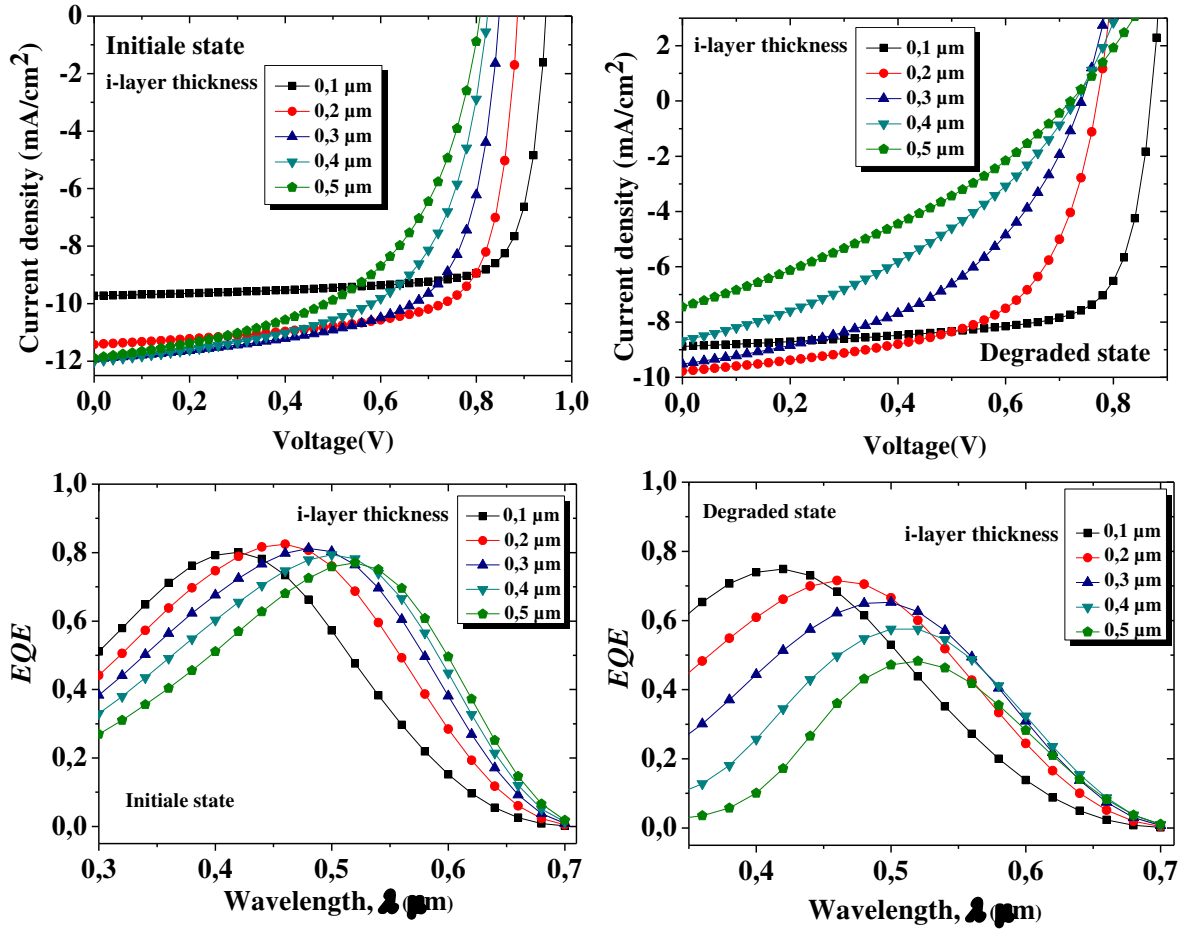

Figure V.27: $J-V$ characteristic and EQE of the a-Si:H single cell vs. i-layer thickness, in initial and degraded states.

We can see that $J-V$ characteristic and EQE curves are sensitive to the i-layer thickness. A thick absorber layer (i-layer) can absorb more light to generate electron and hole (carriers); however, a thicker i-layer degrades the drift electric field or carrier transport. On the other hand, a thin i-layer cannot absorb enough light. Thickness of i-layer is a key parameter that can limit the performance of amorphous thin film solar cells. As shown in figure V.28, increasing the i-layer thickness induces the reduction of the electric field along the bulk of the i-layer, in opposition, the recombination rate increases.

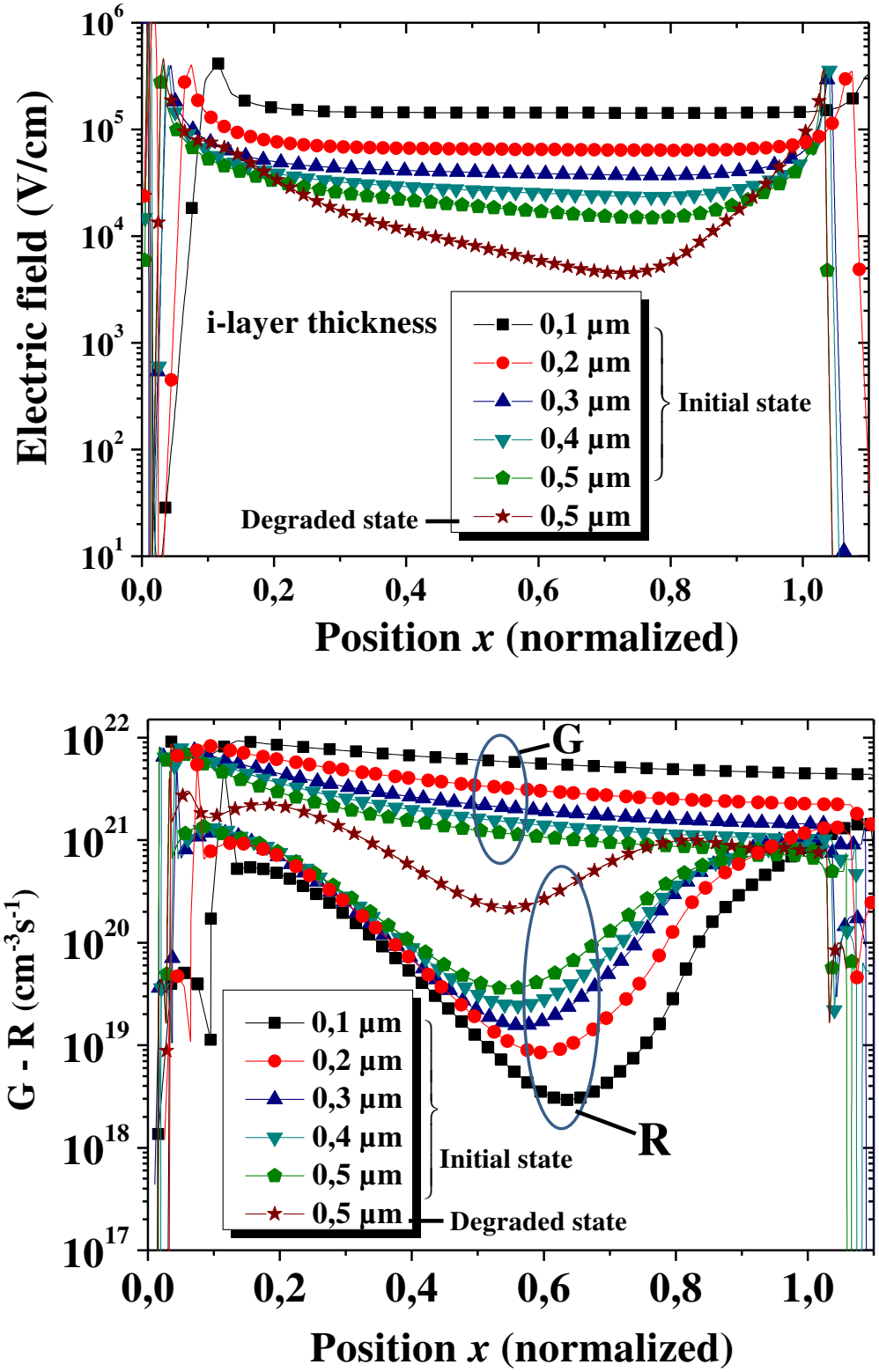

Figure V.28: Distribution of the electric field, generation (G) and recombination (R) rates inside the a-Si:H single cell for different i-layer thicknesses, at short circuit condition.

But this reduction of the field, or the increase of the recombination rate, does not affect the photocurrent yet, at least in short circuit condition, mainly because the electric field at the p/i interface is high enough to ensure the collection of a maximum

number of photo-carriers while the recombination rate is still lower than the generation rate. However, in the opposite open circuit condition (figure V.29),

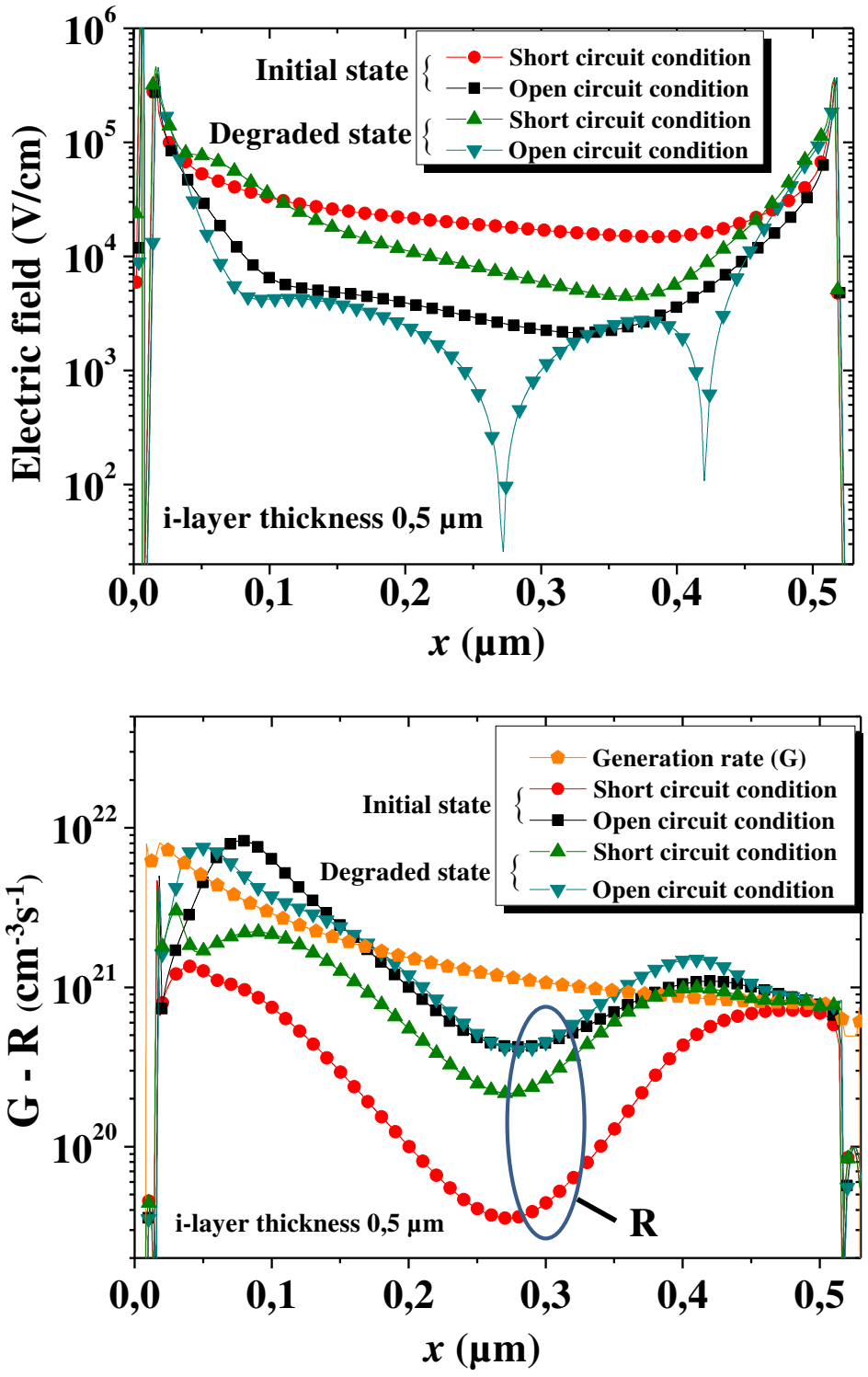

Figure V.29: Distribution of the electric field, generation (G) and recombination (R) rates inside the a-Si:H single cell for the i-layer thickness of 0.5 µm.

the recombination rate becomes more significant than the generation rate in certain regions of the i-layer near the p/i and i/n interfaces, which affect the transport of the

photo-carriers despite the electric field magnitude at the interfaces. So, there must be a compromise between the recombination rate and the electric field.

A way from the short circuit condition, the current (figure V.27) becomes more sensitive to the i-layer thickness and is reduced as this latter is thicker.

Comparatively to the initial state, the electrical characteristics in degraded state are more susceptible to the i-layer thickness variation because the defect density of states, which increased similarly to the defect concentration by four orders of magnitude, is dependent on the thickness. We can clarify this sensitivity at the degraded state in term of the electric field and recombination rate profiles inside the a-Si:H single cell, as shown in figures V.30 and V.31 respectively.

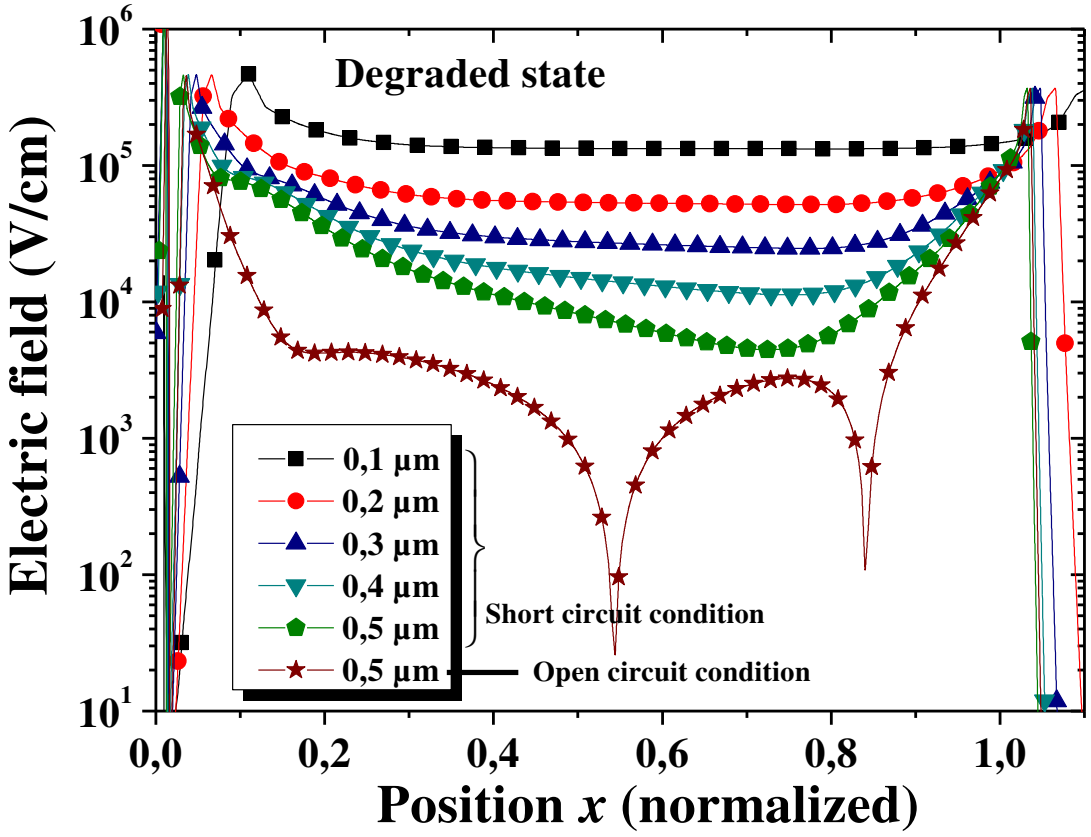

Figure V.30: Distribution of the electric field inside the a-Si:H single cell for different i-layer thicknesses, at degraded state.

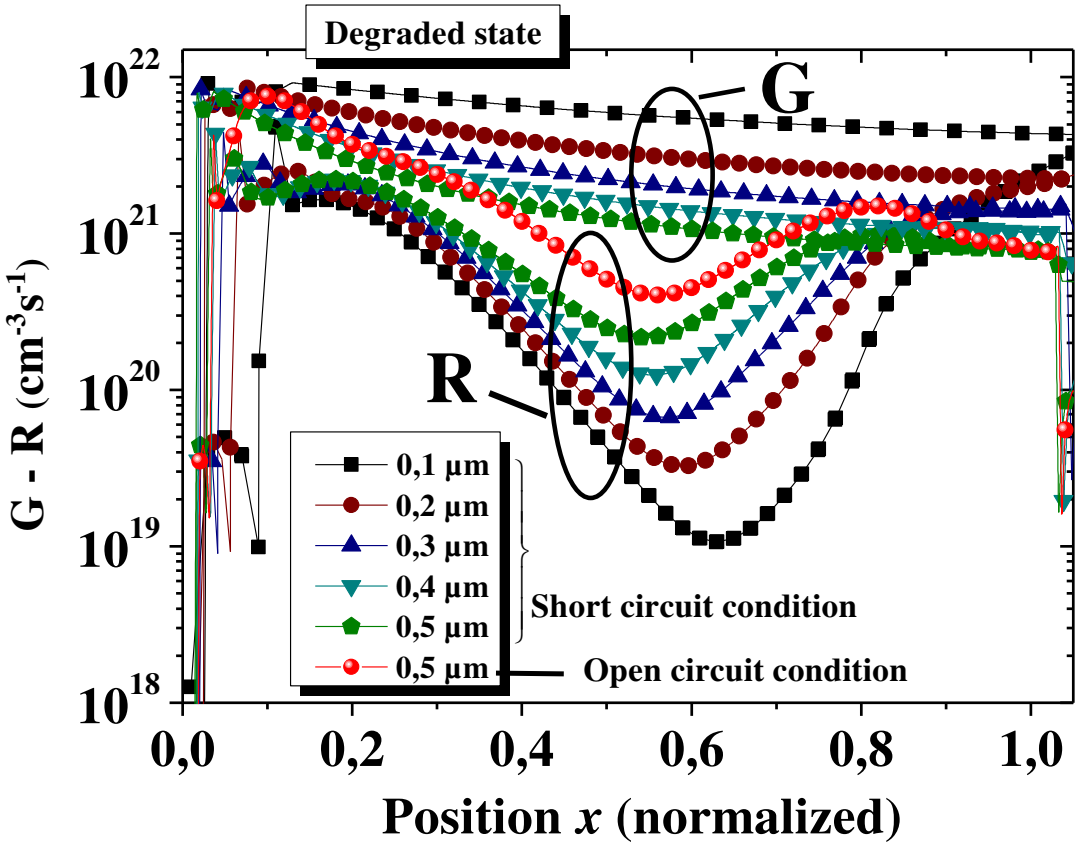

Figure V.31: Generation (G) and recombination (R) rate profiles inside the a-Si:H single cell for different i-layer thicknesses, at degraded state.

Regarding the EQE curves (figure V.27), one can see that, as the i-layer becomes thicker, the maximum photo-response of the cell shifts from short wavelength (blue) to the longer one (green).

To analyse in more detail the behaviour according to the i-layer effect, we present in figure V.32 and table V.7 the thickness dependence of the photovoltaic parameters J_{sc}, V_{oc}, FF and η respectively. In the initial state, the J_{sc} increases at first with increasing i-layer thickness due to the increasing path length of the light in the absorber layer, and once reached its maximum value 12 mA/cm^2 at 0.4 µm , it decreases slightly with a further increase of i-layer thickness. In the degraded state however, the J_{sc} reaches a maximum value of 9,78 mA/cm^2 at 0.2 µm, but then shows a noticeable reduction. The current lowering is mainly attributed to the increase of the defect density of states along the i-layer, which corresponds to an increase of the recombination centres density. Such a lowering is clearly visible as the i-layer is thicker.

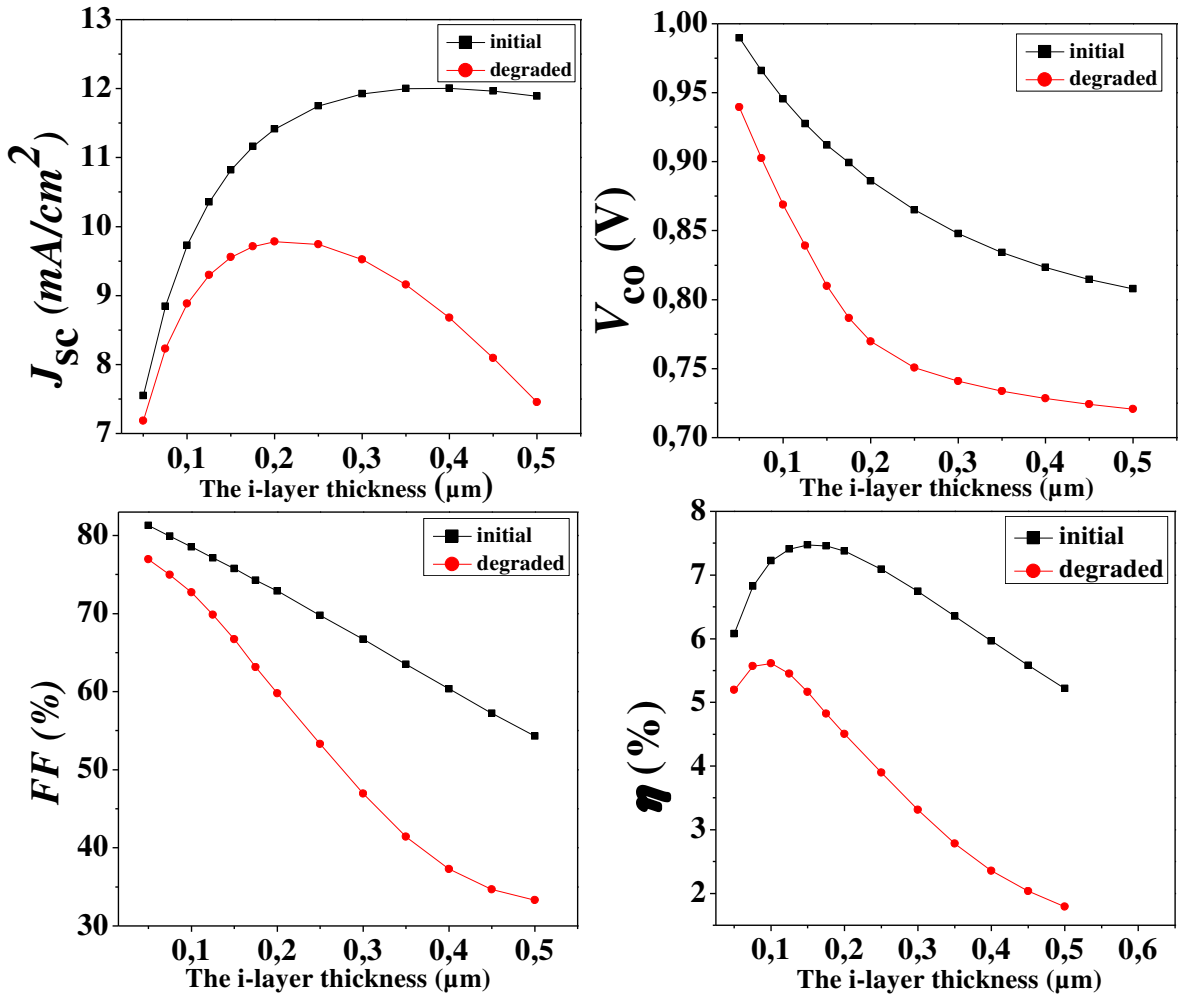

Figure V.32: J_{sc}, V_{oc}, FF and η of the a-Si:H single cell vs. i-layer thickness, in initial and degraded states.

Thickness	Jsc	Jsc	Voc	Voc	FF	FF	Efficiency	Efficiency
µm	mA/cm²	mA/cm²	Volt	Volt	%	%	%	%
	Initial state	Degraded	Initial state	Degraded	Initial state	Degraded	Initial state	Degraded
0,05	7,55023	7,18634	0,98988	0,9395	81,2978	76,974	6,07607	5,19697
0,075	8,84443	8,23038	0,96603	0,90269	79,9006	74,9884	6,82672	5,57123
0,1	9,72857	8,88303	0,94551	0,8689	78,529	72,7224	7,22347	5,61307
0,125	10,359	9,29916	0,92757	0,83912	77,1346	69,8604	7,41162	5,45126
0,15	10,82	9,55964	0,9121	0,81002	75,7689	66,6972	7,47757	5,1647
0,175	11,1635	9,71225	0,89943	0,78669	74,2789	63,1375	7,45823	4,82403
0,2	11,4187	9,78175	0,88604	0,76977	72,9075	59,8034	7,37635	4,50301
0,25	11,7503	9,74137	0,86513	0,75062	69,7776	53,3034	7,09331	3,89758
0,3	11,9247	9,5217	0,84787	0,74089	66,7263	46,9598	6,74643	3,31282
0,35	11,9992	9,15945	0,83424	0,73379	63,4772	41,4167	6,35418	2,78368
0,4	12,0072	8,67673	0,82336	0,72835	60,3436	37,2677	5,96571	2,35522
0,45	11,967	8,09551	0,81464	0,72411	57,2472	34,6941	5,58091	2,03377
0,5	11,8896	7,4564	0,80785	0,72081	54,3278	33,3171	5,21817	1,79067

Table V-7: J_{sc}, V_{oc}, FF and η of the a-Si:H single cell vs. i-layer thickness, in initial and degraded states.

The V_{oc} decreases with increasing i-layer thickness and shows a stabilisation tendency after 0.3 µm. Generally, V_{oc} is influenced by surface and bulk recombination. By increasing i-layer thickness as shown in figures V.33 and V.34, we can see that recombination becomes mainly influenced by recombination near the p/i- interface.

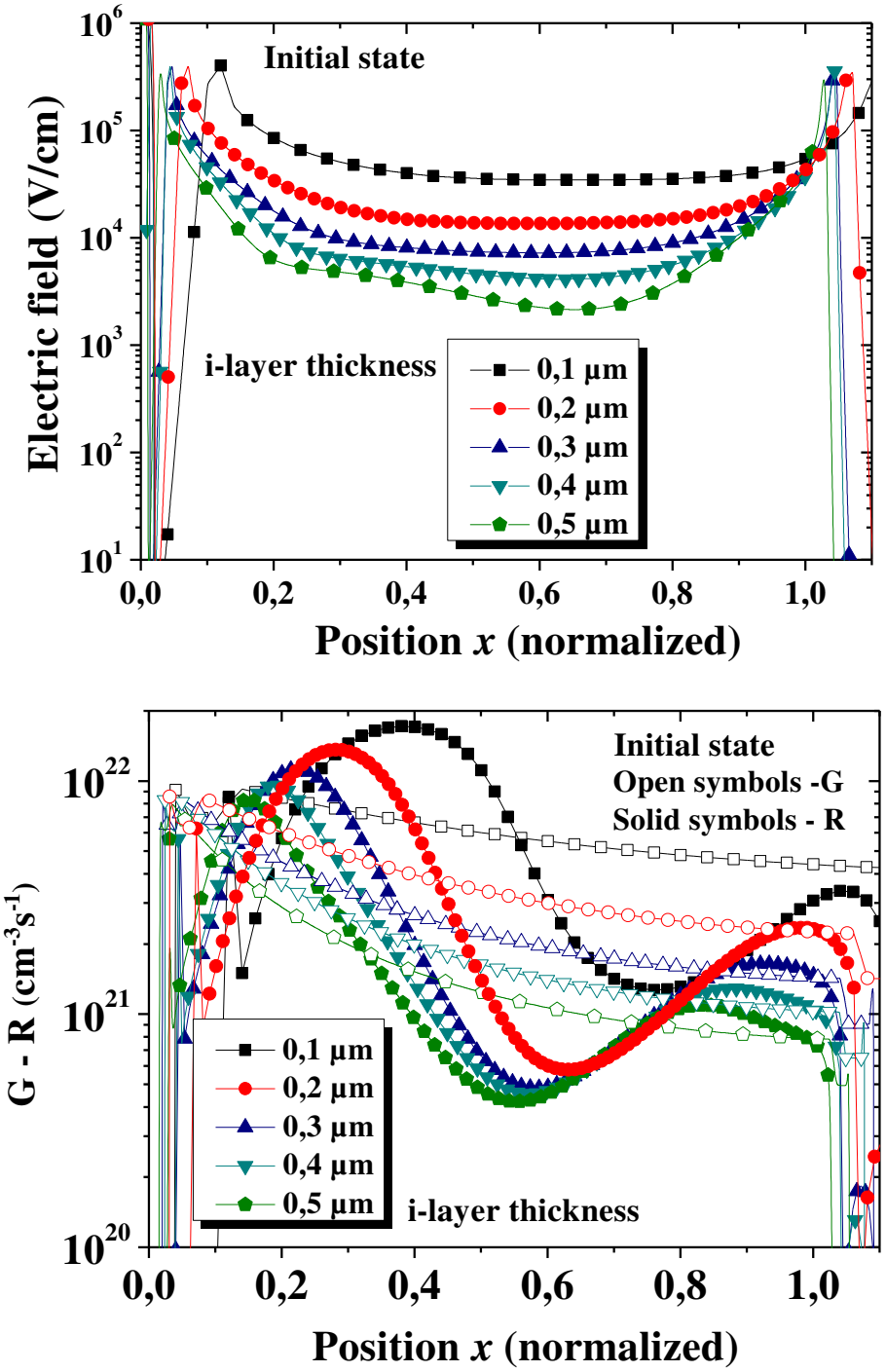

Figure V.33: Distribution of the electric field, generation (G) and recombination (R) rates inside the a-Si:H single cell for different i-layer thicknesses, at initial state and open circuit condition.

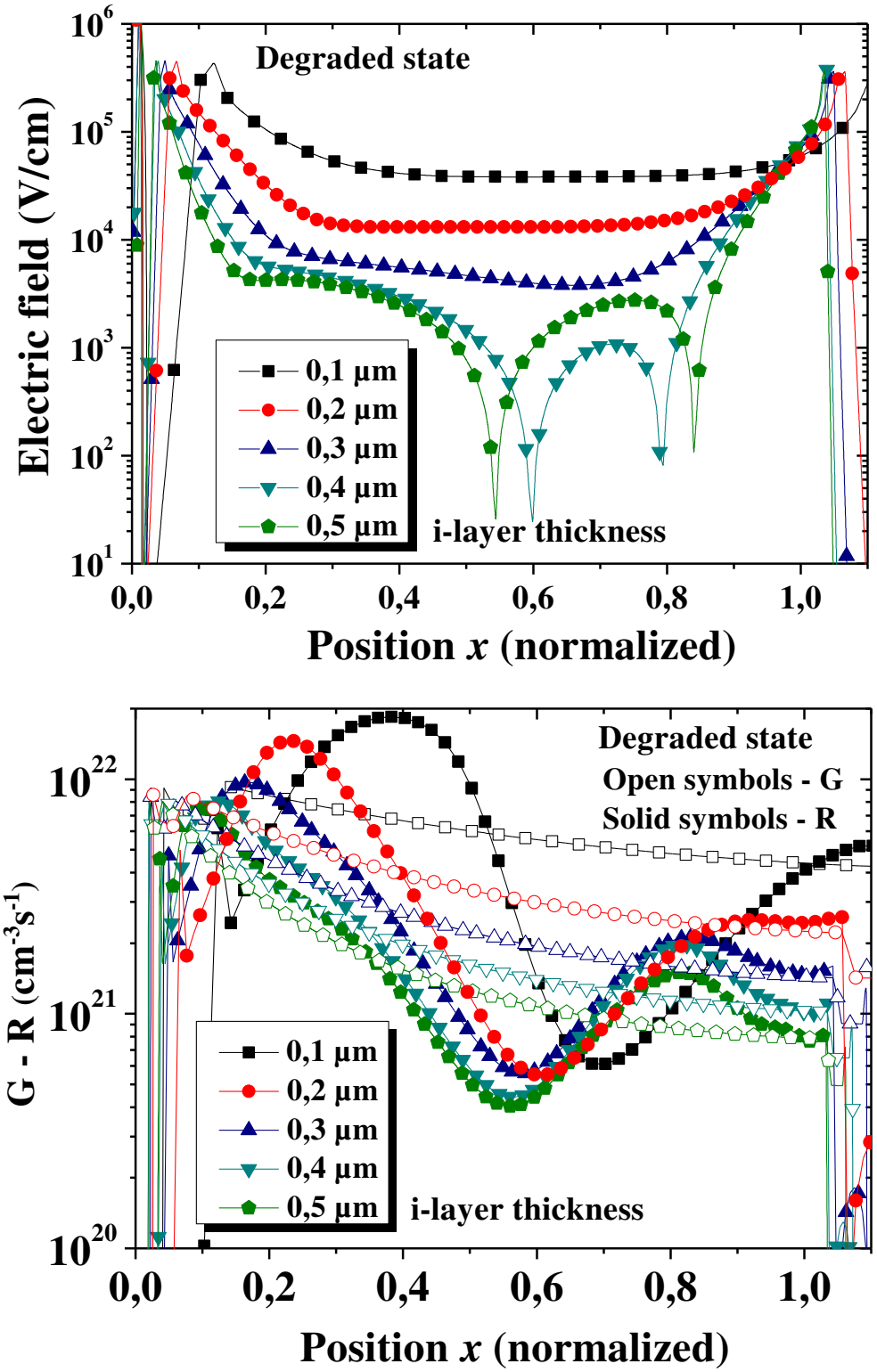

Figure V.34: Distribution of the electric field, generation (G) and recombination (R) rates inside the a-Si:H single cell for different i-layer thicknesses, at degraded state and open circuit condition.

The FF and η are the main indicators of the solar cell's quality, and FF is in general the most sensitive parameter to the i-layer properties in term of defect density and recombination losses. The FF decreases greatly from 81,29% to 54,32% in the initial

state, and from 76,97% to 33,31% in the degraded state as the i-layer increases from 0.1μm to 0.5 μm. A thicker layer affects the charge carrier collection because the charge carriers have to travel a longer distance before reaching the contacts, and with the reduction of the average electrical field over i-layer, recombination losses can be raised and deteriorate the FF .

The conversion efficiency η is determined by the value of J_{sc} in conjunction with the V_{oc} and the FF of the characteristic $J-V$ curve. The optimum η for the initial state of the a-Si:H single cell is 7,47% with an i-layer 0,15 μm thick. At the degraded state where the i-layer density of state is higher by four orders of magnitude, the optimum η is 5,61%, reached at a thinner i-layer 0.1 μm thick. The more the i-layer is thick, the more η is reduced by the increasing of the defect density of states. The decrease in V_{oc} and FF is also responsible for the loss in the efficiency η, and is only partially compensated by the first increase of the J_{sc} to its maximum value.

Figure V.35 shows the $J-V$ characteristic and EQE of the μc-Si:H single cell vs. i-layer thickness. Being closer to the short circuit condition, the current becomes more sensitive to the i-layer thickness. The V_{oc} however, presents less sensitivity. The improvement of the photo-response of the cell, presented by its EQE, is obtained as the i-layer is thicker. Figure V.36 and table V.8 present the thickness dependency of the photovoltaic parameters of the μc-Si:H single cell; J_{sc}, V_{oc}, FF and η respectively, extracted from the $J-V$ characteristic curves.

The J_{sc} increases with increasing i-layer thickness and tends to saturate beyond 4μm. The V_{oc} and FF decreases are less severe than the a-Si:H case, because the recombination, which influences these two parameters, is dominated in the μc-Si:H cell, by a bulk recombination as shown in figures V.37 and V.38 respectively. By reducing the i-layer thickness, the bulk recombination decreases due to the reduced volume and V_{oc}, FF increase. As in the a-Si:H case, recombination at open circuit condition is more significant than at short circuit condition.

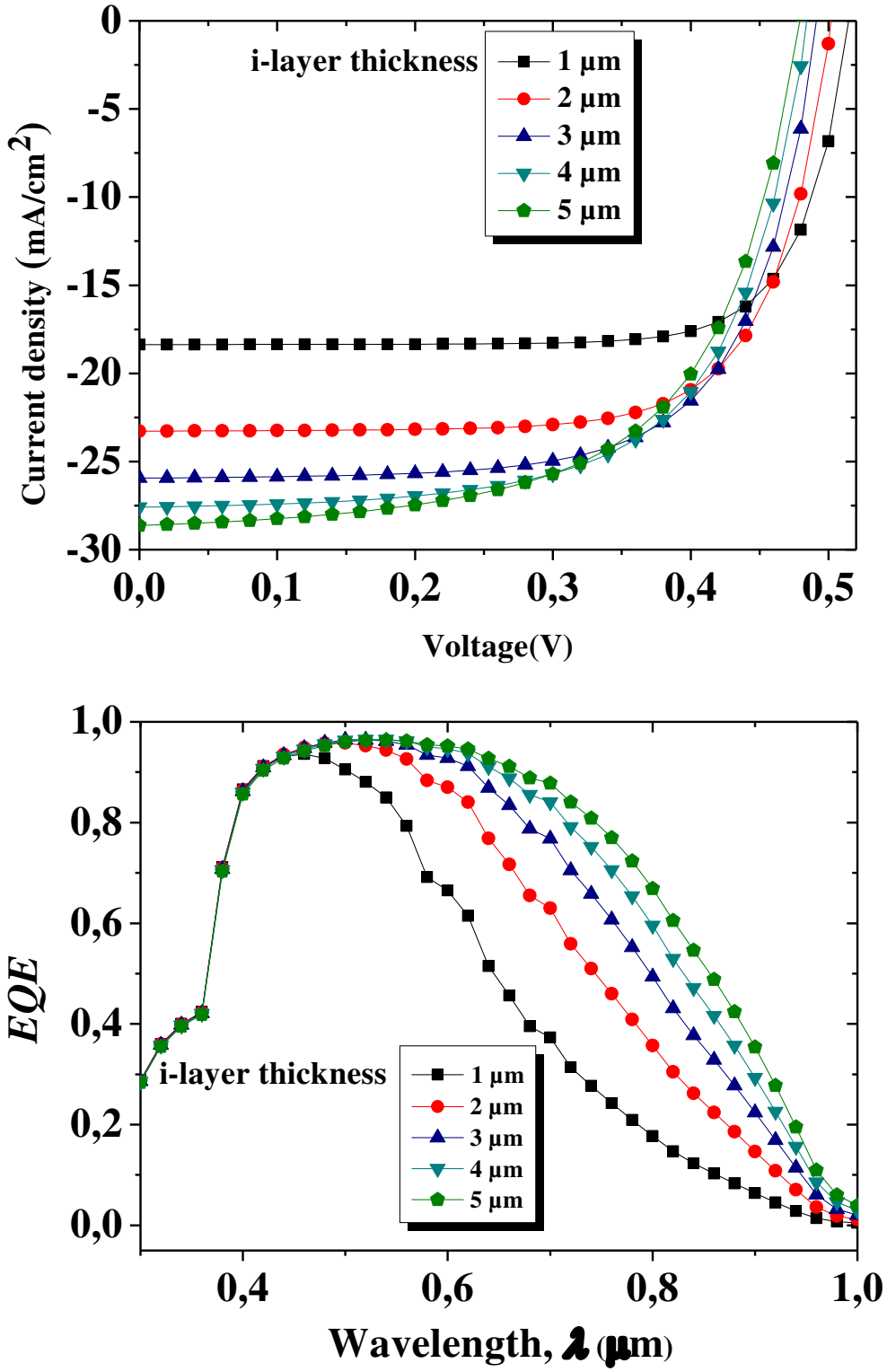

Figure V.35: $J-V$ characteristic and EQE of the µc-Si:H single cell vs. i-layer thickness.

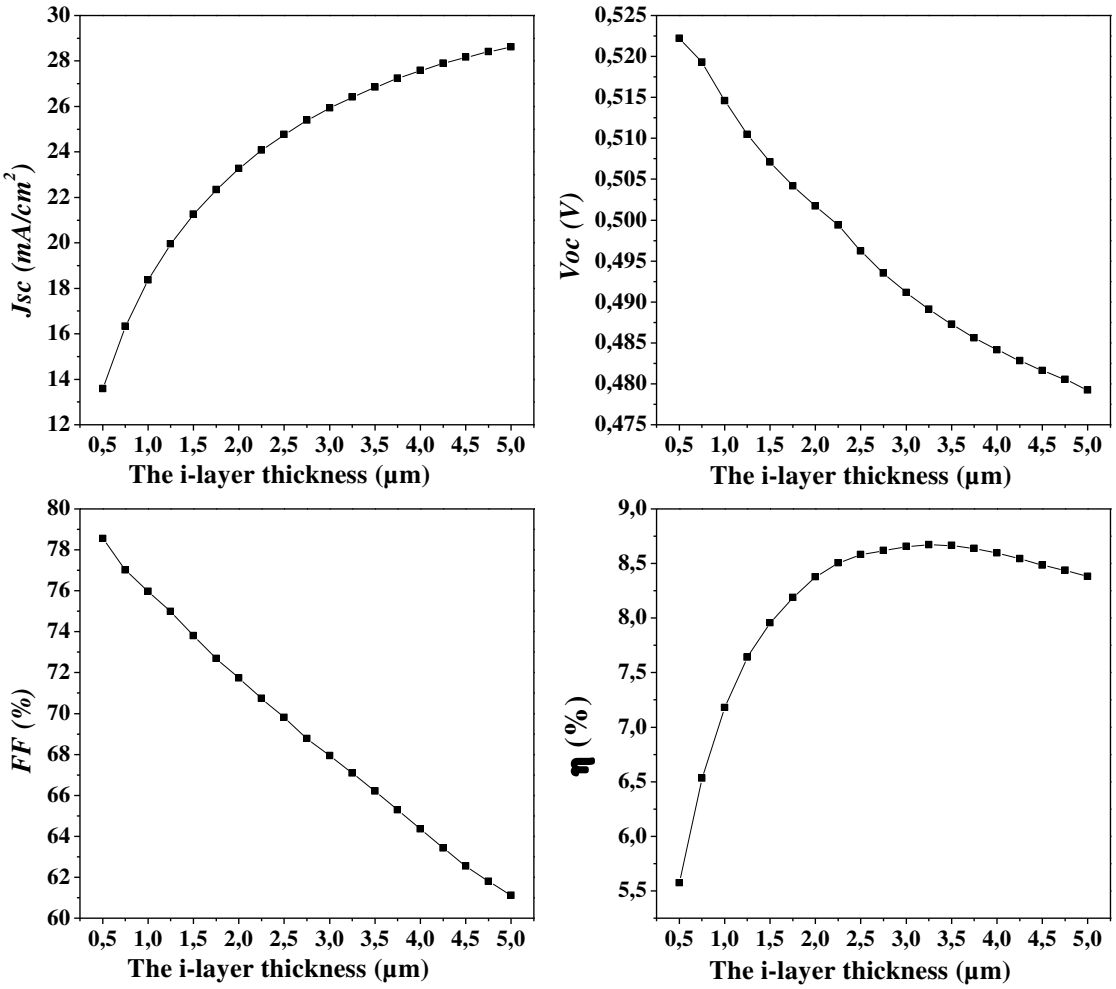

Figure V.36: J_{sc}, V_{oc}, FF and η of the µc-Si:H single cell vs. i-layer thickness.

Thickness	Jsc	Voc	FF	Efficiency
µm	mA/cm²	V	%	%
0,5	13,5872	0,52223	78,5502	5,57364
0,75	16,3331	0,51929	77,0169	6,53224
1	18,3654	0,5146	75,9653	7,17929
1,25	19,9597	0,51047	74,9887	7,64053
1,5	21,2603	0,50709	73,7984	7,95617
1,75	22,3478	0,5042	72,6817	8,18958
2	23,2752	0,50174	71,7476	8,3788
2,25	24,0765	0,49939	70,7441	8,50593
2,5	24,7765	0,49624	69,8091	8,58304
2,75	25,3926	0,49352	68,7814	8,61954
3	25,9387	0,49117	67,9465	8,65663
3,25	26,4243	0,48909	67,1017	8,67218
3,5	26,858	0,48726	66,2119	8,66509
3,75	27,2454	0,48562	65,2947	8,63912
4	27,5911	0,48415	64,3621	8,59764
4,25	27,8994	0,48283	63,4254	8,54377
4,5	28,1722	0,48162	62,5445	8,48626
4,75	28,4123	0,48053	61,8024	8,43781
5	28,6206	0,47926	61,1079	8,38199

Table V-8: J_{sc}, V_{oc}, FF and η of the µc-Si:H single cell vs. i-layer thickness.

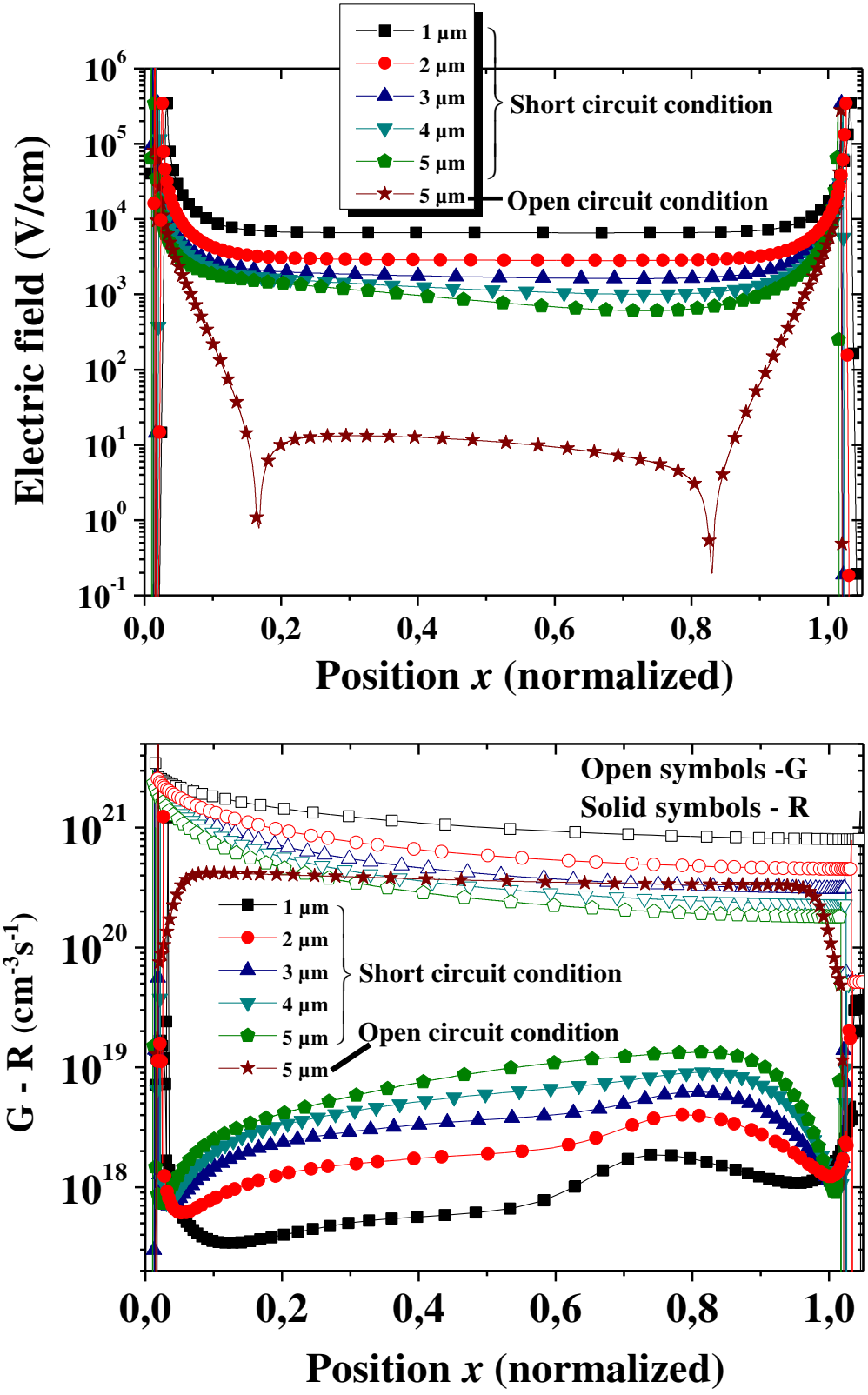

Figure V.37: Distribution of the electric field, generation (G) and recombination (R) rates inside the µc-Si:H single cell for different i-layer thicknesses.

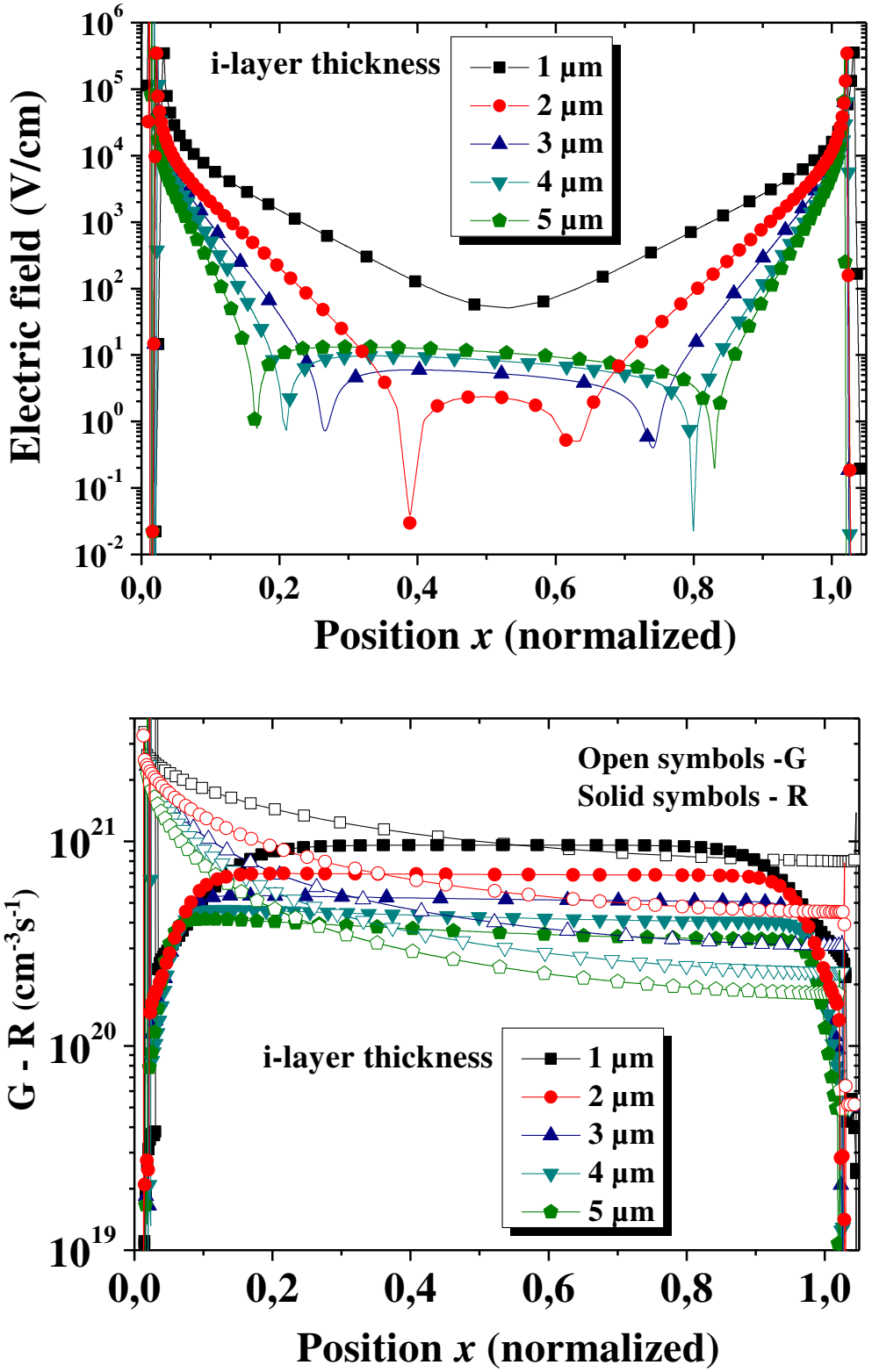

Figure V.38: Distribution of the electric field, generation (G) and recombination (R) rates inside the µc-Si:H single cell for different i-layer thicknesses, at open circuit condition.

While the electric field magnitude at the p/i and n/i interfaces remains almost insensitive to the increasing of the i-layer thickness (figures V.37 and V.38), the electric field over the i-layer shows a noticeable reduction, particularly in the open

circuit condition (figure V.38). As we know, this condition means that the cell is optically forward biased by the established voltage V_{oc} ; as the i-layer becomes thicker, the depletion regions established from the p/i and n/i junctions, which were overlapped, are narrowed back to the p/i and n/i interfaces. This means the appearance of a neutral region in the middle of the i-layer. The electric field along this last region changes its direction and sign, but its magnitude is relatively low. So the charge carrier transport in this part of the cell will depend on diffusion, and the diffusion length will be a critical parameter, especially when the i-layer is thicker. The diffusion length should be long enough to avoid significant losses of the charge carriers by recombination. At the open circuit condition, the total current is zero, so in general, there is a balance between the electric field effect at the interfaces p/i and n/i, and the diffusion, recombination, and electric field effects in the bulk of the i-layer.
From figure V.36 and table V.8, one can see that an I-layer of 3,25 µm shows the highest efficiency; an optimal conversion efficiency of approximately 8,67% is achieved when the i-layer thickness is 3,25 µm.
According to the simplified analytical approach, we remind that the photocurrent density generated in the i-layer can be found as [158]:

$$J_{ph} = q\int_0^W G(x).dx = q.\int_0^W \alpha.\Phi_0 \exp(-\alpha.x)\,dx = q.\Phi_0(1-e^{-\alpha.W}) \quad \text{(V.20)}$$

Where $G(x)$ and $\Phi_0 \exp(-\alpha.x)$ are respectively the optical generation rate and the photon flux as a function of the distance x in the i-layer, α is the photon absorption coefficient, and W is the i-layer thickness.
According to this equation, we expect that the photocurrent (and so J_{sc}) increases as the i-layer increases and saturates on the value of $q.\Phi_0$, which is not the real case because of the electron-hole recombination within the i-layer , and also the optical losses of the incident photons by reflection or sub-absorption. So J_{sc} can undergo a significant reduction after reaching its optimum value (as seen in the degraded state of the a-Si:H cell), or tends to saturate at values less than the ideal case of $q.\Phi_0$ (as seen in the µc-Si:H cell case).
The simplified analytical approach applied to estimate the V_{oc} can be expressed by the following equation [158]:

$$V_{CO} = \frac{k_B T}{q}\, ln(1+\frac{I_{ph}}{I_S}) \quad \text{(V.21)}$$

where I_{ph} is the photocurrent and I_S is the saturation current.

In the ideal case, I_S depends mainly on diffusion phenomenon, which is not the real case, where the recombination can take a significant effect as the interface recombination (seen in the a-Si:H case) and the bulk recombination (seen in the µc-Si:H case), which makes V_{CO} and also FF more sensitive to the i-layer thickness.

Figure V.39 shows the $J-V$ characteristic curves of the 2T- micromorph (a-Si:H/ µc-Si:H) tandem cell for different i-layer thicknesses of the a-Si:H top cell and µc-Si:H bottom cell respectively, at initial and degraded states.

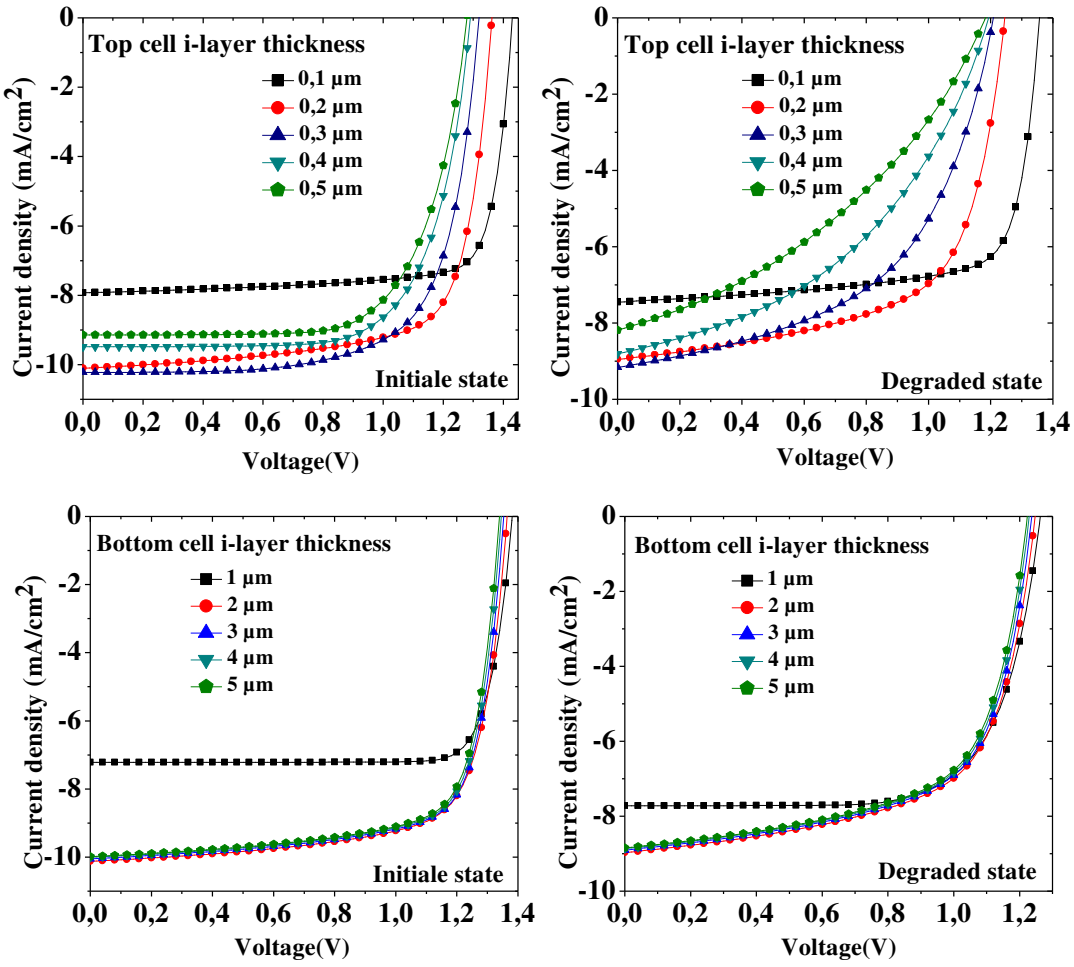

Figure V.39: $J-V$ characteristic of the 2T- micromorph tandem cell for different i-layer thicknesses of the (a-Si:H) top cell and (µc-Si:H) bottom cell respectively, at initial and degraded states.

When the top cell i-layer thickness is varied, the one of the bottom cell is fixed to 2.25 µm. When the bottom cell i-layer thickness is varied, the one of the top cell is fixed to 0.19 µm. Either at the initial state or the degraded one, we can see from this figure that $J-V$ characteristics are mostly sensitive to the variation of the (a-Si:H)

top cell i-layer thickness. The bottom cell i-layer manifests an effect on the current (J_{sc}) only from 1µm to 2µm.

Figure V.40 shows the top and bottom cell EQE of the 2T- micromorph tandem cell for different i-layer thicknesses of the (a-Si:H) top cell, at initial and degraded states.

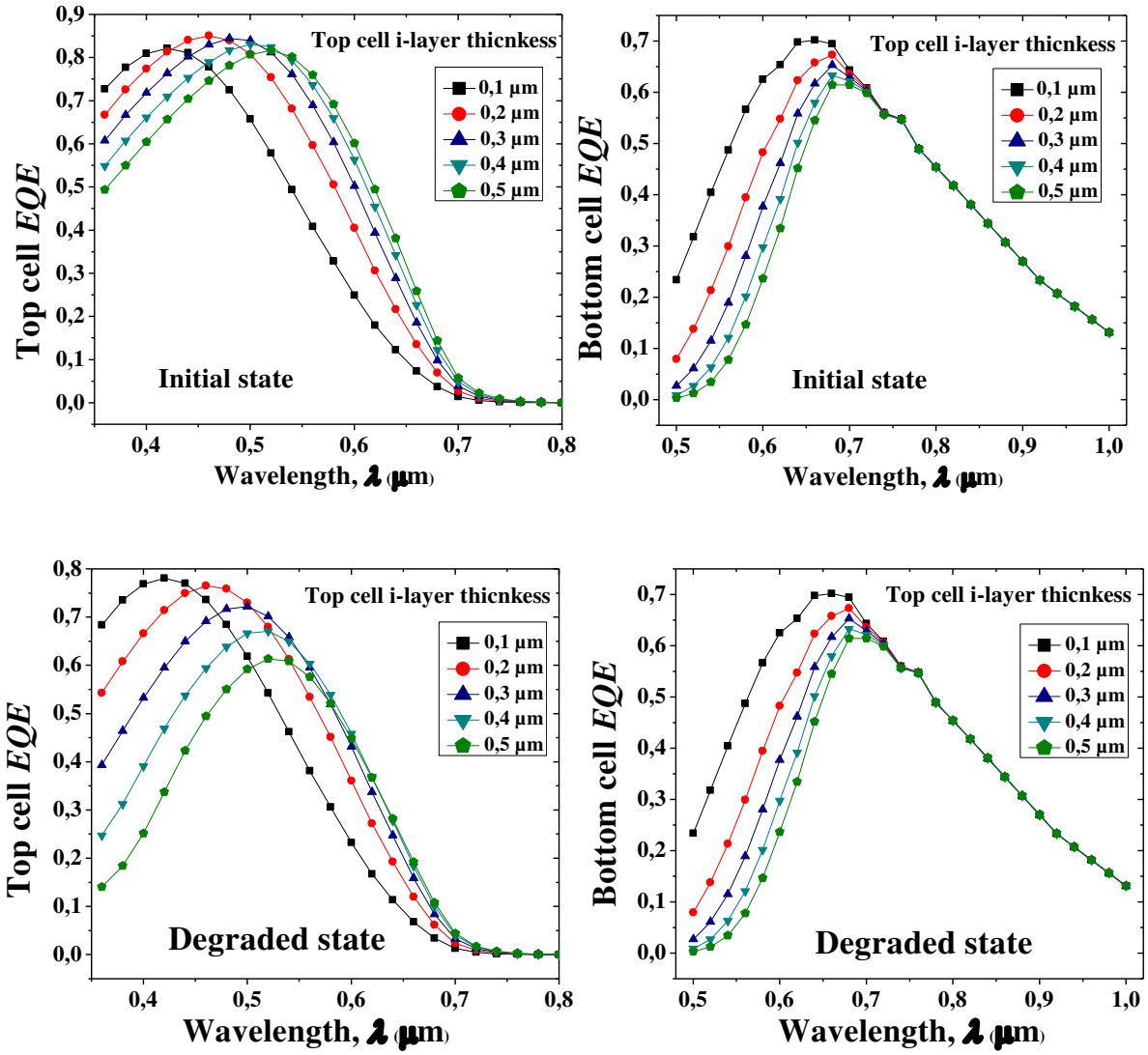

Figure V.40: Top and bottom cell EQE of the 2T- micromorph tandem cell for different i-layer thicknesses of the (a-Si:H) top cell, at initial and degraded states. Bottom cell i-layer is fixed to 2.25 µm.

While the top cell EQE maximum shifts from short wavelength (blue) to the longer one (green) as the i-layer becomes thicker, and knows certain reduction to be less than 0.8 at degraded state, the bottom cell EQE shows an improvement for the thinner i-layer thickness (0.1 µm). This is expected because more the top cell i-layer is thin, less is the effect of the defect density of state, especially with the a-Si:H Staebler Wronski effect.

Figure V.41 shows the EQE of the 2T- micromorph tandem cell for different i-layer thicknesses of the (µc-Si:H) bottom cell, at initial and degraded states.

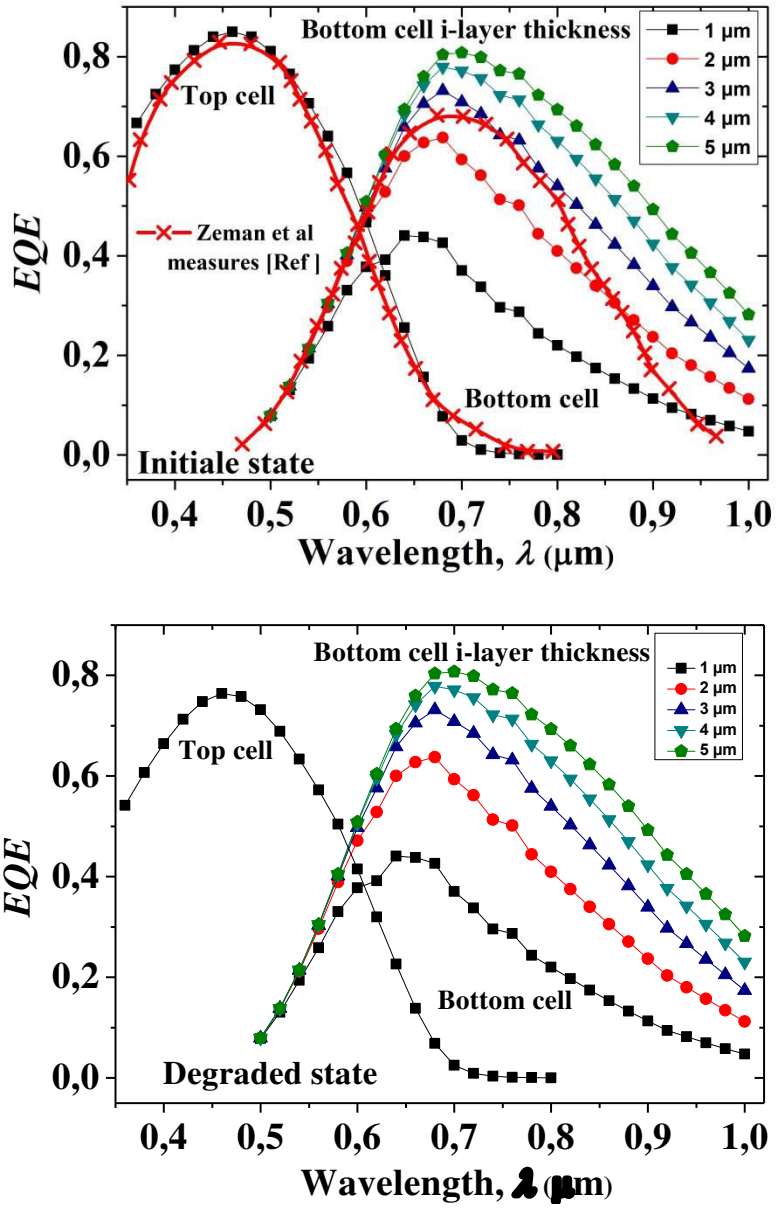

Figure V.41: EQE of the 2T- micromorph tandem cell for different i-layer thicknesses of the (µc-Si:H) bottom cell, at initial and degraded states. Top cell i-layer is fixed to 0.19 µm.

The top cell EQE knows a reduction at the degraded state, but it is insensitive to the (µc-Si:H) bottom cell i-layer thickness variation. The bottom cell EQE shows an improvement as the bottom cell i-layer thickness increases, because of the increasing path length of the light, and so the optical absorption, in this layer.

Figure V.42 shows the J_{sc} behaviour of the 2T- micromorph tandem cell at initial state, for a general scanning of the i-layer thickness, where the a-Si:H top cell i-layer

is varied in the range 0.05µm-0.5µm, and the µc-Si:H bottom cell i-layer is varied in the range 0.5µm- 5µm.

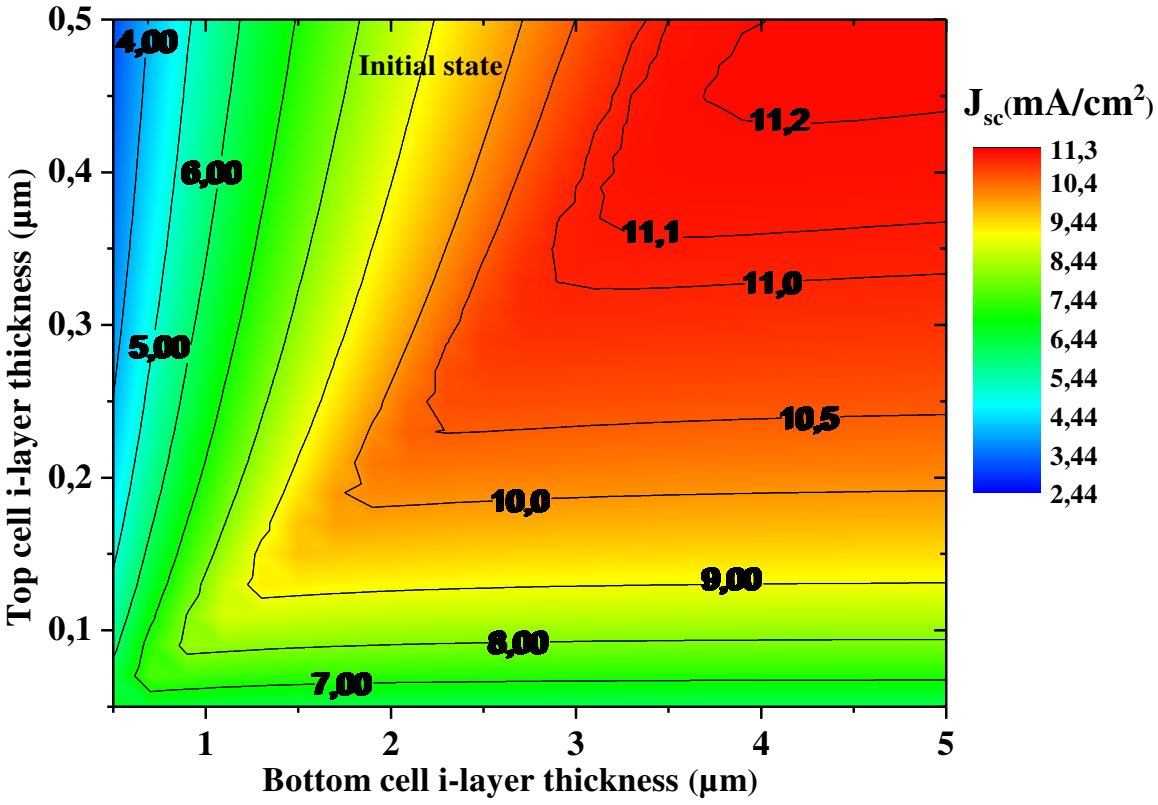

Figure V.42: The J_{sc} vs. i-layer thickness of the 2T- micromorph tandem cell at initial state, for a general scanning of the top and bottom cell i-layer thicknesses.

In general, the J_{sc} increases as the top and bottom cell i-layer thicknesses increases. The best value of J_{sc} is approximately 11.22 mA/cm^2 for top cell i-layer 0,47 µm thick and bottom cell i-layer 4.5 µm thick.

Figure V.43 shows the J_{sc} vs. i-layer thickness, of the 2T- micromorph tandem cell at degraded state, for a general scanning of the top and bottom cell i-layer thicknesses.

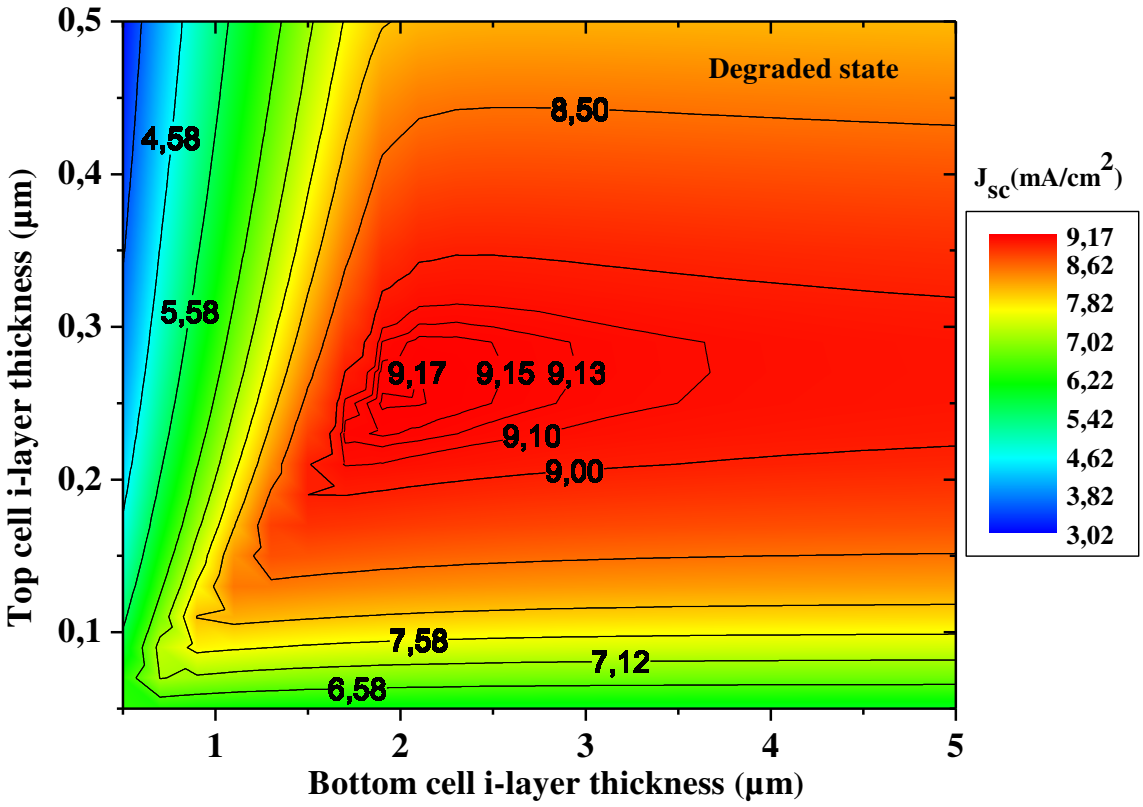

Figure V.43: The J_{sc} vs. i-layer thickness of the 2T- micromorph tandem cell at degraded state, for a general scanning of the top and bottom cell i-layer thicknesses.

Here, J_{sc} knows an optimum value of 9.17 mA/cm^2 for a top cell i-layer 0.25µm thick and bottom cell i-layer 1.9µm thick, but then it reduces for a further increase of both i-layer thicknesses.

Figure V.44 shows the V_{oc} vs. i-layer thickness, of the 2T- micromorph tandem cell at initial and degraded states respectively, for a general scanning of the top and bottom cell i-layer thicknesses. The V_{oc} is mostly affected by the top cell i-layer thickness variation. At the initial state, it reduces from about 1.5 V to 1.3 V when the top cell i-layer increases from 0.05µm to 0.5 µm and the bottom cell i-layer is less than 1µm. But at fixed top cell i-layer thickness, the V_{oc} displays a little dependency on the bottom cell i-layer thickness.

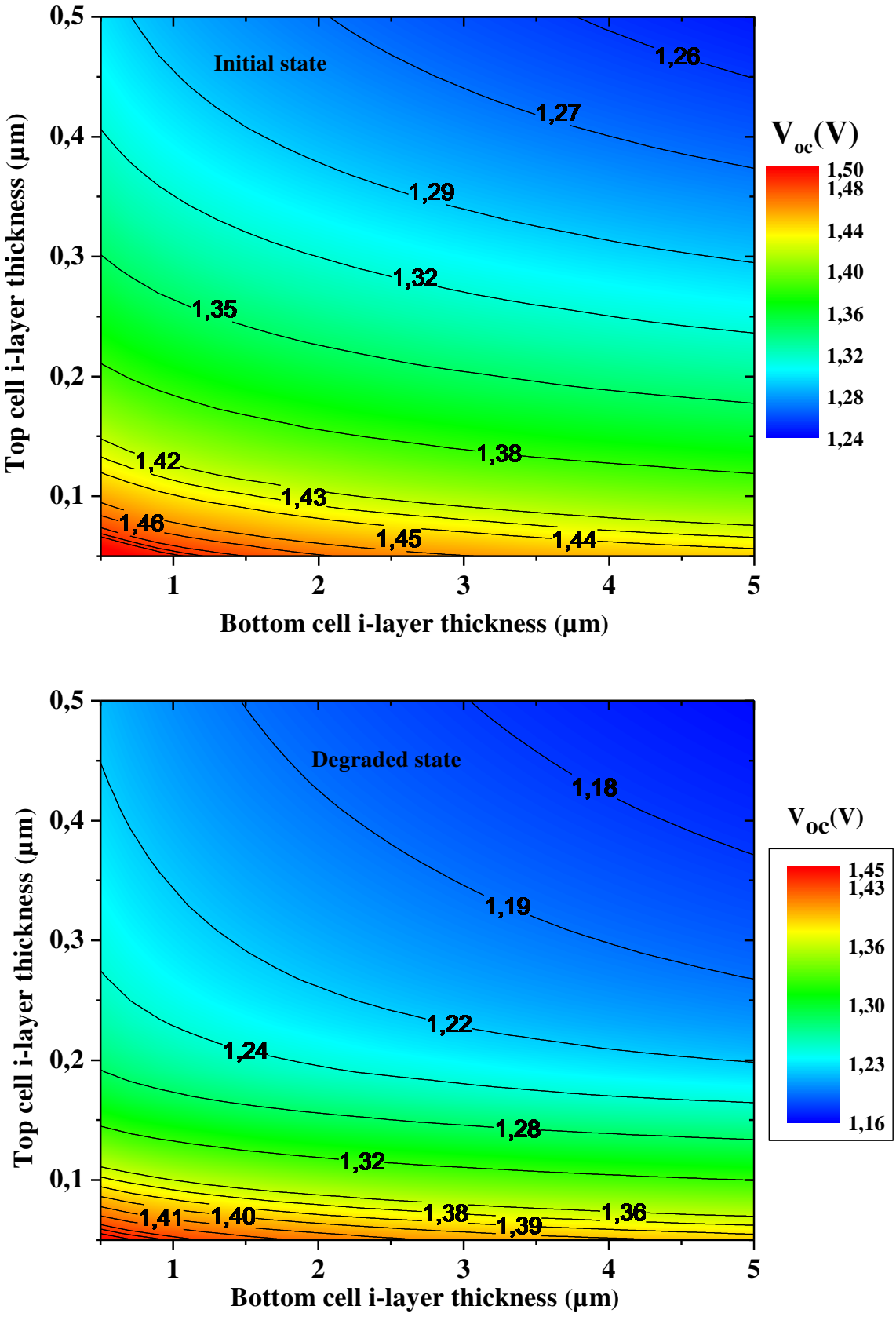

Figure V.44: V_{oc} vs. i-layer thickness, of the 2T- micromorph tandem cell at initial and degraded states respectively, for a general scanning of the top and bottom cell i-layer thicknesses.

For example, when the top cell i-layer is fixed at 0.1 µm and the bottom cell i-layer is varied from 0.5µm to 5µm, the V_{oc} is reduced only from about 1,46 V to 1.4 V. A similar comment can be deduced in the degraded state; the V_{oc} decreases from about 1,44V to 1.2 V when the top cell i-layer increases from 0.05µm to 0.5 µm and the bottom cell i-layer is less than 1µm. When the top cell i-layer is fixed at 0.1 µm and the bottom cell i-layer is varied from 0.5µm to 5µm, the V_{oc} is reduced only from about 1,39 V to 1.33 V.

Figures V.45 and V.46 show the FF vs. i-layer thickness of the 2T- micromorph tandem cell, at initial and degraded states, respectively. FF exhibits optimum values at very thin thicknesses: 0.17µm(top cell i-layer)/0.5 µm(bottom cell i-layer) at initial state for which FF reaches about 86.61%, and 0.13µm(top cell i-layer)/ 0.5 µm(bottom cell i-layer) at degraded state for which FF reaches about 84.36%.

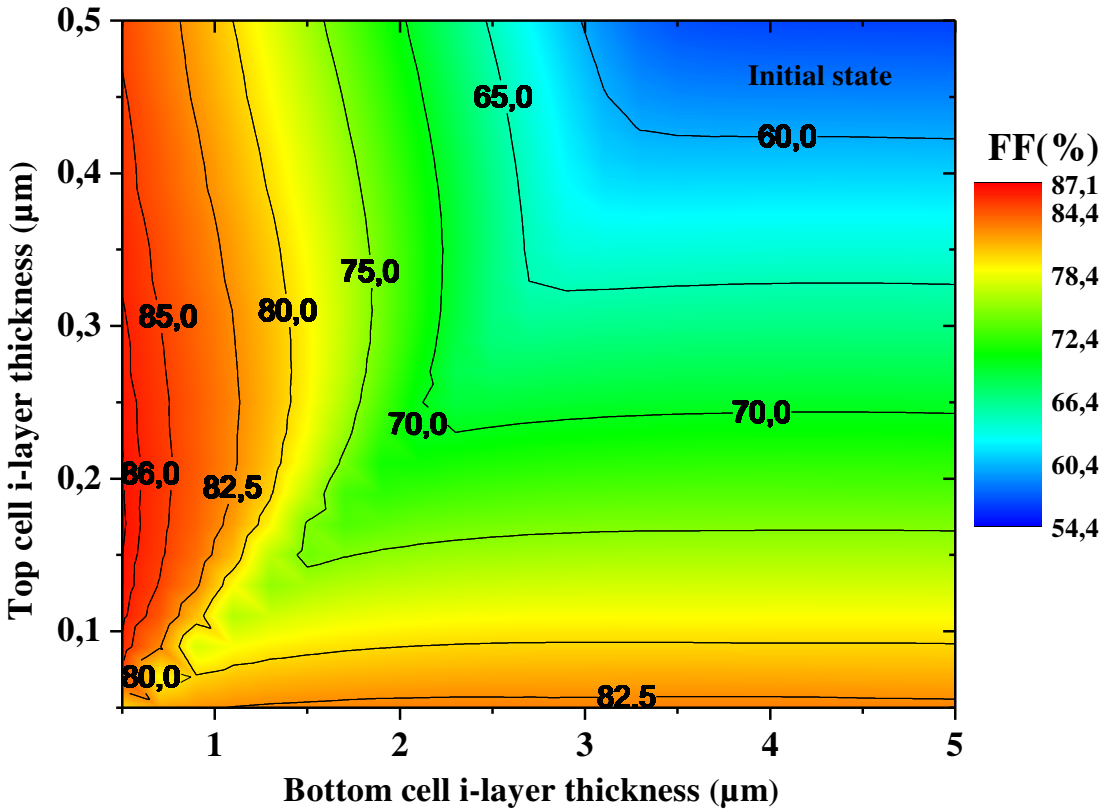

Figure V.45: The FF vs. i-layer thickness of the 2T- micromorph tandem cell at initial state, for a general scanning of the top and bottom cell i-layer thicknesses.

The better values that can be achieved after that will be reduced as the top and bottom cell i-layer thicknesses increase, mainly because of the surface and bulk

recombination explained before. A notable reduction to about 36.15% can be notified at the degraded state for the thicker thicknesses: 0.53µm (top cell i-layer)/ 5.1 µm (bottom cell i-layer).

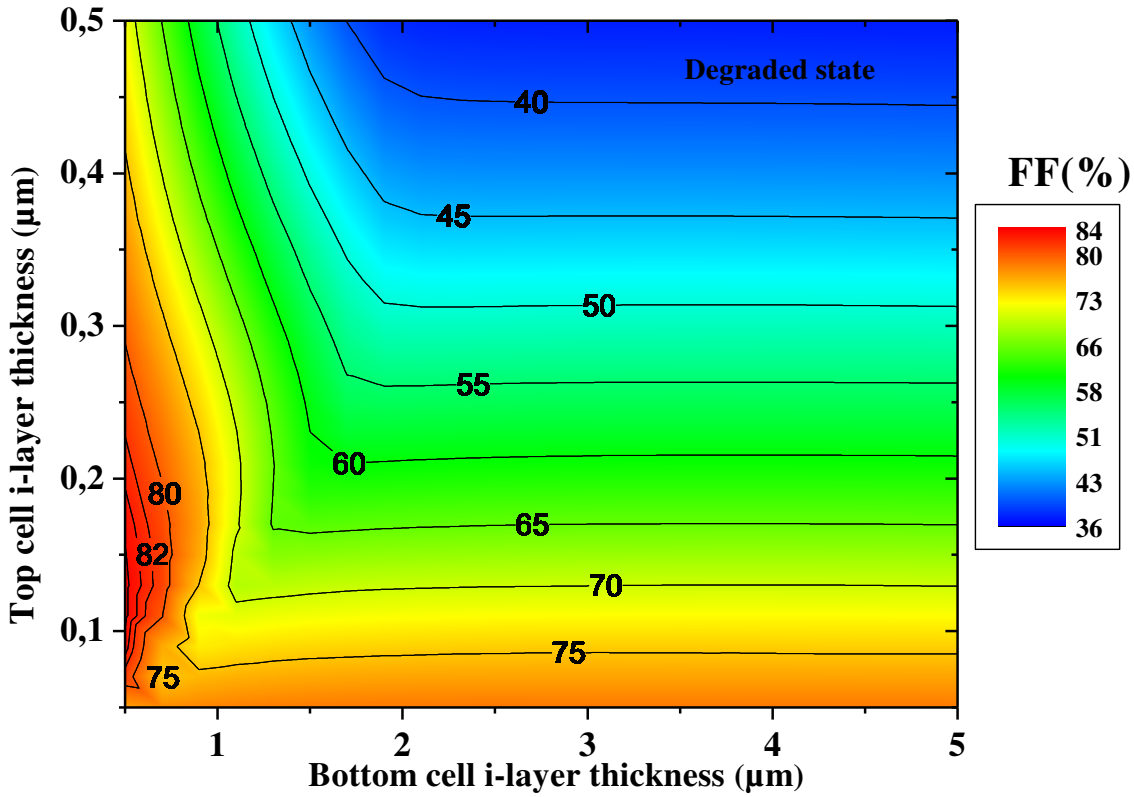

Figure V.46: The FF vs. i-layer thickness of the 2T- micromorph tandem cell at degraded state, for a general scanning of the top and bottom cell i-layer thicknesses.

Figure V.47 shows the conversion efficiency η vs. i-layer thickness, of the 2T-micromorph tandem cell at initial and degraded states respectively, for a general scanning of the top and bottom cell i-layer thicknesses. As we can see, the optimal conversion efficiency that can be achieved at initial state is about 10% with 0.17µm(top cell i-layer)/2.1 µm(bottom cell i-layer). At degraded state however, the best conversion efficiency η obtained is approximately 7.77% with 0.11µm (top cell i-layer)/ 1.1 µm(bottom cell i-layer).

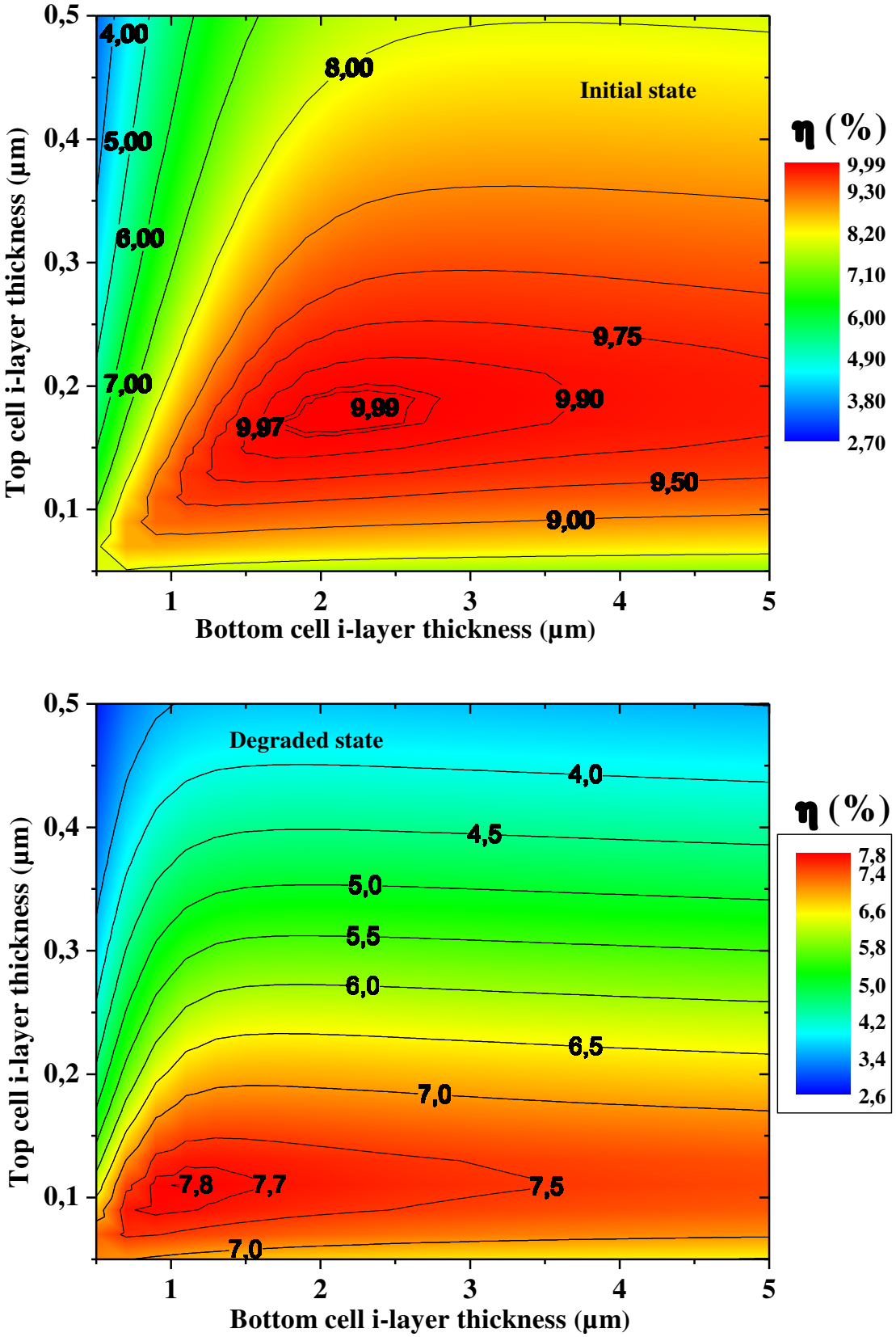

Figure V.47: Conversion efficiency η vs. i-layer thickness, of the 2T- micromorph tandem cell at initial and degraded states respectively, for a general scanning of the top and bottom cell i-layer thicknesses.

Table V.9 shows the J_{sc}, V_{oc}, FF and η values around the optimal η obtained at the initial and degraded states respectively, of the 2T- micromorph tandem cell.

Initial state

Bottom cell µm	Top cell µm	Jsc mA/cm2	Voc Volt	FF %	Efficiency %
1,9	0,45	8,42143	1,28147	72,6272	7,83779
1,9	0,47	8,3243	1,27823	72,2055	7,68293
1,9	0,49	8,23246	1,2751	71,73	7,52965
2,1	0,05	6,20552	1,47038	82,993	7,57267
2,1	0,07	7,20384	1,44904	81,5097	8,50851
2,1	0,09	7,97106	1,43031	80,0393	9,12535
2,1	0,11	8,59144	1,41377	78,5519	9,54116
2,1	0,13	9,09477	1,39936	77,0234	9,80266
2,1	0,15	9,49698	1,38549	75,5324	9,93853
2,1	0,17	9,83937	1,37327	74,0336	10,0035
2,1	0,19	10,1102	1,36244	72,5372	9,99166
2,1	0,21	10,3391	1,35197	71,1269	9,94223
2,1	0,23	10,481	1,3429	69,9354	9,84336
2,1	0,25	10,3784	1,33413	70,1612	9,71461
2,1	0,27	10,1871	1,32616	70,7873	9,56317
2,1	0,29	10,0044	1,31934	71,3111	9,4125
2,1	0,31	9,83441	1,31216	71,6118	9,24101
2,1	0,33	9,67688	1,30604	71,6793	9,05911
2,1	0,35	9,53051	1,30075	71,6921	8,88754
2,1	0,37	9,39408	1,29528	71,539	8,70484

Degraded state

Bottom cell µm	Top cell µm	Jsc mA/cm2	Voc Volt	FF %	Efficiency %
0,9	0,43	5,16836	1,20891	62,1381	3,88244
0,9	0,45	5,09192	1,2069	60,939	3,74497
0,9	0,47	5,02016	1,20497	59,7138	3,61217
0,9	0,49	4,95263	1,20321	58,5241	3,48748
0,9	0,51	4,88892	1,20157	57,3669	3,36995
0,9	0,53	4,82871	1,20006	56,2312	3,25845
1,1	0,05	6,10847	1,4352	78,2977	6,86426
1,1	0,07	6,98994	1,40391	75,9587	7,45401
1,1	0,09	7,62866	1,37512	73,5543	7,71608
1,1	0,11	8,11776	1,34757	71,0966	7,77743
1,1	0,13	8,45837	1,32215	68,6449	7,67672
1,1	0,15	8,2806	1,29878	69,3076	7,45381
1,1	0,17	7,98029	1,27841	70,4145	7,18375
1,1	0,19	7,71586	1,26234	70,766	6,89264
1,1	0,21	7,48192	1,25047	70,7124	6,61579
1,1	0,23	7,27329	1,24209	70,1364	6,33618
1,1	0,25	7,08584	1,23522	69,2729	6,06316
1,1	0,27	6,91633	1,2297	68,1598	5,797
1,1	0,29	6,76212	1,2254	66,9048	5,54393
1,1	0,31	6,6211	1,22177	65,4496	5,29452

Table V-9: The J_{sc}, V_{oc}, FF and η values around the optimal η obtained at the initial and degraded states respectively, of the 2T- micromorph tandem cell.

Figures V.48 and V.49 show the distribution of the electric field, generation (G) and recombination (R) rates inside the 2T-micromorph tandem cell, with the top and bottom cell i-layer thicknesses which display the optimal conversion efficiency η , 10% and 7.77%, at initial and degraded states, respectively.

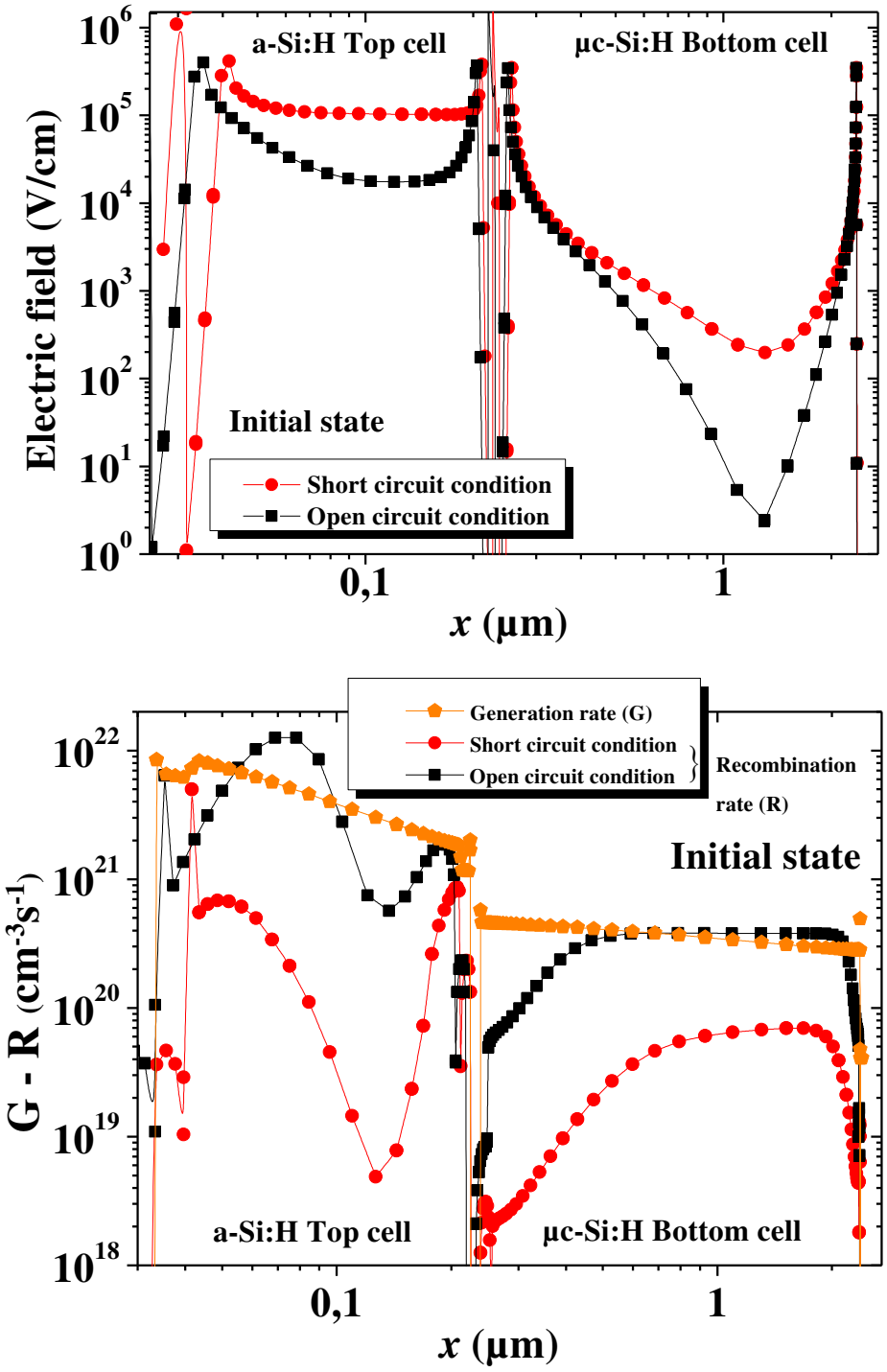

Figure V.48: Distribution of the electric field, generation (G) and recombination (R) rates inside the 2T-micromorph tandem cell at initial state, with 0.17µm (top cell i-layer)/2.1 µm(bottom cell i-layer).

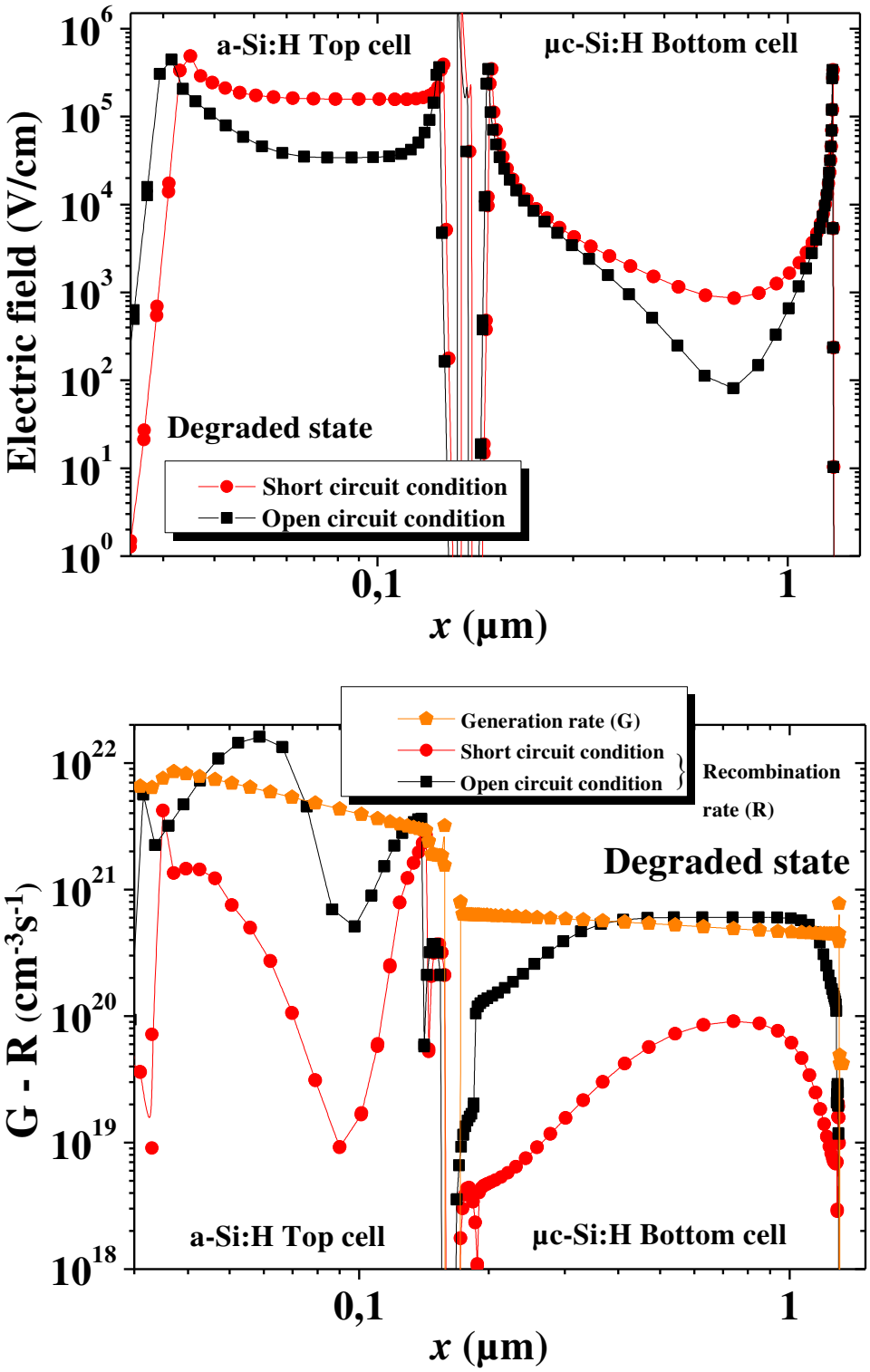

Figure V.49: Distribution of the electric field, generation (G) and recombination (R) rates inside the 2T-micromorph tandem cell at degraded state, with 0.11µm (top cell i-layer)/1.1 µm(bottom cell i-layer).

From these figures, we can see that the electrical parameters of the 2T-micromorph tandem cell are mostly limited by those of the a-Si:H top sub-cell, either at short circuit condition, or at the open circuit one.

Figure V.50 shows the top and bottom sub-cell $J-V$ characteristics of the 4T-micromorph tandem cell, at initial and degraded states respectively, where the top cell i-layer thickness is varied from 0.1µm to 0.5µm, and the one of the bottom cell is fixed to 3.8 µm. In such a configuration, the two sub-cells are optically coupled and electrically decoupled.

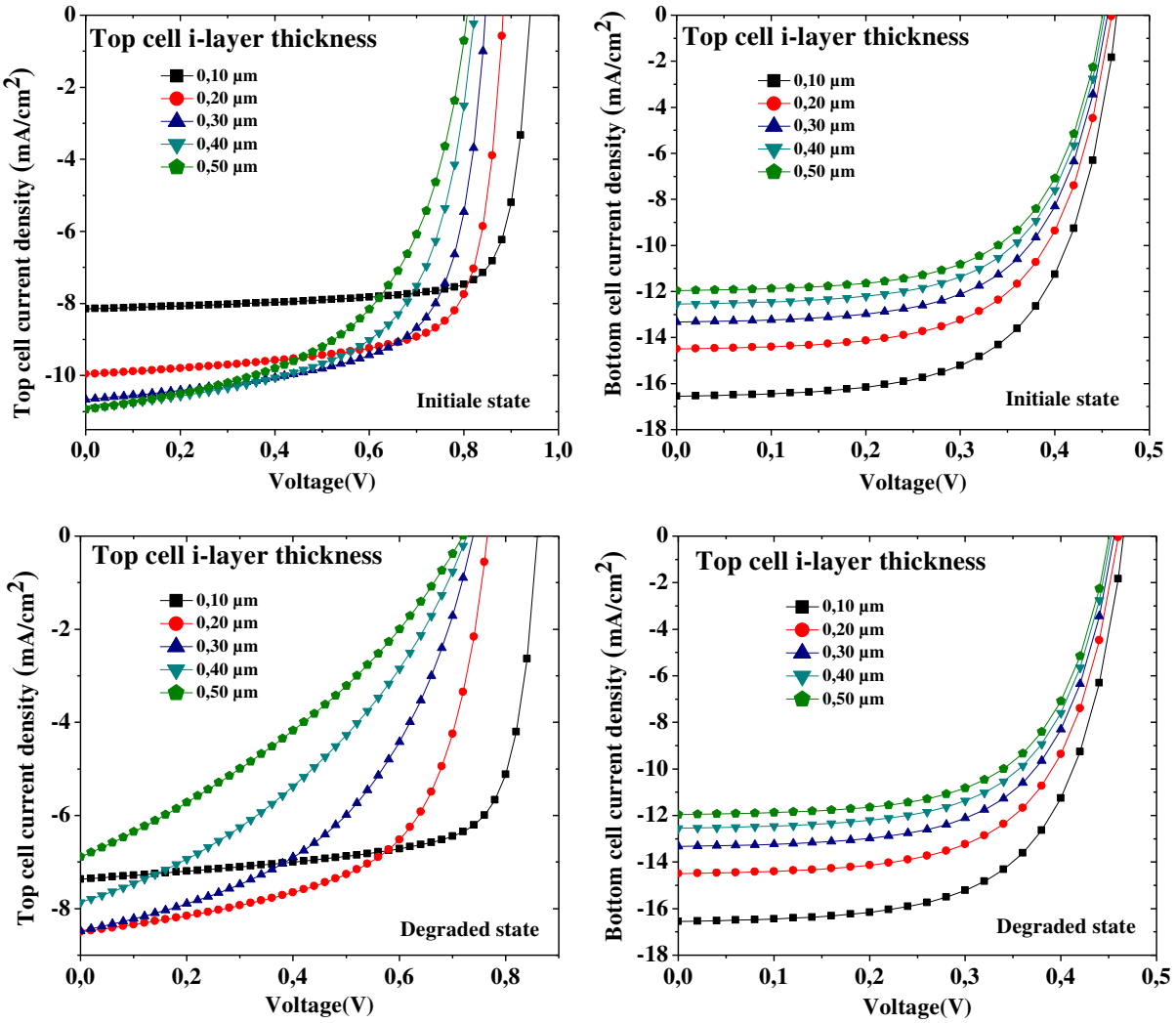

Figure V.50: The top and bottom sub-cell $J-V$ characteristics of the 4T-micromorph tandem cell at initial and degraded states respectively, the top cell i-layer thickness is varied from 0.1µm to 0.5µm, and the one of the bottom cell is fixed to 3.8 µm.

At the initial state, as well as at the degraded one, the top sub-cell $J-V$ characteristics show a noticeable sensitivity to the top cell i-layer thickness. The J_{SC} increases with increasing the top cell i-layer thickness and tends to saturate beyond 0.4µm at the initial state. At the degraded one, it increases at first with increasing the top cell i-layer thickness until 0.2µm, then it decreases with an additional increase of the top cell i-layer thickness. The reduction of V_{OC} with increasing the top cell i-layer

thickness is also discernable for both states because of the recombination which gives a significant effect more the top cell i-layer is thick . The bottom sub-cell V_{OC} however, shows less sensitivity to the top cell i-layer thickness, while its J_{SC} is reduced because most of the light is absorbed by the top cell i-layer as it becomes thicker, and herein the effect of the a-Si:H defect density of state is more significant. To this corresponds a consequent reduction of the bottom sub-cell EQE as shown is figure V.51.

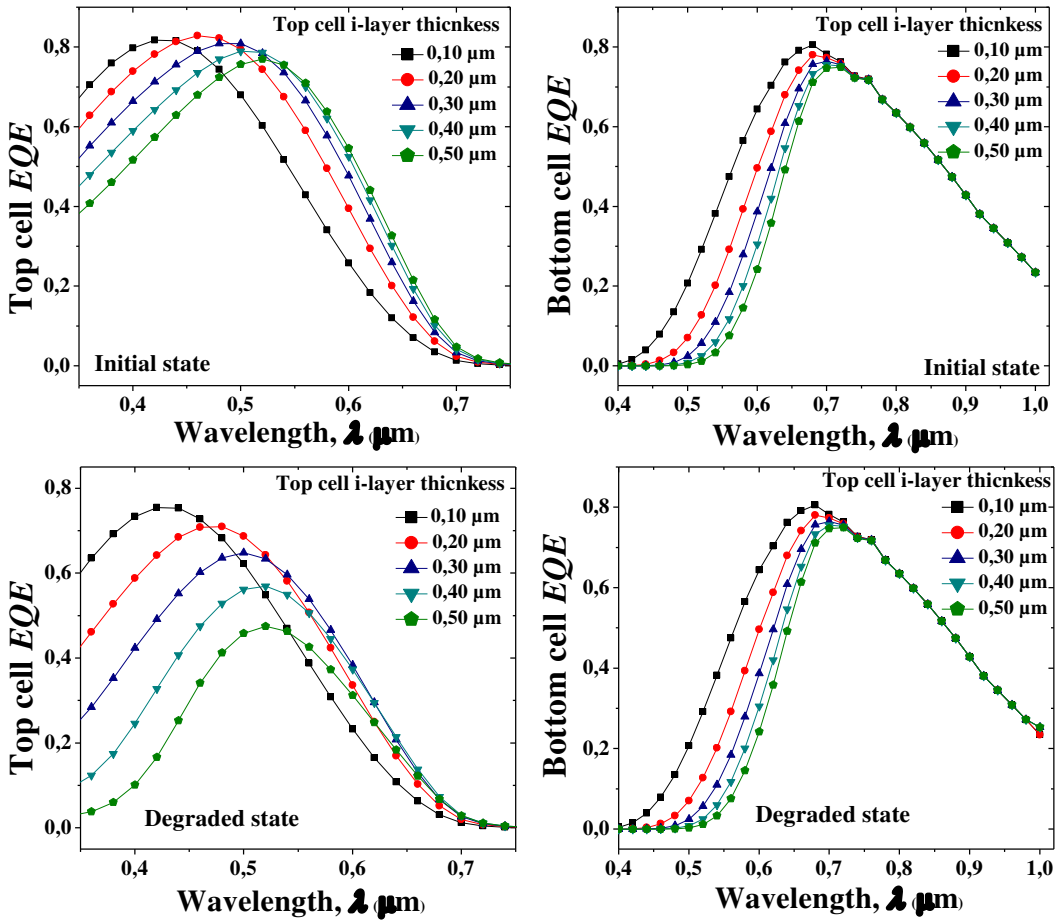

Figure V.51: The top and bottom sub-cell EQE of the 4T-micromorph tandem cell at initial and degraded states respectively, the top cell i-layer thickness is varied from 0.1µm to 0.5µm, and the one of the bottom cell is fixed to 3.8 µm.

Figures V.52 and V.53 show the top and bottom sub-cell $J-V$ characteristics and EQE curves of the 4T-micromorph tandem cell, at initial and degraded states respectively, when the top cell i-layer thickness is fixed to 0.11 µm and the one of the bottom cell is varied from 1µm to 5µm.

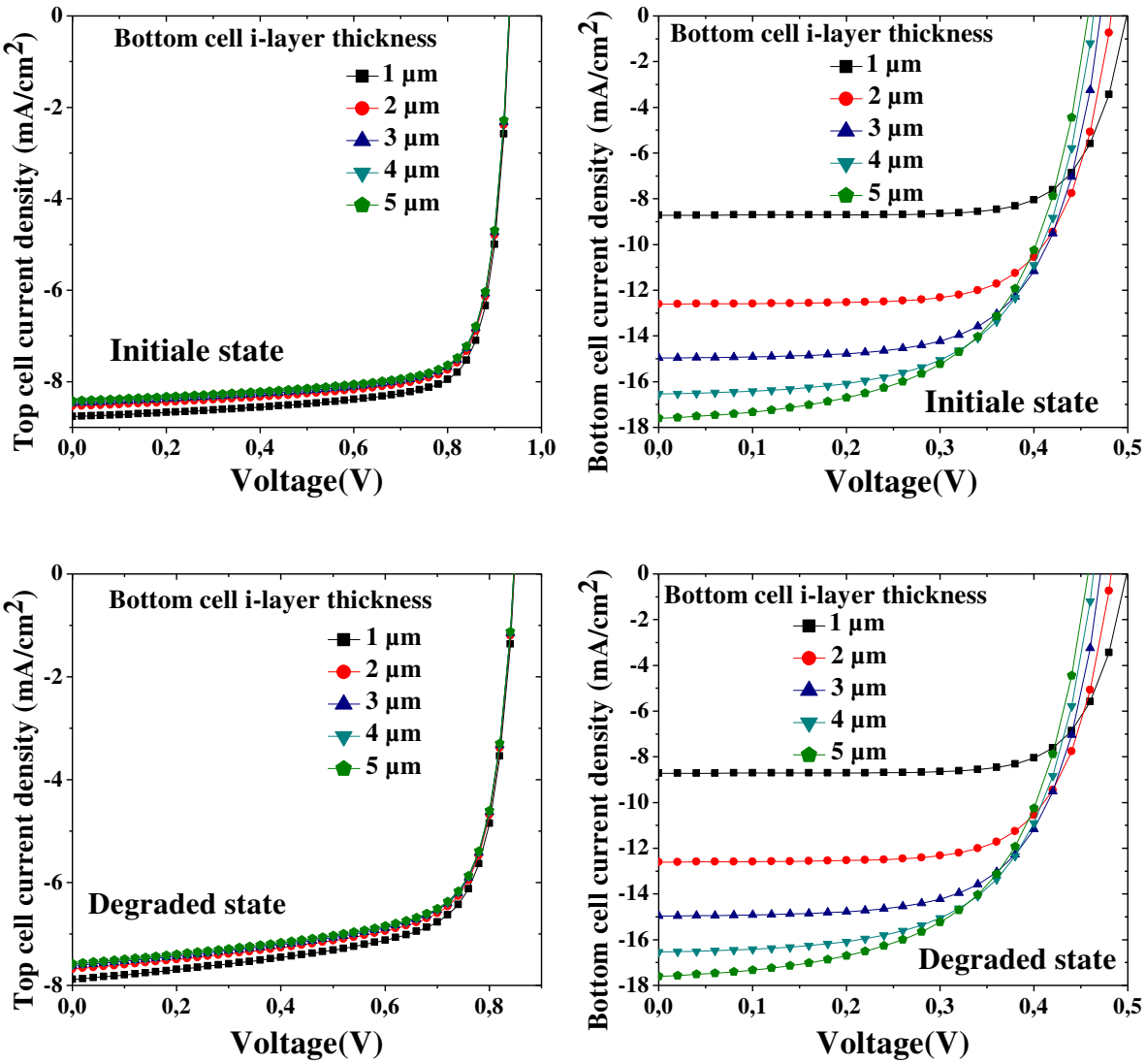

Figure V.52: The top and bottom sub-cell $J-V$ characteristics of the 4T-micromorph tandem cell at initial and degraded states respectively, the top cell i-layer thickness is fixed to 0.11 µm and the one of the bottom cell is varied from 1µm to 5µm.

The top sub-cell $J-V$ characteristics display an insignificant dependency on the bottom cell i-layer thickness; their J_{sc} decreases very slightly with the increasing of the bottom cell i-layer thickness, while their V_{oc} is insensitive.

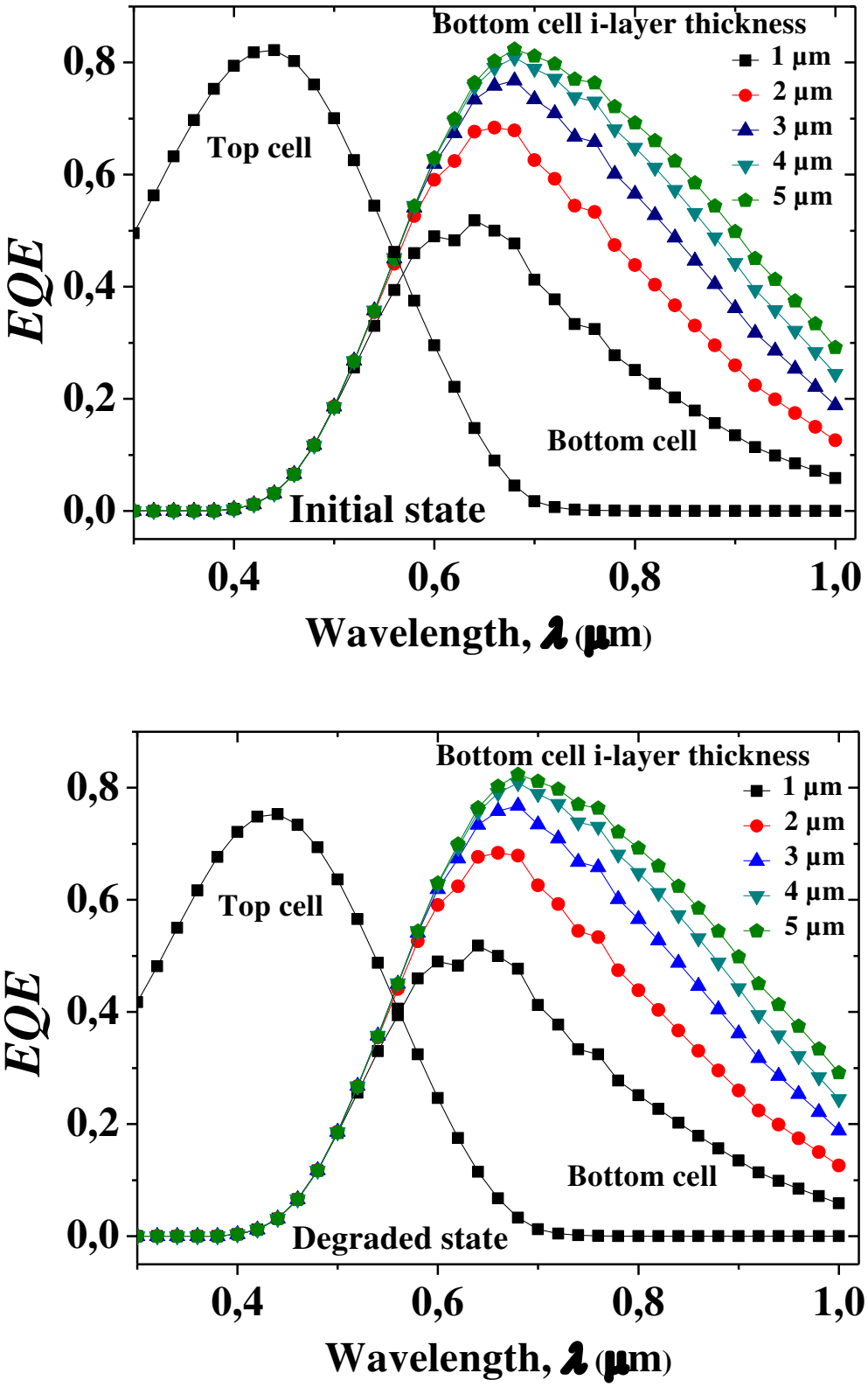

Figure V.53: The top and bottom sub-cell EQE of the 4T-micromorph tandem cell at initial and degraded states respectively, the top cell i-layer thickness is fixed to 0.11 µm and the one of the bottom cell is varied from 1µm to 5µm.

The bottom sub-cell $J-V$ characteristics show a behaviour similar to the one of the single µc-Si:H cell; the J_{sc} increases with increasing the bottom cell i-layer thickness because of the path length of the light which increases and so the optical absorption, while the V_{oc} knows some reduction because of the bulk recombination .

The top cell EQE undergoes some decrease at the degraded state, but does not display any influence by the bottom cell i-layer thickness, while the bottom cell EQE shows an improvement as this latter is increased. It is obvious that the top cell photo-response is mostly limited by the property effect of this one on the incident light, rather than any variation from the bottom sub cell.

Figures V.54 – V.61 show the top and bottom sub-cell J_{sc}, V_{oc}, FF and η vs. i-layer thickness for a full scanning of the top and bottom cell i-layer thicknesses from 0.05µm to 0.5µm and 0.5µm to 5µm respectively, at initial and degraded states.

The best value of the top sub-cell J_{sc} at initial state is about 11.55 mA/cm^2 with 0.43µm (top cell i-layer)/0.5 µm (bottom cell i-layer). At degraded state, it is about 9.15 mA/cm^2 with 0.25µm (top cell i-layer)/0.5 µm (bottom cell i-layer); the top cell i-layer here is thinner because of the light soaked effect. The improvement of the bottom sub-cell J_{sc} is achieved more the bottom cell i-layer is thick; it reaches about 19.76 mA/cm^2 with 0.05µm (top cell i-layer)/5 µm (bottom cell i-layer) both at initial and degraded states.

The top sub-cell V_{oc} displays a clear reduction as the top cell i-layer becomes thicker (figures V.56 and V.57), however it does not show any influence by the bottom cell i-layer thickness. The bottom sub-cell V_{oc} shows some decrease as both top and bottom cell i-layers become thicker, but its reduction is less than the one of the top sub-cell V_{oc} .

The FF exhibits a dependency only on its corresponding i-layer thickness (figures V.58 and V.59); the top sub-cell FF is reduced from about 79.76% to 53.20% at initial state, at the degraded one; it is reduced from 74.55% to 33.20% as the top cell i-layer thickness increases. The bottom sub-cell FF is reduced from about 76.20% to 58.17% at initial state, at the degraded one; it is reduced from 76.54% to 57.84% as the bottom cell i-layer thickness increases.

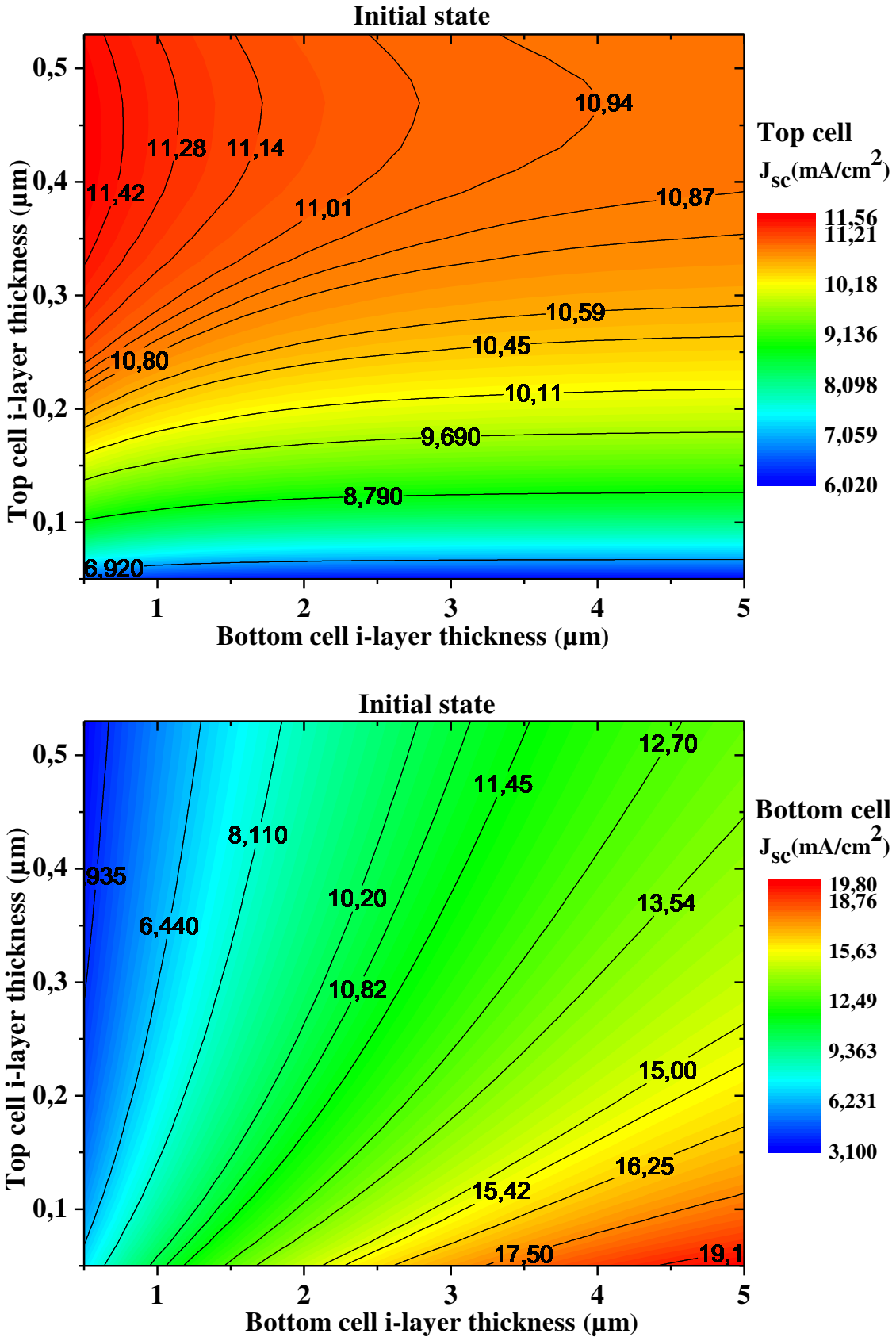

Figure V.54: Top and bottom sub-cell J_{sc} vs. top and bottom cell i-layer thicknesses at initial state.

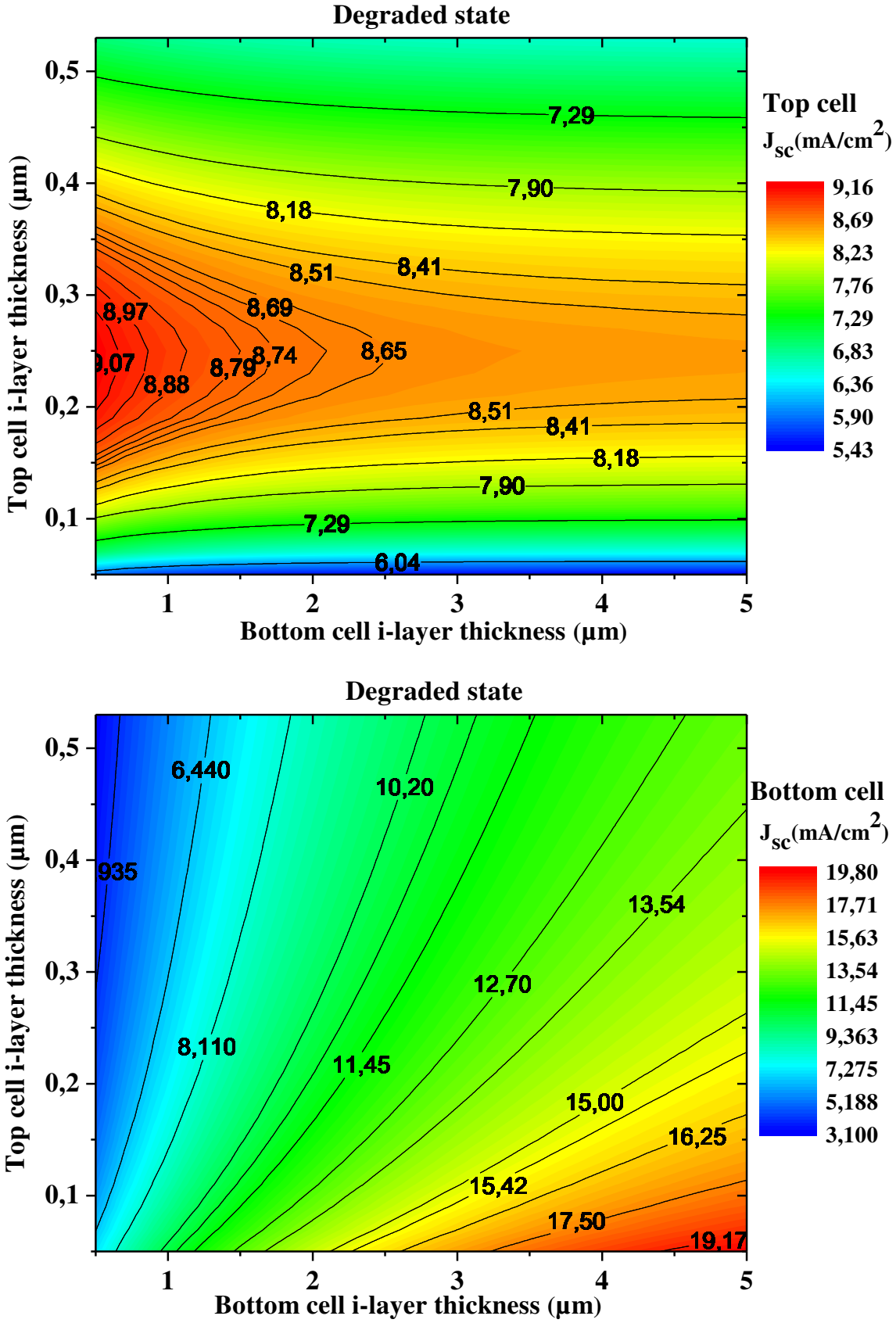

Figure V.55: Top and bottom sub-cell J_{sc} vs. top and bottom cell i-layer thicknesses at degraded state.

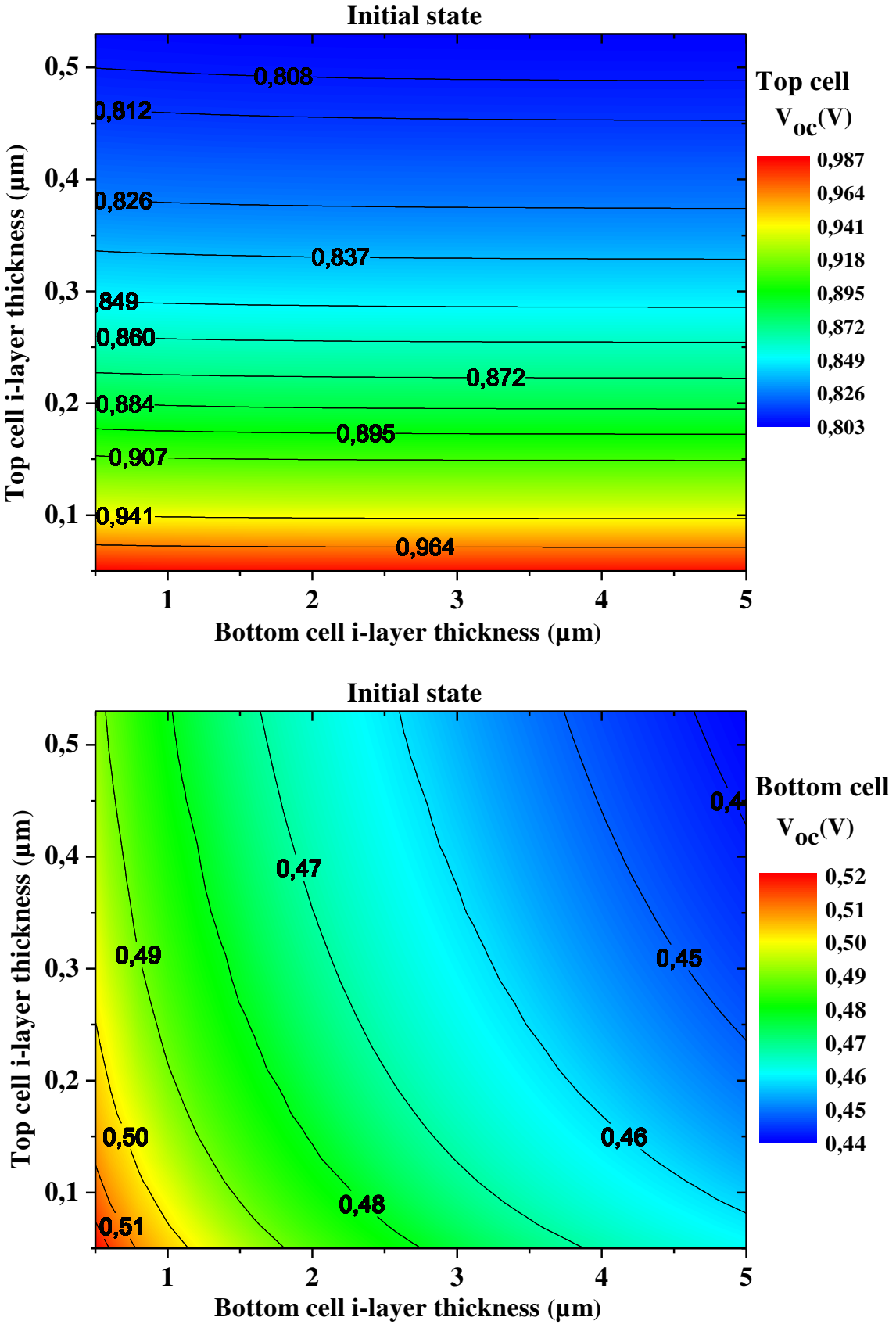

Figure V.56: Top and bottom sub-cell V_{oc} vs. top and bottom cell i-layer thicknesses at initial state.

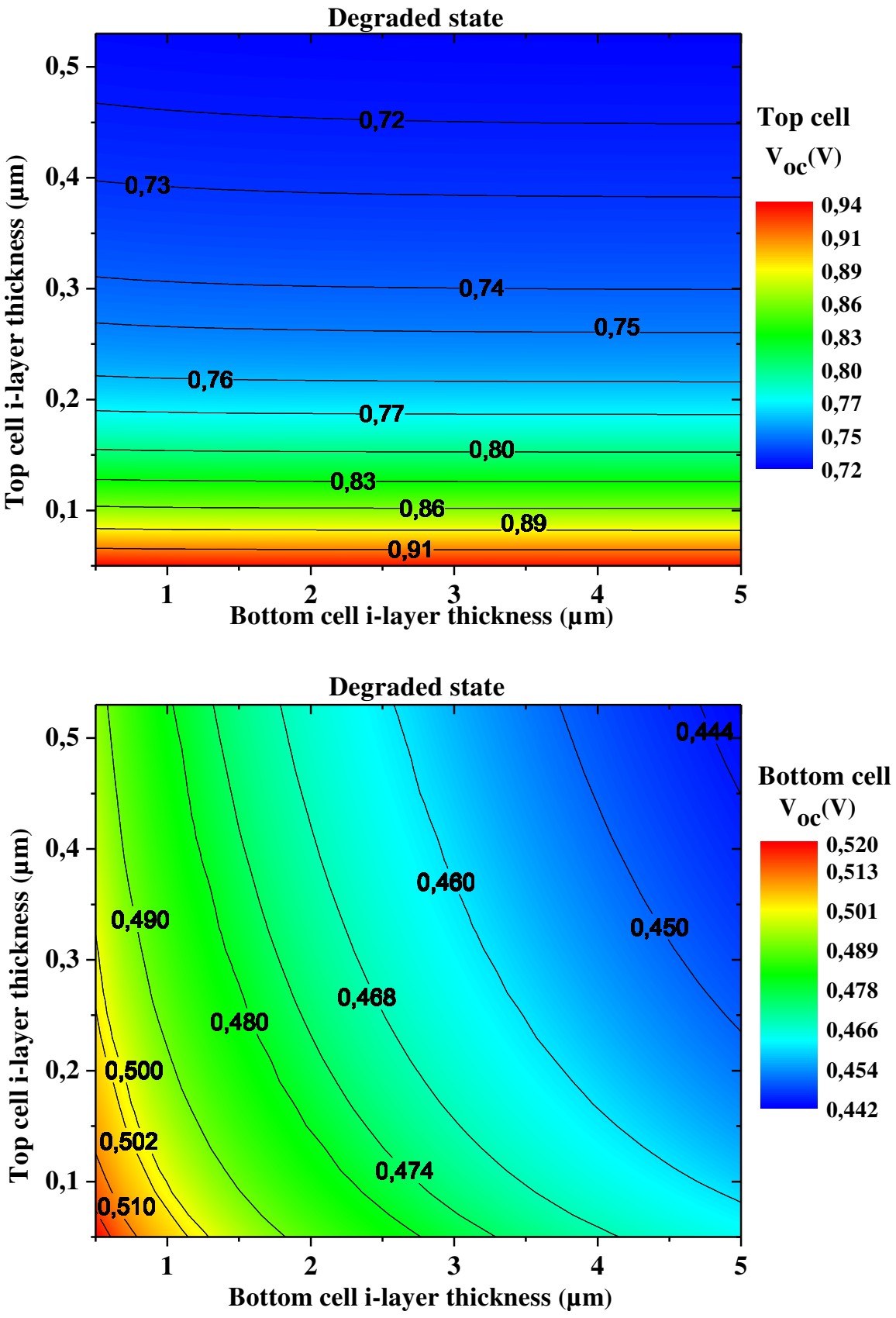

Figure V.57: Top and bottom sub-cell V_{oc} vs. top and bottom cell i-layer thicknesses at degraded state.

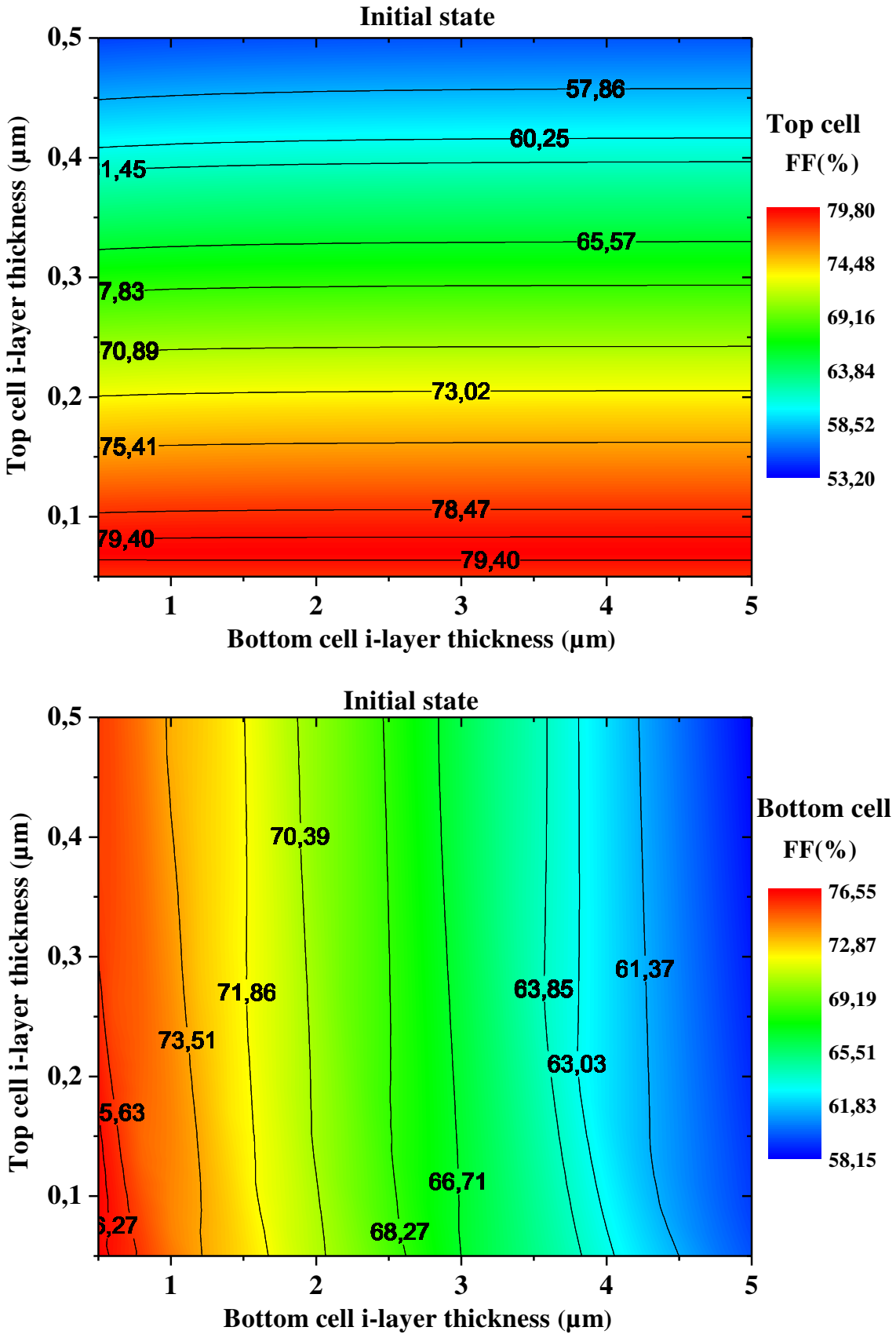

Figure V.58: Top and bottom sub-cell FF vs. top and bottom cell i-layer thicknesses at initial state.

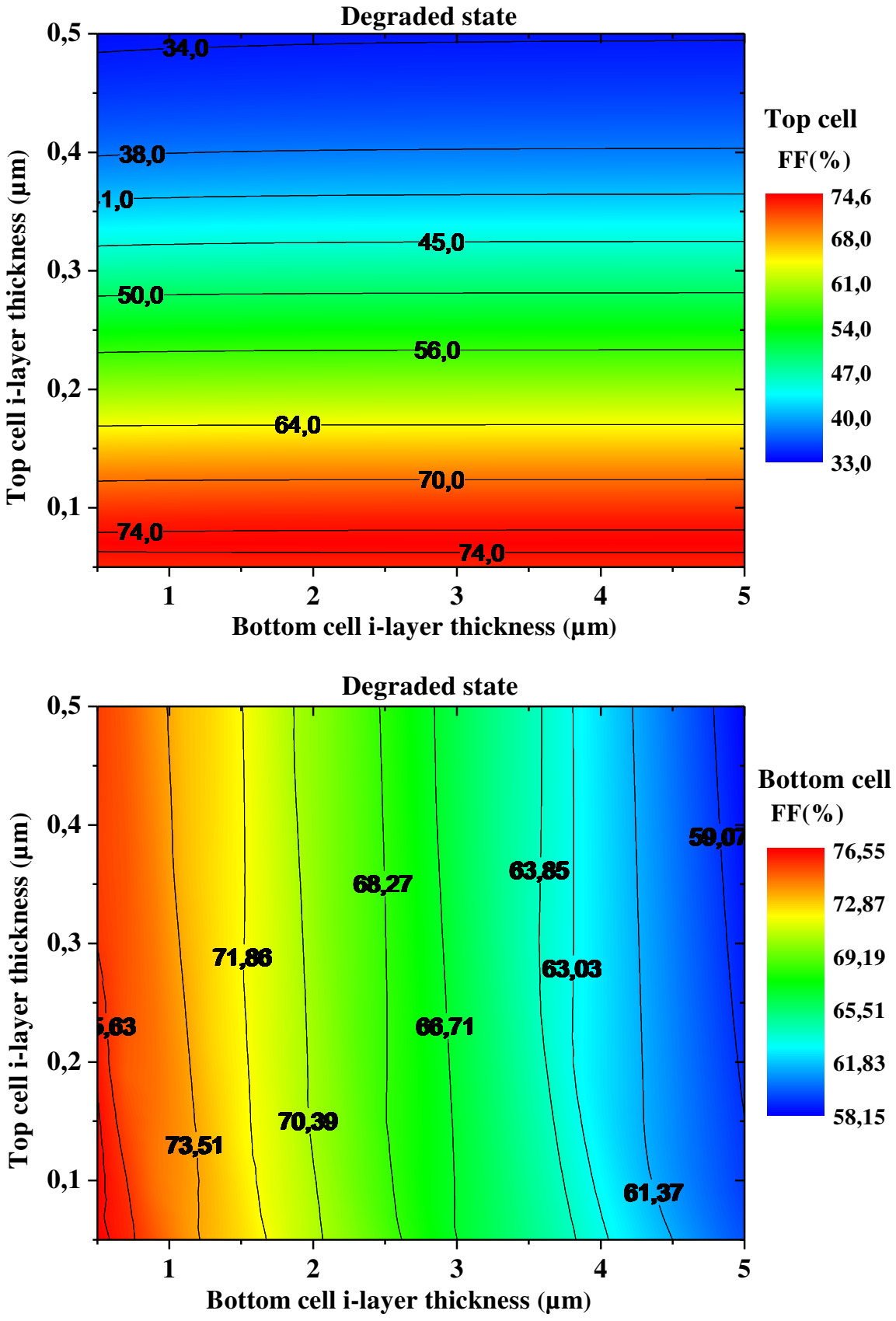

Figure V.59: Top and bottom sub-cell FF vs. top and bottom cell i-layer thicknesses at degraded state.

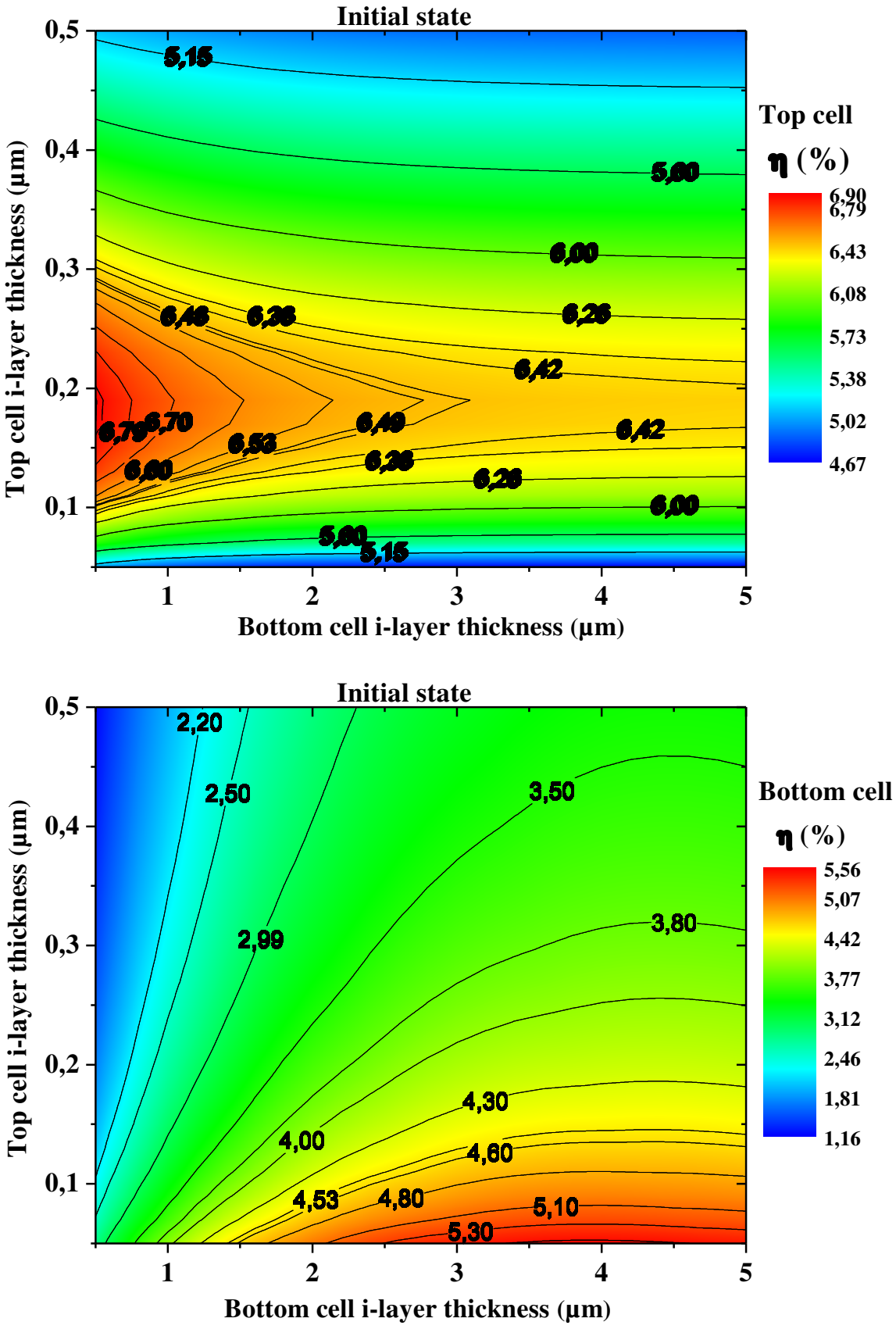

Figure V.60: Top and bottom sub-cell conversion efficiency η vs. top and bottom cell i-layer thicknesses at initial state.

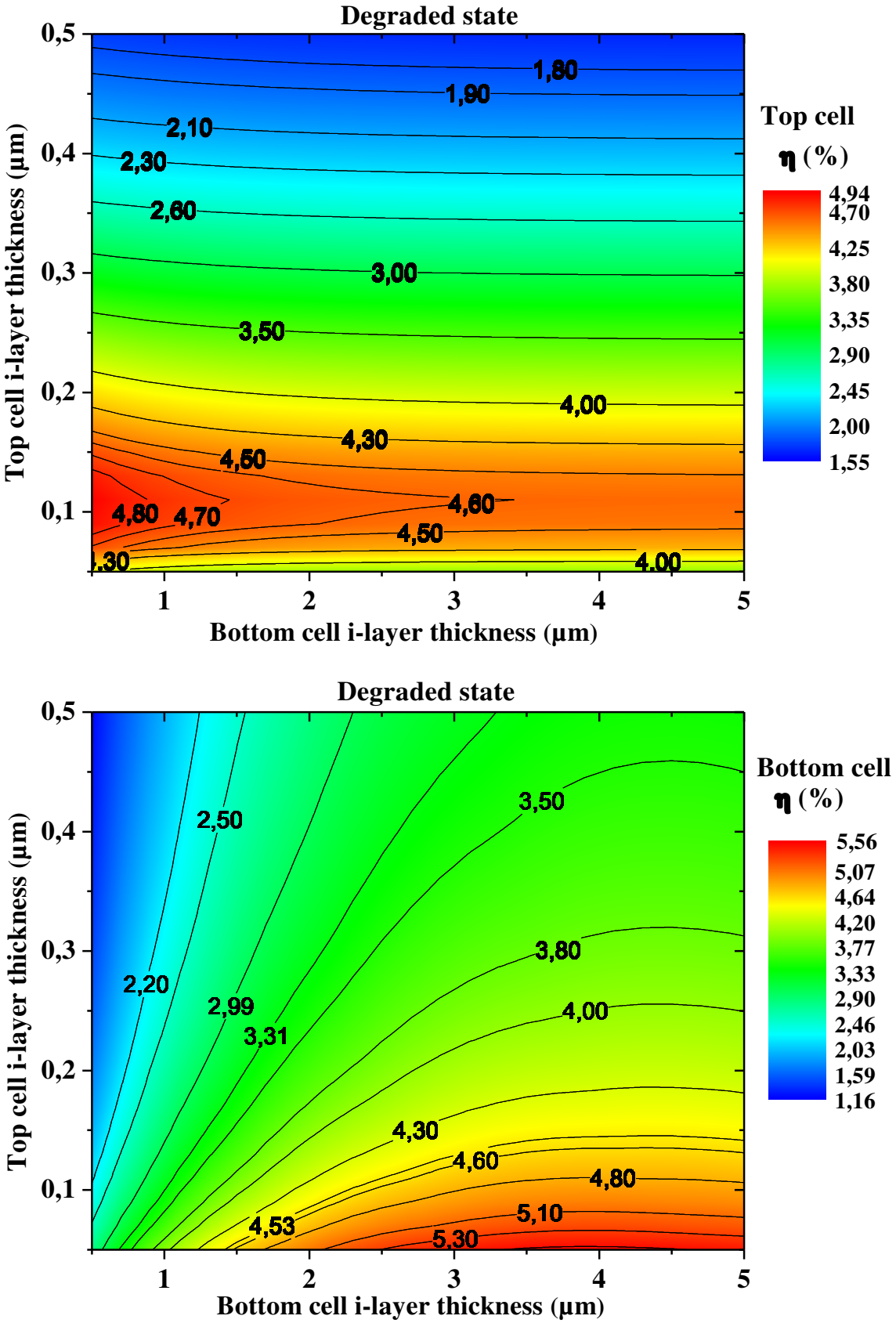

Figure V.61: Top and bottom sub-cell conversion efficiency η vs. top and bottom cell i-layer thicknesses at degraded state.

The best value of the top cell conversion efficiency η is approximately 6.9% at initial state with 0.19µm(top cell i-layer/0.5µm(bottom cell i-layer). At degraded state, it decreases to 4.93% with 0.11µm(top cell i-layer/0.5µm(bottom cell i-layer). The bottom cell conversion efficiency η exhibits an optimal value of 5.54% for 0.05µm(top cell i-layer/4µm(bottom cell i-layer) at both initial and degraded states.

The total conversion efficiency of the 4T-micromorph tandem cell is given by the sum of the top and bottom sub-cell conversion efficiencies presented in figures V.60 and V.61 respectively. Its behaviour vs. top and bottom cell i-layer thicknesses is illustrated in figures V.62 and V.63, at initial and degraded states respectively.

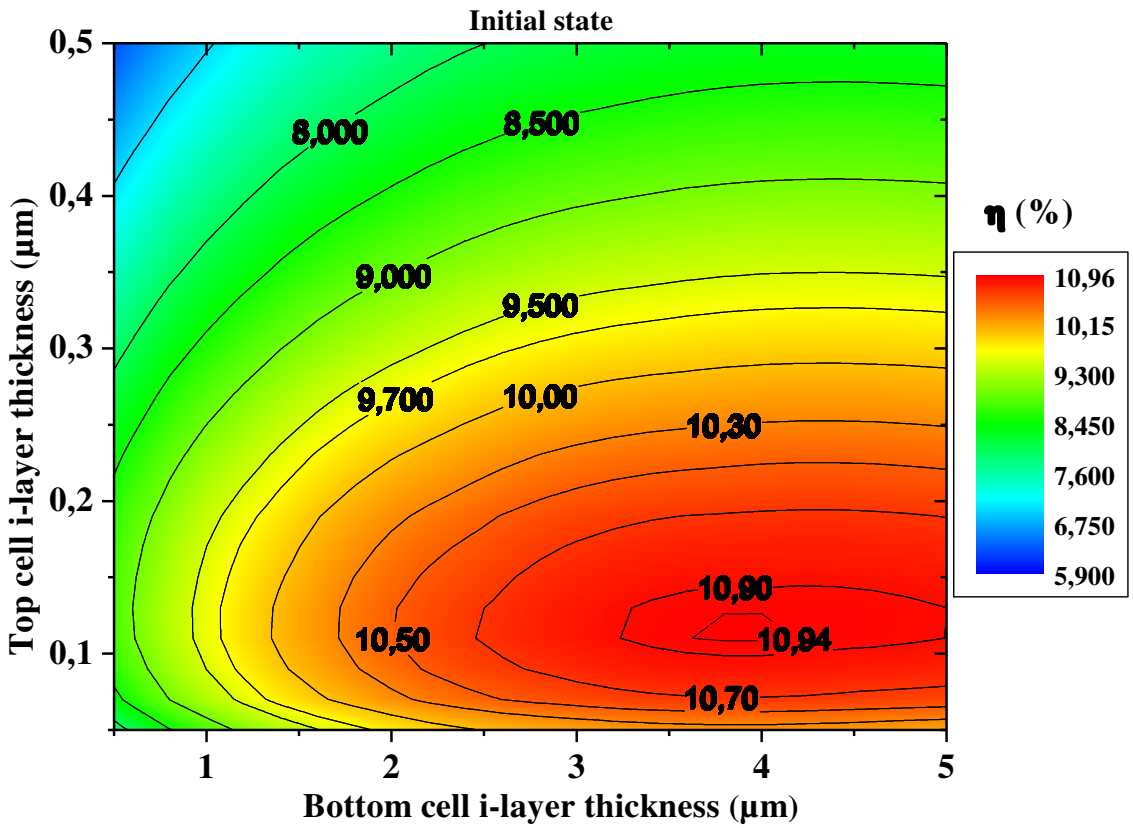

Figure V.62: Conversion efficiency η of the 4T-micromorph tandem cell vs. top and bottom cell i-layer thicknesses at initial state.

At the initial state, the η shows an optimal value of 10.94% for 0.11µm(top cell i-layer) /3.8µm (bottom cell i-layer). At degraded state, the optimal value of η is reduced to 9.59% for 0.07µm(top cell i-layer) /3.8µm (bottom cell i-layer).

We remind that the 2T-micromorph tandem cell exhibits an optimum η of 10% at initial state for 0.17µm(top cell i-layer)/2.1 µm(bottom cell i-layer), and of 7.77% at degraded state for 0.11µm (top cell i-layer)/ 1.1 µm(bottom cell i-layer). We can

deduce that the 4T- device configuration brings some improvement to the solar cell conversion efficiency.

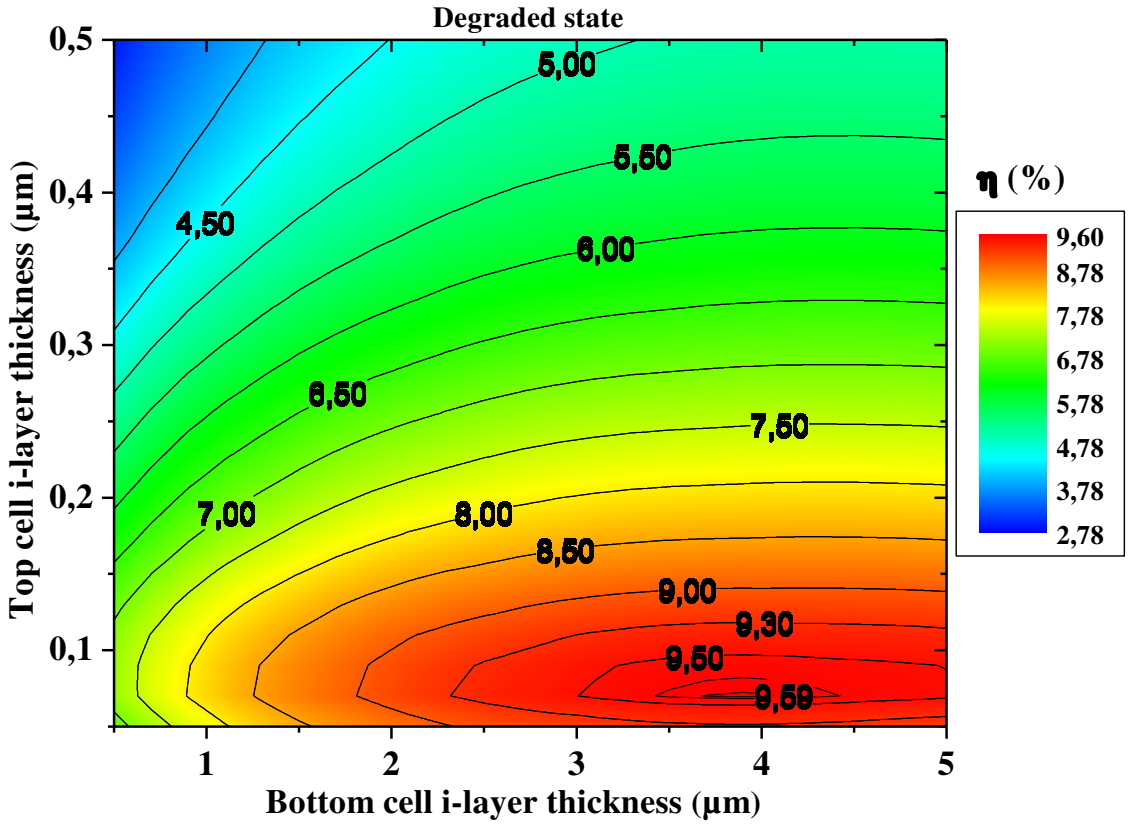

Figure V.63: Conversion efficiency η of the 4T-micromorph tandem cell vs. top and bottom cell i-layer thicknesses at degraded state.

V.4) Mobility effect on a-Si:H and µc-Si:H-based solar cell performance

To achieve some improvements in our studied solar cells, we varied the i-layer mobilities of the single cells based on a-Si:H and µc-Si:H, and of the micromorph tandem cell with 2T and 4T connections, as shown in tables V.10-V.15 respectively. The mobilities are varied in the experimental range from literatures [123, 153-155]. 4T- η (%) in tables V.14 and V.15 refers to the total conversion efficiency of the 4T-micromorph tandem cell which is given by the sum of the top and bottom sub-cell conversion efficiencies.

a-Si:H single cell		I-layer mobilities ($cm^2 V^{-1} s^{-1}$)											
		μ_n/μ_p=10				μ_n=20				μ_n=25			
		μ_n				μ_p				μ_p			
		2	15	20	25	0.2	1	3	6	0.2	1	3	6
J_{sc} (mA/cm^2)	Initial	10.82	11.6996	11.7432	11.7699	11.2739	11.674	11.7677	11.793	11.286	11.6861	11.7797	11.805
	Degraded	9.5596	11.3612	11.479	11.5532	10.5439	11.2768	11.5587	11.646	10.5715	11.304	11.5859	11.6732
V_{co}(V)	Initial	0.9121	0.91757	0.91796	0.918202	0.913374	0.91704	0.91831	0.91870	0.91341	0.917078	0.91834	0.91873
	Degraded	0.8100	0.81941	0.82019	0.820571	0.81164	0.81803	0.82082	0.82158	0.81171	0.818072	0.82083	0.82158
FF(%)	Initial	75.7689	82.5202	82.9411	83.2035	78.6142	82.0827	83.2672	83.6167	78.6912	82.1536	83.3372	83.686
	Degraded	66.6972	77.1677	78.0964	78.7261	72.8071	76.5302	78.8554	79.7743	73.0015	76.7272	79.0458	79.9624
η (%)	Initial	7.4775	8.8588	8.94087	8.99192	8.09513	8.78743	8.99824	9.05923	8.1121	8.80446	9.01529	9.07628
	Degraded	5.1647	7.1839	7.35283	7.46341	6.23072	7.05981	7.48156	7.6329	6.2642	7.09534	7.51734	7.66879

Table V-10: J_{sc}, V_{oc}, FF and η vs. i-layer mobilities of the a-Si:H-based single solar cell.

µc-Si:H single cell	I-layer mobilities ($cm^2 V^{-1} s^{-1}$)											
	μ_n/μ_p=10				μ_n=35				μ_n=50			
	μ_n				μ_p				μ_p			
	15	20	35	50	1.5	2	3.5	5	1.5	2	3.5	5
J_{sc}(mA/cm^2)	26.3893	26.4595	26.5491	26.5851	26.4765	26.5086	26.5491	26.5664	26.498	26.5297	26.5689	26.5851
V_{co}(V)	0.48965	0.48911	0.48836	0.48805	0.48968	0.48913	0.48836	0.48804	0.48969	0.48913	0.48837	0.48805
FF(%)	65.9483	67.2307	69.0503	69.8406	66.171	67.3844	69.0503	69.745	66.2155	67.4413	69.1319	69.8406
η (%)	8.52157	8.70073	8.9529	9.06185	8.57917	8.73716	8.9529	9.04289	8.59201	8.75165	8.97033	9.06185

Table V-11: J_{sc}, V_{oc}, FF and η vs. i-layer mobilities of the µc-Si:H-based single solar cell.

2T- micromorph tandem cell		Bottom cell i-layer mobilities ($cm^2 V^{-1} s^{-1}$)											
		μ_n=15, μ_p=2											
		Top cell i-layer mobilities ($cm^2 V^{-1} s^{-1}$)											
		μ_n/μ_p=10				μ_n=20				μ_n=25			
		μ_n				μ_p				μ_p			
		2	15	20	25	0.2	1	3	6	0.2	1	3	6
J_{sc}(mA/cm^2)	Initial	10.0964	10.9104	10.9514	10.9766	10.6105	10.8982	10.9707	10.991	10.6244	10.9121	10.9844	11.0046
	Degraded	8.95257	10.6105	10.7161	10.7829	10.0772	10.5689	10.7758	10.8423	10.109	10.6004	10.8075	10.8742
V_{co}(V)	Initial	1.36085	1.36557	1.3659	1.36611	1.36238	1.36514	1.3662	1.36654	1.36242	1.36518	1.36623	1.36657
	Degraded	1.2448	1.25478	1.2557	1.25633	1.24735	1.25338	1.2568	1.25819	1.24746	1.2534	1.25679	1.25817
FF(%)	Initial	72.7364	78.4849	78.7665	78.9344	75.9481	78.1962	78.983	79.2123	76.0261	78.2467	79.0213	79.247
	Degraded	62.5226	73.013	73.8772	74.4415	68.955	72.3985	74.572	75.4174	69.136	72.5737	74.7337	75.5672
η (%)	Initial	9.99375	11.6934	11.7823	11.8364	10.9787	11.6337	11.8381	11.8974	11.0047	11.6564	11.8589	11.9176
	Degraded	6.96762	9.72084	9.94107	10.0845	8.6675	9.59052	10.0993	10.2882	8.71845	9.64254	10.1509	10.3388

Table V-12:J_{sc}, V_{oc}, FF and η vs. top cell i-layer mobilities of the 2T-micromorph tandem solar cell.

2T- micromorph tandem cell		Top cell i-layer mobilities ($cm^2 V^{-1} s^{-1}$)											
		μ_n=25, μ_p=6											
		Bottom cell i-layer mobilities ($cm^2 V^{-1} s^{-1}$)											
		μ_n/μ_p=10				μ_n=35				μ_n=50			
		μ_n				μ_p				μ_p			
		15	20	35	50	1.5	2	3.5	5	1.5	2	3.5	5
J_{sc}(mA/cm^2)	Initial	11.0043	11.0046	11.0051	11.0052	11.0044	11.0047	11.0051	11.0052	11.0044	11.0047	11.0051	11.0052
	Degraded	10.8733	10.8743	10.8754	10.8759	10.8736	10.8744	10.8754	10.8758	10.8736	10.8744	10.8755	10.8759
V_{co}(V)	Initial	1.36667	1.36658	1.36645	1.3664	1.36669	1.36658	1.36645	1.3664	1.36669	1.36659	1.36645	1.3664
	Degraded	1.25828	1.25817	1.25803	1.25798	1.2583	1.25818	1.25803	1.25797	1.2583	1.25818	1.25804	1.25798
FF(%)	Initial	78.9554	79.2836	79.7338	79.9109	79.0267	79.3308	79.7338	79.8922	79.0426	79.3495	79.7531	79.9109
	Degraded	75.3198	75.5958	75.943	76.0777	75.3823	75.6317	75.943	76.0644	75.3977	75.6464	75.9563	76.0777
η (%)	Initial	11.8743	11.9232	11.9903	12.0166	11.8853	11.9304	11.9903	12.0138	11.8877	11.9333	11.9932	12.0166
	Degraded	10.305	10.3428	10.3902	10.4087	10.314	10.3479	10.3902	10.4067	10.3161	10.3499	10.3922	10.4087

Table V-13:J_{sc}, V_{oc}, FF and η vs. bottom cell i-layer mobilities of the 2T-micromorph tandem solar cell.

4T-micromorph tandem cell		Top cell												Bottom cell
		I-layer mobilities ($cm^2 V^{-1} s^{-1}$)												
		μ_n/μ_p=10				μ_n=20				μ_n=25				μ_n/μ_p
		μ_n				μ_p				μ_p				
		2	15	20	25	0.2	1	3	6	0.2	1	3	6	15/2
J_{sc}(mA/cm^2)	Initial	8.4317	8.99858	9.02547	9.04185	8.74513	8.9867	9.03901	9.05297	8.75352	8.99509	9.04731	9.06124	16.268
	Degraded	7.58812	8.80097	8.87276	8.91746	8.24566	8.7528	8.91827	8.9672	8.2638	8.7707	8.93603	8.98489	
V_{co}(V)	Initial	0.93055	0.93470	0.93495	0.93511	0.93184	0.9344	0.93515	0.93537	0.93188	0.93444	0.93519	0.93540	0.464633
	Degraded	0.84619	0.85289	0.85347	0.85384	0.84846	0.8522	0.85401	0.85465	0.84854	0.85227	0.85407	0.85470	
FF(%)	Initial	78.2952	83.7016	84.005	84.1922	80.5793	83.405	84.2242	84.4533	80.641	83.4633	84.2809	84.5102	63.5509
	Degraded	71.5501	79.9993	80.6601	81.0874	76.7021	79.571	81.1366	81.6891	76.8698	79.7258	81.2857	81.8369	
η (%)	Initial	6.14317	7.04017	7.08869	7.11856	6.56651	7.0038	7.11939	7.15142	6.57811	7.01544	7.13099	7.16303	4.80359
	Degraded	4.59427	6.00501	6.10811	6.17412	5.3662	5.9354	6.17965	6.2605	5.39026	5.95955	6.20376	6.28462	
4T-η (%)	Initial	10.9468	11.8438	11.8923	11.9222	11.3701	11.8074	11.9230	11.9550	11.3817	11.8190	11.9346	11.9666	
	Degraded	9.3979	10.8086	10.9117	10.9777	10.1698	10.7390	10.9832	11.0641	10.1938	10.7631	11.0073	11.0882	

Table V-14:J_{sc}, V_{oc}, FF and η vs. top cell i-layer mobilities of the 4T-micromorph tandem solar cell.

4T-micromorph tandem cell	Bottom cell												Top cell	
	I-layer mobilities ($cm^2 V^{-1} s^{-1}$)													
	μ_n/μ_p=10				μ_n=35				μ_n=50				μ_n/μ_p	
	μ_n				μ_p				μ_p				25/6	
	15	20	35	50	1.5	2	3.5	5	1.5	2	3.5	5	Initial	Degraded
J_{sc} (mA/cm^2)	16.227	16.2876	16.3617	16.3907	16.2755	16.3149	16.3617	16.3806	16.2874	16.3266	16.3726	16.3907	9.06124	8.98489
V_{co}(V)	0.4651	0.46466	0.46407	0.46382	0.46517	0.46470	0.46407	0.46381	0.46518	0.46472	0.46409	0.46382	0.93540	0.85470
FF(%)	61.9364	63.655	66.1609	67.2707	62.098	63.7768	66.1609	67.1806	62.1287	63.8213	66.2335	67.2707	84.5102	81.8369
η (%)	4.67445	4.81759	5.02362	5.11421	4.70137	4.83531	5.02362	5.10404	4.7073	4.84232	5.03266	5.11421	7.16303	6.28462
4T-η (%)	11.8375	11.9806	12.1867	12.2772	11.8644	11.9983	12.1867	12.2671	11.8703	12.0054	12.1957	12.2772	Initial state	
	10.9591	11.1022	11.3082	11.3988	10.9860	11.1199	11.3082	11.3887	10.9919	11.1269	11.3173	11.3988	Degraded state	

Table V-15:J_{sc}, V_{oc}, FF and η vs. bottom cell i-layer mobilities of the 4T-micromorph tandem solar cell.

The more the i-layer mobilities are better, the more is the amelioration notified in the cell photo-parameters. The best results can be summarized as follow (table V.16):

a-Si:H single cell	**μ_n/μ_p=25/6**	η (%)	**Initial**	9.07628
			Degraded	7.66879
µc-Si:H single cell	**μ_n/μ_p=50/5**	η (%)	9.06185	
2T- micromorph tandem cell	**Top cell i-layer mobilities μ_n/μ_p=25/6**	η (%)	**Initial**	12.0166
	Bottom cell i-layer mobilities μ_n/μ_p=50/5		**Degraded**	10.4087
4T- micromorph tandem cell	**Top cell i-layer mobilities μ_n/μ_p=25/6**	η (%)	**Initial**	12.2772
	Bottom cell i-layer mobilities μ_n/μ_p=50/5		**Degraded**	11.3988

Table V-16: The best conversion efficiency η obtained by increasing the i-layer mobilities.

Increasing μ_n or μ_p mobilities reduces the light soaked effect on the conversion efficiency of the a-Si:H-based single cell as illustrated in table V.17. As the μ_n or μ_p mobilities increase, $\Delta\eta$; which is the conversion efficiency difference between the initial and degraded states respectively: $\Delta\eta = \eta_{Initial} - \eta_{Degraded}$, is reduced.

Regarding the 2T and 4T micromorph tandem cells, the $\Delta\eta$ reduction is mostly achieved by the amelioration of the top cell i-layer mobilities, rather than those of the bottom cell, as we can deduce from Tables V.18-V.21. Minimum value of $\Delta\eta$ is 0.8784 % reached with 4T- device configuration.

a-Si:H single cell		I-layer mobilities ($cm^2 V^{-1} s^{-1}$)											
		μ_n/μ_p=10				μ_n=20				μ_n=25			
		μ_n				μ_p				μ_p			
		2	15	20	25	0.2	1	3	6	0.2	1	3	6
η (%)	Initial	7.4775	8.8588	8.9408	8.9919	8.0951	8.7874	8.9982	9.0592	8.1121	8.8044	9.0152	9.0762
	degraded	5.1647	7.1839	7.3528	7.4634	6.2307	7.0598	7.4815	7.6329	6.2642	7.0953	7.5173	7.6687
$\Delta\eta$ (%)		2.3129	1.6749	1.5880	1.5285	1.8644	1.7276	1.5167	1.4263	1.8478	1.7091	1.4980	1.4075

Table V-17: $\Delta\eta$ vs. i-layer mobilities of the a-Si:H-based single solar cell.

2T- micromorph tandem cell		Bottom cell i-layer mobilities ($cm^2 V^{-1} s^{-1}$)											
		μn=15, μp=2											
		Top cell i-layer mobilities ($cm^2 V^{-1} s^{-1}$)											
		μ_n/μ_p=10				μ_n=20				μ_n=25			
		μ_n				μ_p				μ_p			
		2	15	20	25	0.2	1	3	6	0.2	1	3	6
η (%)	Initial	9.9937	11.693	11.782	11.836	10.978	11.633	11.838	11.897	11.004	11.656	11.858	11.917
	degraded	6.9676	9.7208	9.9410	10.084	8.6675	9.5905	10.099	10.288	8.7184	9.6425	10.150	10.338
$\Delta\eta$ (%)		3.0261	1.9726	1.8412	1.7519	2.3112	2.0432	1.7388	1.6092	2.2862	2.0139	1.7080	1.5788

Table V-18: $\Delta\eta$ vs. top cell i-layer mobilities of the 2T- micromorph tandem cell.

2T- micromorph tandem cell		Top cell i-layer mobilities ($cm^2 V^{-1} s^{-1}$)											
		μ_n=25, μ_p=6											
		Bottom cell i-layer mobilities ($cm^2 V^{-1} s^{-1}$)											
		μ_n/μ_p=10				μ_n=35				μ_n=50			
		μ_n				μ_p				μ_p			
		15	20	35	50	1.5	2	3.5	5	1.5	2	3.5	5
η (%)	Initial	11.874	11.923	11.990	12.016	11.885	11.930	11.990	12.013	11.887	11.933	11.993	12.016
	degraded	10.305	10.342	10.390	10.408	10.314	10.347	10.390	10.406	10.316	10.349	10.392	10.408
$\Delta\eta$ (%)		1.569	1.5804	1.6001	1.6079	1.5713	1.5825	1.6001	1.6071	1.5716	1.5834	1.6010	1.6079

Table V-19: $\Delta\eta$ vs. bottom cell i-layer mobilities of the 2T- micromorph tandem cell

4T- micro-morph tandem cell		Bottom cell i-layer mobilities : μ_n/μ_p=15/2											
		Top cell I-layer mobilities ($cm^2 V^{-1} s^{-1}$)											
		μ_n/μ_p=10				μ_n=20				μ_n=25			
		μ_n				μ_p				μ_p			
		2	15	20	25	0.2	1	3	6	0.2	1	3	6
η (%)	Initial	10.946	11.843	11.892	11.922	11.370	11.807	11.923	11.955	11.381	11.819	11.934	11.966
	degraded	9.3979	10.808	10.911	10.977	10.169	10.739	10.983	11.064	10.193	10.763	11.007	11.088
$\Delta\eta$ (%)		1.5481	1.0352	0.9806	0.9445	1.2003	1.0684	0.9398	0.8909	1.1879	1.0559	0.9273	0.8784

Table V-20: $\Delta\eta$ vs. top cell i-layer mobilities of the 4T- micromorph tandem cell.

4T- micromorph tandem cell		Top cell I-layer mobilities: μ_n/μ_p=25/6											
		Bottom cell I-layer mobilities ($cm^2\ V^{-1}\ s^{-1}$)											
		μ_n/μ_p=10				μ_n=35				μ_n=50			
		μ_n				μ_p				μ_p			
		15	20	35	50	1.5	2	3.5	5	1.5	2	3.5	5
η (%)	Initial	11.837	11.980	12.186	12.277	11.864	11.998	12.186	12.267	11.870	12.005	12.195	12.277
	degraded	10.959	11.102	11.308	11.398	10.986	11.119	11.308	11.388	10.991	11.126	11.317	11.398
$\Delta\eta$ (%)		0,8780	0.8784	0.8785	0.8784	0.8784	0.8784	0.8785	0.8784	0.8784	0.8785	0.8784	0.8784

Table V-21: $\Delta\eta$ vs. bottom cell i-layer mobilities of the 4T- micromorph tandem cell.

V.5) Conclusion

In this chapter, we presented and discussed the main results investigated on the a-Si:H and µc-Si:H-based solar cells in single configuration, and in a micromorph tandem configuration with 2T and 4T electrical connections, in order to optimizing their output parameters. The numerical modeling, combined to the light soaked effect, has been used to provide a better understanding of the device physic, operation and degradation under continued illumination.

In the first part, we explored the photo-degradation (SW) effect on a single (a-Si:H) p-i-n cell illuminated by a monochromatic light beam (530-540 nm), then by the standard solar spectrum (AM1.5), on the basis of the model of the light-induced defect creation in a-Si:H developed by AF. Meftah et al [11-12]. The main results are presented in term of internal parameters such as the free carrier densities, recombination rate and electrical field, and in term of external parameters such as the current density- voltage ($J-V$) characteristics, from which one can extract the cell photo-parameters such as: the short-circuit current density (J_{sc}), the open-circuit voltage (V_{oc}), the fill factor (FF), and the conversion efficiency (η).

Decreases occurring in the photo-parameters can be visualised in terms of percentages: 21 % in J_{sc}, 7.69 % in V_{oc}, 14.86 % in *FF* and 37.81 % in P_{max}. The increase of μ_n from 20 to 25 cm^2/V.S and μ_p from 2 to 6 cm^2/V.S improves the cell photo-parameters and minimizes significantly theirs deteriorations; 4.11 % in J_{sc}, 5.86 % in V_{oc}, 14.27 % in *FF* and 22.61 % in P_{max}. A pretty increase is notified in J_{sc} and the maximum power density P_{max} for both annealed and degraded states, when the full spectrum AM 1.5 condition of illumination is considered.

In the second part, we studied the effect of the i-layer thickness on the performance of the a-Si:H and µc-Si:H- based solar cells, with single configuration, and micromorph (a-Si:H/ µc-Si:H) tandem configuration using 2T and 4T electrical connections, in both un-degraded and degraded states.

The a-Si:H single cell shows an optimum conversion efficiency of 7,47% at initial state with an i-layer 0,15 µm thick. At the degraded state, the optimum η is 5,61%, reached at a thinner i-layer of 0.1 µm thick. The decrease in V_{oc} and FF is also responsible for the loss in the efficiency η. For the single µc-Si:H cell, the optimal

conversion efficiency is approximately 8,67% , achieved when the i-layer thickness is 3,25 µm.

The electrical parameters of the 2T-micromorph tandem cell are mostly limited by the a-Si:H top sub-cell. An optimal conversion efficiency η of 10% is achieved at initial state with 0.17 µm (top cell i-layer)/ 2.1 µm (bottom cell i-layer). At degraded state, the optimal η is reduced to 7.77% with thinner thicknesses of 0.11 µm (top cell i-layer)/ 1.1 µm (bottom cell i-layer).

We can avoid the electrical influence of the two sub-cells on each other by applying the 4T connection, that means we can optimize easily each sub-cell compared to the 2T connection.

The total conversion efficiency of the 4T-micromorph tandem cell is given by the sum of the top and bottom sub-cell conversion efficiencies, At the initial state, the η shows an optimal value of 10.94% for 0.11µm(top cell i-layer) /3.8µm (bottom cell i-layer). At degraded state, the optimal value of η is reduced to 9.59% for 0.07µm (top cell i-layer) /3.8µm (bottom cell i-layer).

More improvements to the studied solar cells are achieved by the variation of i-layer mobilities, as presented in the last part of the work. The more the i-layer mobilities are higher, the more is the amelioration notified in the cell photo-parameters. The best results of η are 9.07% at initial state (reduced to 7.66% at degraded state) for the a-Si:H single cell, 9.06% for the µc-Si:H single cell, 12.01% at initial state (reduced to 10.40% at degraded state) for the 2T-micromorph tandem cell, and 12.27% at initial state (reduced only to 11.39% at degraded state) for the 4T-micromorph device. These results are obtained with μ_n/μ_p=25/6 (for the a-Si:H i-layer) and μ_n/μ_p=50/5 (for the µc-Si:H i-layer).

Increasing μ_n or μ_p mobilities reduces the light soaked effect on the conversion efficiency of the a-Si:H single cell; minimum reduction of η ($\Delta\eta$) due to the light soaked effect is about 1.40%. Regarding the 2T and 4T micromorph tandem cells, the minimum reduction $\Delta\eta$ is mostly achieved by the amelioration of the top cell i-layer mobilities, rather than those of the bottom cell. Minimum reduction $\Delta\eta$ is about 1.57% for the 2T-device, and about 0.87 % reached with 4T- device.

Chapter VI

General conclusion

General conclusion

This work is aimed at understanding the physic and the operation of amorphous (a-Si:H) and microcrystalline (µc-Si:H) silicon- based solar cells, in view of optimizing their performance by modeling in order to create a better micromorph (a-Si:H/µc-Si:H) tandem solar cell. The electrical characteristics of the studied solar cells were investigated by simulating the photodegradation, thickness and mobilities effects on different configurations; single a-Si:H and µc-Si:H-based solar cells, and a micromorph tandem cell with 2T and 4T electrical connections. The aim is to extract their output photo-parameters for a better performance using Atlas simulator which is a module in Silvaco Tcad software.

On the basis of the light-induced defect creation model in a-Si:H; developed by AF. Meftah et al [11-12], we investigated in the first part, the photo-degradation effect on a single a-Si:H p-i-n solar cell by numerical modelling, to provide a better understanding of the physical mechanisms governing the operation and the degradation of the device under continued illumination. In this approach, we have considered first the simple case of a monochromatic light beam nonuniformly absorbed; leading to an exponentially decreasing in generation rate from the illuminated p-side to the n-side of the device. We have interpreted our results on the basis of an inhomogeneously increase of the dangling bond defect distribution, as a consequence of the degradation effect related to the absorbed light profile in the i-layer. Such a distribution induces important changes in the internal variables profiles and the external photo-parameters of the device. These changes can be summarised as follows:

- An important increase in recombination rate, due mainly to the increase of the bulk $n.p$ product, the reason why the current density decreases considerably along the device.
- An abrupt band bending through the p-side and consequently a high electric field in this region, while a low electric field is found in the i-layer. The latter, encourage furthermore the bulk recombination of free carriers.

- The carrier diffusion current densities across the i-layer, neglected in the annealed state, contribute significantly to the total current density (mainly electron diffusion current).

- Decreases occurring in the photo-parameters can be visualised in terms of percentages: 21 % in J_{sc}, 7.69 % in V_{oc}, 14.86 % in *FF* and 37.81 % in P_{max}. The increase of μ_n from 20 to 25 cm^2/V.S and μ_p from 2 to 6 cm^2/V.S improves the cell photo-parameters and minimizes significantly theirs deteriorations; 4.11 % in J_{sc}, 5.86 % in V_{oc}, 14.27 % in *FF* and 22.61 % in P_{max}.

When the results are expanded to the full spectrum AM 1.5 condition of illumination, under which the a-Si:H solar cell usually operates, a pretty increase (relatively to the monochromatic light case) is notified in J_{sc}, and so in the maximum power density P_{max} provided by the cell for both cases; annealed and degraded state.

In the second part, we studied the effect of the i-layer thickness on the performance of the a-Si:H and µc-Si:H- based solar cells in different configurations; single and micromorph (a-Si:H/ µc-Si:H) tandem configuration, with considering the 2T and 4T electrical connections in both un-degraded and degraded states.

The a-Si:H single cell shows an optimum conversion efficiency of 7,47% at initial state with an i-layer 0,15 µm thick. At the degraded state, the optimum η is 5,61%, reached at a thinner i-layer of 0.1 µm thick. The decrease in V_{oc} and FF is also responsible for the loss in the efficiency η. For the single µc-Si:H cell, the optimal conversion efficiency is approximately 8,67% , achieved when the i-layer thickness is 3,25 µm.

The electrical parameters of the 2T-micromorph tandem cell are mostly limited by the a-Si:H top sub-cell. An optimal conversion efficiency η of 10% is achieved at initial state with 0.17 µm (top cell i-layer)/ 2.1 µm (bottom cell i-layer). At degraded state, the optimal η is reduced to 7.77% with thinner thicknesses of 0.11 µm (top cell i-layer)/ 1.1 µm (bottom cell i-layer).

The total conversion efficiency of the 4T-micromorph tandem cell is given by the sum of the top and bottom sub-cell conversion efficiencies, At the initial state, the η shows an optimal value of 10.94% for 0.11µm(top cell i-layer) /3.8µm (bottom cell i-layer). At degraded state, the optimal value of η is reduced to 9.59% for 0.07µm(top cell i-layer) /3.8µm (bottom cell i-layer).

We have brought more improvements to the studied solar cells by the amelioration of the i-layer mobilities, as presented in the last part of the work. The more the i-layer mobilities are higher, the more is the improvement notified in the cell photo-parameters. The best results of η are 9.07% at initial state (reduced to 7.66% at degraded state) for the a-Si:H single cell, 9.06% for the µc-Si:H single cell, 12.01% at initial state (reduced to 10.40% at degraded state) for the 2T-micromorph tandem cell, and 12.27% at initial state (reduced only to 11.39% at degraded state) for the 4T-micromorph device. These results are obtained with μ_n/μ_p=25/6 (for the a-Si:H i-layer) and μ_n/μ_p=50/5 (for the µc-Si:H i-layer).

Increasing μ_n or μ_p mobilities reduces the light soaked effect on the conversion efficiency of the a-Si:H single cell; the minimum reduction of η ($\Delta\eta$) due to the light soaked effect is about 1.40%. Concerning the 2T and 4T micromorph tandem cells, the minimum reduction $\Delta\eta$ is mostly accomplished by the increasing of the top cell i-layer mobilities, rather than those of the bottom cell. Minimum reduction $\Delta\eta$ is about 1.57% for the 2T-device, and about 0.87 % reached with 4T- device.

As a perspective, we envisage to extend the study to the investigation of a triple-junction solar cell with the possible configurations; (a-Si:H/a-Si:H/µc-Si:H), (a-Si:H/µc-Si:H/ µc-Si:H) and (a-Si:H/µc-Si:H/SiGe:H). Thereafter, to introduce a novel promising material in the photovoltaic area; the ternary alloy Indium Gallium Nitride (InGaN) which has an adjustable band gap (approximately 0.77 eV for InN to 3.4 eV for GaN) covering the visible spectrum from IR to UV only by changing the In or Ga content, to study the heterojunction solar cell based on InGaN/Si.

References

1. Nelson, J., *The physics of solar cells*. Vol. 1. 2003: World Scientific.
2. Remache, L., *Silicium poreux passivé par des nitrures et des oxydes de silicium. Application aux revêtements antiréfléchissants*, 2011, thése de Doctorat, Université Mentouri Constantine.
3. EPIA, *Global Market Outlook for Photovoltaics 2014-2018*, 2014. p. 60.
4. Europe(SPE), S., *Global Market Outlook For Solar Power / 2015 - 2019*, 2015. p. 32.
5. News, B. *China Targets 70 Gigawatts of Solar Power to Cut Coal Reliance*. 2014 16/05/2014].
6. Ayre, J. *China's National Energy Administration: 17.8 GW Of New Solar PV In 2015 (~20% Increase)*. 2014 19/03/2015].
7. contributors, W. *Growth of photovoltaics*. 2016; Available from: https://en.wikipedia.org/w/index.php?title=Growth_of_photovoltaics&oldid=702624358.
8. (IEA), I.E.A., *Snapshot of Global PV Markets 1992-2014*, 2014. p. 16.
9. Agency, I.E., *Technology Roadmap: Solar Photovoltaic Energy*, 2014. p. 60.
10. Poortmans, J. and V. Arkhipov, *Thin film solar cells: fabrication, characterization and applications*. Vol. 5. 2006: John Wiley & Sons.
11. MARTIN, J. *Solar PV price check - June*. 2015 [cited 2015 17 june]; Available from: http://www.businessspectator.com.au/article/2015/6/17/solar-energy/solar-pv-price-check-june.
12. Energy, F.I.f.S. and I. Systems. *PHOTOVOLTAICS REPORT*. 2015; Available from: http://www.ise.fraunhofer.de/en/downloads-englisch/pdf-files-englisch/photovoltaics-report-slides.pdf.
13. Ted Sullivan, s.a., Lux Research, . *How thin film solar fares vs crystalline silicon*. 2011 [cited 2016 28 Jan]; Available from: http://www.renewableenergyworld.com/articles/2011/01/how-thin-film-solar-fares-vs-crystalline-silicon.html.

14. Bentouba, S., et al., *L'energie renouvelable en Algerie et l impact sur l'environnement.*

15. Bouchaib, S. *Prix du panneau photovoltaïque en Algérie*. 2014; Available from: http://portail.cder.dz/spip.php?article3925.

16. Solar, S.G. *World Map of Global Horizontal Irradiation, SolarGIS 2013*. 2013; Available from: https://commons.wikimedia.org/wiki/File%3ASolarGIS-Solar-map-World-map-en.png.

17. Spear, W. and P. Le Comber, *Substitutional doping of amorphous silicon.* Solid State Communications, 1975. **17**(9): p. 1193-1196.

18. Carlson, D.E. and C. Wronski, *Amorphous silicon solar cell.* Applied Physics Letters, 1976. **28**(11): p. 671-673.

19. Staebler, D. and C. Wronski, *Reversible conductivity changes in discharge-produced amorphous Si.* Applied Physics Letters, 1977. **31**: p. 292.

20. Yang, J., et al. *High efficiency multi-junction solar cells using amorphous silicon and amorphous silicon-germanium alloys*. in *Photovoltaic Specialists Conference, 1988., Conference Record of the Twentieth IEEE*. 1988. IEEE.

21. Vepřek, S. and V. Mareček, *The preparation of thin layers of Ge and Si by chemical hydrogen plasma transport.* Solid-State Electronics, 1968. **11**(7): p. 683-684.

22. Prasad, K., et al., *Deposition of phosphorus doped microcrystalline silicon below 70 C at 70 MHz.* Journal of Non-Crystalline Solids, 1991. **137**: p. 681-684.

23. Meier, J., et al., *Complete microcrystalline p-i-n solar cell—Crystalline or amorphous cell behavior?* Applied Physics Letters, 1994. **65**(7): p. 860-862.

24. Rath, J.K., F. Tichelaar, and R.E. Schropp, *Heterogeneous growth of microcrystalline silicon germanium.* Solar energy materials and solar cells, 2002. **74**(1): p. 553-560.

25. Yamamoto, K., et al. *High efficiency thin film silicon hybrid cell and module with newly developed innovative interlayer*. in *Photovoltaic Energy Conversion, Conference Record of the 2006 IEEE 4th World Conference on*. 2006. IEEE.

26. Green, M.A., et al., *Solar cell efficiency tables (Version 45).* Progress in photovoltaics: research and applications, 2015. **23**(1): p. 1-9.

27. Collins, R., et al., *Evolution of microstructure and phase in amorphous, protocrystalline, and microcrystalline silicon studied by real time spectroscopic ellipsometry.* Solar energy materials and solar cells, 2003. **78**(1): p. 143-180.

28. Finger, F., et al., *Stability of microcrystalline silicon for thin film solar cell applications.* IEE Proceedings-Circuits, Devices and Systems, 2003. **150**(4): p. 300-308.

29. Nebo, C.U., *Understanding Uc-Si: H solar cell performance and its optimization using modeling*, 2009, TU Delft, Delft University of Technology.

30. Schicho, S., *Amorphous and microcrystalline silicon applied in very thin tandem solar cells*. Vol. 99. 2011: Forschungszentrum Jülich.

31. Carlson, D., *Monolithic amorphous silicon alloy solar modules.* Solar energy materials and solar cells, 2003. **78**(1): p. 627-645.

32. Vaseashta, A.K., D. Dimova-Malinovska, and J.M. Marshall, *Nanostructured and Advanced Materials for Applications in Sensor, Optoelectronic and Photovoltaic Technology: Proceedings of the NATO Advanced Study Institute on Nanostructured and Advanced Materials for Applications in Sensors, Optoelectronic and Photovoltaic Technology Sozopol, Bulgaria, 6-17 September 2004*. Vol. 204. 2005: Springer Science & Business Media.

33. Zimmermann, T., *High-rate growth of hydrogenated amorphous and microcrystalline silicon for thin-film silicon solar cells using dynamic very-high frequency plasma-enhanced chemical vapor deposition*2013: Forschungszentrum Jülich.

34. Finger, F., et al., *Improvement of grain size and deposition rate of microcrystalline silicon by use of very high frequency glow discharge.* Applied Physics Letters, 1994. **65**(20): p. 2588-2590.

35. Shah, A.V., et al., *Basic efficiency limits, recent experimental results and novel light-trapping schemes in a-Si: H, µc-Si: H andmicromorph tandem'solar cells.* Journal of Non-Crystalline Solids, 2004. **338**: p. 639-645.

36. Street, R.A., *Hydrogenated amorphous silicon*2005: Cambridge University Press.

37. Despeisse, M., *Etude et caractérisation d'un capteur en silicium amorphe hydrogéné déposé sur circuit intégré pour la détection de particules et de rayonnements*, 2006, LPM, INSA Lyon.

38. MEFTAH, A., *Etude des propriétés de transport dans les structures photovoltaïques à base de Silicium Amorphe Hydrogéné (a-Si :H) en régime stationnaire et transitoire.*, in *DEPARTEMENT DE PHYSIQUE*2005, UNIVERSITE DE BISKRA.

39. Powell, M. and S. Deane, *Improved defect-pool model for charged defects in amorphous silicon.* Physical Review B, 1993. **48**(15): p. 10815.

40. Powell, M. and S. Deane, *Defect-pool model and the hydrogen density of states in hydrogenated amorphous silicon.* Physical Review B, 1996. **53**(15): p. 10121.

41. Afak, M., *Etude de la formation et la dynamique des défauts dans les matériaux photo-actifs de type a-Si :H*, in *departement de physique*2004/2005, L'UNIVERSITE DE BISKRA.

42. Rockett, A., *Amorphous Semiconductors.* The Materials Science of Semiconductors, 2008: p. 357-393.

43. Rockett, A., *The materials science of semiconductors*2007: Springer Science & Business Media.

44. Pankove, J.I., *Hydrogenated Amorphous Silicon: Device Applications*1984: Academic Press.

45. Mott, N.F., *Conduction in non-Crystalline systems.* Philosophical Magazine, 1970. **22**(175): p. 7-29.

46. Nagels, P., *Electronic transport in amorphous semiconductors*, in *Amorphous Semiconductors*, M. Brodsky, Editor 1985, Springer Berlin Heidelberg. p. 113-158.

47. Mott, N.F., *Conduction in non-crystalline materials.* Philosophical Magazine, 1969. **19**(160): p. 835-852.

48. Staebler, D. and C. Wronski, *Reversible conductivity changes in discharge-produced amorphous Si.* Applied Physics Letters, 1977. **31**(4): p. 292-294.

49. Fritzsche, H., *Development in understanding and controlling the Staebler-Wronski effect in a-Si: H.* Annual Review of Materials Research, 2001. **31**(1): p. 47-79.

50. Godet, C., *Metastable hydrogen atom trapping in hydrogenated amorphous silicon films: a microscopic model for metastable defect creation.* Philosophical Magazine B, 1998. **77**(3): p. 765-777.

51. Kołodziej, A., *Staebler-Wronski effect in amorphous silicon and its alloys.* Opto-electronics review, 2004. **12**(1): p. 21-32.

52. Biswas, R. and B. Pan, *Defect kinetics in new model of metastability in a-Si: H.* Journal of Non-Crystalline Solids, 2002. **299**: p. 507-510.

53. Branz, H.M., *Hydrogen collision model: Quantitative description of metastability in amorphous silicon.* Physical Review B, 1999. **59**(8): p. 5498.

54. Stutzmann, M., W. Jackson, and C. Tsai, *Light-induced metastable defects in hydrogenated amorphous silicon: A systematic study.* Physical Review B, 1985. **32**(1): p. 23.

55. Branz, H.M., *The hydrogen collision model: theory and experiment.* Journal of Non-Crystalline Solids, 2000. **266**: p. 391-396.

56. Branz, H.M., *The hydrogen collision model of metastability after 5 years: experimental tests and theoretical extensions.* Solar energy materials and solar cells, 2003. **78**(1): p. 425-445.

57. Usui, S. and M. Kikuchi, *Properties of heavily doped GD□Si with low resistivity.* Journal of Non-Crystalline Solids, 1979. **34**(1): p. 1-11.

58. Meier, J., et al., *Complete Microcrystalline p-i-n Solar Cell-Crystalline or Amorphous Cell Behavior.* Appl. Phys. Lett., 1994. **65**: p. 860-862.

59. Meier, J., et al. *Intrinsic microcrystalline silicon (μc-Si:H)-a promising new thin film solar cell material*. in *Photovoltaic Energy Conversion, 1994., Conference Record of the Twenty Fourth. IEEE Photovoltaic Specialists Conference - 1994, 1994 IEEE First World Conference on*. 1994.

60. Meier, J., et al. *On the way towards high efficiency thin film silicon solar cells by the "Micromorph" concept*. in *MRS Proceedings*. 1996. Cambridge Univ Press.

61. i Cabarrocas, P.R., *Plasma enhanced chemical vapor deposition of amorphous, polymorphous and microcrystalline silicon films.* Journal of Non-Crystalline Solids, 2000. **266**: p. 31-37.

62. Meier, J., et al. *Recent Progress in Up-Scaling of Amorphous and Micromorph Thin Film Silicon Solar Cells to 1.4 m 2 Modules*. in *MRS Proceedings*. 2007. Cambridge Univ Press.

63. Tawada, Y., H. Yamagishi, and K. Yamamoto, *Mass productions of thin film silicon PV modules.* Solar energy materials and solar cells, 2003. **78**(1): p. 647-662.

64. Shah, A., *Thin-film silicon solar cells*2010: EPFL press.

65. Shah, A., R. Platz, and H. Keppner, *Thin-film silicon solar cells: a review and selected trends.* Solar energy materials and solar cells, 1995. **38**(1): p. 501-520.

66. Wang, Y., et al., *Stability of microcrystalline silicon solar cells with HWCVD buffer layer.* Thin solid films, 2008. **516**(5): p. 733-735.

67. Werner, J. and R. Bergmann, *Perspectives of crystalline silicon thin film solar cells.* Technical Digest PVSEC-11, 1999. **24**.

68. McEvoy, A., et al., *Practical handbook of photovoltaics: fundamentals and applications*2003: Elsevier.

69. Vallat-Sauvain, E., et al., *Microstructure and surface roughness of microcrystalline silicon prepared by very high frequency-glow discharge using hydrogen dilution.* Journal of Non-Crystalline Solids, 2000. **266**: p. 125-130.

70. Sendova-Vassileva, M., S. Klein, and F. Finger, *Instability phenomena in μc-Si: H solar cells prepared by hot-wire CVD.* Thin solid films, 2006. **501**(1): p. 252-255.

71. Meillaud, F., et al. *Light-induced degradation of thin film amorphous and microcrystalline silicon solar cells*. in *Photovoltaic Specialists Conference, 2005. Conference Record of the Thirty-first IEEE*. 2005. IEEE.

72. Ganguly, G., et al., *Hydrogenated microcrystalline silicon germanium: A bottom cell material for amorphous silicon-based tandem solar cells.* Applied Physics Letters, 1996. **69**(27): p. 4224-4226.

73. Konagai, M., *Deposition of new microcrystalline materials, µc-SiC, µc-GeC by HWCVD and solar cell applications.* Thin solid films, 2008. **516**(5): p. 490-495.

74. Huang, Y., et al., *Highly transparent microcrystalline silicon carbide grown with hot wire chemical vapor deposition as window layers in nip microcrystalline silicon solar cells.* Applied Physics Letters, 2007. **90**(20): p. 3502.

75. Miyajima, S., A. Yamada, and M. Konagai, *Aluminum-doped hydrogenated microcrystalline cubic silicon carbide films deposited by hot wire CVD.* Thin solid films, 2006. **501**(1): p. 186-189.

76. Chen, T., et al., *Aluminum doped silicon‐carbon alloys prepared by hot wire chemical vapor deposition.* physica status solidi (c), 2010. **7**(3-4): p. 754-757.

77. Chittick, R.C., *Properties of glow-discharge deposited amorphous germanium and silicon.* Journal of Non-Crystalline Solids, 1970. **3**(3): p. 255-270.

78. Howling, A., et al. *The influence of plasma chemistry on the deposition of microcrystalline silicon for large area photovoltaic solar cells*. in *16th EC Photovoltaic Solar Energy Conference*. 2000.

79. Becquerel, A., *Recherches sur les effets de la radiation chimique de la lumière solaire au moyen des courants électriques.* Comptes Rendus de LAcadémie des Sciences, 1839. **9**: p. 145-149.

80. Mangersnes, K., *Back-contacted back-junction silicon solar cells*, 2010, University of Oslo.

81. Favre, W., *Silicium de type n pour cellules à hétérojonctions: caractérisations et modélisations*, 2011, Université Paris Sud-Paris XI.

82. Pérez-Higueras, P. and E.F. Fernández, *High Concentrator Photovoltaics: Fundamentals, Engineering and Power Plants*2015: Springer International Publishing.

83. Pinto, M.R., C.S. Rafferty, and R.W. Dutton, *PISCES II: Poisson and continuity equation solver*1984.

84. Nelson, J., *Quantum-Well Structures for Photovoltaic Energy.* Advances in Research and Development: Homojunction and Quantum-Well Infrared Detectors: Homojunction and Quantum-Well Infrared Detectors, 1995. **21**: p. 311.

85. Hovel, H.J., *Semiconductors and semimetals. Volume 11. Solar cells.* 1975.

86. Ding, K., et al., *Characterization and simulation of a-Si: H/μc-Si: H tandem solar cells.* Solar energy materials and solar cells, 2011. **95**(12): p. 3318-3327.

87. Aberle, A.G., *Thin-film solar cells.* Thin solid films, 2009. **517**(17): p. 4706-4710.

88. Liu, H., et al., *Transparent conducting oxides for electrode applications in light emitting and absorbing devices.* Superlattices and Microstructures, 2010. **48**(5): p. 458-484.

89. Matsuda, A., *Microcrystalline silicon.: growth and device application.* Journal of Non-Crystalline Solids, 2004. **338**: p. 1-12.

90. Tanaka, Y., et al. *Improvement of Voc upward of 600mV/cell with CIGS-based absorber prepared by Selenization/Sulfurization*. in *Conference proceedings, 17th EC photovoltaic solar energy conference, Munich*. 2001.

91. Schropp, R.E., R. Carius, and G. Beaucarne, *Amorphous silicon, microcrystalline silicon, and thin-film polycrystalline silicon solar cells.* MRS bulletin, 2007. **32**(03): p. 219-224.

92. AVRUTIN, V., N. IZYUMSKAYA, and H. MORKOÇ, *Amorphous and micromorph Si solar cells: current status and outlook.* Turkish Journal of Physics, 2014. **38**(3): p. 526-542.

93. Razykov, T., et al., *Solar photovoltaic electricity: current status and future prospects.* Solar Energy, 2011. **85**(8): p. 1580-1608.

94. Vetterl, O., et al., *Intrinsic microcrystalline silicon: A new material for photovoltaics.* Solar energy materials and solar cells, 2000. **62**(1): p. 97-108.

95. Hanni, S., et al., *On the interplay between microstructure and interfaces in high-efficiency microcrystalline silicon solar cells.* Photovoltaics, IEEE Journal of, 2013. **3**(1): p. 11-16.

96. Zeman, M., *Advanced amorphous silicon solar cell technologies.* Thin Film Solar Cells, 2006: p. 173-236.

97. Meillaud, F., et al., *Efficiency limits for single-junction and tandem solar cells.* Solar energy materials and solar cells, 2006. **90**(18): p. 2952-2959.

98. Meier, J., et al. *Intrinsic microcrystalline silicon (μc-Si: H)-a promising new thin film solar cell material*. in *Photovoltaic Energy Conversion, 1994., Conference Record of the Twenty Fourth. IEEE Photovoltaic Specialists Conference-1994, 1994 IEEE First World Conference on*. 1994. IEEE.

99. Meier, J., et al. *The" Micromorph" Solar Cells: a New Way to High Efficiency Thin Film Silicon Solar Cells*. in *13th EC Photovoltaic Solar Energy Conference*. 1995.

100. Yoshimi, M., et al. *High efficiency thin film silicon hybrid solar cell module on 1 m/sup 2/-class large area substrate*. in *Photovoltaic Energy Conversion, 2003. Proceedings of 3rd World Conference on*. 2003. IEEE.

101. McEvoy, A., L. Castaner, and T. Markvart, *Solar cells: materials, manufacture and operation*2012: Academic Press.

102. Kherani, N.P., *Towards Application of Selectively Transparent and Conducting Photonic Crystal in Silicon-based BIPV and Micromorph Photovoltaics*, 2013.

103. O'Brien, P.G., *Selectively Transparent and Conducting Photonic Crystals and their Potential to Enhance the Performance of Thin-Film Silicon-Based Photovoltaics and Other Optoelectronic Devices*, 2011, Department of the Faculty of Materials Science and Engineering, University of Toronto.

104. Söderström, T., et al., *Asymmetric intermediate reflector for tandem micromorph thin film silicon solar cells.* Applied Physics Letters, 2009. **94**(6): p. 063501.

105. Buehlmann, P., et al., *In situ silicon oxide based intermediate reflector for thin-film silicon micromorph solar cells.* Applied Physics Letters, 2007. **91**(14): p. 143505.

106. Meier, J., et al., *Microcrystalline/micromorph silicon thin-film solar cells prepared by VHF-GD technique.* Solar energy materials and solar cells, 2001. **66**(1): p. 73-84.

107. Shah, A., et al., *Thin-film silicon solar cell technology.* Progress in photovoltaics: Research and applications, 2004. **12**(2-3): p. 113-142.

108. Fischer, D., et al. *The "micromorph" solar cell: extending a-Si: H technology towards thin film crystalline silicon*. in *Photovoltaic Specialists Conference, 1996., Conference Record of the Twenty Fifth IEEE*. 1996. IEEE.

109. Yamamoto, K., et al., *A high efficiency thin film silicon solar cell and module.* Solar Energy, 2004. **77**(6): p. 939-949.

110. Hudanski, L., et al. *Multiterminal structures for improved efficiency a-Si/μc-Si tandem devices*. in *Photovoltaic Specialists Conference (PVSC), 2011 37th IEEE*. 2011. IEEE.

111. Reynolds, S. and V. Smirnov. *Modelling of two-and four-terminal thin-film silicon tandem solar cells*. in *Journal of Physics: Conference Series*. 2012. IOP Publishing.

112. Yan, B. and G.J. Adriaenssens, *Electron emission from deep states and evaluation of the density of states in a-Si: H.* Journal of applied physics, 1995. **77**(11): p. 5661-5668.

113. Main, C., et al., *Investigation of collection efficiencies much larger than unity in a-Si: Hp-in structures.* Journal of applied physics, 1999. **85**(1): p. 296-301.

114. Seynhaeve, G., *Time of flight photocurrents in hydrogenated amorphous silicon*, 1989, Ph. D. thesis, KU Leuven.

115. Lips, K. and W. Fuhs, *Transport and recombination in amorphous p-i-n-type solar cells studied by electrically detected magnetic resonance.* Journal of applied physics, 1993. **74**(6): p. 3993-3999.

116. Deng, J. and C. Wronski, *Carrier recombination and differential diode quality factors in the dark forward bias current-voltage characteristics of a-Si: H solar cells.* Journal of applied physics, 2005. **98**(2): p. 024509-024509.

117. Pieters, B., et al., *Determination of the mobility gap of intrinsic μc-Si: H in pin solar cells.* Journal of Applied Physics, 105 (4), 2009, 2009.

118. Yang, G., *High-efficient nip thin-film silicon solar cells*, 2015, TU Delft, Delft University of Technology.

119. Goering, R. *Mixed-signal simulation tool supports Linux*. 6/7/2004; Available from: http://www.eetimes.com/document.asp?doc_id=1150368.

120. Valco, G. *Getting Started with the Silvaco TCAD Software for EE637 and EE734*. 2010/04/13; Available from: http://www2.ece.ohio-state.edu/~valco/silvaco/index.html.

121. Sarkar, C.K., *Technology Computer Aided Design: Simulation for VLSI MOSFET*2013: CRC Press.

122. Michael, S., A. Bates, and M. Green. *Silvaco Atlas as a solar cell modeling tool*. in *Photovoltaic Specialists Conference, 2005. Conference Record of the Thirty-first IEEE*. 2005. IEEE.

123. SILVACO, I., *Atlas User's Manual', Device Simulation Software, software ver. 5.10.* R, Santa Clara, 2005.

124. McCloy, D.J., *High Efficiency Solar Cells: A Model in Silvaco*, 1999, DTIC Document.

125. Sanders, M.H., *Modeling of operating temperature performance of triple junction solar cells using Silvaco's ATLAS*, 2007, DTIC Document.

126. Framework, A.D.S., *version 5.10. 0.* R, Silvaco International, 2005.

127. YACINE, M., *Modélisation des cellules solaires en InGaN en utilisant Atlas Silvaco*, 2013, Université Mohamed Khider de Biskra.

128. Aguinaldo, R., *Modeling solutions and simulations for advanced III-V photovoltaics based on nanostructures*2008: ProQuest.

129. Michael, S. and A. Bates, *The design and optimization of advanced multijunction solar cells using the Silvaco ATLAS software package.* Solar energy materials and solar cells, 2005. **87**(1): p. 785-794.

130. Bailat, J., et al. *Recent developments of high-efficiency micromorph tandem solar cells in KAI-M PECVD reactors*. in *Proceedings of the 5th World Conference on Photovoltaic Energy Conversion, Valencia, Spain*. 2010.

131. Jia, H., T. Matsui, and M. Kondo, *Thin film solar cells incorporating microcrystalline SiIxGex as efficient infrared absorber: an application to double junction tandem solar cells.* Prog. Photovolt: Res. Appl, 2010. **18**: p. 48-53.

132. Kondo, M., et al. *Four terminal cell analysis of amorphous/microcrystalline Si tandem cell*. in *Photovoltaic Energy Conversion, 2003. Proceedings of 3rd World Conference on*. 2003. IEEE.

133. Hu, J., et al. *Progress in four-terminal nano-crystalline Si/amorphous Si solar cells*. in *Photovoltaic Specialists Conference, 2005. Conference Record of the Thirty-first IEEE*. 2005. IEEE.

134. Madan, A., *Flexible displays and stable high efficiency four terminal solar cells using thin film silicon technology.* Surface and Coatings Technology, 2005. **200**(5): p. 1907-1912.

135. Dadouche, F., et al., *Geometrical optimization and electrical performance comparison of thin-film tandem structures based on pm-Si: H and μc-Si: H using computer simulation.* EPJ Photovoltaics, 2011. **2**: p. 20301.

136. Meftah, A., A. Meftah, and A. Merazga. *Modelling of Staebler-Wronski effect in hydrogenated amorphous silicon under moderate and intense illumination*. in *Defect and Diffusion Forum*. 2004. Trans Tech Publ.

137. Meftah, A., A. Meftah, and A. Merazga, *A theoretical study of light induced defect creation, annealing and photoconductivity degradation in a-Si: H.* Journal of Physics: Condensed Matter, 2004. **16**(18): p. 3107.

138. Wu, Z., J. Siefert, and B. Equer, *Preparation and physical properties of RF-sputtered amorphous films in the Al2O3/AlN system.* J Non-Cryst Solids, 1991. **137**: p. 138-227.

139. Morigaki, K. and H. Hikita, *Model of the light-induced creation of two types of dangling bonds in a-Si: H.* Journal of Non-Crystalline Solids, 2000. **266**: p. 410-414.

140. Powell, M., R. Wehrspohn, and S. Deane, *Nature of metastable and stable dangling bond defects in hydrogenated amorphous silicon.* Journal of Non-Crystalline Solids, 2002. **299**: p. 556-560.

141. Jackson, W., *Role of hydrogen complexes in the metastability of hydrogenated amorphous silicon.* Physical Review B, 1990. **41**(14): p. 10257.

142. Godet, C. and P.R. i Cabarrocas, *Role of Si–H bonding in a-Si: H metastability.* Journal of applied physics, 1996. **80**(1): p. 97-102.

143. Han, D., *Search for the Factors Determining the Photodegradation in High Efficiency a-Si: H Solar Cells.*

144. Cheong, H.M., et al., *Light-induced long-range hydrogen motion in hydrogenated amorphous silicon at room temperature.* Applied Physics Letters, 2000. **77**(17): p. 2686-2688.

145. Bouhdjar, A., et al., *Computer modelling and analysis of the photodegradation effect in a-Si: H p—i—n solar cell.* Journal of Semiconductors, 2015. **36**(1): p. 014002.

146. Schmidt, J., et al., *Light-induced defects in hydrogenated amorphous silicon studied by the constant-photocurrent method.* Physical Review B, 1997. **55**(15): p. 9621.

147. Schmidt, J., et al., *Light-induced creation of metastable defects in hydrogenated amorphous silicon studied by computer simulations of constant photocurrent measurements.* Physical Review B, 1999. **59**(7): p. 4568.

148. Zeman, M. and J. Krc, *Optical and electrical modeling of thin-film silicon solar cells.* Journal of Materials Research, 2008. **23**(04): p. 889-898.

149. Rau, U., D. Abou-Ras, and T. Kirchartz, *Advanced characterization techniques for thin film solar cells*2011: John Wiley & Sons.

150. Luque, A. and S. Hegedus, *Handbook of photovoltaic science and engineering*2011: John Wiley & Sons.

151. Carasco, F. and W. Spear, *Photogeneration and geminate recombination in amorphous silicon.* Philosophical Magazine Part B, 1983. **47**(5): p. 495-507.

152. Schiff, E., *Diffusion-controlled bimolecular recombination of electrons and holes in a-Si: H.* Journal of Non-Crystalline Solids, 1995. **190**(1): p. 1-8.

153. Pieters, B.E., *Characterization of thin-film silicon materials and solar cells through numerical modeling*2008: TU Delft, Delft University of Technology.

154. Shaoying, K., et al., *Numerical simulation of the performance of the a-Si: H/a-SiGe: H/a-SiGe: H tandem solar cell.* Journal of Semiconductors, 2014. **35**(3): p. 034013.

155. Chan, K.-Y., et al., *Influence of crystalline volume fraction on the performance of high mobility microcrystalline silicon thin-film transistors.* Journal of Non-Crystalline Solids, 2008. **354**(19): p. 2505-2508.

156. Foldyna, M., et al. *Model dielectric functional of amorphous materials including Urbach tail*. in *Microwave and Optical Technology 2003*. 2004. International Society for Optics and Photonics.

157. Krc, J., M. Zeman, and F. Smole, *Optical modeling of a-Si: H solar cells deposited on textured glass/SnO2 substrates.* Journal of applied physics, 2002. **92**: p. 749-755.

158. Neamen, D., *Semiconductor physics and devices*2002: McGraw-Hill, Inc.

Appendix

Micromorph tandem cell *I-V* measurements

A.1. Introduction:

Our visit to Dundee (Scotland) University (December 2012), gave us the opportunity to access to various experimental methods which complete our experience in semiconductor theory and numerical simulations. Techniques available in Dundee include solar cell characterisation under AM1.5 and monochromatic illumination, defect spectroscopies including Transient Photoconductivity and Constant Photocurrent method, accelerated Staebler-Wronski degradation and standard materials characterisation using IR (Infrared spectroscopy), AFM (Atomic Force Microscopy), and SEM (Scanning Electron Microscopy).

We attended a training program intended to provide underpinning of simulation and measurement procedures relevant to the development of solar cells, and in particular, design criteria for optimization of tandem solar cells.

A.2. Micromorph tandem cell *I-V* measurements:

Technologically, it is not straight forward to design a tandem solar cell with optimum sub-cell thicknesses for maximum efficiency. In series connected (2T) tandem solar cells, the overall short circuit current is limited by the subcell delivering the lower current. ***Current matching*** implies equal short circuit currents in the two sub-cells and thus a maximum overall short circuit current density, but it results in a minimum fill factor.

The solar cell characterizing parameters are determined in the current - voltage (*I-V*) characteristic for tandem solar cell. The *I-V* curve is given by the superposition of the (*I-V)*-curves of its sub-cells. The total voltage of a cell is the sum of the subcell voltages while the total current corresponds to the minimum current of both cells. Experimentally, however, the *I-V* characteristics of the sub-cells are not accessible. The subcell layer thicknesses needed for maximum power are only accessible from calculations based on the measured quantum efficiency or simulations of the entire cell physics.

Figure A-1 shows the equipment used to measure the *I-V* characteristics of the micromorph (a-Si:H/µc-Si:H) tandem solar cell from the Institute of Energy Research 5 – Photovoltaic (IEK-5), Research Center Jülich.

Figure A-1: Measure equipment of the micromorph tandem cell *I-V* characteristic at Dundee University.

The proposed experimental method consists of measurements of the (I-V)-curve under varied spectra. Increasing one subcell current by changing the irradiation in the respective wavelength regime is similar to changing the subcell layer thickness. The reference tandem solar cell is characterized by measuring the quantum efficiency, then, current-voltage (*I-V)* curves are acquired under varied spectra. In a next step, (*I-V*) curves are acquired while infrared (IR) and blue LED illumination is added to the sun simulator spectrum. The chosen LEDs each affect only one subcell. Figure A-2 shows the measurement spectra of the sun simulator. The black line marks the AM1.5 standard spectrum. Then, LED light is added. First only the infrared LED is turned on.

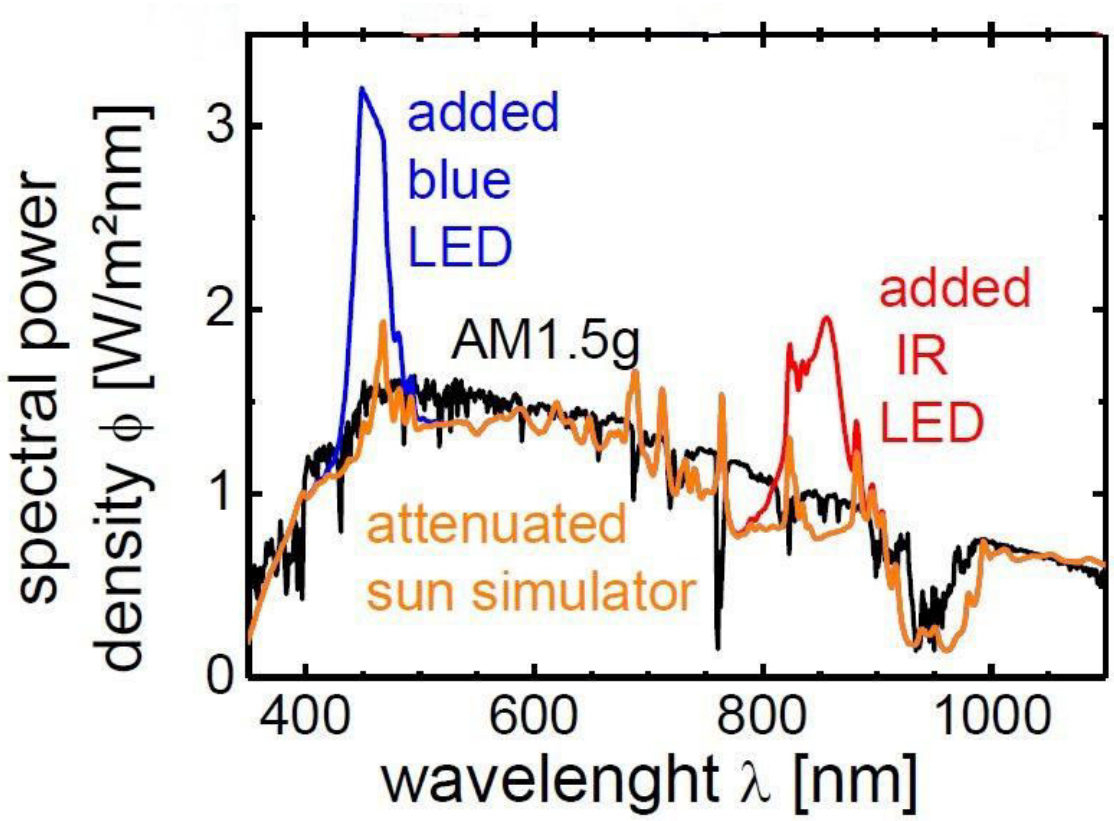

Figure A-2: The measurement spectra of the sun simulator, and the illuminated power density with extra blue and IR LEDs.

The spectrum of the sun simulator is attenuated (orange line) and the infrared (IR) and blue LED light is added (marked in red and blue) such that the integrated overall power is equal to AM1.5g (black) conditions. The intensity of the two LEDs is changed from IR on - blue off to IR off - blue on in equidistant power steps (**figure A-3**)

The current increase due to additional infrared or blue LED illumination is equivalent to an increased bottom or top cell layer thickness, respectively.

The total short circuit current density *J*sc (black squares-figures (A-4)-(A-6)) is maximized when the subcell currents are equal.

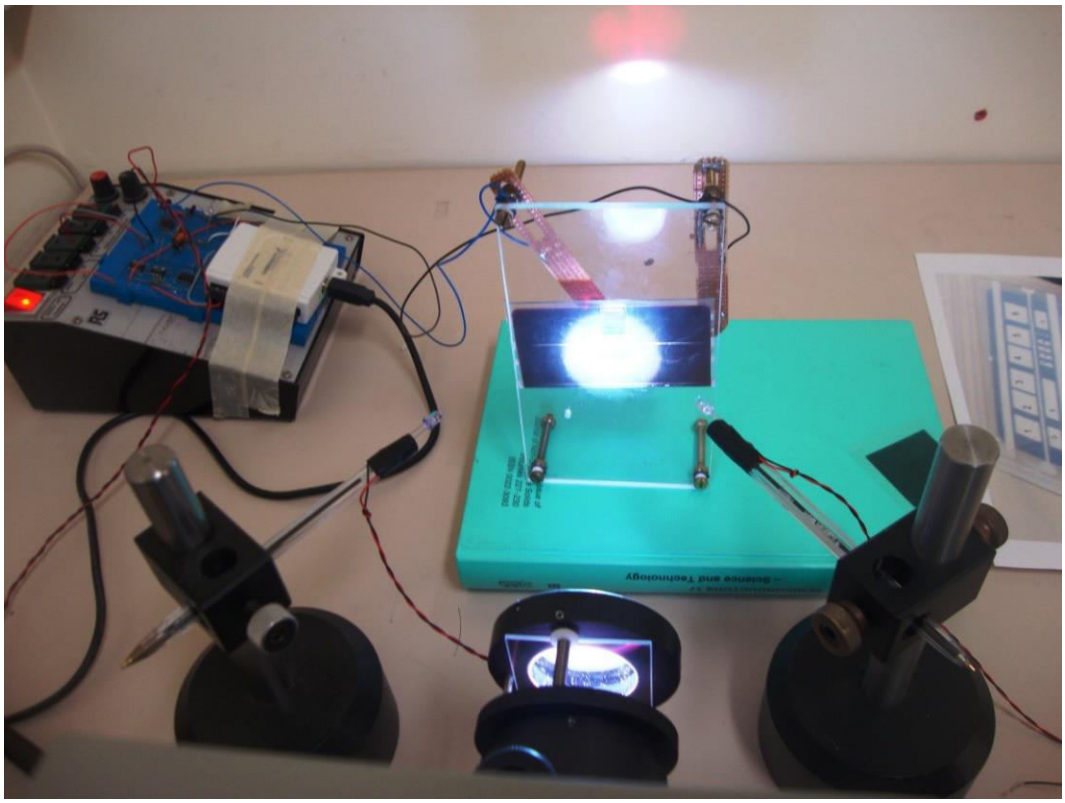

Figure A-3: Solar cell exposed to the sun simulator spectrum, and IR and blue extra LEDs

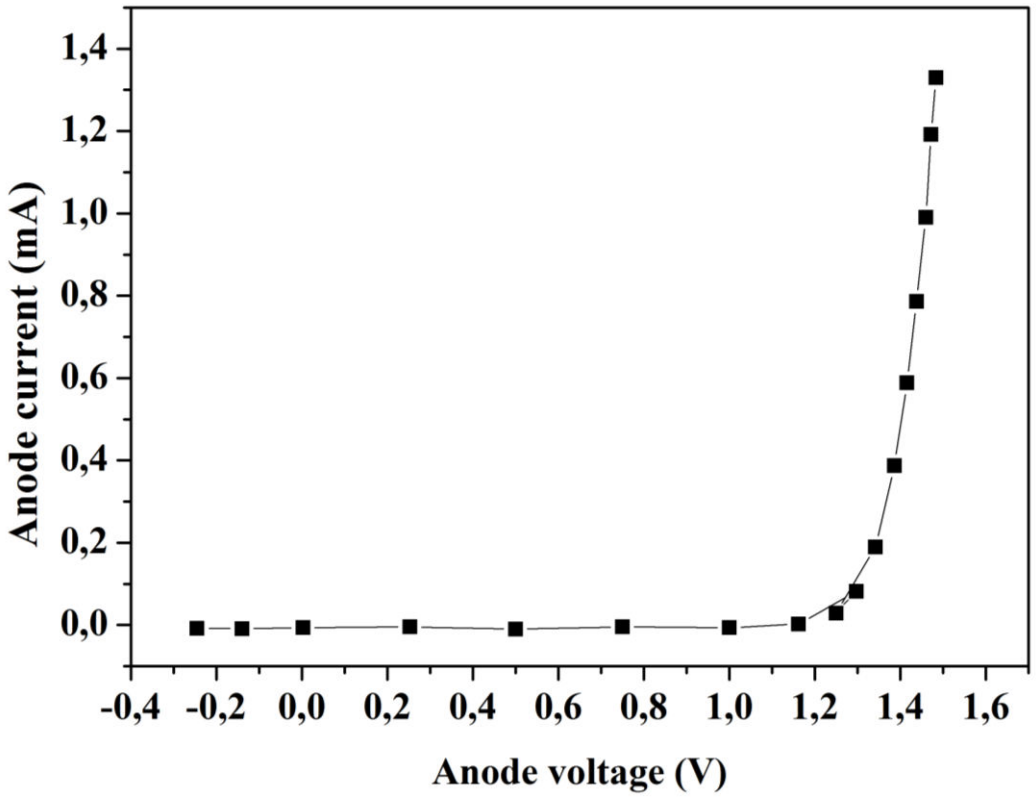

Figure A-4: Measured I-V characteristics illuminated only with blue LED.

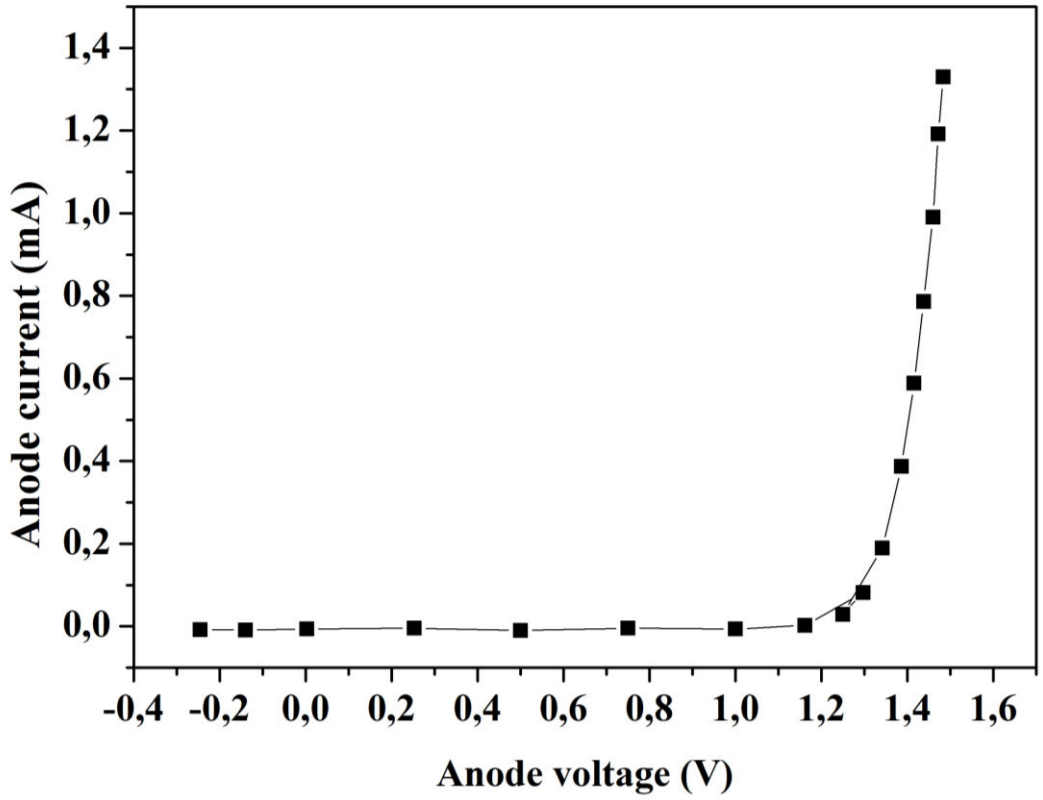

Figure A-5: Measured I-V characteristics illuminated only with IR LED.

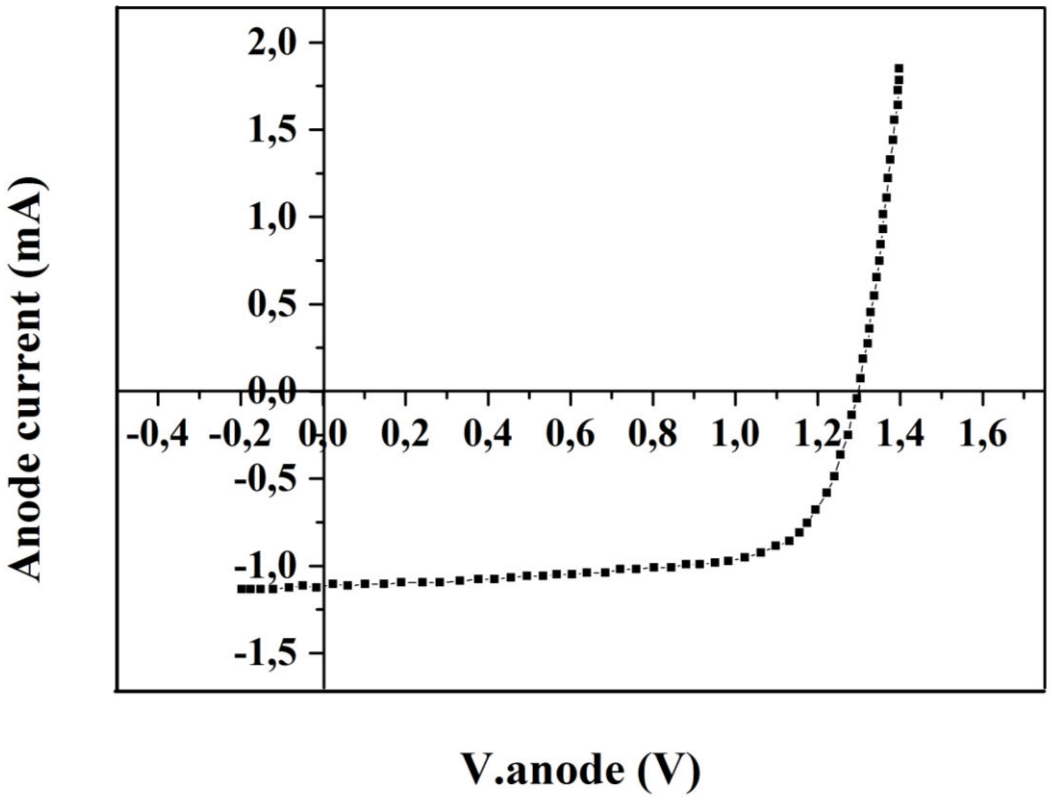

Figure A-6: Measured I-V characteristics illuminated with the spectrum of the sun simulator.

Two LEDs are used in the measurement procedure, each affects only one subcell. The spectrum of the sun simulator is attenuated (orange line) and the infrared (IR) and blue LED light is added (marked in red and blue) such that the integrated overall power is equal to AM1.5g (black) conditions. The intensity of the two LEDs is changed from IR on, blue off to IR off, blue on in equidistant power steps.

Figure A-7 shows the measured J_{sc} with varied IR and blue intensities extra LEDs, which allows the calculation of the fill factor *FF* variation (figure A-8); depending on relative illumination of the top and bottom cells by blue and IR LEDs, respectively.

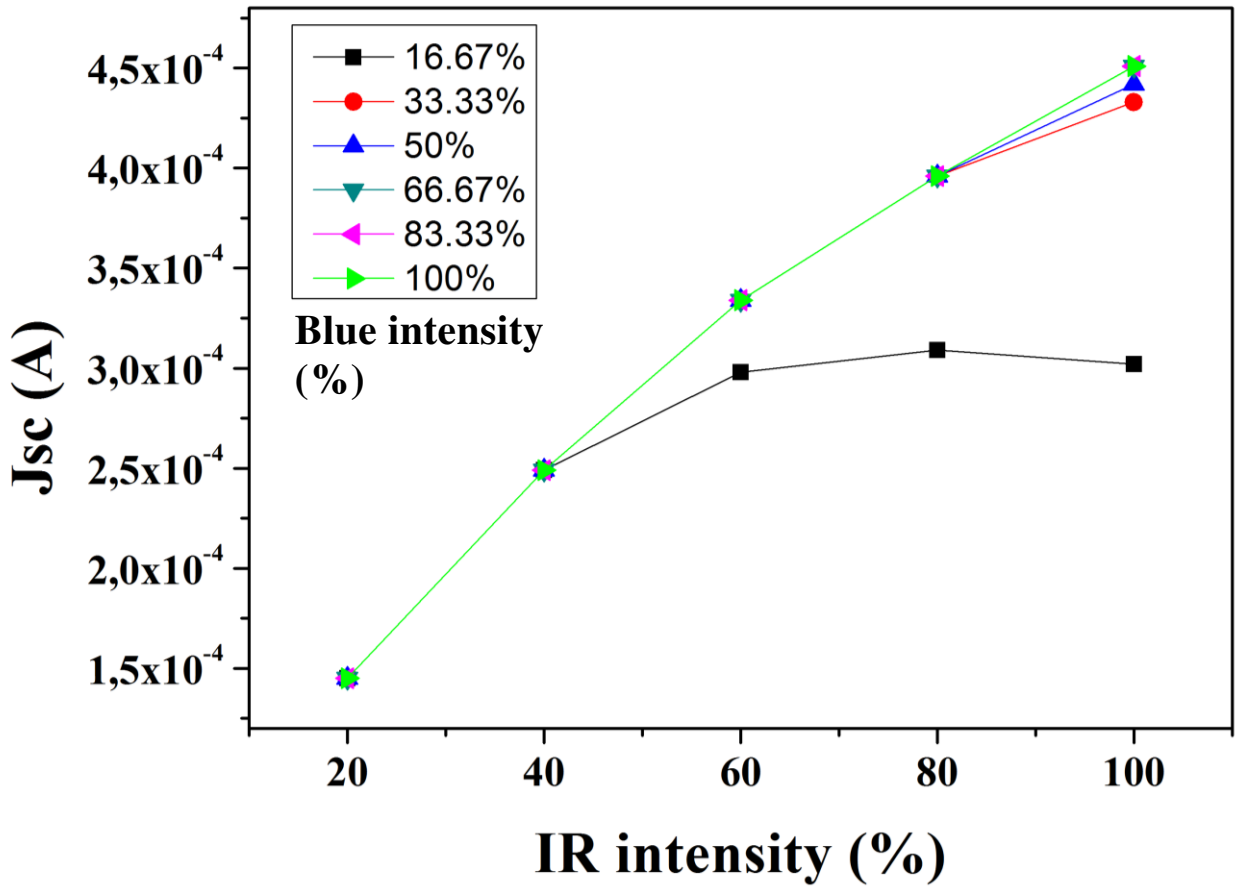

Figure A-7: The measured J_{sc} with varied IR and blue intensities extra LEDs.

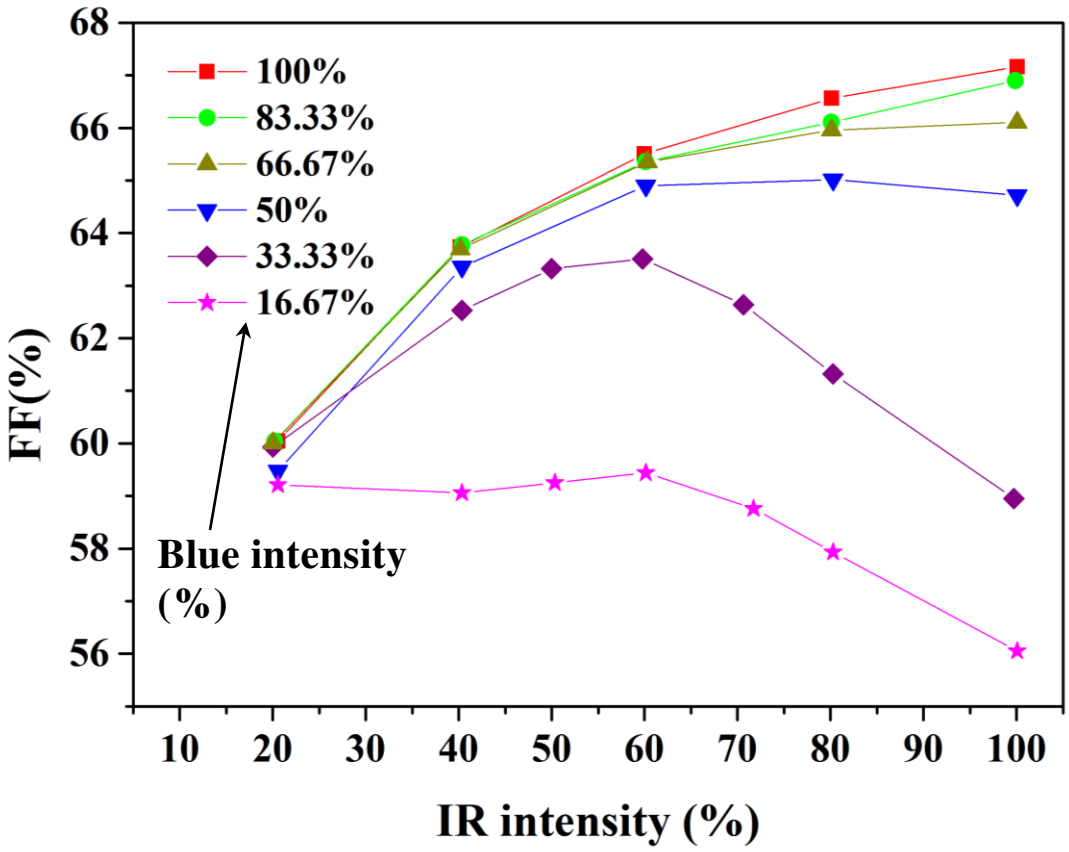

Figure A-8: The measured *FF* with varied IR and blue intensities extra LEDs.

We can see clearly that the matching currents affect the performance of the cell, the J_{sc} increase due to the additional infrared or blue LED illumination, the total short circuit current J_{sc} is maximized when the subcell currents are equal, but if one of the LEDs has less intensity, the total current is minimized.

The same remark for the fill factor, in the beginning the fill factor is minimized under the bottom current limitation even if we increase the top current, the same thing in the last, and the fill factor is minimized under the top current effect. The fill factor is maximized when the currents are matched.